BEGA – as a STARTER / GENERATOR with VECTOR CONTROL

Teză destinată obţinerii
titlului ştiinţific de doctor inginer
la
Universitatea "Politehnica" din Timişoara
în domeniul "INGINERIE ELECTRICA"
de către

Vasile Coroban-Schramel

Conducător ştiinţific:	prof.univ.dr.ing. Ion Boldea
Referenţi ştiinţifici:	prof.univ.dr.ing. Ioan Adrian Viorel
	prof.univ.dr.ing. Mircea Radulescu
	prof.univ.dr.ing. Gheorghe Daniel Andrescu

Ziua susţinerii tezei: 16.04.2009

Seriile Teze de doctorat ale UPT sunt:

1. Automatică
2. Chimie
3. Energetică
4. Ingineria Chimică
5. Inginerie Civilă
6. Inginerie Electrică
7. Inginerie Electronică şi Telecomunicaţii
8. Inginerie Industrială
9. Inginerie Mecanică
10. Ştiinţa Calculatoarelor
11. Ştiinţa şi Ingineria Materialelor

Universitatea „Politehnica" din Timişoara a iniţiat seriile de mai sus în scopul diseminării expertizei, cunoştinţelor şi rezultatelor cercetărilor întreprinse în cadrul şcolii doctorale a universităţii. Seriile conţin, potrivit H.B.Ex.S Nr. 14 / 14.07.2006, tezele de doctorat susţinute în universitate începând cu 1 octombrie 2006.

România, 300159 Timişoara, Bd. Republicii 9,
tel. 0256 403823, fax. 0256 403221
e-mail: editura@edipol.upt.ro

PREFACE

This thesis represents a contribution on the integrated starter-alternator systems used in hybrid electric vehicles powertrain. The proposed starter-alternator system is a biaxial excitation generator for automobiles (BEGA) which is a permanent-magnet synchronous reluctance motor with a dc-dc excitation winding in the rotor. The machine is driven with a three-phase inverter fed by a 48V battery stand

Outline of the thesis

The thesis is organized in eight chapters and deals with two major issues in automotive industry: valve-regulated lead acid batteries state-of-charge and integrated starter-generators for hybrid electric vehicles.

In *the first chapter* an overview of the automobile electrification trends is presented. Thirteen of the most important applications in automotive industry that use (or will use) electric actuators are treated more or less in detail.

In *the second chapter* a novel algorithm for battery internal resistance estimation, based on battery current and voltage derivative, is introduced. Then an algorithm for lead-acid batteries state-of-charge estimation is presented.

In *the third chapter* the mathematical and Matlab-Simulink model of BEGA is described. A detailed Simulink model for three-phase inverter and dc-dc excitation converter model is presented.

In *the fourth chapter* the implementation of BEGA vector control at high and unity power factor operation during motoring and generating is presented.

In *the fifth chapter* the active-flux state observer for BEGA motion sensorless control is introduced. Simulations and experiments with encoder proves the theoretical background behind the active-flux observer.

In *the sixth chapter* simulation and experimental results for BEGA driven without encoder, for a wide speed range, are presented. In *the seventh chapter* the experimental setup is described. In the *eight chapter* of the thesis are summarized the original contributions of this work.

ACKNOWLEDGEMENT

I wish to express my deeply-felt gratitude to my supervisor Prof. Ion Boldea for his guidance, support, patience and encouragement during the course of this work.

I would like to thank to Prof. Gheorghe Daniel Andreescu from Faculty of Automation and Computers, Timisoara, for the technical discussions and his support during the development of the thesis. His numerous inputs during the experimental work were invaluable.

I want to thank to all of those who contributed to my engineering education and also to my colleagues from Intelligent Motion Control Laboratory at Faculty of Electrical Engineering, Timisoara. Ph. d Student Robert Antal, Assoc. Prof. Lucian Tutelea and Dr. Sever Scridon from BEE Speed Automatizari deserve many thanks.

Finally, I am forever indebted to my father for his support and my wife for her understanding, endless patience and encouragement when it was most required.

Timisoara, March 10th , 2009
Vasile Coroban-Schramel

Coroban-Schramel, Vasile

BEGA – as a Starter/Generator with Vector Control

Teze de doctorat ale UPT, Seria X, Nr. YY, Editura Politehnica, 2009, 168 pagini, 39 figuri, 27 tabele.

ISSN: 1842-7022

ISBN : 978-973-625-861-9.

Keywords: BEGA, unity power factor, vector control, battery state-of-charge, battery internal resistance, sensorless control, active flux

Objectives of the thesis
The main objectives of the thesis are:

- To present an overview of the automobile electrification trends.
- To find an algorithm for battery internal resistance estimation.
- To introduce a novel, on-line battery state-of-charge algorithm for valve-regulated lead-acid batteries.
- To develop a simulation model for the complete BEGA control system including the three-phase PWM inverter and dc-dc excitation converter
- To implement a vector control strategy for BEGA.
- To prove that BEGA has a very large constant power speed range at unity power factor operation.
- To find a minimization strategy of the copper losses in BEGA.
- To find a strategy for improvement of BEGA electromagnetic torque response
- To develop a sensorless control strategy for BEGA operation in a wide speed range.

CUPRINS

Chapter I

Automobile Electrification Trends 8
1.1 Introduction 8
1.2. Steering system 9
  1.2.1 Hydraulic power steering system 10
  1.2.2 Electro-hydraulic power steering system 11
  1.2.3 Electric power steering system 12
  1.2.4 Steering by wire 16
1.3 Braking System 17
  1.3.1 Classification of braking system 17
  1.3.1.1 Wheel brakes 18
  1.3.2 Hydraulic brake system 20
  1.3.3 Electro-hydraulic brake systems 21
  1.3.4 Electromechanical braking system (or brake-by-wire) 22
  1.3.5 e-brake Concept 26
1.4 Electromagnetic valves 29
  1.4.1 Concept of EMVD and Operating Principle 30
  1.4.2 Variable valve timing using electromagnetic valves 30
  1.4.3. Variable valve timing using electric motors 32
1.5 Electric suspension 35
1.6 Electrically driven turbochargers 40
1.7 Exhaust-gas electric energy recovery 45
1.8 Integrated starter-alternators system 46
1.9 Clutch-by-wire 44
1.10 Double clutch transmission 50
1.11 Hybrid oil pump 55
1.12 Transfer case 60
1.13 Engine cooling system 61
Summary 65

Chapter II

Battery On-Line Modeling with Test Results and Discussion 70
2.1 Importance of battery internal resistance and state-of-charge 70
2.2. Battery internal resistance 72
  2.2.1 Review of battery internal resistance existing methods 73
    2.2.1.1 DC load pulse 73
    2.2.1.2 Electromechanical impedance spectroscopy (EIS) 74
  2.2.2 The proposed method for internal resistance estimations 75
  2.2.3 Power discharge capability 87
  2.2.4 Battery discharged power measurement 90
  2.2.5 Battery state-of-health estimation 93
2.3 Battery state-of-charge estimation 93
  2.3.1 Review of battery state-of-charge estimation 94
  2.3.2 Proposed algorithm for battery state-of-charge estimation 95
Summary 111

Chapter III

BEGA – Mathematical model and simulation results 115

3.1 Introduction 115
3.2. BEGA – Mathematical model 117
3.3 Matlab-Simulink simulation environment of BEGA 120
    A. BEGA model 121
    B. Three Phase Voltage Source Inverter Model 122
    C. BEGA DC-DC Converter model 136
    D. Stimuli 141
3.4 Simulation results 141
    3.4.1 Current controller's validation 138
    3.4.2 Speed controller validation 143
    3.4.3 Back-EMF compensation 146
    3.4.4 Unity power factor operation 147
Summary 149

Chapter IV
BEGA – Motor/Generator Operation at Unity Power Factor 151
4.1 Introduction 151
4.2. BEGA mathematical model at unity power factor 152
4.3. Dc excitation induced voltage 156
4.4 Energy conversion 157
4.5 Experimental platform and test results 158
4.6. Proposed vector control scheme at unity power factor 159
    4.6.1 Back-EMF Compensation 164
4.7 Simulation results 166
4.8 Torque response improvement 180
4.9 Experimental results 183
Summary 195

Chapter V
Active-Flux State Observer for Biaxial Excitation Generator for Automobiles (BEGA) Vector Control 198
5.1 Introduction 110
    5.1.1 Method based on stator inductance calculation 110
    5.1.2 Back-EMF integration 199
    5.1.3 Extended electromotive force (EMF) 199
    5.1.5 Model Reference Adaptive System (MRAS) 201
    5.1.6 Sliding Mode Observer 202
    5.1.7 High frequency signal injection 203
    5.1.8 Low frequency signal injection 205
    5.1.9 INFORM 205
    5.1.10 Adaptive control 207
5.2. Active flux concept 208
5.3. Active flux observer 212
    A. Active flux observer 213
    B. Position and Speed Estimator 214
5.4 BEGA vector control system 216
5.5. Digital simulation results 218
Summary 236

Chapter VI

Active-Flux Motion Sensorless Control of BEGA: digital simulations and experimental validation **242**
6.1 Digital simulations 242
  6.1.1 High speed operation 243
  6.1.2 Medium speed operation 246
  6.1.3 Low speed operation 248
6.2. Experimental results 251
6.3. Initial rotor position detection 266
Summary 271

Chapter VII

Experimental Platform and Software Implementation **273**
7.1 Experimental setup 273
7.2 Induction machine and bidirectional power inverter 274
7.3 Three phase inverter 275
7.4 Dc-link power supply 275
7.5 Current measurement 276
7.6 Position and speed measurement 277
7.7 DC-DC converter for dc excitation 277
7.8 Control hardware dSpace DS1103 278
7.9 BEGA Control Software 281
Summary 284

Chapter VIII

Conclusion and Contributions **285**
8.1 Conclusion 285
8.2 Original contributions 286

1. AUTOMOBILE ELECTRIFICATION TRENDS

This chapter presents an overview of the automobile electrification trends. The number of electric actuators used in automotive applications has increased considerable in the last years. Most of the applications such as steering-by-wire, brake-by-wire, hybrid oil pump. The X-by-wire technology involves using of electric motors instead of conventional hydraulic or pneumatic actuation.

1.1. Introduction

Since the beginning of the automotive business, electrical drives are known being a part of the car. The electrical traction drive, which was in use hundred years ago, was soon substituted by internal combustion engines, mainly because of the poor storage possibilities of the electrical energy. A next step was the introduction of some “fundamental” electrical drives like starter, generator, wiper, blower and fuel pump. These electrical drives were realized with brushed DC-motors, and even today. These functions are mainly served by conventional DC-motors. Some decades ago, electrical drives started to become one major growing field inside the car. The applications can be clustered into the following sections:

- Comfort (e.g. window lift, mirror and seat adjustment).
- Safety (e.g. ABS-motor).
- Drivetrain (e.g. water pump, engine cooling fan, electronic throttle plate)

Today, in a modern passenger car of the luxury class, one can find more than 100 electrical drives. Many of these drives are conventional DC-motors (e.g. window lift, seat adjustment, fuel pump, wiper, engine cooling fan, etc.). The main reasons why (for the time being) DC-motors are dominating the electrical drive technology in cars are:

- Costs (simplicity of the motor, existing production facilities).
- Quality (simplicity of the motor, experience over decades in the automotive industry).
- Time to market (new applications can be served by modifying existing ones).
- Functionality is achievable.

The most important technical trend in the automotive industry is that more and more mechanics and
hydraulics will be substituted by “mechatronics”. Some examples are the electrical throttle plate (avoiding the well-known cable) and the electrical steering assistance (substituting the belt-driven hydraulic pump). The main challenges are, to realize these functions at least with the same quality level like before and to guarantee low costs.

High-temperature electronics will become a decisive success factor. Because of miniaturization and integration and because of the ever increasing ambient temperature under the hood, there is a very strong necessity to realize electronic systems that can operate at temperatures of 120°C and even above. For example in hybrid oil pump the oil temperature is defined for a range of 40 to 120 oC and the electric motor is immersed in the oil

1.2. Steering system

The steering system converts the rotational movement of the steering wheel into a displacement of the vehicle steering wheels.
The steering ratio is defined as the ratio of steering wheel angle to front wheel steer angle (see Fig.1.1):

$$r_t = \frac{\delta_{fw}}{\delta_{sw}} \tag{1.1}$$

where: r_t is the steering transmission ratio, δ_{fw} is the front wheel steer angle, δ_{sw} is the steering wheel steer angle.

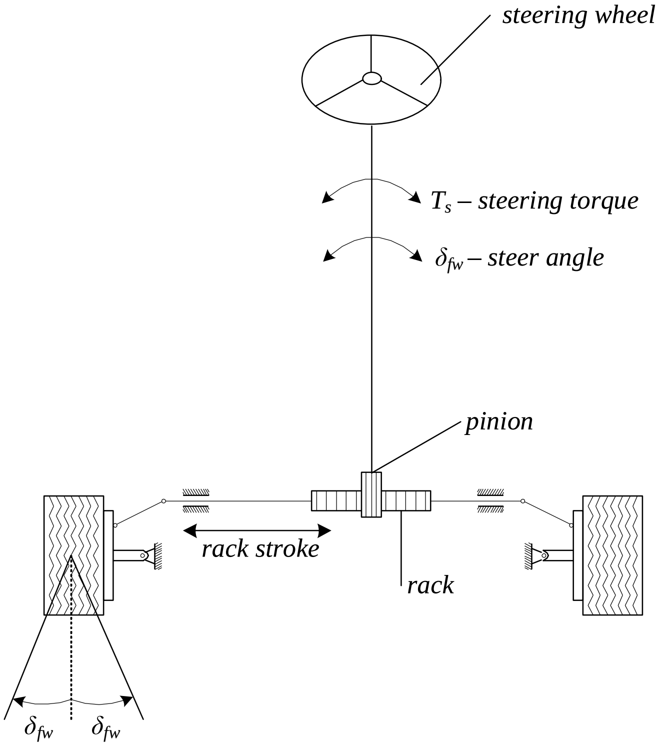

Fig.1.1. Basic principle of steering system

Classification of steering systems

The steering systems can be classified as a function of the energy source applied to the front wheels:

- Manual (muscular-energy) steering system in which the steering torque/force is produced exclusively by the driver. Such steering system is generally found only on small vehicles because the torque that the driver has to apply in the case of larger vehicles is often too great for most persons, especially when the vehicle is stopped or travelling at low speed. Usually, if the actuating force at the steering wheel exceeds 250N, this type of steering system cannot be used and power assistance becomes necessary.
- Power-assisted steering system in which the steering torque/force is produced by the muscular energy of the driver and by an energy source. This type of steering system is currently used in high-speed vehicles such as cars. Among the drawbacks of power-assisted steering systems, there is the fact that they require many parts which increase the weight and the costs of the vehicle. They also require a lot of power from the engine to drive the pump which is not acceptable if the energy consumption of the vehicle is a critical factor, such as in an electric vehicle where the power efficiency must be kept as high as possible to obtain a suitable range
- Power-steering system (full power steering or steering-by-wire) in which the steering torque/force is produced exclusively by an energy source in the vehicle

Another classification of the steering system can be done considering the mechanical connection between the steering wheel and the wheels:

- Steering system with mechanical connection (classical solution)
- Steer-by-wire systems without a mechanical connection.

From the assistance source of energy, the steering systems can be classified as follows:

- Hydraulic power steering system
- Electro-hydraulic steering system
- Electric steering system

1.2.1.1 Hydraulic power steering system

Hydraulic power steering systems are still most widely used. This method of using oil under pressure to boost the servo is sophisticated but advantageous in terms of cost, space and weight. The oil pump is directly driven by the engine and constantly generates hydraulic power (Fig. 1.2). No hydraulic power is generated when the engine is off, so that the driver is not able to turn the steering wheel. The hydraulic power steering is design in such a way that a sufficient supply volume is available for fast steering movements even at low speed engine. In order to limit the supplied oil volume at high speeds, limiting valves is used. This valve is a pressure relief valve used to prevent a dangerous build-up of the pressure when hydraulic cylinder piston reaches the end of the cylinder. This valve limits the supply flow to about 8 l/min in order to prevent the hydraulic losses that would occur at high engine speeds, also. Depending on the driving assembly and pump design, the additional fuel consumption can be between 0.2 and 0.8L/100km [1.1].

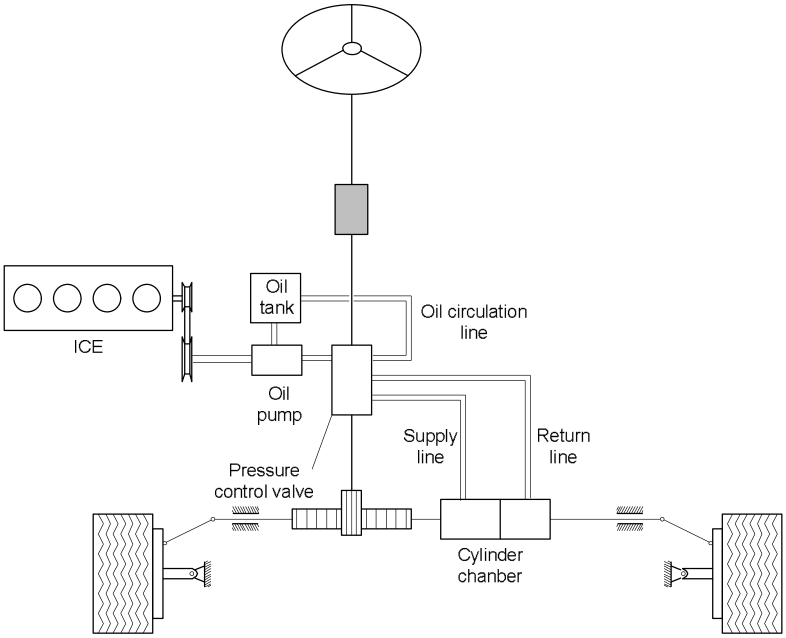

Fig.1.2. Schematic diagram of a hydraulic power assisted steering system

1.2.1.2 Electro-hydraulic power steering system

The schematic of the electro-hydraulic power steering system is shown in Fig. 1.3. With electro-hydraulic power steering system (EHPS), the power steering pump driven by the engine via V-belts is replaced with a pump driven by an electric motor. The pump is electronically controlled – when servo boost is not required, the oil supply is reduced. One big advantage of the electro-hydraulic power steering system over hydraulic power system is that the first allows greater flexibility with regard to the position of the power pack. Compared with purely hydraulic system, the pressure lines can be made considerable shorter and there is no cooling circuit.

The electro-hydraulic power steering systems offer the following advantages over the hydraulic power steering system [1.1]:

- The pressure supply unit can be placed in an appropriate position
- Servo boost is also guaranteed by the electrical pressure supply even when the engine is not running (suitable for hybrid electric vehicles, also)
- Electric pressure controlled system generates only the amount of oil required for a particular driving situation. Compared with standard power steering systems, the amount of energy is reduced even more than 20%.
- The steering characteristics (sensitivity, speed dependency) can be adjusted by the control electronics individually for a particular vehicle.

In Table 1. are listed the specifications and main dimensions for an IPMSM that is employed in a 42V-EPHS system in an automobile.

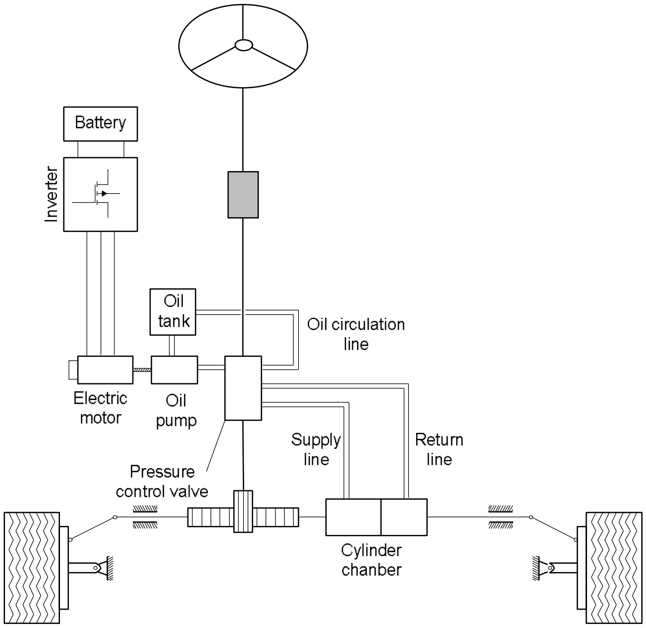

Fig. 1.3 Schematic diagram of an electro-hydraulic power assisted steering system

Table 1. Specification for IPMSM [1.8]

Item	Value	Unit
No. of phase/slots/pole	3/9/6	-
DC Link Voltage	42	V
Rated Speed	3500	rpm
Rated Torque	9.8	Nm
Resistance per phase	12.5	Ω
Air-gap	1.0	mm
Stack Length	40	mm
Core material	S18	-
Br	1.2	T

1.2.1.3 Electric power steering system

The bypass of the hydraulic circuit and direct steering boost with the help of an electric motor has additionally advantages in terms of space and weight compared with electro-hydraulic steering systems due to the missing of hydraulic components. Also, more variations of the steering boost are possible, due to the electronic signal processing.

The electrical servo unit can be installed on the steering column pinion or gear rack. The steering angle loads and maximum gear rack forces are, depending on the arrangement, about 650kg and 6000N up to 1300 kg and 10000N [1.2].

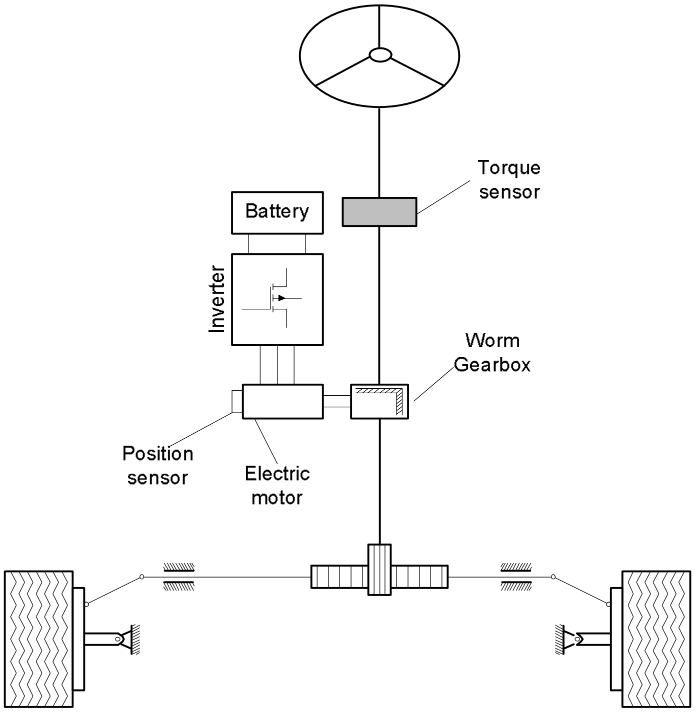

Fig. 1.4 Schematic diagram of an electric power-assisted steering system

Electric power steering (EPS or EPAS) is designed to use an electric motor to reduce effort by providing assist to the driver of a vehicle. Most EPS systems have variable assist, which allows for more assistance as the speed of a vehicle decreases and less assistance from the system during high-speed situations. This functionality requires a delicate balance of power and control that has only been available to manufacturers in recent years. The EPS system has replaced the hydraulic steering system (HPS or HPAS) in many passenger cars recently: EPS is so far limited to passenger cars, as a higher voltage electrical system is necessary to operate EPS in larger vehicles.

Unlike HPS systems, EPS systems do not require a hydraulic pump, which is belted into the engine. Rather the EPS system's electric motor is powered by the vehicle's alternator which is belted into the engine. The efficiency advantage of an EPS system is derived from the fact that it is activated only when needed. Thus, a vehicle equipped with EPS may achieve an estimated improvement in fuel economy of 3% compared to the same vehicle with conventional HPAS (Fig. 1.5). However, any fuel economy benefit of EPS over HPS can be negated in situations where a vehicle is not driven on straight-aways very often, or where a vehicle's wheels are out of alignment

An electrical steering system design by ZF has currents up to 105A with a 12V electrical system and up to 35A with a 42V system [1.1].

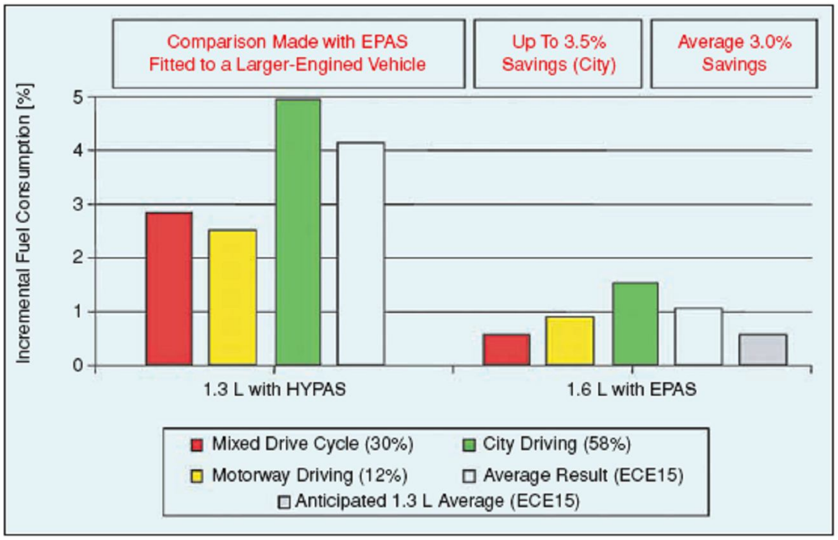

Fig. 1.5 Fuel consumption comparison between EPAS and EHPS [1.16]

Depending on the point of assist in the system, electric power steering systems can be classified into three categories (Fig. 1.6):

- Column Assist
- Pinion Assist
- Rack Assist

The assist torque versus vehicle speed for a typical electric power steering system is shown in Fig 1.7. The value of the assist torque is increasing with the speed, for the same steering angle.

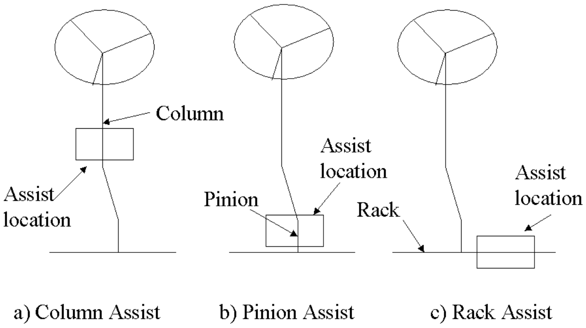

Fig. 1.6 Schematic Representations of Electric Power Steering System Configurations [1.13]

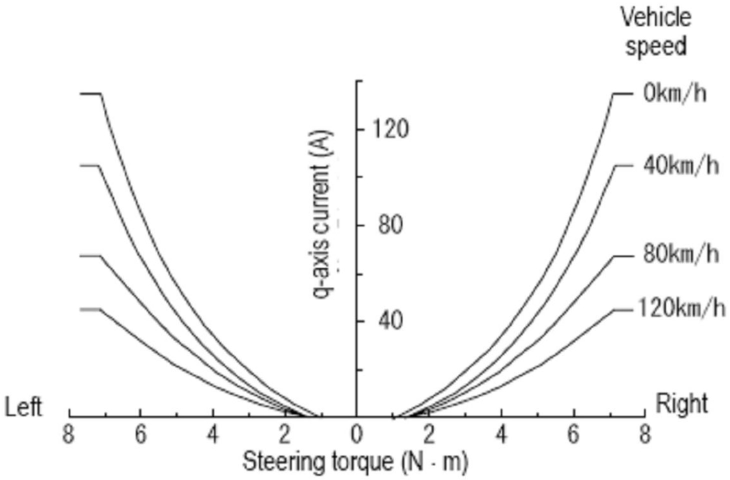

Fig. 1.7 The assist torque versus the steering wheel torque of a typical electric power steering system

The electric motors that are used in electric power steering system should have low cogging torque, low torque ripples, and high torque density. Conventional PMSM that are employed in EPS systems generally have 1.5 slot/pole ratio (such as 6/4, 12/8, and 18/12), or a 3.0 slot/pole ratio (such as 36/12). The motors with 1.5 slot/pole ratio have high, low frequency cogging torque and large torque ripples. The motors with 3.0slot/pole ratio have high, low frequency cogging torque large torque ripples and low torque density [1.12].

Fig. 1.8 Electric Power Steering Unit [1.4]

1.2.1.4 Steering by wire

The aim of steer-by-wire technology is to completely do away with as many mechanical components (steering shaft, column, gear reduction mechanism, etc.) as possible. Completely replacing conventional steering system with steer-by-wire holds several advantages, such as:

- The absence of steering column simplifies the car interior design.
- The absence of steering shaft, column and gear reduction mechanism allows much better space utilization in the engine compartment.
- The steering mechanism can be designed and installed as a modular unit.
- Without mechanical connection between the steering wheel and the road wheel, it is less likely that the impact of a frontal crash will force the steering wheel to intrude into the driver's survival space.
- Steering system characteristics can easily and infinitely be adjusted to optimize the steering response and feel.

Presently, there are no production cars available that rely solely on steer-by-wire technology due to safety and reliability concerns, but this technology has been demonstrated in numerous concept cars

The architecture of steering-by-wire system is shown Fig. 1.9.

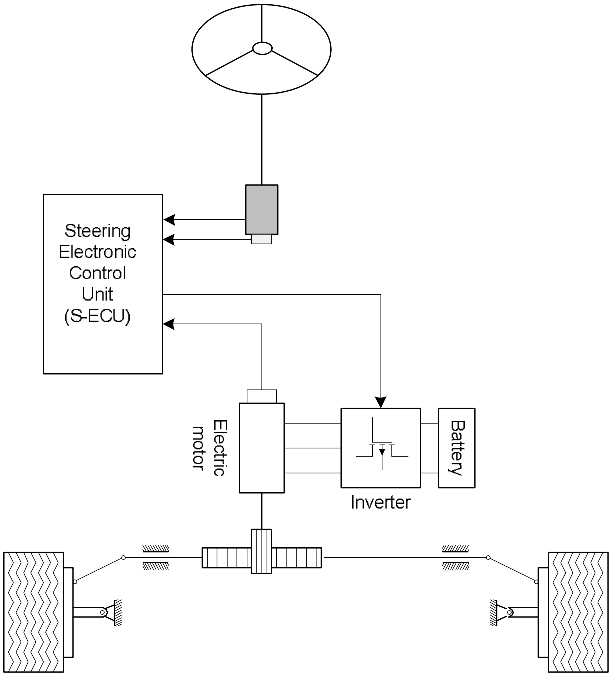

Fig. 1.9 Electrical steering-by-wire system architecture

The steering wheel angle is measured with a position sensor and provides the information to the steering electronic control unit (S-ECU). Then the S-ECU is controlling the electric motor so that the steering angle is adjusted according to the driver request (wheel steering angle).

From the efficiency pint of view the steering-by-wire systems seems to be the best solution. Anyway, the major problems in these systems are related to the safety. Many redundant systems are proposed in the literature regarding this major concern.

1.3 Braking system

The braking system of a vehicle has the following functions:

- Reducing the speed of the vehicle
- Bringing the vehicle to a halt
- Keeping the vehicle stationary when it is stopped
- Prevent unwanted acceleration during downhill driving

On most conventional car braking systems, the force applied by the driver is transmitted mechanically by the lever action of the brake pedal to the vacuum brake servo and from there in amplified form to the master cylinder. The pressure thus generated is used to achieve the desired braking effect with the individual brakes on each wheel.

1.3.1 Classification of braking system

The architecture of the braking system used in passenger cars is shown in Fig. 1.10. The brake pedal forms the interface between the driver and the braking system. The pedal brake transmits the foot force on the pedal exerted by the driver to the brake booster via the push rod. The brake booster boosts the foot force applied by the driver at the pedal by adding an “auxiliary force”. The modulator is represented by the inlet and outlet valves commanded by the electronic control unit. The wheel braking can be performed using: i) an electric generator that converts the mechanical energy in electric energy, ii) conventional braking system, iii) thermal engine – it uses the energy produced in the fourth (exhaust) stroke of the engine for braking, as pressure is developed against the closed discharge outlet.

The vacuum booster is used in most modern hydraulic brake systems. The vacuum booster is attached between the master cylinder and the brake pedal and multiplies the braking force applied by the driver. This force, in addition to the driver's foot force, pushes on the master cylinder piston. A relatively small diameter booster unit is required; for a very conservative 50% manifold vacuum, an assisting force of about 1500 N is produced by a 20cm diaphragm with an area of 0.03m2. The diaphragm will stop moving when the forces on both sides of the chamber reach equilibrium

The hydraulic booster has a greater energy density, compared with vacuum booster and consequently, it is needed for less space to install.

Main defect of traditional structure of the brake boosters is the necessity of an external energy source. The analysis of redistribution of power streams occurring during at braking of the automobile shows that it is possible to use the force component of the driving automobile kinetic energy for the drive of a booster (so-called kinetic booster). The power consumed by a booster is taken from power developed during brake action thereby it promotes vehicle slowing down.

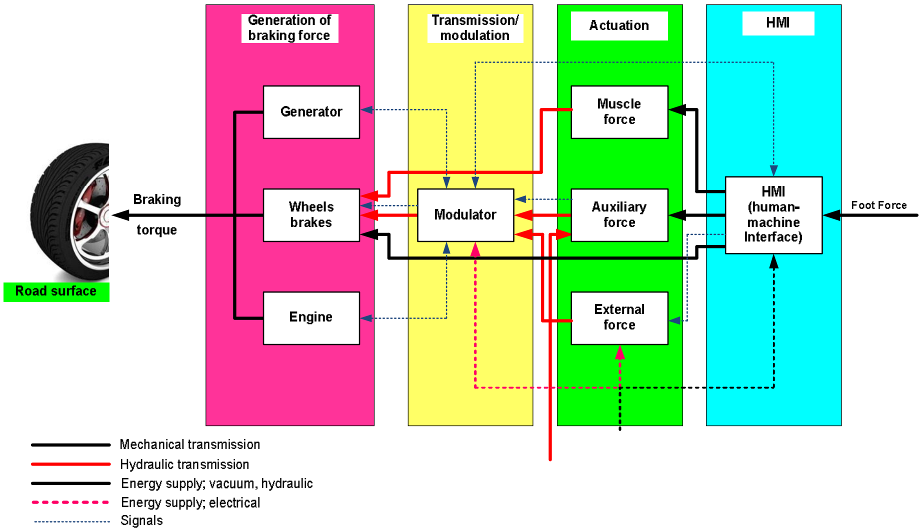

Fig. 1.10 Generic architecture of the braking system of an automobile

A classification of brake system used in automobiles is given in Fig. 1.11.

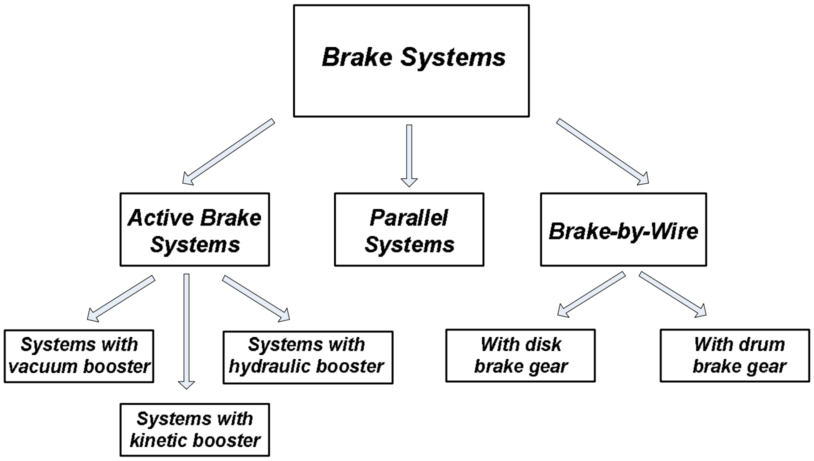

Fig. 1.11 Brake systems classification

1.3.1.1. Wheel brakes

In conventional braking systems there are two types of brakes:

- Drum brakes
- Disc brakes

The working principle of these two wheel brake systems is shown in Fig. 1.12.

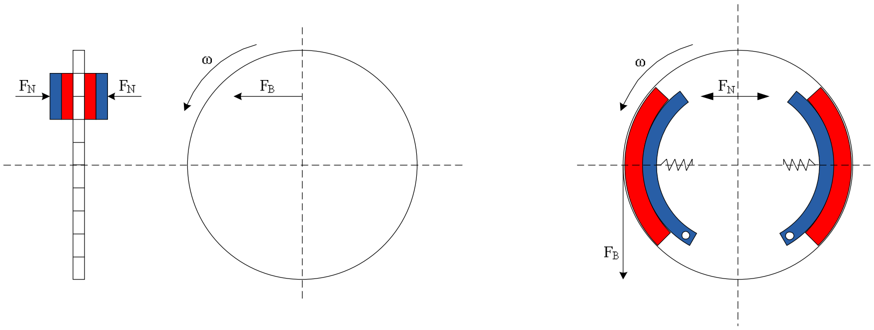

Disk brake

Drum brake

Fig. 1.12 Types of wheel brakes

Drum brakes

A drum brake assembly is used to bring the rear wheels of most vehicles to a stop. Fluid pressure from the master cylinder causes the wheel cylinder to push the brake shoes against the brake drums which are attached to the vehicle's rear wheels. The friction between the stationary shoes and the revolving drums causes the drums to slow and stop the rear wheels. Worn drums and shoes, however, can cause unreliable stopping, excessive pedal effort, or brake pedal pulsation.

Advantages

The advantages of drum brakes, which are still used in modern cars, are:

- There can be engineering and cost advantages. They are often applied to the rear wheels since most of the stopping happens in the front of the vehicle and therefore the heat generated in the rear is significantly less.
- Drum brakes are also occasionally fitted as the parking (and emergency) brake even when the rear wheels use disk brakes as the main brakes. In this situation, a small drum is usually fitted within or as part of the brake disk.

An advanced technology hybrid car using drum rear brakes is the Toyota Prius. (4-wheel discs are used in certain markets - Hybrid vehicles greatly reduces everyday wear on braking systems owing to their energy recovery motor-generators, see regenerative braking).

Disadvantages

The disadvantages of drum brakes are:

- When the drums are heated by hard braking, the diameter of the drum increases due to thermal expansion of the material, and the brakes must be further depressed to obtain effective braking action. Due to the design of drum brakes, the shoe (friction material) is in contact most of the way around the drum, reducing cooling effectiveness compared to disc brakes which have a much lower contact ratio.

- The higher contact ratio leads to an overheating or glazing of the brake lining adhesive. This effect can lead to driver panic and brake failure in extreme circumstances. Under normal driving conditions it is seldom noticed, especially when drums of appropriate size are fitted.

Disk brakes

Because a disc brake assembly can absorb more heat than a drum brake assembly, most cars use disc brakes for their front brake systems. When the brake pedal is pushed, brake fluid from the master cylinder compresses the brake pads against the rotors attached to the vehicle's front wheels. The friction between the stationary pads and the revolving rotors causes the rotors and wheel to slow and stop. In day-to-day driving, these rotors and pads are subject to much abuse, and should be checked periodically for wear. Faulty disc brakes can cause excessive pedal travel, pumping or fighting pedal, vibration during braking action, and brake failure.

Advantages

The advantages of disc brakes are:

- better stopping performance than comparable drum brakes, including resistance to "brake fade" caused by the overheating of brake components, and are able to recover quickly from immersion (wet brakes are less effective).
- Unlike a drum brake, the disc brake has no self-servo effect and the braking force is always proportional to the pressure placed on the braking pedal or lever. Many early implementations for automobiles located the brakes on the inboard side of the driveshaft, near the differential, but most brakes today are located inside the wheels. An inboard location reduces the unsprung weight and eliminates a source of heat transfer to the tires. For example this is very important in Formula One racing.

Disc brakes were most popular on sports cars when they were first introduced, since these vehicles are more demanding about brake performance. Discs have now become the more common form in most passenger vehicles, although many (particularly light weight vehicles) use drum brakes on the rear wheels to keep costs and weight down as well as to simplify the provisions for a parking brake. As the front brakes perform most of the braking effort, this can be a reasonable compromise.

1.3.2 Hydraulic brake system

The hydraulic brake system has a number of substantial advantages over the conventional pneumatic brake system:

- High response speed
- Better assembling
- More efficient distribution of drive forces between front and rear wheels
- High efficiency (around 0.95)

- Considerable economic advantages

1.3.3. Electro-hydraulic brake system

Electro-hydraulic braking system (EHBS) represents a new generation of braking systems.
With an electrohydraulic braking system, this purely mechano-hydraulic chain of effect is broken. In its place there are:

- sensors,
- an ECU connected to the brake-pressure modulators, and
- a source of hydraulic pressure.

Under normal operating conditions, there is no mechanical link between the brake pedal and the wheels cylinders. The system detects the brake pedal travel electronically using duplicated sensor signals in an ECU (electronic control unit). The hydraulic modulator controls the pressure in the individual brakes by means of solenoid valves. Operation of the brakes is affected hydraulically using brake fluid as the transmission medium.

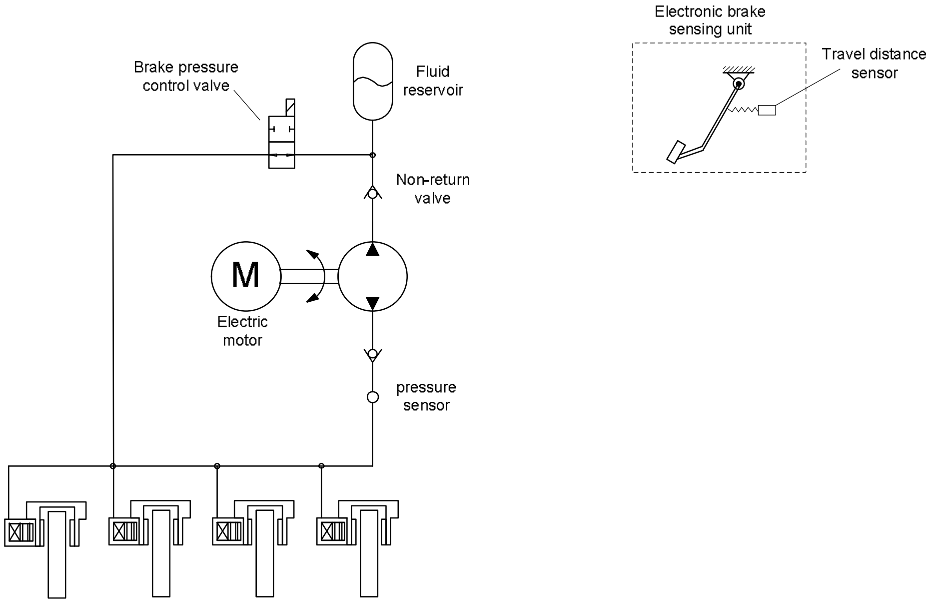

Fig. 1.13 Schematic diagram of an electro-hydraulic brake-by-wire system

Compared to the operation of conventional braking systems, by depressing the brake pedal with the electro-hydraulic brake system the appropriate command is transmitted electronically to the electronic controller of the hydraulic unit. This determines the optimum braking pressure and actuates the brake calipers hydraulically.

Brake pressure regulator involves a high pressure pump (see Fig 1.13) which is driven by an electric motor controlled by an electronic control unit (ECU). The pressure outlet of the pump is connected to the brake caliper of the wheel brake. The brake-fluid reservoir is connected to the inlet of the high-pressure pump

Advantages of the electro-hydraulic braking system are:

- Shorter braking and stopping distances
- Optimized braking and stability behavior
- Optimized pedal feel
- No pedal vibration during ABS mode
- Improved crash worthiness
- Improved packaging, less installation effort
- Capable of realizing all required braking and stability functions such as ABS, EBD, TCS, ESP, BA, ACC etc.
- Can be easily networked with future traffic management systems

The brake-by-wire systems use inputs from a brake pedal position sensor (that works much like a throttle position sensor), wheel speed sensors, a steering angle sensor, yaw rate and lateral acceleration sensors to determine the optimum amount of brake pressure to apply at each wheel.

1.3.4 Electromechanical braking system (or brake-by-wire)

Electromechanical braking systems (EMB), also referred to as brake by-wire, replace conventional hydraulic braking systems with a completely “dry” electrical component system. This occurs by replacing conventional actuators with electric motor driven units. This move to electronic control, eliminates many of the manufacturing, maintenance, and environmental concerns associated with hydraulic systems.

Because there is no mechanical or hydraulic back-up system, reliability is critical and the system must be fault-tolerant. Implementing EMB requires features such as a dependable power supply, fault-tolerant communication protocols (i.e., TTCAN and FlexRay™), and some level of hardware redundancy.

As in electro-hydraulic braking (EHB), EMB is designed to improve connectivity with other vehicle systems, thus enabling simpler integration of such higher-level functions as traction control and vehicle stability control. This integration may vary from embedding the function within the EMB system, as with ABS, to interfacing to these additional systems using communication links.

Both EHB and EMB systems offer the advantage of eliminating the large vacuum booster found in conventional systems. Along with reducing the dilemma of working with increasingly tighter space in the engine bay, this elimination helps simplify production of right- and left-hand drive vehicle variants. When compared to those of EHB, EMB systems offer decreased flexibility for the placement of components by totally eliminating the hydraulic system.

The key benefits of electromechanical brake systems are:

- Connects with emerging systems, such as adaptive cruise control
- Reduces system weight to provide improved vehicle performance and economy
- Assembles the system into the host vehicle simpler and faster

- Reduces pollutant sources by eliminating corrosive, toxic hydraulic fluids
- Removes the vacuum servo and hydraulic system for flexible placement of components
- Reduces maintenance requirements
- Supports features such as hill hold.
- Removes mechanical components for freedom of design
- Eliminates the need for pneumatic vacuum booster systems

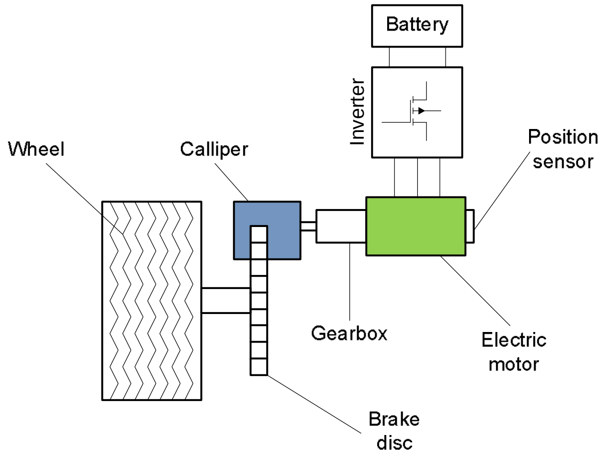

Fig. 1.14 General architecture of an electromechanical braking (EMB) system for one wheel

The general architecture of an electromechanical braking (EMB) system in a drive-by-wire car is shown in Fig. 1.14.
Once the driver inputs a brake command to the brake system controller (BSC) via the brake lever position, four independent brake commands are generated by the BSC based on brake lever position and high level brake functions such as anti-lock braking system (ABS) or vehicle stability control (VSC). These command signals are sent to the four electric calipers (e-calipers) via a communication network. Of course, these four break control units can be inside of the same chip.

In each e-caliper a controller uses the brake command (received from BSC) as a reference input. The controller provides drive control commands for a power control module. This module controls three phase drive currents for the brake actuator which is an electric motor, energized by 42V sources. In addition to tracking its reference brake command, the caliper controller also controls the position and speed of the brake actuator. Thus, two sensors are vitally required to measure the position and speed of the actuator in each e-caliper. Because of the safety critical nature of the application, even missing a limited number of samples of these sensory data should be compensated for. Hoseinnezhad et al. have proposed a new memory efficient method with a low computational overhead to compensate for missing samples of such vital sensory data [1.15]-[1.17].
In modern vehicle braking systems, speed vehicle, steer angle, wheel slip, yaw rate and engine torque are essential information for better performance of braking

system during cornering and for guaranteeing a better stability of the vehicle (Fig. 1.16).

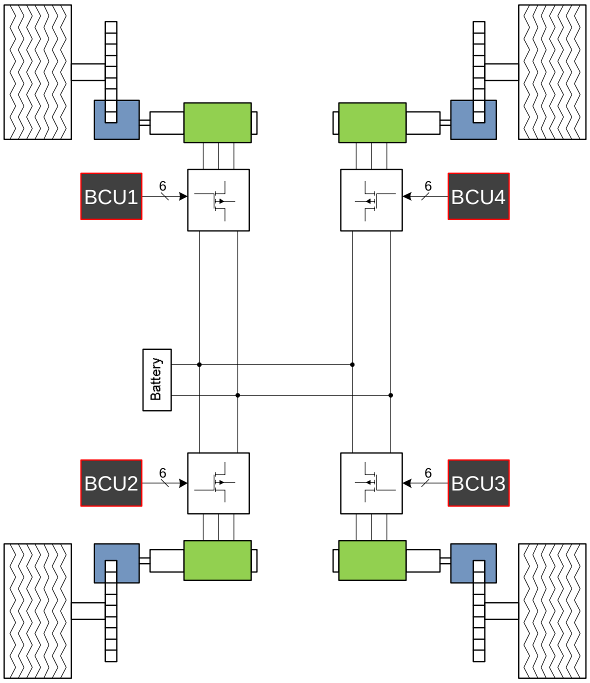

Fig. 1.15 General architecture of an electromechanical braking (EMB) system in an automobile

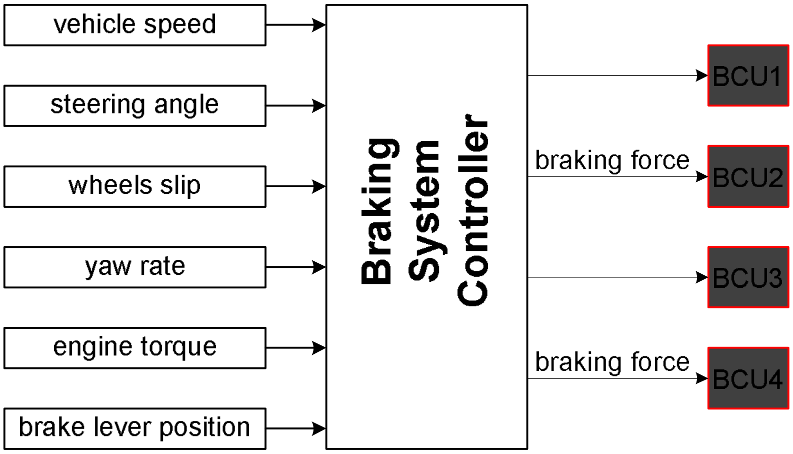

Fig. 1.16 Inputs/Outputs of an electromechanical braking (EMB) system

The base brake function allows interpretation of the driver's demand and the brake actuation systems to decelerate the vehicle. The electronic pedal module contains a device that emulates the desired force versus displacement characteristics, as well as the force and travel sensors required to interpret the driver's demand. Having an architecture with brake clamp force control rather than position control is acceptable during brake actuation. During stand-by, however, position control is required to manage the air gap between the brake pads and brake rotor. Both modes of operation are achieved by switching between outer position and force control loops across the contact point between the brake pads and disc brake rotor. Advanced braking functions such as anti-lock braking, traction control, vehicle stability, and chassis control allow optimization of vehicle braking and stability, but are not required for basic deceleration performance.

The brake force control system diagram, for one wheel, is shown in Fig. 1.17. A typical profile for the motor speed, torque and braking force during actuation is given in Fig. 1.18.

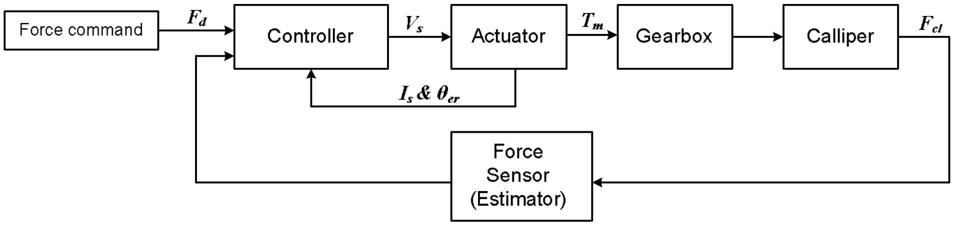

Fig. 1.17 EMB force control system structure [1.24]

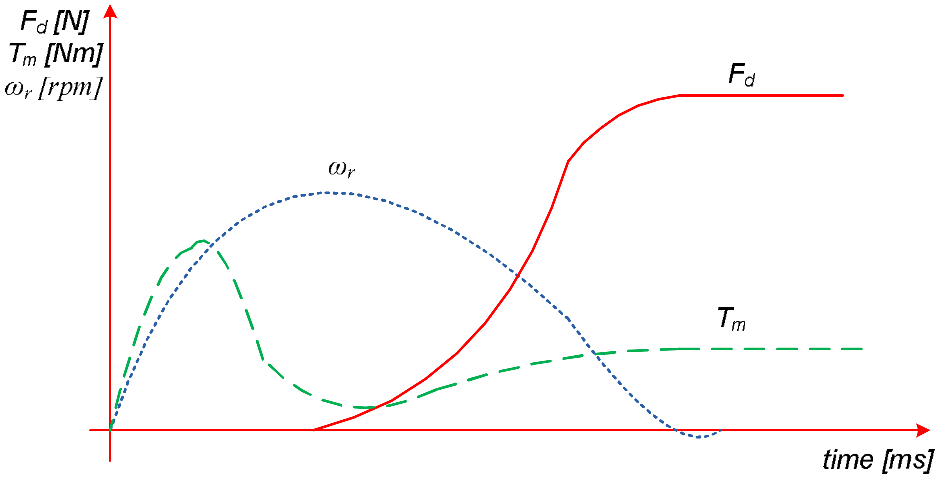

Fig. 1.18 Typical profile for motor speed, motor torque and braking force vs time during braking

In contrast to hydraulic brakes, where the clearance of brake pads adjusts automatically when the hydraulic pressure is released, electro-mechanical brakes must actively adjust the clearance by actuator rotor movement.

To perform precise actuator rotor release, the “kiss position” point of contact between the brake pads and the disk must be known. The inner brake pad can then be moved to a defined position in order to adjust the desired clearance. It is also necessary to know the contact point between the pads and the disk because this point is also the start braking position, when clamping brake force is about to begin. The “kiss position” detection algorithm is first run for initialization of the EMB actuator when the automobile system is started. It also processes the brake signals of individual braking applications during normal driving, to preserve the zero value and to continually adapt this “kiss position” to be more immune to the brake pads’ wear. The car braking behavior is preserved for the driver’s comfort, and if an individual brake pad must be replaced, the EMB controller can issue a notification.

Requirements for brake-by-wire systems

There are several requirements for automotive brake-by-wire systems [1.26]:

- Safety - after one arbitrary fault, the system must be available in a satisfying manner e.g., the brakes have to work with an adequate brake force.
- Reliability - the reliability of a by-wire system must be at least as high as a comparable mechanical system.
- Availability - the availability must be at least as high as present systems.
- Maintainability - the maintainability intervals must be at least as long as present systems.
- Lifetime - the lifetime must be at least as long as present systems.
- Costs - must be not more than to those of conventional systems.
- Compartment - must be small enough for easy integration of the components.
- Actuators - the brake actuator must be free of braking torque in case of power loss.
- Sensors - triple redundancy shall be used for the pedal sensors to get one valid pedal measurement by the loss of one sensor.
- Power supply - two independent power supplies must be used.
- Communication - the communication system must be fail-operational after one fault.
- Software - the software must be certified

1.3.5 e-brake® Concept

e-brake® is a new "brake-by-wire" technology developed at the German Aerospace Center and it is bases on an electric powered controlled friction brake with high self-reinforcement capability. This is a purely electromechanical braking system which could replace in the near future the conventional hydraulic or pneumatic braking system. A comparison of the conventional braking principle and the electronics braking principle is illustrated in Fig 1.19.

In the conventional braking system the braking (actuation) force has to be built up directly. The new brake concept merely tries to replace hydraulic or pneumatic brake units with electro-hydraulic, electro-pneumatic or all electric powered solutions. For an all electric brake-by wire approach the electric motor has to build up the full normal force (Fm=Fn).

Furthermore the actuator has to supply the energy absorbed by and then stored within the elastic caliper. This results in an extremely high energy requirement for the braking actuator. Further capacity has to be provided to guarantee high system dynamics considering the high inertia within the power train. To achieve these goals large, heavy and expensive electric actuators, spindle units or gears have to be used leading to increased space requirements and increased primary un-sprung masses within the chassis.

In contrast, the EWB uses the vehicle's momentum to assist the electric actuator. An auxiliary force, Faux, derived from the self-reinforcement effect is used to help build up the normal force. Therefore the braking actuator only has to supply a small portion of the required normal force. Furthermore, much of the energy needed to extend the caliper is taken from the vehicle's kinetic energy.

The Wedge Principle

From a mathematical point of view the following relationship exists between the braking force Fb created and the motor force Fm required, expressed as an amplification factor (characteristic brake factor C*), and/or the efficiency of a brake design. The function is derived from the force balance (see Fig. 1.19). The right diagram shows the dependency on the friction force Fb on the friction coefficient µ between brake pad and brake disk. The reaction force R is supported on the abutment and acts at the wedge angle α relative to the normal force.

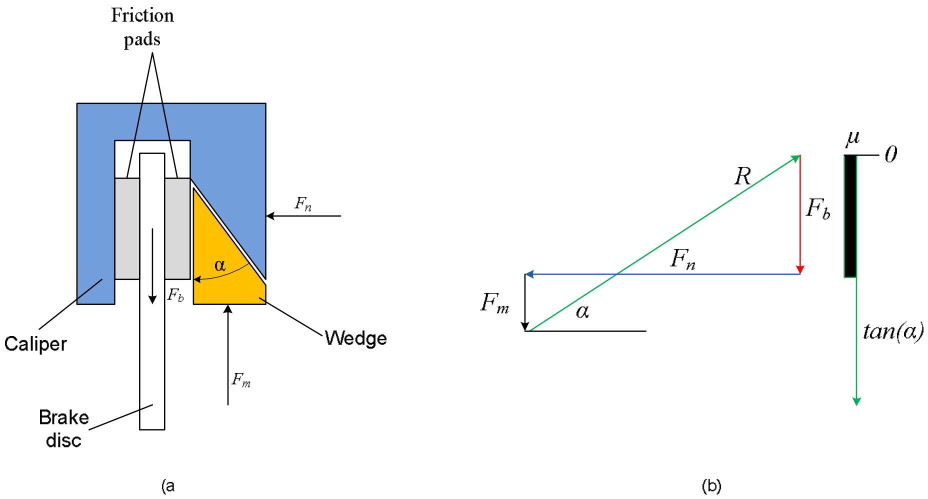

Fig. 1.19 (a) Principle of wedge brake and (b) force balance [1.22]

The brake lining is equipped with an edge on its backside which is rested on abutment. The actuator presses the brake lining in between the abutment and the

brake disc with the motor force F_m. The braking force F_b resulting from the contact between the brake disc and the brake lining acts in the same direction as the motor force which results in the anticipated self-reinforcement.
From the force balance can be derived:

$$F_m = F_b \frac{\tan\alpha - \mu}{\mu} \tag{1.2}$$

For the characteristic brake factor C^* then applies:

$$C^* = \frac{F_b}{F_m} = \frac{2\mu}{\tan\alpha - \mu} \tag{1.3}$$

Considering the lowest coefficient of friction shown (μ=0.25), this requires a clamping force of 35kN in comparison to a demanded actuator force of 3.5kN (Fig. 1.20).

The efficiency of a conventional floating caliper brake, defined as $C^* = 2\mu$, only has a reinforcement value of 0.5 at this point in comparison with a reinforcement of 5 in the wedge system. This is equivalent to a factor of 10 in the necessary actuation forces. As the friction coefficient approaches the value at the optimal operating point, the actuation force advantage of the EWB increases further.

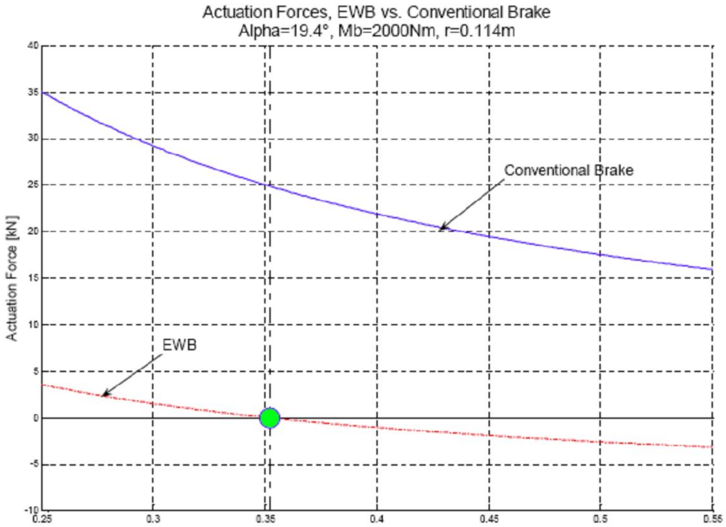

Fig. 1. 20 Comparison of braking power between conventional system and e-brake system [1.25]

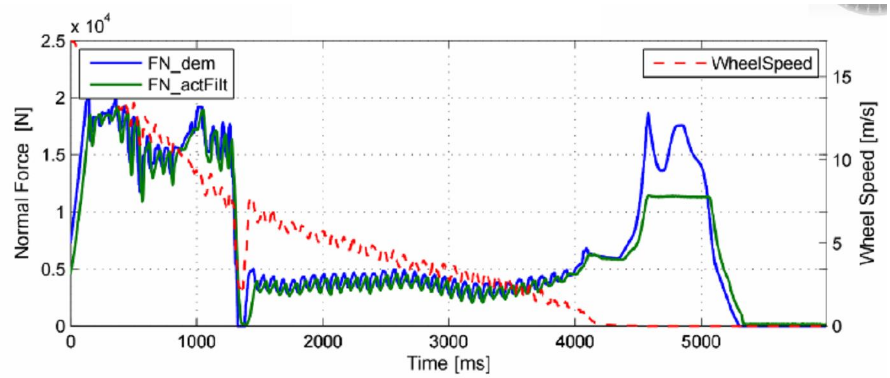

Fig. 1.21 General architecture of an electromechanical brake [1.28]

Actuators for EMB

The electronic wedge brake involves position control for electromechanical actuators. The actuators can be: three phase permanent magnet synchronous motor, brushless dc motor, induction motor or switched reluctance motor. The volume is an important constraint that should be taken into account and from this point of view the permanent magnet synchronous motor would be a good candidate for this application. Switched reluctance motor has been already tested, by Delphi, as a potential solution for electro-mechanical brake applications. The potential of switched reluctance motor is analyzed in [1.25]. For EMB application an 8/6 motor configuration has been chosen by the authors due to ability to produce a relative uniform torque as a function of rotor position down to zero speed which is a highly beneficial feature in this application. The converter has been designed for 12V/45A. The motor rated torque was 0.8Nm/1500rpm while at 5000rpm the motor has been able to develop a torque of 0.22Nm. The time response of the brake system to a maximum clamping force (1. p.u.) command was 200ms while the time response for a fast brake release from the maximum clamping force was 120ms.

Selection criteria for actuators used in EMB applications:

- High power/torque density (volume constraint)
- Smooth torque over a wide speed range, especially at very low speed
- Very low inertia in order to assure a fast speed/position response
- High temperature operating range

1.4 Electromagnetic valves

In conventional internal combustion engine (ICE) the engine valve timing is fixed with respect to crankshaft angle. Flexible controlled valve timing offers significant improvements in fuel efficiency, engine performance and emissions [1.29]. One way to achieve variable valve timing (VVT) is by using an electromechanical valve drive (EMVD).

In conventional ICE, engine valves are actuated by cams that are located on a belt-driven or chain-driven camshaft. Each valve’s kinematics profile is of fixed shape and timing relative to the engine crankshaft position. The shape of these cams is determined by considering tradeoffs between engine efficiency, torque requirement and maximum power. This optimization results in an engine that is highly efficient only at certain operating conditions. Optimized overall performance can only be obtained at certain operating conditions (at high speed, wide-open throttle operating conditions). The ICE in which the timing of the valve transitions and durations with respect to crankshaft angle can be controlled are called variable valve timing (VVT) engines.

An electromechanical valve drive (EMVD) realizing variable timing was proposed in [1.30], [1.31] and it was shown by theoretical analysis and preliminary simulation that the proposed EMVD exhibits a number of advantages over previous EMVD architectures, especially in its ability to realize soft valve landing with reasonable power consumption and fast transition times.

1.4.1 Concept of Electromechanical Engine Valve Drive and Operating Principle

VVT can be achieved using either mechanical or electromechanical actuation system. With VVT alone, a 1% improvement in fuel economy can be achieved [1.30]. Furthermore, if the lift (how much each valve is opened) of the valves is controlled, another 10% improvement can be gained [1.31]. The average power losses associated with driving the engine valves is approximately 3kW for 16 valves in a 2.0L, 4 cylinder engines at 6000rpm engine speed and wide open throttle.

Shortly, the advantages of variable valve timing engines are [1.42]:

- Improves gas mileage (by a demonstrated 15% and up to 20-25% with system optimization)
- Reduce emissions of all kinds: HC up to 50%, NOx up to 50% and CO2 by 15% or more
- Develop more peak power (about 15%) and more torque (about 20%) for the same engine size

The electrification of variable valve timing can be done by using;

- an electric motor that is driving a valve spring system
- an electromagnetic valve

1.4.2 Variable valve timing using electromagnetic valves

The electromechanical valve system (Fig. 1.22) consists of two electromagnets, an armature, which moves between two magnets, two springs and an engine valve. When no one of solenoid is energized the armature is held equidistant fro both solenoids by two springs located above the solenoid 1 and solenoid 2. This system is then used to control the position of the engine valve.

The electromagnetic valve can be in three positions: a) valve closed b) neutral position and c) valve open. During closed position the solenoid 1 is energized and the armature moves on top position until when the phase is not energized. During neutral position the valve is semi-open. During open position the solenoid 2 is energized and the armature moves on bottom position. The supply voltage vs valve position profile is illustrated in Fig. 1.23. In [1.39] a mathematical model and a control system was developed and tested for an electromechanical actuator having the configuration similar to that one in Fig. 1.23. The PWM supply voltage was 180V and the PWM frequency was 10 kHz. The time constant of the circuit was L/R≈50(mH)/5(Ω) ≈10ms.

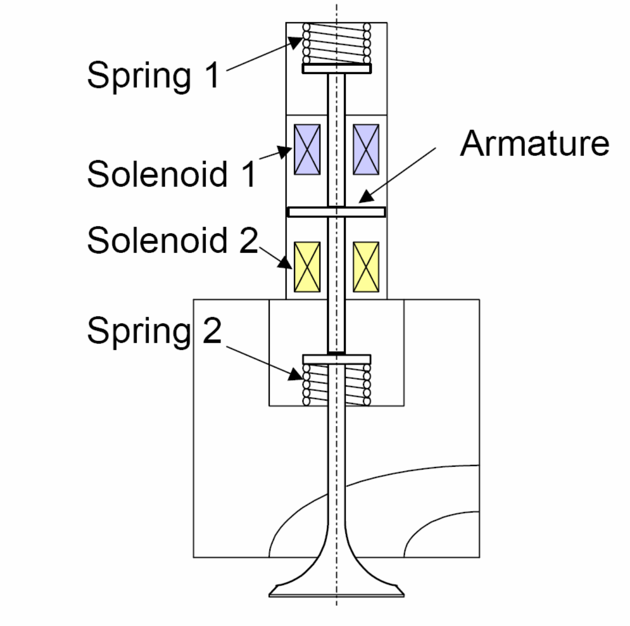

Fig. 1.22 Electromagnetic valve cross-section

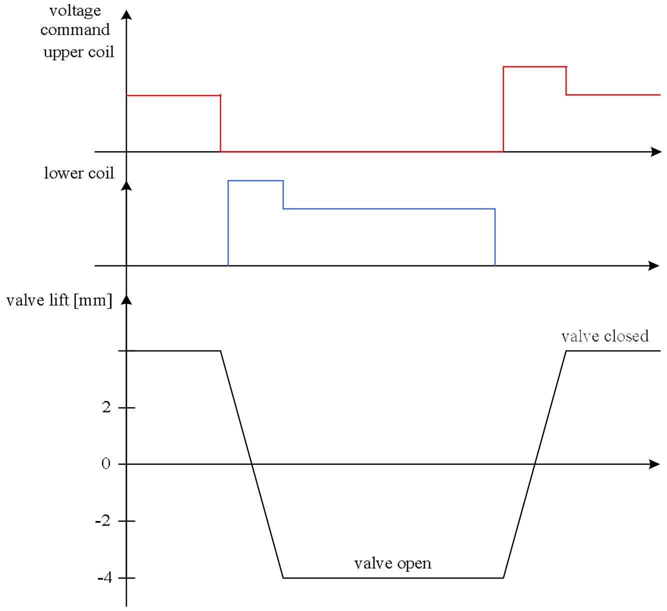

Fig. 1.23 Schematic of electromagnetic valve opening and commanded voltage

The block diagram of an electromagnetic valve control unit in a modern car is shown in Fig. 1.24. The control algorithm of the electromagnetic valve is located in combustion engine control unit (ECU). The ECU control the valve opening and closing thorough the DC-DC converter. The ECU sends PWM signals to the DC-DC converter, controlling the current in the valve coils.

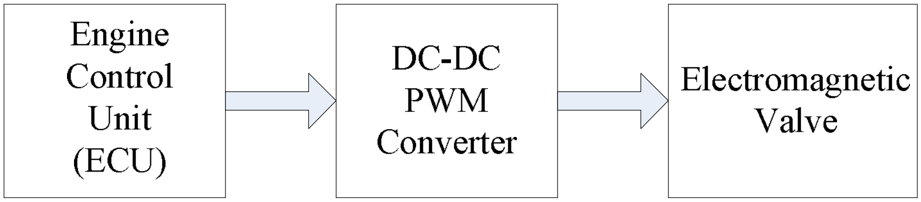

Fig. 1.24 Block diagram of an electromagnetic valve system for thermal engine

1.4.3. Variable valve timing using electric motors

An electromagnetic valve drive system (EMVD) consists of an electric motor that is coupled to a resonant valve-spring system via a slotted cam which acts as a nonlinear mechanical transformer (NMT) [1.29]-[1.31]. As the motor rotates, the roller moves within the slotted cam, allowing the valve to move vertically. As the valve moves, it compresses one spring and extends to other.
In the case of valve spring systems, the forces are largest at the ends of the stroke because the spring forces increases linearly with valve displacement from the middle

of the stroke. If the relationship between valve lift and motor shaft would be linear, these large holding forces would make difficult to hold the valve in the open or closed position without using large motor torque and consequently a lot of electrical power. Additionally, an accurate control of valve seating velocity would require precise control of motor velocity. This problem is solved using a cam with a special profile (Fig. 1.25).

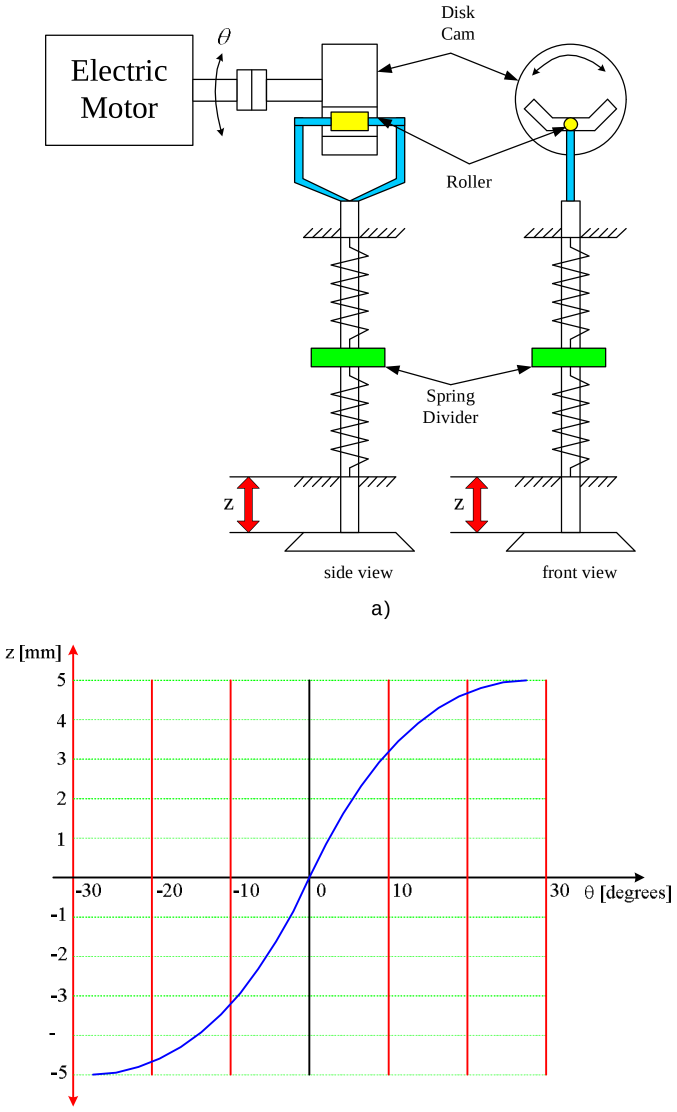

Fig. 1.25. a) Schematic of a motor actuated electromechanical valve drive, b) desirable transfer characteristic for the nonlinear mechanical transformer [1.31]

The main advantages of such a solution are as follows:
a) At either end of the stroke, the slope of the cam characteristic (dz/d□) is very small. This means that the inertia of the motor reflected in z domain is very large, creating inherently smooth valve kinematics profiles because the valve is slowed down by large effective inertia near the ends of the stroke. This characteristic makes it easier to control the motor velocity at the ends of the stroke in the z domain are transformed into small torques in the θ domain.
b) Because the gas force on the exhaust valve is largest at the opening end of the exhaust stroke, the reflected gas force in the θ domain is also small, making it easier to open the exhaust valve against a large gas force.

Based on the current profile seen from experiments, the authors of the paper [1.31] estimate the total electric power consumption of the stiff spring-based EMVD in a typical 2.0L, 16-valve engine operating at 6000rpm under full-load (wide-open-throttle) conditions around 2.56kW, which is the same order as that of the mechanical power consumption of a conventional camshaft-driven valve train assuming 50% alternator efficiency.
Seating velocity of the stiff spring-based EMVD systems are in the range of 15.5-27.2 cm/s.

The block diagram of an EMVD system is shown in Fig. 1.26. The spring valve is driven by a three phase electric motor, which is coupled to the camshaft via a mechanical transmission. The three phase motor is supplied from a three phase inverter controlled by the engine control unit. The control system of an EMVD system is shown in Fig 1.27.

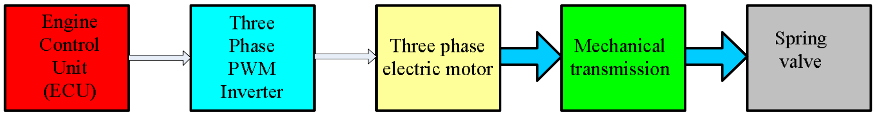

Fig. 1.26 Block diagram of an electromagnetic valve system using an electric motor

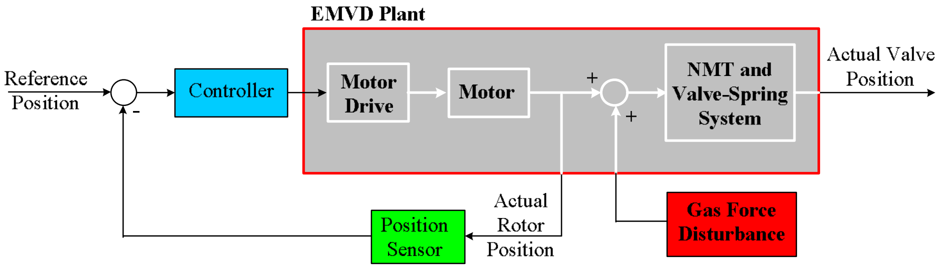

Fig. 1.27 Block diagram of the feedback-controlled EMVD apparatus

Performance indices

The closing and seating performance of the closed-loop controlled EMV system can be quantified by using the following indices:

- *Closing time, t_c*: the time it takes for the valve to move from 90% of the maximum lift to 10% of the maximum lift
- *Seating tail-length, t_s*: run a free response test for the EMV system and record the moment that the engine valve reaches he lowest piston (closest to its seat) as time t_0. Then for each quieting-seating control test, record the moment of the frst time the engine valve gets to the seating position as t_f.
- *Valve seating velocity, v_s*: the instant velocity of engine valve at the first time it gets to its seating position.
- *Armature crossing velocity, v_c*: the average velocity of armature moving from 0.05 mm above the valve seating position to 0.05 mm below valve seating position.
- *Armature seating velocity, v_a*: the instant velocity at the first time it gets to t_s own mechanical boundary.

1.5 Electric active suspension

Traditionally automotive suspension designs have been a compromise between the three conflicting criteria of road holding, load carrying and passenger comfort. The suspension system must support the vehicle, provide directional control during handling maneuvers and provide effective isolation of passengers/payload from road disturbances. Good ride comfort requires a soft suspension, whereas insensitivity to applied loads requires stiff suspension. Good handling requires a suspension setting somewhere between the two. Due to these conflicting demands, suspension design has had to be something of a compromise, largely determined by the type of use for which the vehicle was designed. Active suspensions are considered to be a way of increasing the freedom one has to specify independently the characteristics of load carrying, handling and ride quality.

The suspension systems currently in use can be classified as passive, semi-active and active. Also, they maybe classified as low bandwidth systems or high bandwidth systems.

The passive suspension systems are the most commonly used due to their low price and high reliability. However, this system can not assure the desired performance from a modern suspension system. An important improvement of the suspension performance is achieved by active systems. Nevertheless, they are only used in a much reduced number of automobile models because they are expensive and complex. Another disadvantage of active systems is the relatively high energy consumption. The use of electromagnetic linear/rotating actuators is an alternative for the implementation of active suspensions. Moreover, this solution has the advantage of suspension energy recovery. In spite of the materials development, the electromagnetic actuators are still expensive to produce.

A passive suspension system has the ability to store energy via a spring and to dissipate it via a damper. Its parameters are generally fixed, being chosen to achieve a certain level of compromise between road holding, load carrying and comfort.

An active suspension system has the ability to store, dissipate and to introduce energy to the system. It may vary its parameters depending upon operating conditions and can have knowledge other than the strut deflection the passive system is limited to.

High bandwidth systems

In a high bandwidth (or “fully active”) suspension system we generally consider an actuator connected between the sprung and unsprung masses of the vehicle. A fully active system aims to control the suspension over the full bandwidth of the system. In particular this means that we aim to improve the suspension response around both the "rattle-space'' frequency (10-12 Hz) and "tyre-hop'' frequency (3-4Hz). The terms rattle-space and tyre-hop may be regarded as resonant frequencies of the system. A fully active system will consume a significant amount of power and will require actuators with a relatively wide bandwidth. These have been successfully implemented in Formula One cars and by, for example, Lotus.

Low bandwidth systems

Low bandwidth systems are known as slow-active or band-limited systems. In this class the actuator will be placed in series with a road spring and/or a damper. A low bandwidth system aims to control the suspension over the lower frequency range, and specifically around the rattle space frequency. At higher frequencies the actuator effectively locks-up and hence the wheel-hop motion is controlled passively. With these systems we can achieve a significant reduction in body roll and pitch during maneuvers such as cornering and braking, with lower energy consumption than a high bandwidth system.

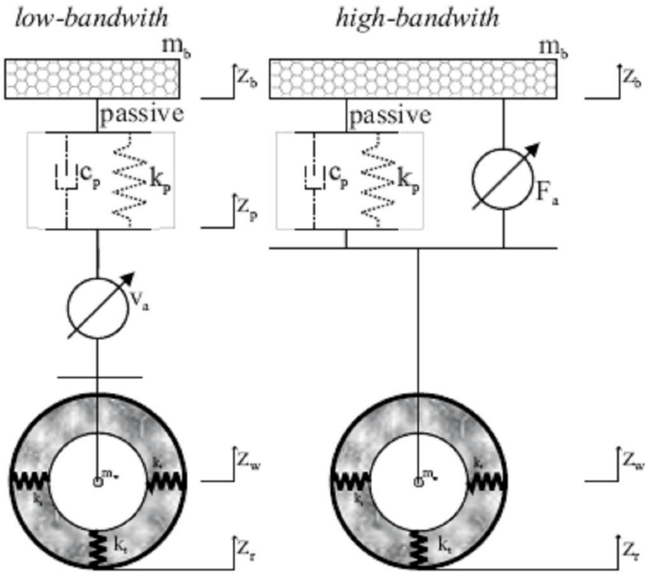

Fig. 1.28 Low–bandwidth and high–bandwidth suspension models [1.44]

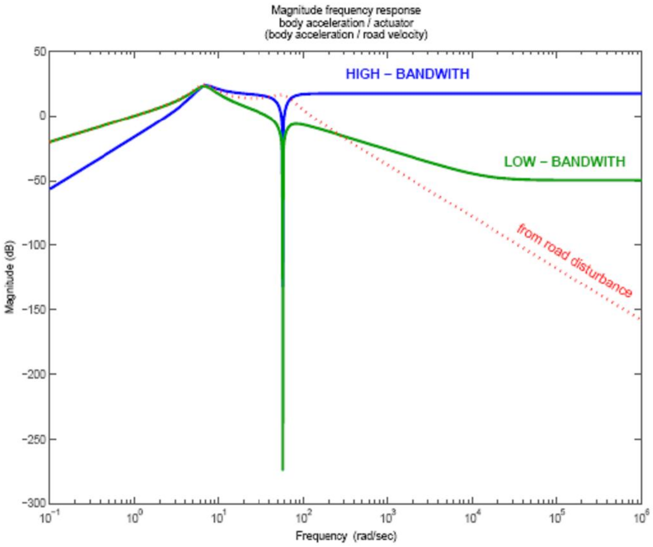

Fig. 1.29 High vs. low bandwidth comparison [1.44]

Human perception

It is necessary to discuss the human vibration perception, because the human being is not sensible to vibration at each disturbance frequency in the same way. Therefore it is important to distinguish the frequencies where passenger is sensitive to vibration considerably and the frequencies where he is not.

Moreover it should be noticed that human sensitivity to vibration is different for the vertical and horizontal direction. The vertical model of passenger has been derived above and the horizontal influences of active suspension can be observed from car pitching and rolling. Typically it is assumed human being is most sensitive in the range:

4 … 8Hz (25 … 50rad/s) for the vertical motions

1 … 2Hz (6:3 … 12.6rad/s) for the horizontal motions

Therefore the frequency dependent acceleration tolerance function should be band-stop filter with the frequency ranges mentioned above.

Electro-mechanical active suspension

Today, suspension systems used in automobiles consist of hydraulic or pneumatic actuators (for example installed on Citroen, Roll-Royce, Mercedes) which offer a high force density and ease in design due to the commercial availability of the parts. However, these systems have a relatively low bandwidth (around 1 Hz) [1.57],[1.58] probably due to leakage in the valves and pressure hoses and limited bandwidth of the pump. Furthermore, these systems are inefficient due to the need of continuous pressurized system. In general, electromagnetic suspension systems have a very small response time and therefore are more suitable to absorb road vibrations and to react in lane change maneuvers. An example of semi-active suspension system is the magnetoreological damper [5.56], developed by Delphi which has the ability of changing its damper characteristic within 1ms [5.60]. However, since it is a semi-active suspension system, no active force can be applied and therefore, total roll and pitch elimination is impossible.

To overcome these drawbacks electro-mechanical active suspensions that incorporate an electric motor (rotary or linear) are proposed.

The cross-section of an active suspension system with a rotary electric motor is shown in Fig 1.30. The system inputs are the signals coming from a set of sensors which measure: vehicle speed, steering angle, vehicle vertical acceleration. The outputs of the control logic are the command sent to the actuators.

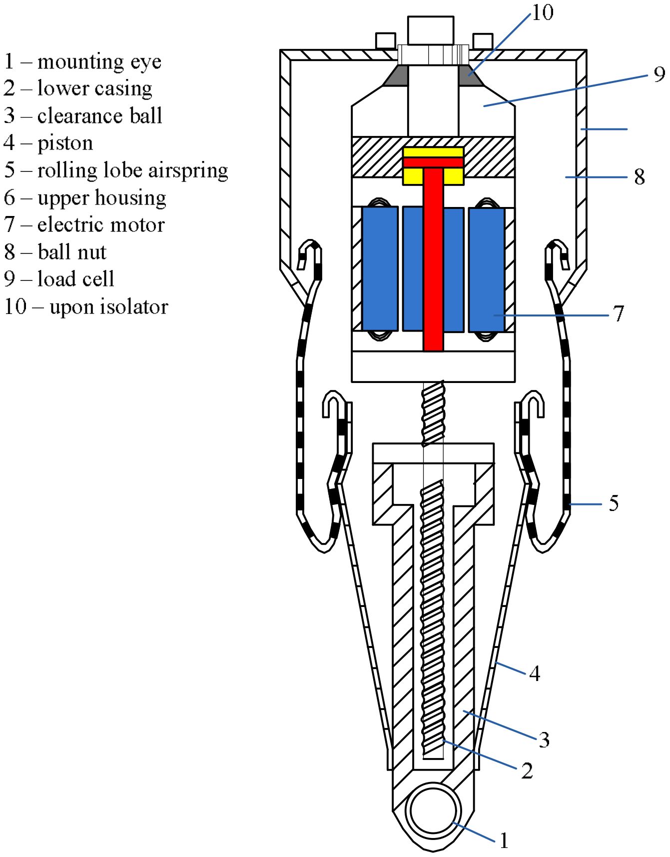

Fig. 1.30 Active suspension with rotary electric motor cross-section

The actuator can be: a linear motor or a permanent magnet synchronous motor.Linear motor translator movements take place with high velocities (up to approximately 200m/min), large accelerations (up to g multiples), and forces (up to kN). As mentioned above, the electromagnetic force can be applied directly to the payload without the intervention of a mechanical transmission, what results in high rigidity of the whole system, its higher reliability and longer lifetime. In practice, the most often used type is the synchronous three-phase linear motor.

Table 2. Specification for a linear electric motor [1.49]

Item	**Value**	**Unit**
Peak force	2027	N
Peak current	21.8	A
Electrical time constant	1.26	ms
Continuous working voltage	320	Vac
Maximum phase temperature	100	oC

In [1.50] is proposed an electromagnetic active suspension system comprising a brushless tubular permanent magnetic actuator, in parallel with a mechanical spring. The actuator have a relatively high force density due to the tubular structure and excellent servocharacteristics with a bandwidth above 50Hz. A great advantage of such a system is given by the bidirectional power flow, allowing regenerative braking. To have an idea about the forces magnitude in an automobile, experimental results from [1.50] are presented in Fig. 1.31.

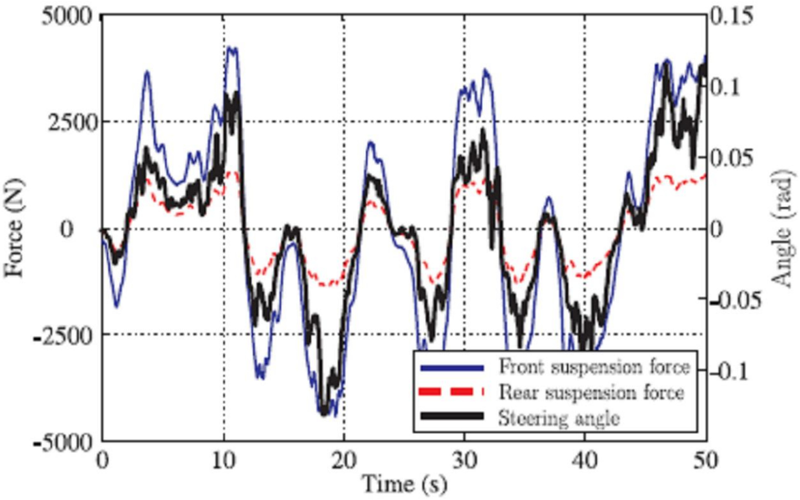

Fig. 1.31 Roll forces calculated from steering angle and lateral acceleration

According to Fig. 1.31, a peak and rms force of 4kN and 2kN, respectively is necessary for a vehicle with a weight of 1613 kg. The rms power for such a system is around 1.5kW/actuator. So around 4-6 kW are necessary to control the suspension system.

The specifications of the suspension system are given in Table 3.

Table 3. Specifications of a suspension system [1.50]

Specification	Value	Description
$F_{\text{rms roll}}$	1000 N	Rms force at 0.1 m/s for active roll control
$F_{\text{max roll}}$	4000 N	Max. force at 0.1 m/s for active roll control
$F_{\text{rms damp}}$	762 N	Rms force at 1 m/s for active damping
$F_{\text{max damp}}$	2050 N	Max. force at 1 m/s for active damping
ΔT_{max}	80 °C	Maximum increase in temperature
v_{max}	1 m/s	Maximum speed
z_{max}	140 mm	Minimum stroke

The overview of an active-suspension system for automobiles is shown in Fig. 1.32. Several sensors information is required to achieve a good comfort for the driver. Based on this information the electronic control unit controls four actuators. Each actuator is controlled via a three phase inverter.

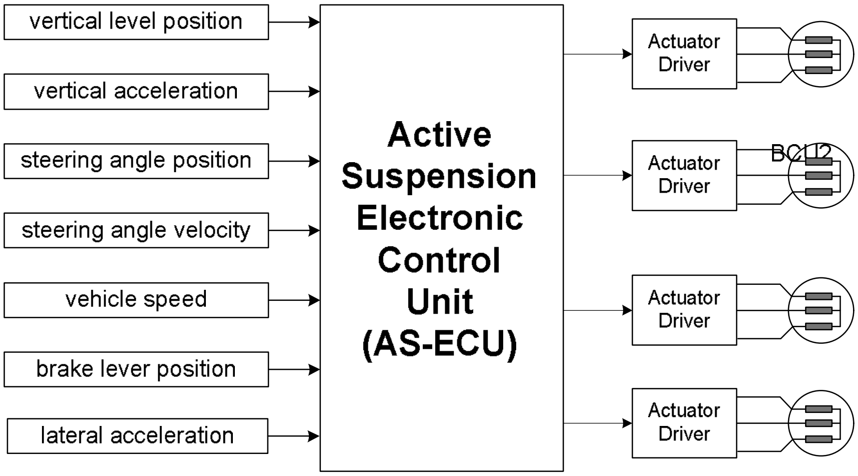

Fig. 1.32. Block diagram of an active-suspension system for automobiles

1.6 Electrically driven turbochargers

Electrically driven turbochargers are a new technology under development whose main purpose is to increase the overall engine efficiency and to improve the time response of the engine torque. In comparison to the conventional turbocharging system the electrical assisted turbocharging systems are using an electric motor within the turbocharger between the turbine and the compressor.

The configuration of such a system can be seen in Fig. 1.33, 1.34.

The compressor has to provide air to the engine in such a quantity that this will increase the efficiency of the fuel burning inside the cylinder. In conventional system the compressor is driven by the exhaust turbine. At low speeds the turbine will not provide enough torque to the compressor. At high speeds and load the turbine will provide too much torque for the compressor.

To overcome these drawbacks of the conventional turbocharging system, the electrical driven turbocharger has been proposed. The conventional turbocharging system was an open-loop system while the electrically assisted turbocharger system is a closed-loop one.

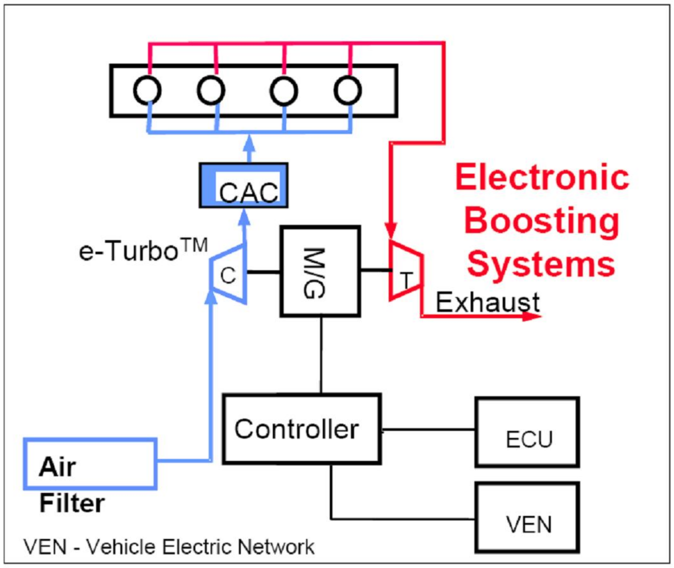

Fig. 1.33 Electrically assisted turbocharging system configuration

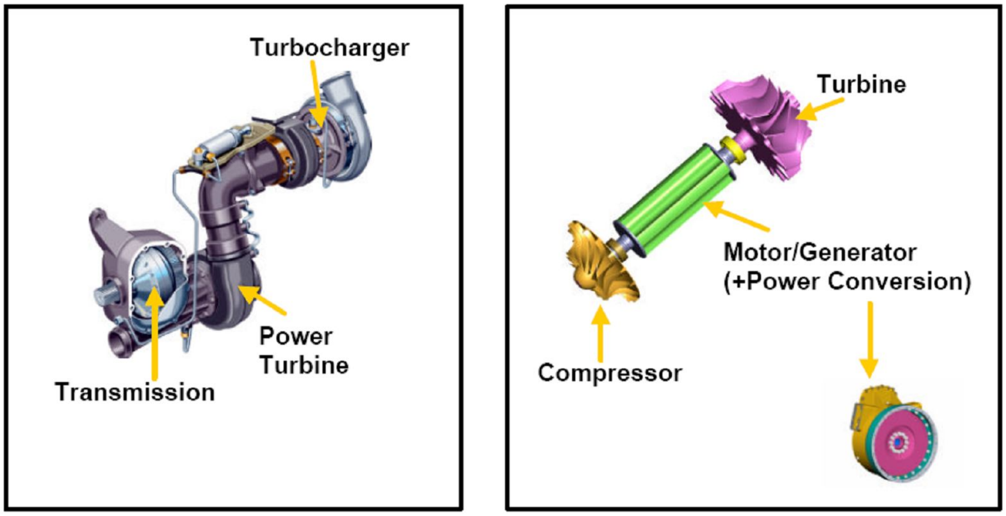

Fig. 1.34 Turbocompounding: mechanical (right side) versus electrical (right side)

In Fig. 1.35 is illustrated the torque response versus time for an engine with and without electrically torque boosting, while in Fig. 1.36 is shown the improvement of ICE torque at steady state as a benefit of electrically assisted turbocharger systems.

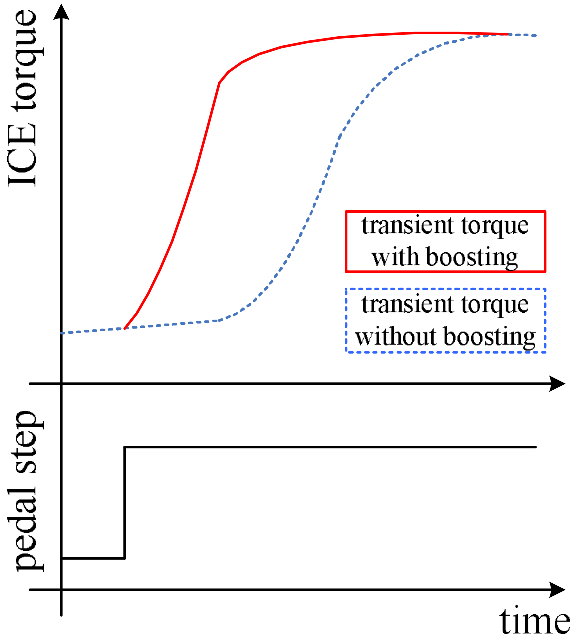

Fig. 1.35 ICE torque improvement during transient with electrical assisted turbocharging

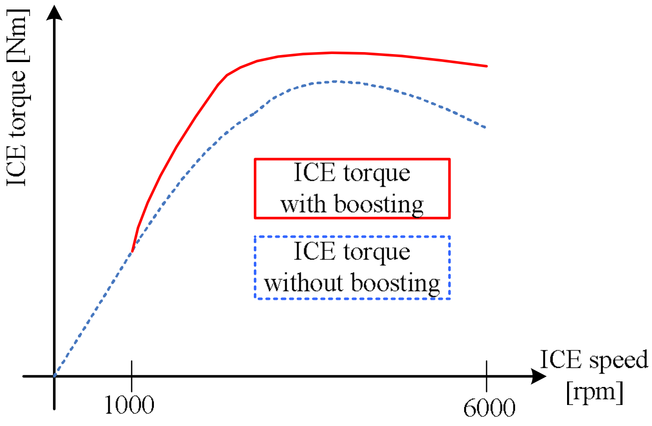

Fig. 1.36 ICE map at steady-state with/without electrical assisted turbocharging

In [1.66] is described an ultra-high speed permanent magnet synchronous motor drive for turbocharger, with a maximum speed of 220.000 rpm at 2kW power. A pseudo-current source inverter, which has a current controlled chopper across the dc bus, is employed to drive the motor with 120o conduction pattern because conventional sinusoidal PWM techniques are unable to regulate the current in such an ultra-high speed range.
The schematic of pseudo-current source inverter is presented in Fig. 1.37. The fundamental frequency of the motor reaches as high as 3.7 kHz at the maximum operating speed, while the switching frequency of the chopper is as high as 30 kHz.

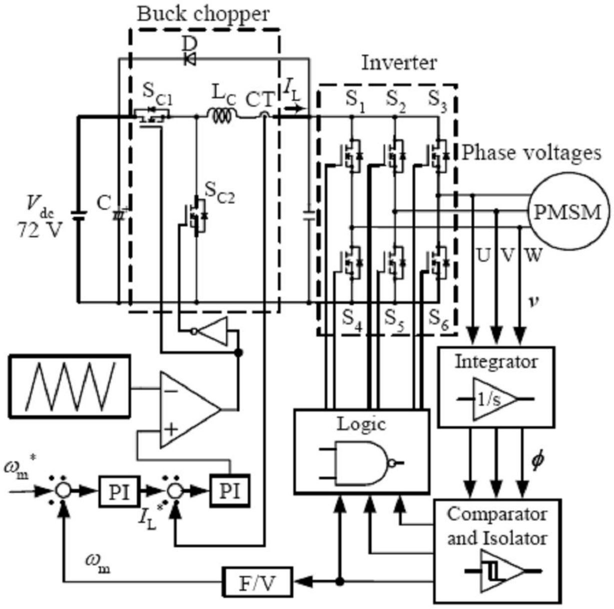

Fig. 1.37. The schematic of pseudo-current source inverter is presented

The motor current amplitude is controlled by controlling the chopper duty cycle. The MOSFETs are used only to switch between the energized phases, so the losses on the semiconductors are much lower.

An electromagnetic analysis of the 3-slot motor and the 6-slot motor was done in [1.66], showing that the 6-slot motor has a great advantage over 3-slot motor in reducing the total losses which are approximately 50% of the 3-slot motor's losses.

Table 4 presents the main specifications of the ultra-high speed PMSM drive.

Table 4. Ultra-high speed PMSM specifications

Rate power (continuous)	2 (kW)
Rate power (continuous)	0.159 (Nm)
Rate power (continuous)	120.000 (r/min)
Maximum speed	220.000 (r/min)
Overload	200% - 2 (s)

According to [6.6] the combustion engine efficiency and engine output power can be improved by 8% and 150% by applying 1 kW assisting power to the turbocharger, while 12% and 200% improvement of efficiency and power can be achieved by using a 2 kW assisting power to the turbocharger. According to the assessments of transient characteristics, from the simulations, the turbo lag was reduced by 50% with a 1.3 kW motor assist and by 70% with 2 kW. This electrical assisted turbocharger was used for a 2L diesel engine equipped with an intercooler.

In [1.68] a surface permanent magnet motor (SPMM), 150.000rpm, 1.5 kW fed by a low voltage battery (12V) is discussed. The developed prototype has a variety of unique features from electrical and mechanical viewpoints, and some experimental test results are presented to demonstrate its potential. In [1.69] a 160,000-r/min, 2.7-kW permanent-magnet synchronous motor drive is discussed and its experimental test results are presented showing very good performances of the proposed system. The motor is open loop control below 10 000rpm, while above the motor is switching to speed sensorless close-loop control.

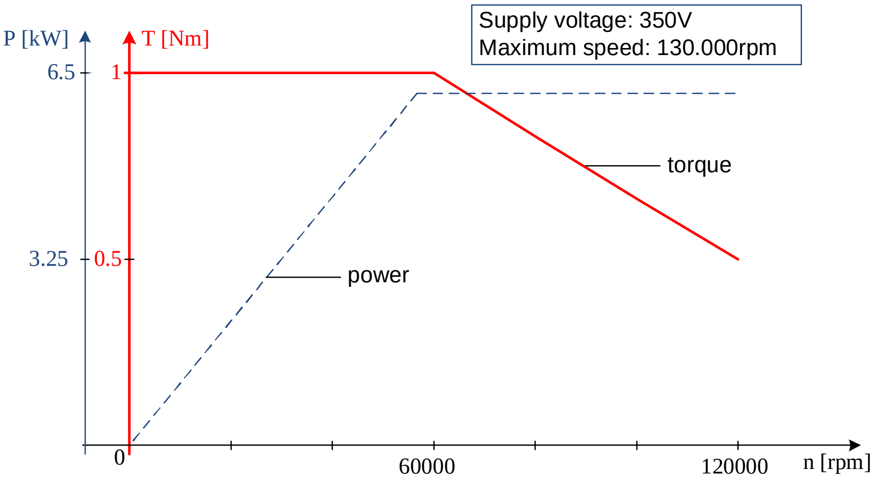

Fig. 1.38 Torque, power vs speed demand of an electric motor used in electrically driven turbocharger system [1.61]

To confirm the benefits of electrically assisted turbocharging in paper [1.65] a 3.0 Liter engine has been downsized with 40% to a 1.8 Liter. The 3.0 Liter engine steady state characteristic has been measured with the engine driven by a conventional turbocharging system. The 1.8 Liter characteristic has been measured with the engine having electrically assisted turbocharging. The experimental results are presented in Fig. 1.39.

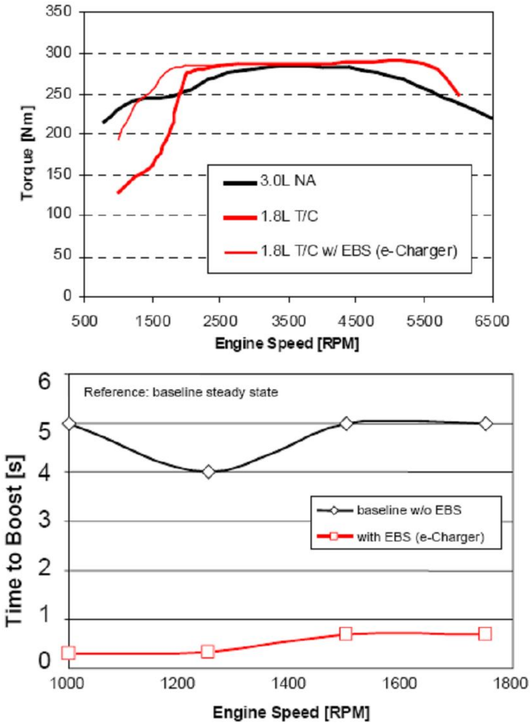

Fig. 1.39 Comparison between 3.0L engine and 1.8L engine with electrically assisted turbocharging (left side), b) Comparison of time response of the engine with/without electrically assisted turbocharging (right side) [1.65]

Advantages of e-Turbo technology are:

- Improve the ICE engine torque response time
- Increase the engine torque at low speed during steady-state
- By increasing the engine torque a downsizing of the engine can be realized. A smaller engine gives many benefits such as cost, weight reduction, packaging and friction reduction
- Improves the fuel economy
- EGR rates, exhaust temperature can be controlled to give optimum results

1.7 Exhaust-gas electric energy recovery

The efficient generation of relatively large quantities of electrical energy in vehicles is becoming an increasingly more important issue due to increasing of electrical loads such as climate control, navigation/entertainment equipment, adoption of X-by-wire technology and electrically-driven ancillaries. The average total electrical power consumption in the short term is expected to be around 2.5 kW.

An attractive solution to meet these electrical power demands is to recover the energy which would otherwise go to waste as heat in the exhaust gas, by means of an electric generator driven by a high speed exhausted mounted turbine. The partial recovery of this energy has the potential to offer significant benefits in terms of increasing the overall engine/vehicle efficiency.

Fig. 1.40 shows a schematic of exhaust gas energy recovery system, in which the turbine is placed in a pre-catalyst position in the exhaust flow. The exhaust gas conditions determine the available energy for recovery. At high speeds or high torque the recover energy potential is higher. The turbine is directly coupled to the electric generator and, typically, operates at speeds up to 100.000rpm. The electrical power generated by the electric generator supplies the system dc bus, to which the vehicle electric loads are connected. During periods of high energy recovery (e.g. highway driving) the excessive energy will be used to charge the battery. Up to 6 kW instantaneous power can be recovered during highway driving [1.71].

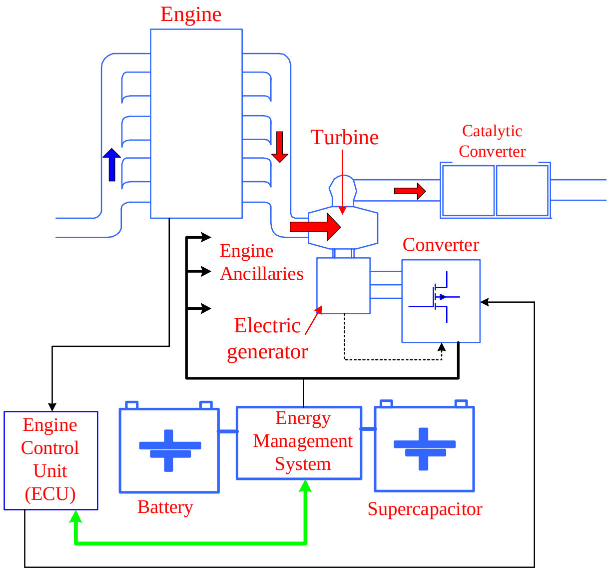

Fig. 1.40 Schematic of exhaust gas energy recovery system [1.71]

1.8 Integrated starter-alternator systems

The integrated starter-alternator system combines the conventional starter and alternator in a single electrical machine which works as a bidirectional electromechanical converter. It is primarily used for internal combustion engine

cranking and generating power for battery charging, thereby performing the function of starter and generator respectively. Additional functions include: power assist, regenerative braking, and pure electric propulsion of the vehicle.

Hybrid electric vehicles are classified as:

- Parallel hybrid electric vehicles
- Series hybrid electric vehicles
- Series-parallel hybrid electric vehicles
- Electric vehicles

Series hybrid drivetrain

A schematic picture of the series hybrid drivetrain is shown in Fig 1.41.

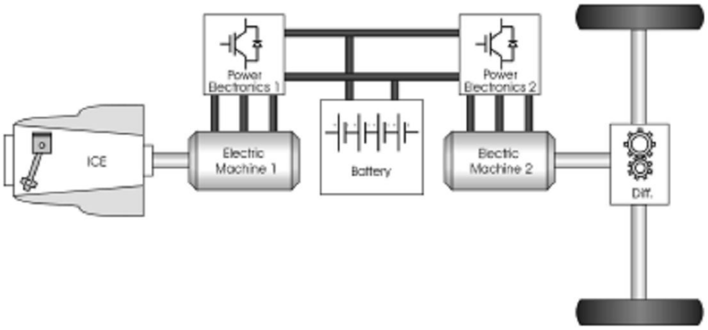

Fig. 1.41 Series hybrid drivetrain

The thermal energy stored in the tank is converted to mechanical energy in the combustion engine. The mechanical energy is then transformed to electric energy in the generator and stored in the electric energy buffer via a power electronic converter. The electric energy is then transformed back tomechanical energy via the electric traction motor and its associated power electronic converter. The advantages and disadvantages of the series hybrid powertrain are summarized in Table 5.

The series hybrid is not suitable for high way traffic due to the many energy conversions. However, in urban traffic it can be made very efficient with the proper control. In addition, the packaging advantages make the series hybrid drivetrain suitable for heavy vehicles, such as commercial buses and military vehicles.

Table 5. Advantages and disadvantages of the series hybrid drivetrain

Advantages	**Disadvantages**
Mechanical decoupling of the ICE and wheels. Allows the ICE working point to be chosen for high efficiency	Require a large traction motor as it is the only torque sources. Has to be designed for peak power
Simple speed control due to a single torque sources connected to the wheels	The many energy conversion leads to low overll system efficiency
Using an electric machine as the only torque source eliminates the need for a multi grear transmission	Needs two electric machines and two sets of power electronics
Simple packaging as the ICE and the egenrator can be mounted separately from the traction motor	

Parallel hybrid drivetrain

The parallel hybrid drivetrain consists of an ICE and at least one electric machine, which are both mechanically connected to the wheels as shown in Fig 1.41. The electric motor can be connected to the drivetrain in several different ways and can be located anywhere along the transmission. The mechanical coupling can be a gearbox, a belt or the rotor of the electrical machine being a part of the shaft. The basic operation of the parallel hybrid is that the speed of the ICE is chosen with the gearbox in order to keep the engine speed within its limits. The electric machine can then be used to add or subtract torque to the engine torque in order to achieve a high ICE efficiency. The electric machine can also be used during regeneration to charge the energy storage. In some configurations, where the ICE can be disengaged from the drivetrain, the vehicle can be run in pure electric mode.

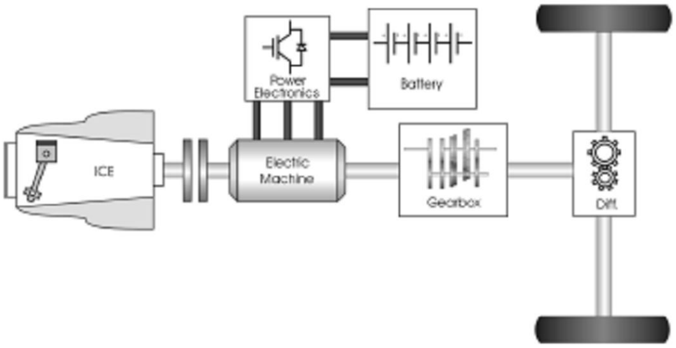

Fig. 1.42 Parallel hybrid drivetrain

The advantages and disadvantages of the parallel hybrid are summarized in Table 6. The major advantage of the parallel hybrid compared to the series hybrid is that the ICE is directly coupled to the wheels. This eliminates the inefficiency of converting mechanical power to electricity and back. Unlike the series hybrids, this makes the parallel hybrid drivetrains suitable for highway traffic. However, the mechanical coupling is also a drawback of the parallel configuration, since the ICE is to some extent forced to follow the power request. This is, however, not a major problem, since a gearbox is normally used and the operating point of the ICE can thereby be varied. The compactness of the parallel hybrid drivetrain and the fact that it can be used both for city- and highway traffic makes it suitable for both small and heavy vehicles.

Table 6. Advantages and disadvantages of the parallel hybrid drivetrain

Advanatges	**Disadvanatages**
Both the engine and the motor are connected directly to the wheels, which leads to fewer energy conversion	The mechanical coupling of the ICE to the wheels leads to a more limited choice of operating points
Compact configuration and no need for a generator	
Can use a smaller battery pack and a smaller traction motor	

Series-parallel hybrid drivetrain

The series-parallel hybrid drivetrain, also known as the power split hybrid (PSH), is a configuration intended to combine the advantages of the series and the parallel configuration. The configuration consists of one ICE and two electric machines as seen in Fig 1.43.

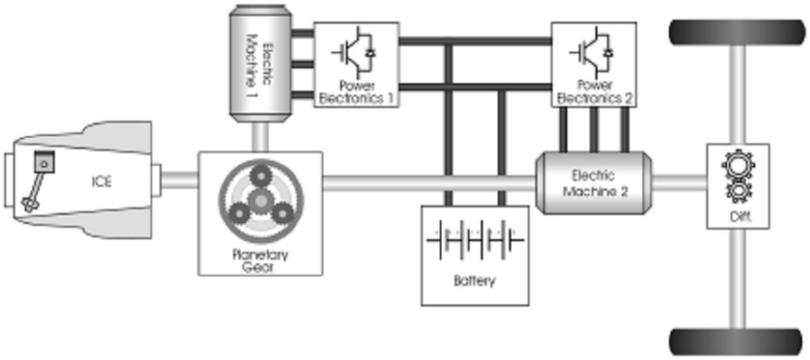

Fig. 1.43 Series-parallel hybrid drivetrain

A planetary gear set is used to connect the electric machines and the ICE. The first electric machine, often referred to as the generator, is connected to the sun wheel, the ICE is connected to the planet carrier and the second electric machine, often referred to as the traction motor, is connected to the ring wheel. The generator is used to adjust the speed of the ICE, while the task of the traction motor is to adjust the torque.

Thus, the operating point of the ICE can be continuously varied by the electric machines. The planetary gear, together with the electrical machines, work as a continuously variable transmission (CVT). The difference between a CVT and an ordinary transmission is that the CVT can vary the ratio continuously, while the ordinary transmission has discrete steps for each gear.

One drawback with this configuration is that the generator has to be designed to meet the peak torque of the ICE. One other drawback is that, if the generator or the power electronics controlling it malfunctions, the vehicle will not move at all. In the case with the parallel configuration, the vehicle can still be propelled by the ICE.

Parallel hybrid electric vehicles are classified as:
- Micro hybrid electric vehicles (Micro-HEV)
- Mild hybrid electric vehicles (M-HEV)
- Full hybrid electric vehicles (F-HEV)

The functions fulfilled by ISA systems, depends on the hybrid vehicle configuration and they are presented in Table 7. The typical torque versus speed characteristics of ISA systems are in the range shown in Fig. 1.44.

Table 7. ISA Functions for different HEV configurations

Hybrid System	**Engine Start/Stop**	**Engine Assist**	**Regenerative Brake**	**Electric Launch**
Micro-HEV	YES (>0.3s)	NO	NO	NO
Mild-HEV	YES	Minimal (<6 kW)	Minimal (<3 kW)	NO
Medium-HEV	YES	YES	YES	NO
Full-HEV	YES	YES	YES	YES

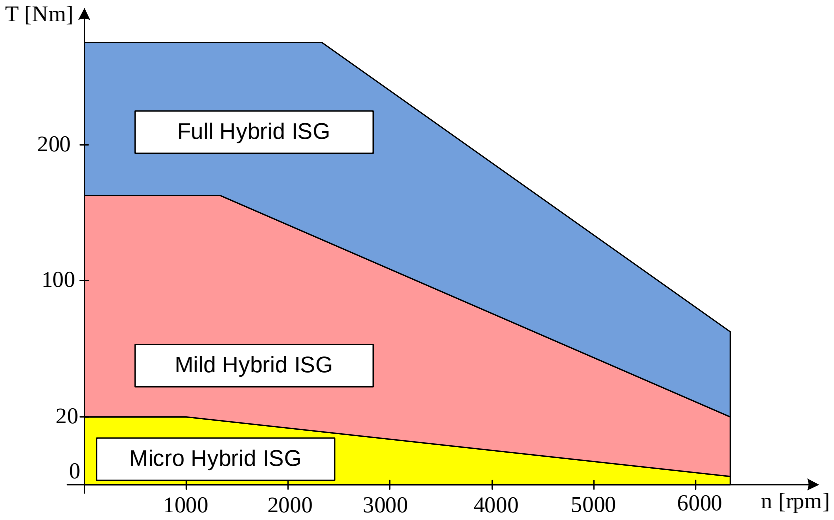

Fig. 1.44 Torque vs. speed characteristic of ISG used in parallel hybrid-electric vehicles

1.9 Clutch-by-wire

Clutch-by-wire is a new technology in automotive industry and involves one electrical actuator for clutch actuation, instead of conventional hydraulic actuation system. The number of automotive powertrain applications where a clutch is involved is dependent on the traction performance of the vehicle. The conventional on-road vehicles contain one clutch, between the internal combustion engine and

manual gearbox. At least two clutches are used in the vehicles with an automated manual transmission. Another clutch can be found in the torque transfer case (box). The rear lock differential (RLD) system employs one clutch for torque transmission to the rear wheel, also.
The control of so many clutches in an vehicle using a convention hydraulic system would be a very complex task and the overall cost of the actuation system for the clutches will be very expensive and space inefficient. Therefore using the clutch-by-wire technology, the clutches actuation becomes simpler and efficient.

The layout of a clutch-by-wire system is illustrated in Fig. 1.45.

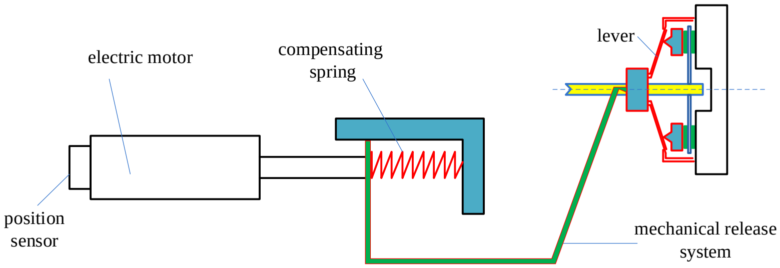

Fig. 1.45. Overview of the clutch-by-wire system

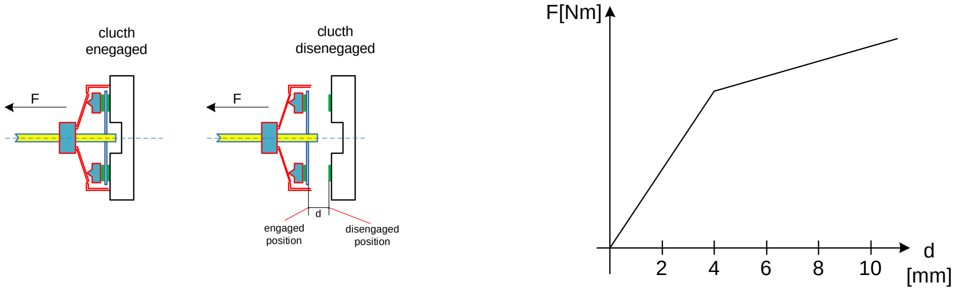

Fig. 1.46 Force vs distance profile for clutch actuation

The profile of the clutch actuation force versus disengagement distance is shown in Fig. 1.46. Clutch control is a position close-loop control system. The torque versus speed characteristic of the electric motor used in clutch-by-wire application is presented in Fig. 1.48. Brushless dc motors with ±2 degrees accuracy position sensor are suitable for this application. This way a good position control of brushless dc motor is achieved in comparison with brushless dc motor equipped with hall sensors where high speed/position oscillation are expected.

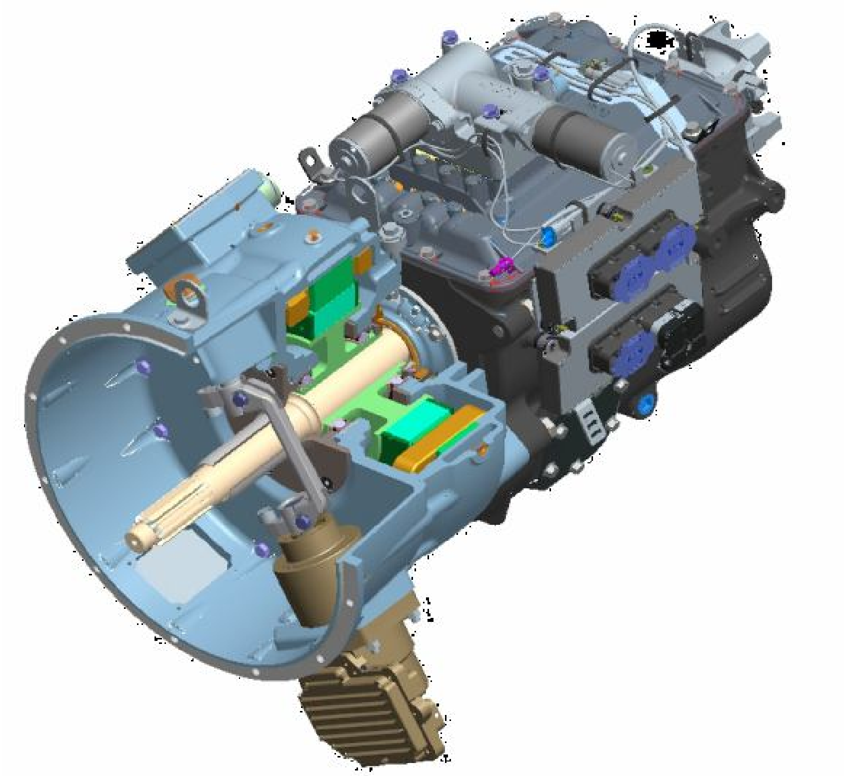

Fig. 1.47. Clutch-by-wire system in Eaton 6-speed Hybrid Drive Transmission

The automotive OEM supplier, Valeo, has launched the first clutch-by-wire system. The unit replaces the mechanical link between clutch and pedal with an electrical clutch actuator, an electric clutch pedal and an electronic control unit (ECU). A pedal sensor measures the position of the clutch pedal and transmits this information to the ECU which also receives information about car behavior. The ECU in turn controls the clutch actuator and depending upon the driver's wishes, the system can not only correct driver mis-operations but offer complete clutch automation.

The system is designed to require lower stroke and effort to the pedal and improves pedal feel with "virtual" resistance to foot pressure. More compact than a conventional clutch actuation, the clutch-by-wire system improves driver crash protection since it enables an optimized, less intrusive, pedal box design.

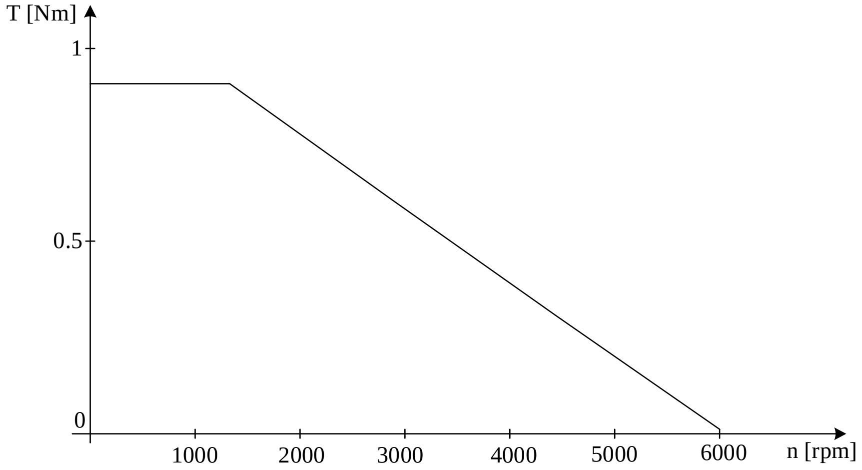

Fig. 1.48 Torque vs speed demand of an electric motor for clutch-by-wire application

1.10 Doble clutch transmission

A twin-clutch gearbox, double clutch transmission or dual clutch transmission (DCT) is a semi-automatic transmission with separate clutches for odd and even gears. The outer clutch drives the odd numbered gears, while the inner clutch drives the even numbered gears. Shifts can be accomplished without interrupting power, by applying the engine's torque to one clutch just as the engine's torque is being disconnected from the other clutch. Since the synchronizers that select an odd gear can be moved while driving the car in an even gear, and vice versa, DCT's have been configured which shift more quickly than Formula One and other cars equipped with single-clutch AMT's (automated-manual transmissions, acknowledged as single-clutch semi-automatics). Also, with a DCT, shifts can be made more smoothly than with an AMT, making a DCT more suitable for street-driving.

A twin-clutch gearbox eliminates the torque converter used in traditional automatic transmissions. Instead, dual clutch transmissions that are currently on the market use wet multi-plate clutches, similar to the clutches used in traditional automatic transmissions. A 7-speed version that uses dry clutches, like those usually associated with manual transmissions, will be introduced by VW in the 2009 Golf and Jetta. Getrag has a dry DCT under development, and others are rumored to be in development by several manufacturers.

At the top the Fig. 1.50 shows a shifting profile. In the next part the capacity (torque) of two clutches and then the engine torque can be seen. At the bottom the speed of the two shafts and the engine speed is illustrated for the requested shifting profile. The upshifts are characterized by the crossing of the clutch capacities and the change of engine speed between the transmission shaft speeds.

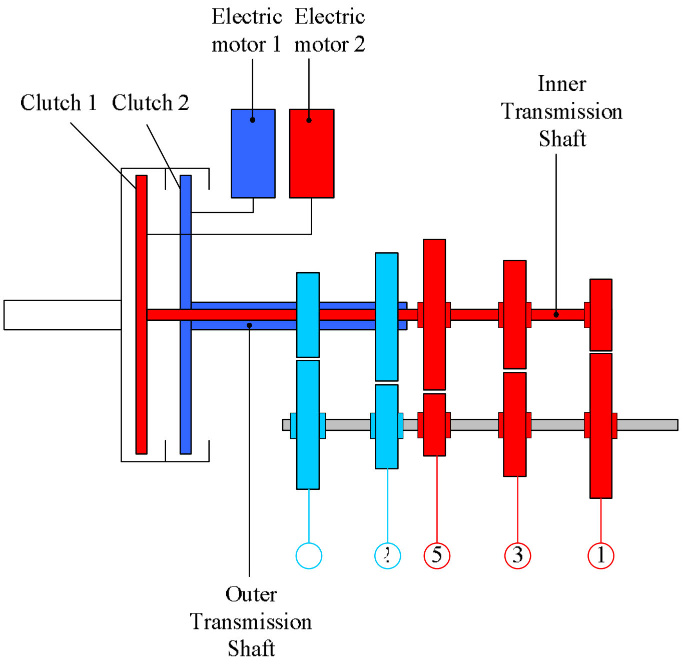

Fig. 1.49 Layout of a twin-clutch gearbox

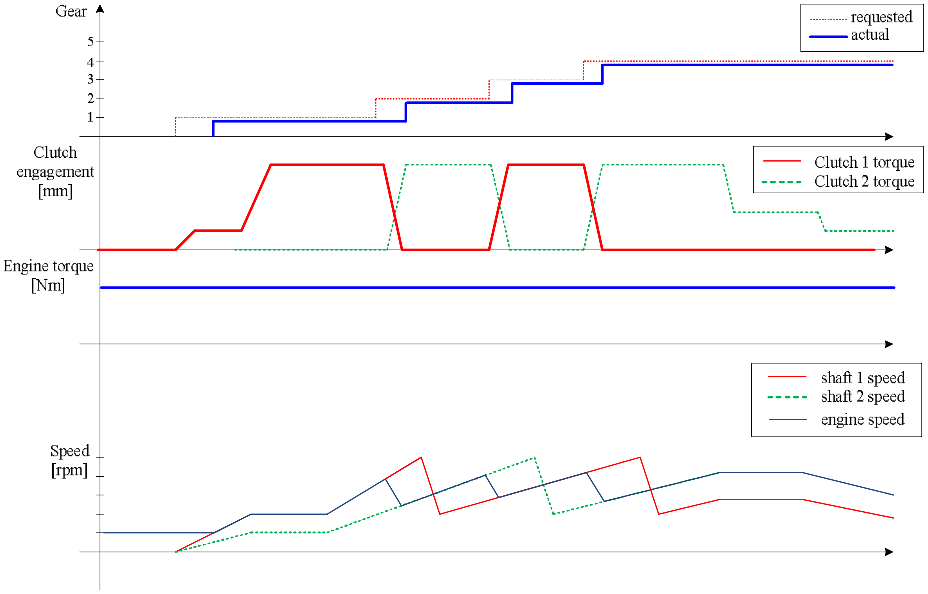

Fig. 1.50 Gear, clutch and engine torque, engine speed profile in a five-speed double-clutch transmission

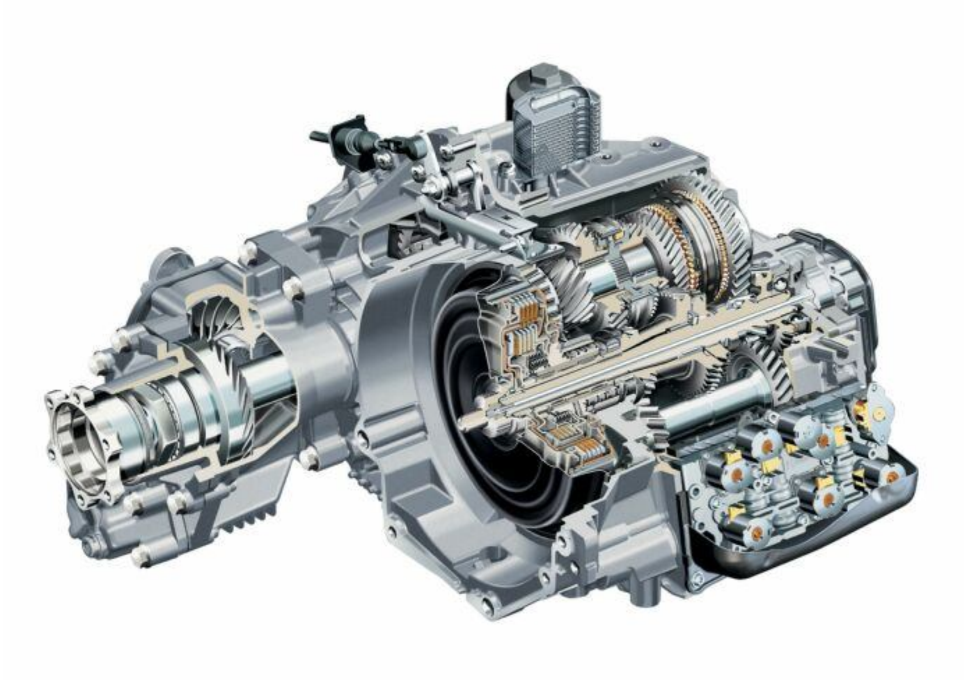

Fig. 1.51 Double clutch transmission

Compared to an automatic transmission the advantages of an automated manual transmission (AMT) are:

- Increased Comfort
- Lower production cost
- Greater efficiency
- Lower weight

1.11 Hybrid oil pump

The hybrid transmission under development uses pressurized oil for gear shifting operations, clutch activation and cooling. Conventional automatic transmissions usually have a hydraulic pump driven by the combustion engine for pressurizing the oil. In the hybrid electric vehicle transmissions, oil pressure is necessary also when the combustion engine is not running. Therefore a hybrid oil pump is needed. The structure of a hybrid oil pump is given in Fig. 1.53.

The output produced by the pump, by an intelligent control system, can be precisely matched to the flow demanded by the hydraulic system in the transmission. Compared to a conventional transmission pump where the output is constrained to the engine speed, less power is needed because of the demand oriented flow production. A reduction in driving power of up to 50% for a highway cruise cycle can be achieved by incorporating the electro-hydraulic pump into a transmission. This corresponds to a total fuel saving of approximately 1.8%. A conventional mechanical

oil pump have a maximum overall efficiency of 60-65%, while under the same conditions the hybrid oil pump efficiency increases to around 85%.
The oil pump circuit consists of:

- Oil tank
- Electric motor
- Proportional electrovalves (PWM valves)
- Internal gear pump

The check valve, clack valve, non-return valve or one-way valve is a mechanical device, a valve, which normally allows fluid (liquid or gas) to flow through it in only one direction. Check valves are two-port valves, meaning they have two openings in the body, one for fluid to enter and the other for fluid to leave.
A proportioning valve is a valve that relies on the laws of fluid pressure to distribute input forces to one or more output lines. A proportioning valve can increase or decrease forces for each output, depending on the cross-sectional surface areas of those output lines.

A Gear pump uses the meshing of gears to pump fluid by displacement. They are one of the most common types of pumps for hydraulic fluid power applications. There are two main variations; external gear pumps which use two external spur gears, and internal gear pumps which use an external and an internal spur gear. A cross section of an internal gear pump is presented in Fig. 1.52. Gear pumps are fixed displacement, meaning they pump a constant amount of fluid for each revolution.

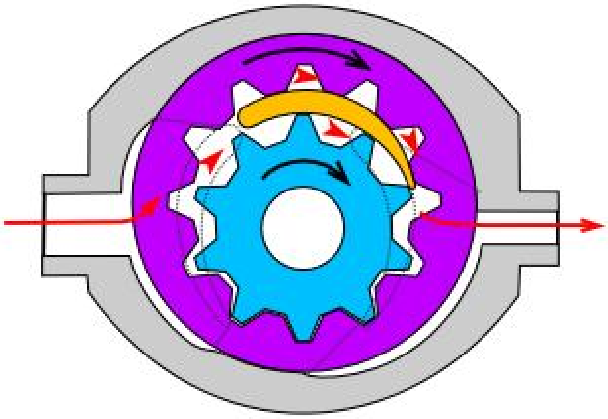

Fig. 1.52 Internal Gear Pump

The pressure generated by the oil pump is limited by regulating the slide valves (selector slide valve, gear control valve, converter pressure valve, converter control valve, etc). The current through the electrovalves varies typically between 100mA to 900mA.

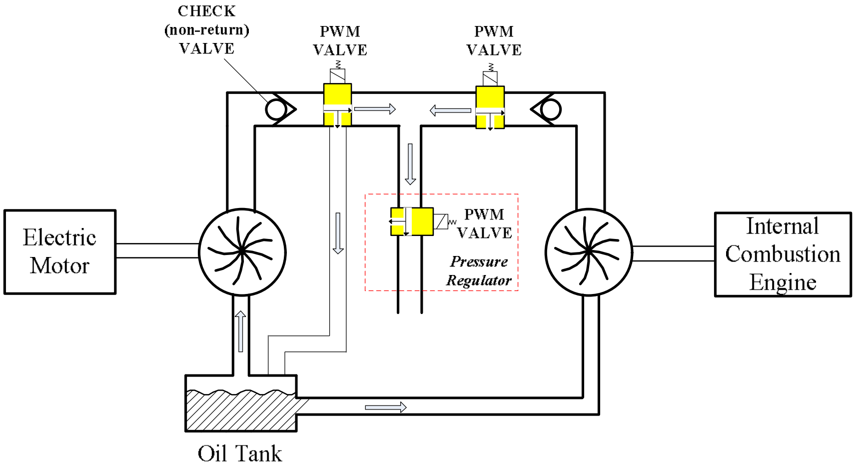

Fig. 1.53. Hybrid oil pump structure for automatic gearbox

A comparison between the conventional oil pump and hybrid oil pump is shown in Fig. 1.54. In general, in oil pumps the flow volume of the oil is proportional to the pump speed. The mechanical oil pump is dimensioned so that at the idle speed to be the minimum requested pressure (flow volume) necessary to the actuators for gear changing or cooling. At high engine speed the flow volume of the oil is much more than enough.

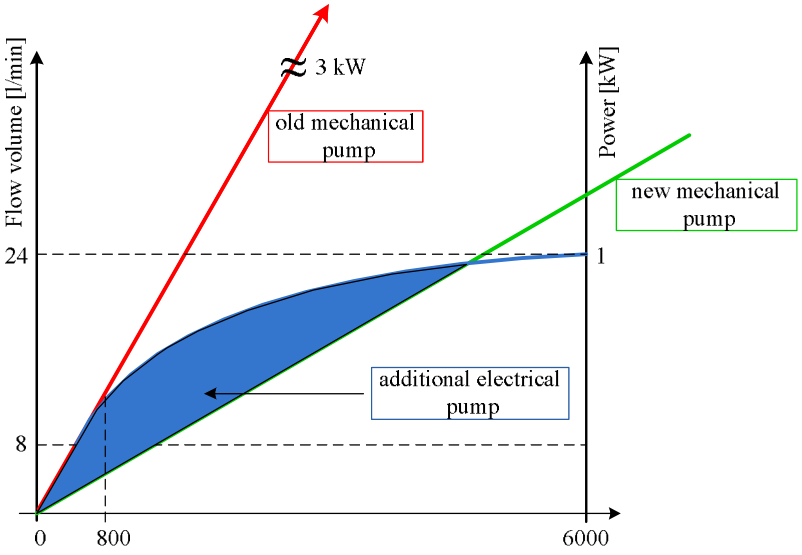

Fig. 1.54 Comparison between conventional mechanical and hybrid oil pump

Consequently at high speed the efficiency of the system is decreasing sharply. With the hybrid configuration the new mechanical pump is downsized and the electric oil pump supplies the additional oil volume to keep the pressure at the requested (nominal) value.

A very big advantage of such a configuration is that for hybrid electric vehicles for speeds lower than the idle speed, the line pressure of the gearbox is kept at the nominal value due to electric oil pump which works independently of the thermal engine.

In Fig. 1.55 are shown the inputs and outputs of a control system that regulates the pressure provided by the hybrid oil pump. Oil temperature is measured by a PTC thermistor (positive temperature coefficient resistor) located in the hydraulic unit.

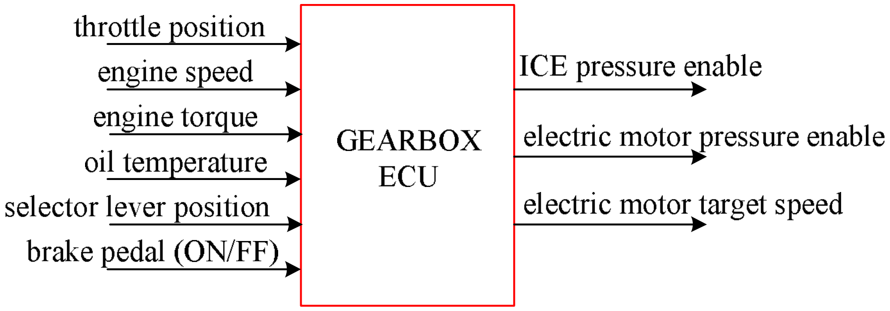

Fig. 1.55 Inputs/outputs of a control system for hybrid oil pump

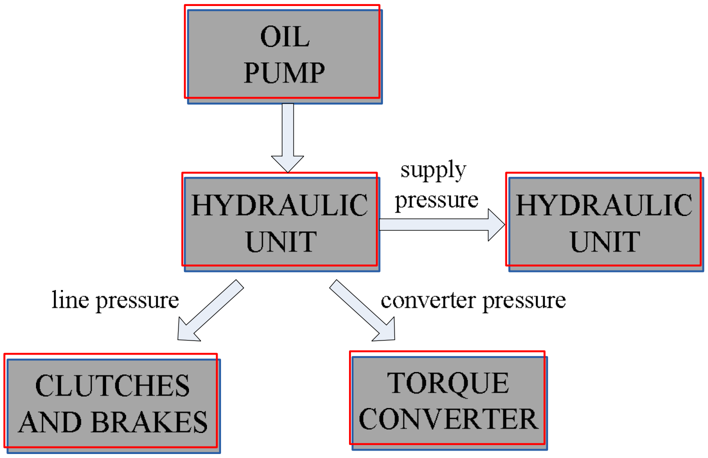

Fig. 1.56 Oil pressure distribution in an automatic gearbox

The main components of hydraulic circuit are:
- The oil pump
- The hydraulic distribuitor (or unit)

The purpose of these elements is to:
- Supply the clutches and the brakes
- Supply an control the torque converter
- Supply the transmission lubrification circuit
- Cool the transmission by circulating the oil through a heat exchanger

There are three types of pressure in the hydraulic circuit:
- The supply pressure for the lubrification circuit
- The converter pressure for supplying and controlling it
- The line pressure (the pressure set up on the pistons of the operated brakes and clutches)

The activation of ICE driven oil pump and electric oil pump is determined by the overall efficiency of these two systems. In the case of hybrid electric vehicle, when the engine is off, only electric oil pump will be active. Also, at idle, the electric oil pump due to low engine torque. In some cases, the best efficiency is achieved if both pumps are running. For the cases when the mechanical oil pump is running at high efficiency, only this is active. So, the efficiency is governing the operating mode of these two types of pumps. A graphical representation of the explanation is given in Fig 1.57.

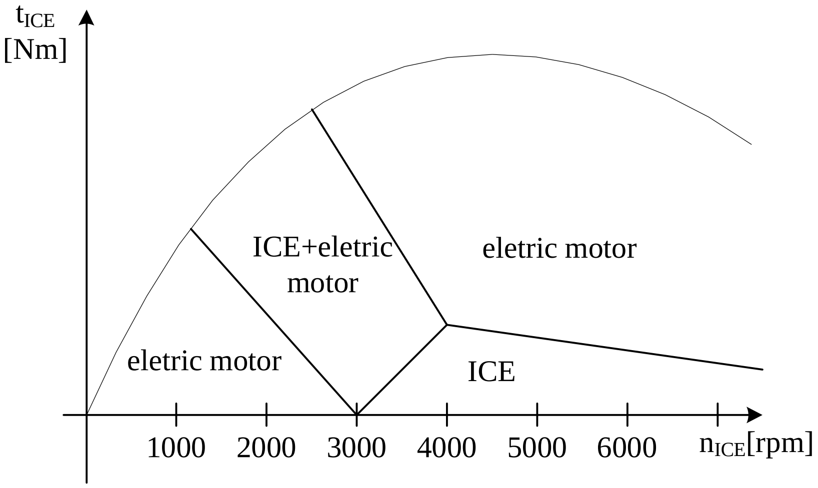

Fig. 1.57 Oil pressure created by ICE and electric motor vs ICE engine map

The behavior of the hydraulic pressure during clutch engagement is shown in Fig. 1.58. The pressure drops down due to the engine speed which drops down also. With the hybrid configuration the pressure drop is small, decreasing the time needed for gear changing.

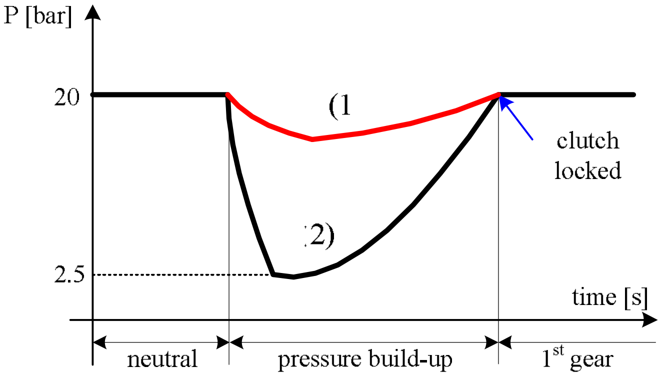

Fig. 1.58 Hydraulic system pressure at engine idling speed: (1) with hybrid oil pump, (2) with conventional oil pump

1.12 Transfer case

A transfer case is a part of a four wheel drive system found in four wheel drive (4WD) and all wheel drive (AWD) vehicles. The transfer case receives power (torque) from the transmission and splits it up between the front and rear axles (Fig. 1.59). The ratio between the torque driven to the front wheels and the torque transmitted to the rear wheels depends on the manufacturer. The torque transfer case includes an input shaft connected to the output of the main transmission, a rear output shaft connected to drive the vehicle rear wheels, a front output shaft connected to drive the front wheels (Fig. 1.61).

This can be done with a set of gears, but the majority of transfer cases, manufactured today, are chain driven. On some vehicles, such as four wheel drive trucks or vehicles intended for off-road use, this feature is controlled by the driver. The driver can put the transfer case into either "two wheel drive" or "four wheel drive" mode. The integration of a transfer case in a vehicle transmission system is shown in Fig. 1.60.

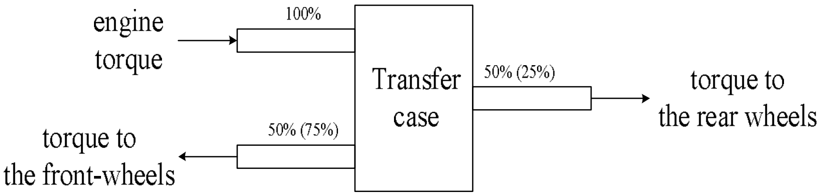

Fig. 1.59 Transfer case

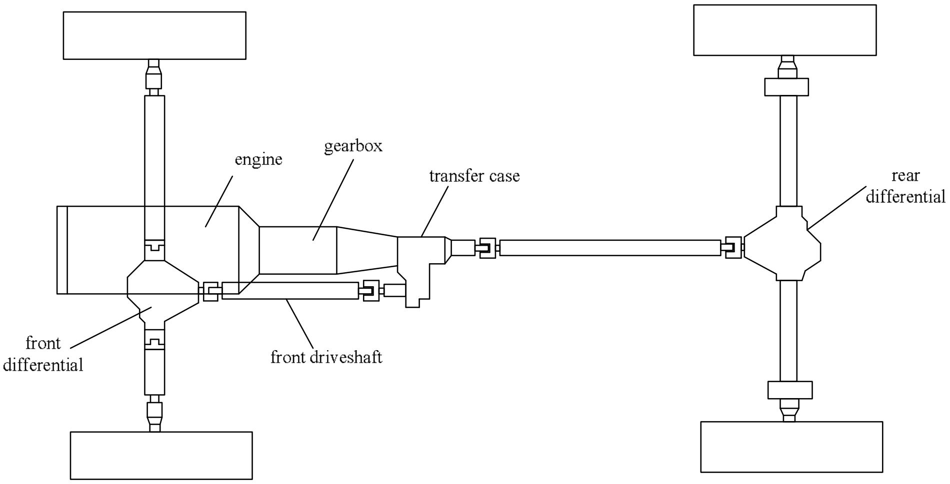

Fig. 1.60 Four-wheel drive system configuration

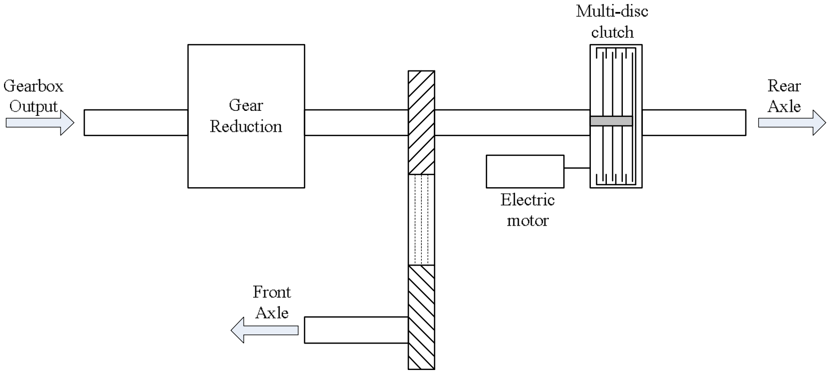

Fig. 1.61 Structure of a transfer case

1.13 Engine cooling system

The function of engine cooling system is to remove the excess heat from the engine, to keep the engine operating at the most efficient temperature, and to allow the engine to reach its ideal operating temperature in the shortest time possible. The efficiency of an internal combustion engine is around 33%. This means that one third of the energy from the fuel is converter into mechanical work. Another third goes out on the exhaust pipe, and the remaining becomes heat energy.

Traditional automotive water pumps are belt-driven by the vehicle engine, forcing pump shaft speed to turn to the engine speed multiplied by the belt speed ratio. In some cases, such as idling after a period of high load, the water pump must provide flow and pressure sufficient to cool a hot engine at low shaft speeds. Pumps can be designed to operate efficiently at a specific operating point, but can not be simultaneously at high and low speeds. A motor driven pump provides constant input speed and also consumes less energy by only pumping when needed. Traditional water pumps are run continuously and utilize a thermostat-controlled bypass when engine cooling not required.

The cooling system of a water-cooled engine system consists of:
- The engine water jacket
- Thermostat
- Water pump – electric driven
- Radiator
- Cooling fan – electric driven
- Hoses
- Heater core
- Expansion tank

The layout of en engine water cooling system is illustrated in Fig. 1.62. In the conventional engine cooling system the cooling fan was driven by the thermal engine via a V-belt. The trend is now to drive the cooling fan by means of an electric motor. Also the water pump is electric driven. Both motor are close-loop speed control. It is worth to mention that this application is a slow dynamic, from the electric motor control point of view. This have a direct impact on the control strategy of the electric motors used in such an application. Sensorless brushless dc motors are the best candidate for this application due to the lowest cost/performance ratio. Even if the starting of brushless dc motors is not a very robust one, due to the slow dynamic (lower thermal time constant) of the thermal process, the low cost sensorless control solution is a good solution for this application.

Speed-controller electric water pump offers up to 80% reduction in energy consumption [1.76].

The electric engine cooling system involves electronic thermal management algorithms that reduces pump power consumption through gains in controllability and efficiency, and also provides for additional control of heat rejection management and variable control of coolant, oil, and engine temperatures.

Advanced thermal management system benefits are as follows [1.77]:
- Variable flow and temperature control allow for semi-independent regulation of two or more temperatures (e.g. engine metal temperature and coolant temperature)
- Capability to proactively respond to transient engine conditions.
- Capability to automatically optimize engine thermal management in cold and hot environments.
- Reduced parasitic loads from the water pump and fan.
- Increased engine thermal efficiency.
- Ability to eliminate hot soaks at engine shutoff.
- Improved engine warm-up, heater performance and cab warm-up.

- Improved packaging, as the electric components are not necessarily tied to the FEAD.
- Auxiliary cooling for high heat rejection.

In [1.77] is presented the design, bench testing, and wind-tunnel vehicle testing of an advanced system comprised of an electric pump, electronic water flow proportioning valve, 42V alternator, 36V starter, and an electronic control system which commands the performance of the valve, pump, and fan clutch in relation to the cooling demand on a 1999 Volvo VN tractor equipped with a Cummins N14 engine. System design and test data are compared from both the stock cooling system and the advanced thermal management system (ATMS).

In [1.78] is presented an advance thermal management system for a 5.7L, 244hp engine. The active cooling system is comprised of a 14 V electric BLDC water pump, electric 2-way flow-control valve, dual BLDC electric fans, fan shroud, and thermal system controller. The system is powered by the production 140A alternator. The condenser, radiator, and heater core were retained from the base configuration. The electric water pump is powered by a 300W brushless dc electric motor. The electric variable-speed fans are powered by 250W BLDC motors and driven by 12V component controllers which receive a PWM speed signal from the thermal management controller.

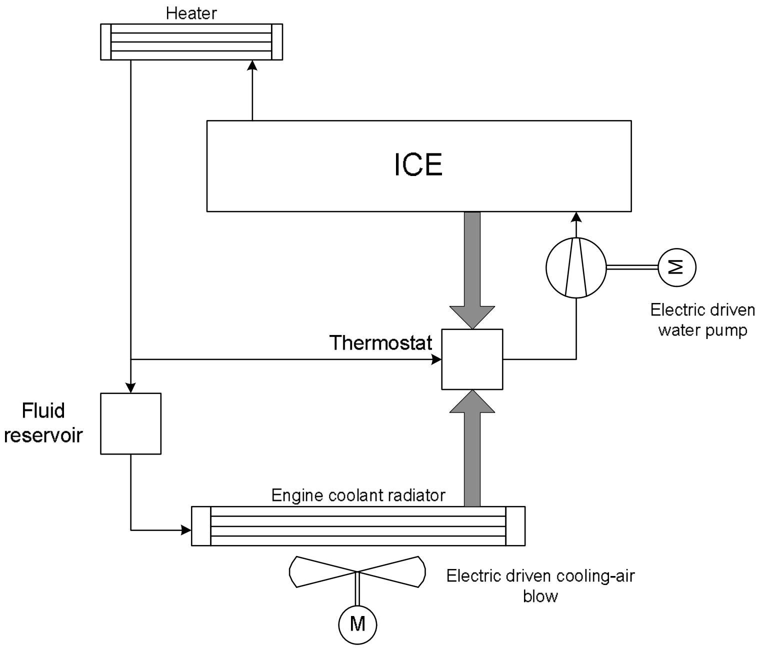

Fig. 1.62. Block diagram of an engine water-cooling pump

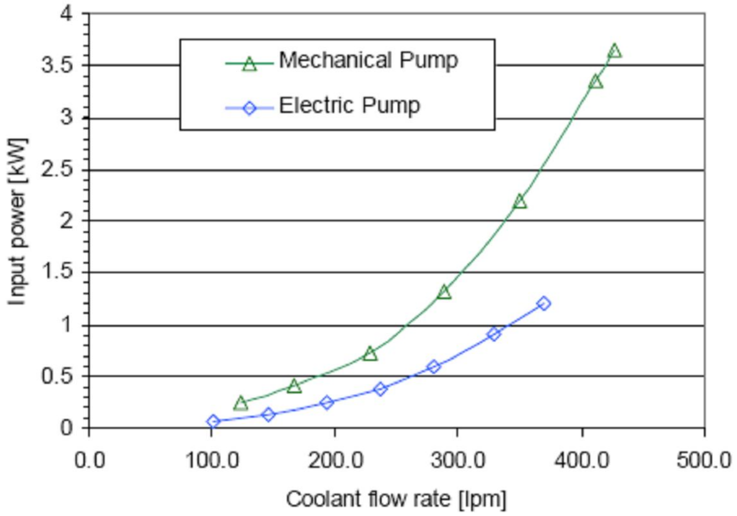

Fig. 1.63. Water pump power consumption versus coolant flow rate [1.77]

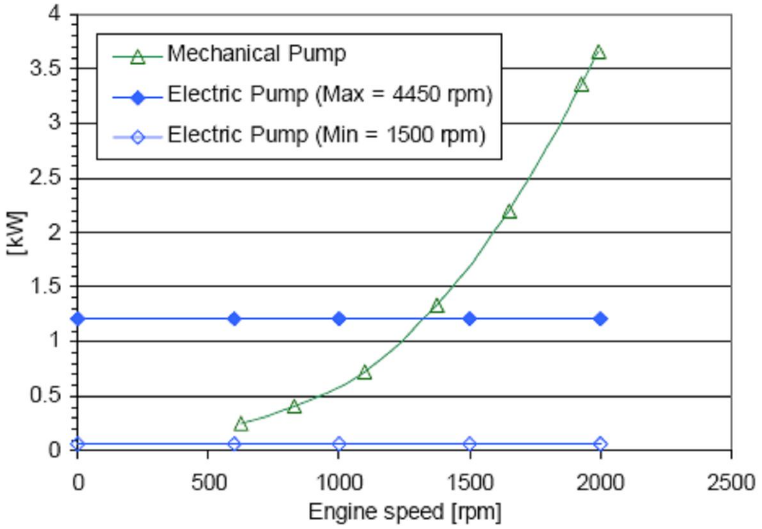

Fig. 1.64. Cooling system power consumption versus engine speed [1.77]

Engine specifications:
Peak power: 358 kW (480 HP)
Peak torque: 2509 Nm, 1200rpm
Engine heat rejection: 131 kW peak power

At the minimum pump speed, the electric pump consumes 70W. Assuming an average speed of 1600rpm, the electric pump reduces parasitic losses by 1.96 kW.

SUMMARY

In this chapter an overview of the main existing and future applications of electric motor in automobiles industry is provided. In the past the number of automotive applications that used electric motors, with rate power of a few hundreds of watts, was limited. Clutch-by-wire, and double-clutch gearbox with electric shift are new technologies on the market. Steering-by-wire and brake-by-wire are still under development due to major concern on safety issues. Hybrid oil pump for automatic gearbox are a new application in automotive industry and most probably they will be on the market, in series production, the next year. Electric engine cooling systems are already available on the market. The potential of integrated starter-alternator system is huge due to the increasingly demand of hybrid electric vehicles.

REFERENCES

[1.1] J. Reinpell, H. Stoll, J. W. Betzel. "The Automotive Chassis: Engineering Principles", Butterworth Heineman, 2001

[1.2] Bosch Automotive Handbook, Robert Bosch, 2000

[1.3] R. Fleck, "Active Steering – an important first step to steer-by-wire", Conference of Automotive Steering, Essen, 2003

[1.4] P. Brenner, "Electrical Components of the Active Front Steering from ZF Lenksysteme Gmbh", Conference of Automotive Steering, Essen, 2003

[1.5] D. Iles-Klumpner, I. Boldea, "Comparative Optimization Design for an Interior Permanent Magnet Synchronous Motor for an Active Steering System", PESC, 2004

[1.6] D. Iles-Klumpner, "Automotive Permanent Magnet Actuation Technologies", Ph. D. Thesis, Timisoara, 2005

[1.7] J. Hur, "Characteristic Analysis of Interior Permanent Magnet Synchronous Motor in Electrohydraulic Power Steering System", IEEE Trans. IE, Vol. 55, no. 6, June, 2008

[1.8] B.C. Kim, D.H. Lee, J.W. Ahm, "Performance of a SR Drive for Hydraulic Pump", ICEMS, 2005, Vol. 1, pp. 659-663

[1.9] N. Bianchi, M. D. Pre, S. Bolognani, "Design of a Fault-Tolerant IPM Motor Drive for Electric Power Steering ", PESC2005

[1.10] C. Oprea, C. Martis, B. Karoly, "Six-Phase Brushless DC Motor for Fault Tolerant Electric Power Steering Systems", ACEMP 2007, pp. 457-462.

[1.11] A. D. Crapo, T. A. Walls, R. E. Hartsfield, ""Electric Power Steering System Including a Permanent Magnet Motor, Patent No: US 7,034,423 B2, April 2006

[1.12] S. Murthy, T. Sebastian, B. Liu, "Implications of 42V Battery Power on the Design of Motors for Electric Power Steering System", SAE 2000

[1.13] A. Badawy, B. Liu, S. Murthy, T. Sebastian, "Design considerations of drive motors for electric power steering", Proceedings of the 32nd International Symposium on Automotive Technology and Automation (ISATA), track-Automotive electronics and New Products, June 14-18, 1999 Austria, Vienna. pp.: 195-198.

[1.14] S. Kodama, K. Tsutsumi, "Development for Brushless EPS System", Technical Report

[1.15] M. Wellenzohn, T. Presta, “Improved Fuel Consumption through Steering Assist with Power on Demand”, SAE 2008
[1.16] A. W. Burton, “Innovation Drivers for Electric Power-Assisted Steering”, IEEE Control System Magazine, Vol. 23, No. 6, pp. 30-39, December 2003
[1.17] Saric S., Bab-Hadiashar A. and Hoseinnezhad R., “Clamp Force Estimation for a Brake-by-Wire System: A Sensor Fusion Approach”, IEEE Transactions on Vehicular Technologies, 2006
[1.18] Hoseinnezhad R., Bab-Hadiashar A. and Rocco T.,“Real-Time Clamp Force Measurement in Electro-Mechanical Brake Calipers”, accepted for publication in IEEE Transactions on Vehicular Technology, 2008.
[1.19] Hoseinnezhad R., Saric S.and Bab-Hadiashar A.,“Estimation of Clamp Force in Brake-by-Wire Systems: A Step-by-Step Identification Approach”, SAE Transactions, 2006, Volume 115-6, SP-2017.
[1.20] H. Hartmann, M. Schautt, A. Pascucci, B. Gombert, “eBrake® - the Mechatronic Wedge Brake”, SAE 2001
[1.21] R. Roberts, M. Schautt, H. Hartmann, B. Gombert, “Modeling and Validation of the Mechatronic Wedge Brake”, SAE 2003
[1.222] R. Roberts, B. Gombert, H. Hartmann, D. Lange, M. Schautt, “Testing the Mecatronic Wedge Brake”, SAE 2004
[1.23] L. M. Ho, R. Roberts, H. Hartmann, B. Gombert, “The Electronic Wedge Brake -EWB”, SAE 2006
[1.24] J. Fox, R. Roberts, C. Baier-Welt, L. M. Ho, L. Lacraru, B. Gombert, "Modeling and Control of a Single Motor Electronic Wedge Brake", SAE 2007
[1.25] H. Klode, A. M. Omekanda, B. Lequesne, S. Gopalakrishnan, A. Khalil, S. Underwood, I. Husain, ”The Potential of Switched Reluctance Motor Technology for Electro-Mechanical Brake Applications”, SAE 2006
[1.26] D. Jhalani, S. Dhir, "Survey of Fault Tolerance Techniques in Automotives"
[1.27] http://www.freescale.com/files/dsp/doc/app_note/AN1999.pdf
[1.28] http://www.vehicledynamics-expo.com/07vdx_conf/day_2/baier_welt.pdf
[1.29] Y. H. Qiu, T. A. Parlikar, W.S. Chanh, M. D. Seeman, T. A. Keim, D. J. Perreault, J. G. Kassakian, “Design and Experimental Evaluation of an Electromechanical Engine Valve Drive”, IEEE-PESC, 2004, Aachen, Germany
[1.30] W. S. Chang, T. A. Parlikar, J. G. Kassakian, T. A . Keim, ”An Electromechanical Valve Drive Incorporating a Nonlinear Mechanical Transformer”, SAE World Congress, Detroit, March 2003
[1.31] W. S. Chang, T. A. Parlikar, M. D. Seeman, D. J. Perreault, J. G. Kassakian, T. A. Keim, “A New Electromagnetic Valve Actuator”, IEEE Workshop on Power Electronics in Transportation, pp. 109-118, Auburn Hills, October 24-25, 2002
[1.32] R. Flierl, M. Kluting, “The Third Generation of Valvetrains – New Fully Variable Valvetrains for Throttle-Free Load Control”, SAE Technical Paper Series, 2000
[1.33] S. Butzmann, et all, “Sensorless Control of Electromagnetic Actuators for Variable Valve Train”, SAE Technical paper Series, 2000
[1.34] C. Schernus at al. “Modeling of Exhaust Valve Opening in a Camless Engine”, SAE Technical Paper Series, 2002
[1.35] I. Boldea, et all, “A Novel Linear PM Electromagnetic Valve Actuator: FE Optimal Design and Dynamic Modeling”, Record of Electromotion 2007, Bodrum, Turkey, Sept. 2007
[1.36] I. Boldea, S. A. Nasar, “Linear Motion Electromagnetic Devices”, Book, Taylor & Francis, 2001

[1.37] I. Boldea, “Automobile Electrification Trends: a Review”, Invited paper of Electromotion 2007, Bodrum, Turkey, Sept. 2007

[1.38] P. Barkan, T. Dresner, “A Review of Variable Valve Timing Benefits and Modes of Operation”, SAE Technical paper Series, Paper 891676, 1989

[1.39] Y. Wang, T. Megli, M. Haghgooie, K. S. Peterson, A. G. Stepanopoulou, “Modeling and Control of Electromechanical Valve Actuator“, SAE World Congress, 2002

[1.40] I. Boldea, S Agarlita, L. Tutelea, F. Marignetti, “Novel linear PM valve actuator: FE design and dynamic model”, LDIA 2007

[1.41] I. Boldea, S. Agarlita, F. Marignetti, L. Tutelea, “Electromagnetic, thermal and mechanical design of a linear PM valve actuator laboratory model”, OPTIM 2008

[1.42] T. Ahmad, M. A. Theobald, “A Survey of Variable-Valve-Actuation Technology”, SAE Technical Paper Series, Paper 891674, 1989

[1.43] K. S. Peterson, A. G. Stepanopoulou, Y. Wang, T. Megli, M. Haghgooie, “Virtual lash Adjuster for an Electromechanical Valve Actuator Through Iterative Learning Control”, Proceedings of ASME International Mechanical Engineering Congress, November 21-23, 2003

[1.44] A. Kruczek, A. Stribrsky, “A Full-Car Model for Active Suspension - Some Practical Aspects”, ?????

[1.45] F. B. Hoogterp, J. H. Beno, D. A. Weeks, “An Energy-Efficient Electromagnetic Active Suspension”, SAE Paper, 1998

[1.46] D. A. Weeks, D. A. Bresie, J. H. Beno, A. M. Guenin, “The Design of an Electromagnetic Linear Actuator for an Active Suspension”, SAE Paper, 1999

[1.47] R. I. Davis, P. B. Patil, “Electrically Powered Active Suspension for a Vehicle”, Patent No: 5,060,959, October 1991

[1.48] A. Stribrsky, K. Hyniova, J. Honcu, A. Kruckzeck, “Energy Recuperation in Automotive Active Suspension with Linear Electric Motor”, Proceedins of the 15th Mediterranean Conference on Control & Automation, 2007, Athens, Greece

[1.49] A. Stribrsky, A. Kruckzeck, “H□ Control of Automotive Control Suspension with Linear Motor”

[1.50] B. L. J. Gysen, J. L. G. Jassesn, J. J. H. Paulides, “Design Aspects of an Active Electromagnetic Suspension System for Automotive Applications”, IEEE Industry Applications Society Annual Meeting, October, 2008

[1.51] Meessen, K.J., Gysen, B.L.J., Paulides, J.J.H, Lomonova, E. “Optimal Halbach Permanent Magnet Shapes for Slotless Tubular Actuators”, IEEE International Magnetics Conference,
IEEE INTERMAG 2008. (pp. 1157-1157)

[1.52] Gysen, B.L.J., Meessen, K.J., Paulides, J.J.H, Lomonova, E., “Semi-Analytical Calculation of the Armature Reaction in Slotted Tubular Permanent Magnet Actuators”, IEEE International Magnetics Conference, 2008. IEEE INTERMAG 2008. (pp. 1289-1289)

[1.53] Bart L.J. Gysen, Johannes J.H. Paulides, Jeroen L.G, “Active Electromagnetic Suspension System. for Improved Vehicle Dynamics”, IAS 2008, Edmonton, Canada

[1.54] J. Paulides, E. Lomonova, A Vandenput, “Design Consideration for an Active-Electromagnetic Suspension System”, INTERMAG 2006

[1.55] Gysen, B.L.J., Paulides, J.J.H, Lomonova, E., “Measurements on an electromagnetic active suspension system for automotive applications”, Proceedings of the 4th IEEE Young Researchers Symposium, Eindhoven

[1.57] R. Rajamani, J. K. Hedrick, “Performance of Active Automotive Suspensions with Hydraulic Actuators: Theory and Experiment”, Proceedings of American Control Conference, Vol. 2, pp. 1214-1218, June 1994

[1.58] Y. Sam, K. Hidha, “Modeling and Force Tracking Control of Hydraulic Actuator for an Active Suspension”, IEEE Conference on Industrial Electronics and Applcations, pp. 1-6, May 2006

[1.59] S. Guo, S. Li, S. Yang, “Semi-active Vehicle Suspension System with Magnetoreological Dampers”, IEEE International Conference on Vehicular Electronics and Safety, 2006

[1.60] Delphi Corporation, http://delphi.com

[1.61] M. Algrain, U. Hopmann, “Diesel Engine Waste Heat Energy Recovery Utilizing Electric Turbocompound Technology”, DEER Conference, Newport, 2003

[1.62] I. Kolmanovsky, A. G. Stepanopoulou, B. K. Powell, “Improving Turbocharged Diesel Engine Operatio with Turbo Power Assist System ”, SAE Paper, 2003

[1.63] F. Millo, O. Ryder, et all, “The Potential of Electric Exhaust Gas Turbocharging for HD Diesel Engines”, DEER Conference, Chicago, 2005

[1.64] S. George, G. Morris, J. Dixon, D. Pearce, G. Heslop, “Optimal Boost Control for an Electrical Supercharging Application”, SAE Paper, 2004

[1.65] H. Uchida, “Trend of Turbocharging Technologies”, ????

[1.66] T. Noguchi, Y. Takata, Y. Yamashita, Y. Komatsu, S. Ibaraki "220,000-r/min, 2kW Permanent Magnet Motor Drive for Turbocharger", IEE-Japan Trans. on Industry Applications, vol. 125, no. 4, 2005

[1.67] M. Kano, T. Noguchi, "Efficiency Improvement and Loss Analysis of Ultra-High Speed Permanent Magnet Motor"

[1.68] T. Noguchi, M. Kano, "Development of 150000 r/min, 1.5 kW Permanent Magnet Motor for Automotive Supercharger"

[1.69] T. Noguchi, Y. Takata, Y. Yamashita, Y. Komatsu, S. Ibaraki "160,000-r/min, 2.7kW Electric Drive of Supercharger for Automobiles", PEDS, 2005

[1.70] M. Michon, S D. Calverley, R. Clark, D. Howe, P. Sykes, “Switched Reluctance Turbo-Generator for Exhaust Gas Energy Recovery”, EPE-PEMC 2006

[1.71] S. D. Calverley, “Design of a High Speed Switched Reluctance Machine for Automotive Turbo-Generator Applications”, Ph. D. Thesis, University of Sheffield, UK, 2001

[1.72] M. P. Lasecki, J. M. Cousineau, “Controllable Electric Oil Pumps in Heavy Duty Diesel Engines”

[1.73] A. J. Silveri, M. P. Kraska, W.. Ortmann, “Hybrid Electric Vehicle Auxiliary Oil Pump”, Patent No: US 6,805,647 B2, ct 19, 2004

[1.74] R. L. Moses, J. R. Maten, “Integrated Electric-Motor Driven Oil Pump for Automatic Transmissions in Hybrid Applications”, Patent No: US 6,964,631 2, Nov. 15, 2005

[1.75] D. Ledger, G. Dolan, F. Cadwell, J. Bolsmer, “Electric Oil Pump System and Controls for Hybrid Electric Vehicles”, Patent No: US 7,395,03 B2, Jul. 8, 2008

[1.76] J. T. Allsion, “Design Optimization Model for an Automotive Electric Water Pump ”

[1.77] R. D. Chalgren, L. Barron, “Development and Verification of a Heavy Duty 42/14 Electric Powetrain Cooling System”, SAE, 2003

[1.78] R. D. Chalgren, “Thermal Comfort and Engine Warm-up Optimization of a Low-Flow Advanced Thermal Management System”, SAE 2004

2. BATTERY ON-LINE MODELING WITH TEST RESULTS AND DISCUSSION

This chapter reports a novel algorithm, proposed for battery internal resistance estimation as well as a new algorithm for battery on-line state-of-charge estimation. Battery internal resistance estimation is based on the voltage and current variation measured at the battery terminals. Although, there are a few methods for battery internal resistance estimation, the proposed solution aims to provide a better understanding of the internal resistance meaning, and underline the importance of this parameter in development of battery models and battery behavior prediction. The proposed approach for battery state-of-charge estimation is based on identification of seven states, with different dynamics, which allows the estimation of the static value of OCV.

2.1 Importance of battery internal resistance and battery state-of-charge

Hybrid Electric vehicles are a viable alternative to conventional internal combustion engine (ICE)-based vehicles for the automobile industry due to environmental issues and exhaustible petroleum resources. Recent efforts in HEV research have been directed toward developing energy efficient and cost effective propulsion system. Propulsion system converts energy stored in fuel and batteries into mechanical energy through ICE and electric motor. A globally efficient propulsion system uses much energy from the battery, consequently more stress on the battery.

The primary role of valve regulated lead-acid batteries (VRLA) in conventional cars is to provide the required energy to the starter system for the start-up of the internal combustion engine. In contrast to conventional cars, where the battery energy is used from time to time, in hybrid electric vehicles the battery is activated almost all the time.

The efficiency of HEVs depends strongly on the characteristics of the batteries. The most important parameters of the batteries are: state-of-charge (SOC), state-of-health (SOH), power discharge capability (PDC), power acceptance capability (PAC) and the internal resistance of battery. The latter is a strong indicator of the state-of-health and it is of paramount importance in the estimation of state-of-charge.

A good estimation of internal resistance provides an accurate state-of-charge and state-of-health of the batteries. Although, there is some literature on the some pertinent measurement of internal resistance, the so far proposed algorithms are not suitable for an on-line battery management system. The major requirement for a measurement system of internal resistance is on-line capability.

Internal resistance measurement should take no more that 1 second and the system must measure, on-line, the resistance with very high accuracy.

Electrochemical batteries started to play a very important role in automobile market, due to the migration of the standard configuration of an automobile to a hybrid electric vehicle configuration. The dynamic performance, the cost and the efficiency of a hybrid electric vehicle are directly related on the battery parameters and performance. In the conventional automobiles the main role of the battery has been to assure a safe engine cranking and to be an energy buffer. In hybrid electric vehicles the battery requirements are more, and a few of them are listed bellow:

- Battery have to provide a safe engine cranking
- Battery have to have a longer life (more charge/discharge cycle) in more stressful conditions
- Battery have to be able to provide more power (higher currents) for longer time periods
- Battery have to be able to capture high power (energy) pulses

The battery managements system (BMS) has to provide the following information about the battery:

- State-of-charge (SOC) level
- State-of-health (SOH)
- Maximum instantaneous discharge power
- Maximum instantaneous charge power
- Overcharge and overdischarge protection
- Overtemeperature protection
- Battery life prediction
- Cell balancing (especially for Ni-MH and Li-Ion batteries)

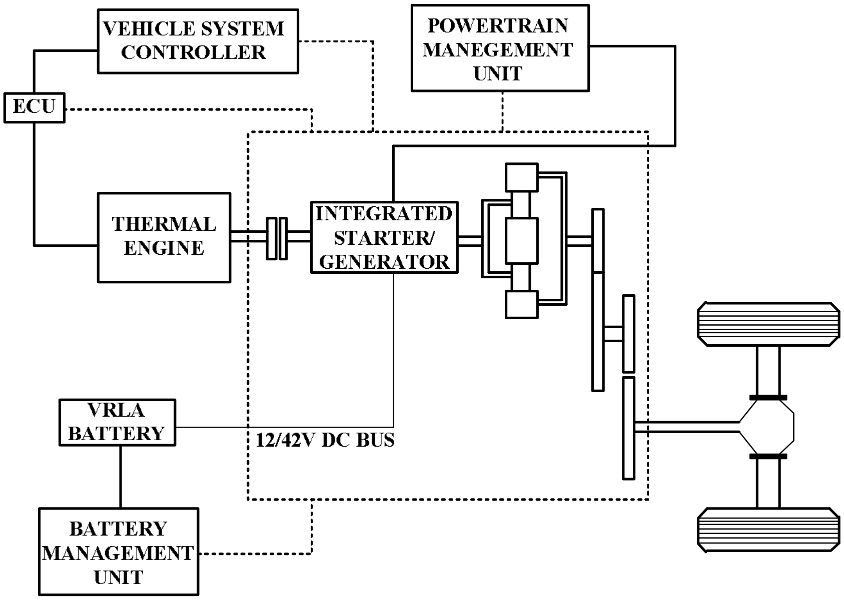

Fig. 2.1. General configuration of a hybrid electric vehicles (HEV)

The integration of a battery management system (unit) in a hybrid electric vehicle is shown in Fig. 2.1. It directly communicates with the Powetrain Management Unit, providing the required information necessary for a good torque/power distribution between ICE and electric motor.

2.2 Battery internal resistance

The internal resistance of electro-chemical batteries used in HEV, is a relevant parameter that characterizes the batteries. It is very useful in state-of-charge estimation, state-of-health estimation, and prediction of maximum discharged power of the battery. The estimation (measurement) of battery internal resistance with a very good accuracy contributes to a higher accuracy in the above enumerated parameter estimation.

The internal resistance of valve-regulated lead acid (VRLA) batteries used in HEV, basically, has two components: the electronic resistance and ionic resistance. The behavior of these two components is different in time and our purpose is to understand the usefulness of such parameters in issues regarding VRLA batteries.
The electronic resistance encompasses the resistance of the actual mass such as metal covers and internal components; as well as, how these materials interact with each others and wires resistance [2.1]. The effect of this resistance occurs very quickly and can be seen in the first microseconds after the battery is under load.
The ionic resistance is the resistance to current flow within the battery due to various electrochemical factors such as, electrolyte conductivity, ion mobility and electrode surface area [2.1]. These polarization effects occur more slowly than electronic resistance, and the effect can be seen after a few milliseconds after the battery is under load. The battery voltage drop due to this resistance we call the polarization voltage,
The impact of electronic and ionic resistance can be observed easily in Fig. 2.26 using a pulse load test.
Cold temperatures slow down the electrochemical reactions that take place in the battery and reduce the ion mobility in electrolyte, leading to a change of resistance value. That is why the battery resistance is affected by temperature. The temperature information is required for a better understanding and prediction behavior of such parameters.

A good knowledge of internal resistance variation is a basis in the analysis of electrochemical processes that occurs in the battery. The internal resistance of the electrochemical batteries is affected by the following parameters:

- state-of-charge
- state-of-health (ageing)
- temperature

A decrease of battery state-of-charge leads to an increase of internal resistance. At very low levels of SOC the internal resistance has values up to double compared with high levels of SOC. The reference values of internal resistance are considered those obtained from measurements performed at a temperature of 20oC.
Temperatures higher than 20oC lead to a decreasing of internal resistance values. A typical range for battery temperature used in HEV, during operation, is between -20oC and 50oC; however the latest requirements in automotive industry have indicated that the batteries should be capable of providing enough energy for a safe cranking of internal combustion engine (ICE), even at -40oC.

Battery state-of-health produces significant changes of the battery internal resistance values. The ageing process of batteries is irreversible and it contributes the battery performance. A battery with a higher degree of ageing (low state-of-health) produces a three times, and even more increasing of battery's internal resistance value.

2.2.1 Review of existing internal resistance estimation methods

An analysis and review of the already known methods of estimating (measurements) battery internal resistance is performed below. The analysis try to shown and to distinguishes between different meanings of the battery internal resistance. An explanation of electromechanical impedance spectroscopy principle used for battery characterization is given, also. Two methods are used in literature for battery internal resistance measurement:

a. dc load pulse
b. electrochemical impedance spectroscopy

Each method has its own perception regarding the nature of internal resistance.

2.2.1.1. DC load pulse

This is the oldest method used for battery internal resistance measurement. The estimation of internal resistance is based on Ohm Law. Using Ohm Law we measure the total effective resistance of the battery [2.2], [2.3].

A load is applied to battery for seconds up to minutes and the voltage drop divided by the current provides the internal resistance value. The principle is illustrated in Fig. 2.2.

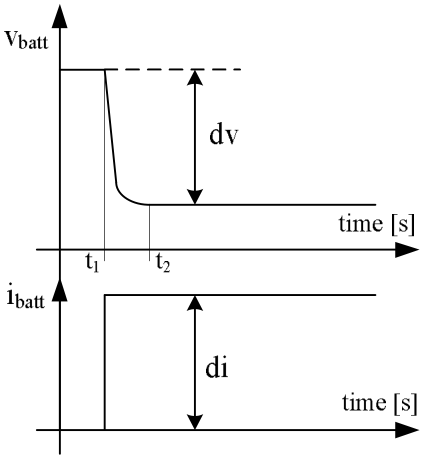

Fig 2.2. Internal resistance measurement using dc-load pulse

The internal resistance is given by equation (2.1).

$$R_{int} = \frac{|dv|}{|dt|} \qquad (2.1)$$

where the voltage derivative is given by $V_{|t1}$ - $V_{|t2}$;
$V_{|t1}$ is the battery open circuit voltage and $V_{|t2}$ is the battery voltage after complete stabilization during discharging. The value of $|t_2\text{-}t_1|$ is of order of seconds. Although many authors, in their publications, call the left term from equation (2.1), "internal resistance", in fact it is the total impedance of the battery.

The advantages of this method are: simplicity, is it good for development of simple model of the battery, only, during steady-state, it is a low cost solution, suitable for on-line implementation, is no time consuming. It is limited for applications that require the battery modeling during transients, prediction the capabilities of the battery, study of battery parameters behavior. Therefore, the internal resistance measured with this method is used, mostly, only in simulations, that proposed a very simple model for the battery given by a voltage source connected in series with a resistance.

2.2.1.2. Electromechanical impedance spectroscopy (EIS)

Electrochemical impedance spectroscopy is a powerful technique used for understanding of electrochemical systems like: batteries [2.4], [2.5], [2.6], [2.10], [2.11], ultracapacitors [2.12] and fuel cells [2.13]. Due to this technique, the recent advances in the development of electrochemical devices have been made possible by an improved understanding of the fundamental electrochemical processes. The investigation of various processes like ohmic conduction, charge transfer, interfacial charging, and mass transfer is possible with the help of electrochemical impedance spectroscopy.

Electrochemical impedance spectroscopy supposes that a small ac voltage is applied to the battery (terminals) under investigation and its ac current response is measured. From ac current and measured ac voltage response, the impedance is then determined (see Fig. 2.3).

The principle of the impedance spectroscopy is that the impedance of an electrical circuit can be determined with a good accuracy if the circuit is excited with a sinusoidal voltage and the current response is measured (see Fig. 2.3.). However, these tests have to be performed over a wide range of frequencies.

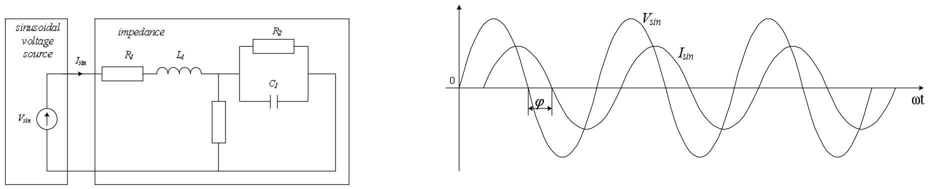

Fig. 2.3. Impedance spectroscopy

The impedance of the circuit is expresses as:

$$Z^* = \frac{V_{sin}}{I_{sin}}$$
$$Z^* = |Z| e^{j\varphi} \qquad (2.2)$$
$$Z^* = Z' + Z''$$

The impedance has two components: real part (Z') and imaginary part (Z") .
The behavior of the real and imaginary part of an impedance as a function of frequency is shown in Fig. 2.4.

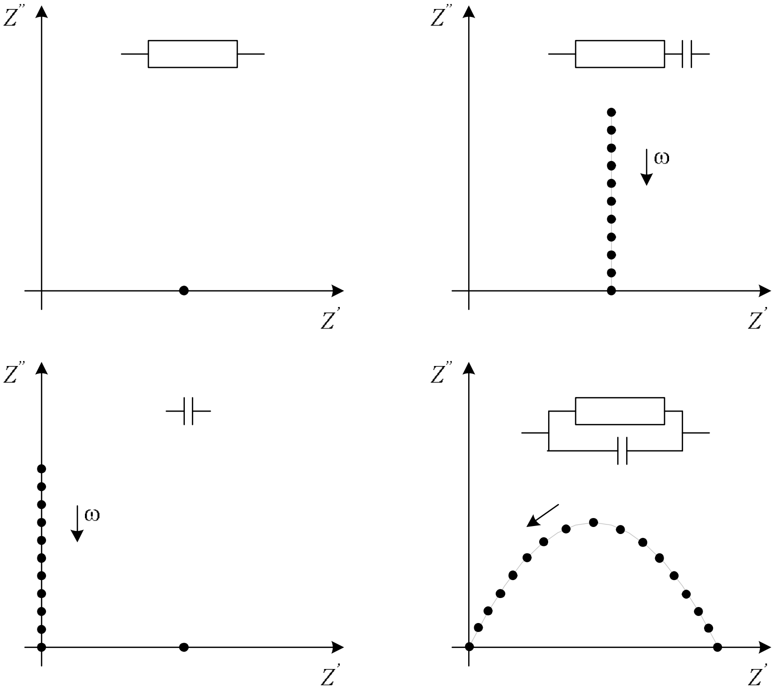

Fig. 2.4. Real and imaginary impedance part for different RC combinations

With modern hardware it is possible to measure the impedance as a function of frequency directly. The frequency of the applied signal is varied over a wide range (e.g. from 10^{-4} to 10^{6}Hz) and the system response is measured directly.

EIS data is commonly analyzed by fitting it to an equivalent electrical circuit model. Most of the circuit elements in the model are common electrical elements such as resistors, inductors and capacitors.

There are on the market commercial impedance analyzer. A few impedance analyzers with their main characteristics are:

- **EIS300:** measure impedances in the range of [2mΩ....10TΩ], over a wide range of frequencies [10mHz....1MHz]. Impedance error is: <0.5% in magnitude, <0.5% in phase. The applied signal magnitude is in the range of [2.75uV...1.425Vrms]

- **True-Data EIS 30:** measure impedances in the range of [0.1mΩ...15Ω] over a frequency range of [10mHz...100kHz]. Impedance error is: <1% in magnitude, <1% in phase. The ac current amplitude is up to 250mA. The dc maximum voltage is 10V, while dc maximum current is 150A.

- **IM6ex:** measure impedances in the range of [10uΩ....100MΩ], over a wide range of frequencies [10uHz....3MHz]. The ac amplitude is in the range of [1mV....1V]. The dc maximum voltage is 14V.

To perform the basic EIS experiments and alternating voltage is superimposed on a dc voltage Vdc:

$$V_{sin} = V_{dc} + V_0 \sin(\omega t) \tag{2.3}$$

The value of V_o is around 5mV. Since the ac signal is very small, the resultant polarization of the electrode is in a linear potential region. Therefore, there is no destructive damage of the electrode, and EIS can be used to evaluate the time relation of the interface parameters.

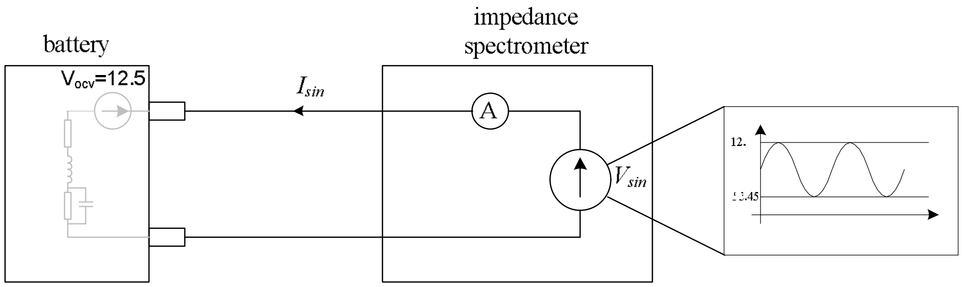

Fig. 2.5. Battery impedance measurement with impedance spectrometer

EIS is a very sensitive technique, and offers a wealth of information about battery such as [2.4]:

- analysis of state of charge
- study of reaction mechanism
- change of active surface area during operation
- separator evaluation
- passivating film behavior
- separation and comparison of electrode kinetics on each electrode
- identification of possible electrode corrosion processes
- investigation of the kinetics at each electrode

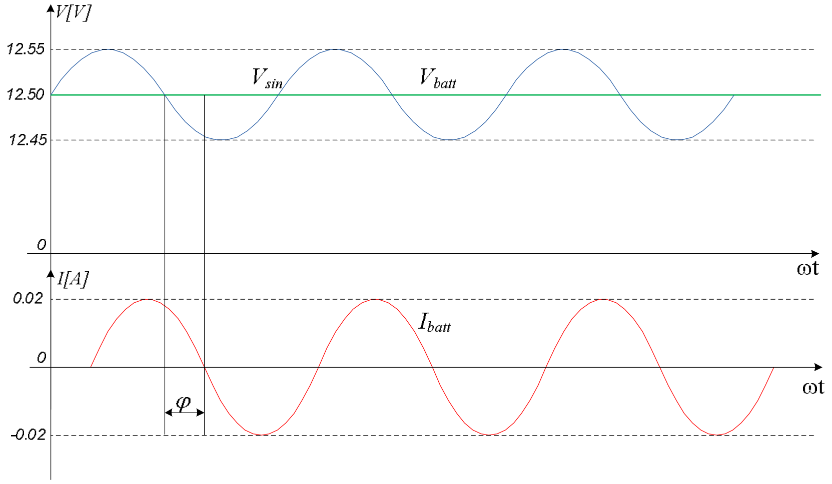

Fig. 2.6. Typical impedance spectrometer output voltage, battery voltage and battery current during testing a 12V battery (Vocv=12.5V)

A very good and accurate image of battery impedance is provided by EIS. Despite of these advantages, EIS is not suitable for HEV. It is an off-line method rather than an on-line method. It is time consuming and needs powerful computation resources.

Battery impedance

The processes in an electrochemical battery may be divided into fast and slow processes having time scales in the order of miliseconds and hours (even days) respectively. the fast processes are related to the double-layer impedance at positive and negative electrode, and the slow processes to the electrochemical of the same electrodes [2.7].

A battery, which is a dynamic system, can be described by means of an impedance-base small-sigmal equivalent circuit. Such a typical equivalent circuit obtained by EIS for battery impedance is shown in Fig 2.7, where Cdx represents a double layer capacitor that characterizes the double layer process, Wx represents the Warburg impedance that characterizes faradic processes, Ri is internal resistance and Li is the inductance. So EIS is more suitable to measure the impedance outside of vehicles and for large batteries. So this technique is limited, though good in precision in its ability to measure the internal resistance real-time on HEV

Another method is the dc load method. A load is applied to battery for a few miliseconds and the voltage drop divided by the current provides the internal resistance value. The load current ranges is from 5A to hundred of amps for short period of times. Even this method has been known for decades it is not clear yet how it is applied for battery testing.

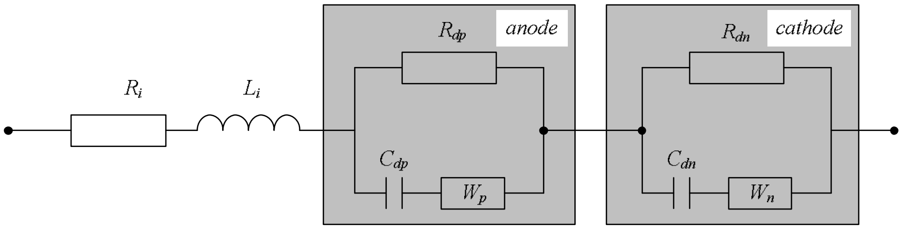

Fig. 2.7. Typical equivalent circuit of a lead acid battery impedance[2.1]

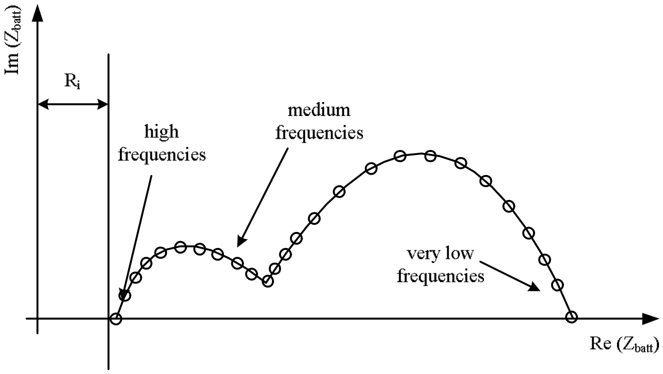

Fig. 2.8. Real and imaginary part of battery impedance with frequency

The internal resistance accuracy depends on the accuracy of the voltage and the current acquiring. A precision of 5mV for voltage and 50mA for the current is enough for internal resistance measurement with a precision lower than miliOhms. A few researchers showed that the impedance of the battery depends on the frequency [2.8], while the internal resistance is constant for the same conditions. In [2.9] it is demonstrates that for a typical impedance of lead-acid battery at frequencies between 200 Hz and 2kHz, the impedance character is resistive-inductive while for low frequencies the character tends to be capacitive.

2.2.2 The proposed method for internal resistance estimations

The internal resistance is represented by the resistance of inter-cell connections - which is more or less constant -, and the electrolytic resistance of the solution, which depends on the ionic concentration (state-of-charge) and on the temperature (mobility).

In our approach we started from the equivalent circuit of the battery impedance from Fig. 2.7. For simplicity, we assume that the Warburg impedance is neglected and then we write the total impedance of the battery based on the circuit from Fig. 2.7.

The total impedance is given by equation (2):

$$Z_{batt} = \omega L_i + R_i + Z_{dp} + Z_{dn} \qquad (2.4)$$

where Z_{dp} and Z_{dn} are given by equation (3):

$$Z_{dp} = \frac{R_{dp} \cdot \dfrac{1}{j\omega C_{dp}}}{R_{dp} + \dfrac{1}{j\omega C_{dp}}} \quad ; \quad Z_{dn} = \frac{R_{dn} \cdot \dfrac{1}{j\omega C_{dn}}}{R_{dn} + \dfrac{1}{j\omega C_{dn}}} \qquad (2.5)$$

A simple frequency analysis of impedance Z_{dp} and similar for impedance Z_{dn}, shows that for very low and low frequencies, the circuit tends to have capacitive effect which means that the capacitive effect prevails over the resistive effect. At high frequencies the capacitive effect tends to zero and the total impedance towards zero.

The experiments pointed out that during battery discharging over a pure resistive circuit, the current increases from zero to 200A in less than 1ms. This proves that the battery inductance is very small and its effect can be completely neglected.

Taking into account, the above mentioned assumptions, for high frequencies, the battery impedance is given only by internal resistance. An illustration of battery impedance behavior as a function of frequencies is given in Fig. 2.9.

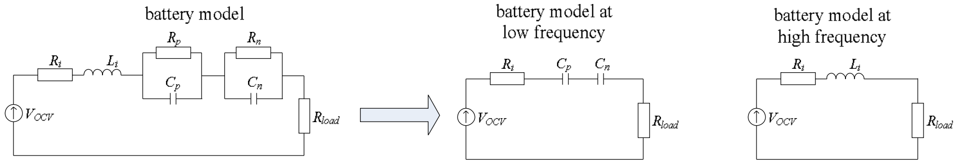

Fig.2.9. Battery internal impedance at low and high frequency

The measurement of internal resistance is based on the variation of the voltage during current variation. The calculation is based on the following formula:

$$R_i = \left.\frac{dv}{di}\right|_{di/dt > Ithresh} \qquad (2.6)$$

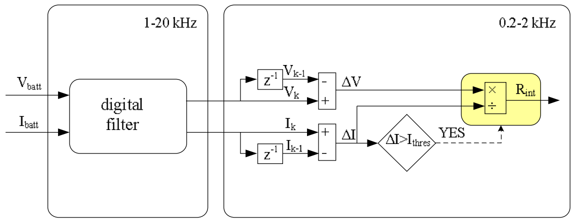

Fig. 2.10. Block diagram of internal resistance on-line computation

A. Simulation results

A set of simulations has been performed in order to demonstrate de validity of the proposed solution. The battery model consists of electrical RLC components and it is shown in Fig. 2.11. A load is connected at the battery terminal. The simulations were executed for a range of frequencies between 0.1Hz and 1000Hz, in order to prove the capacitive character of battery impedance at very low frequencies and respectively the resistive character at high frequencies. The simulation results for frequencies of 10Hz, 100Hz and 1000Hz are illustrated in Fig. 2.12. In order to excite the battery at different frequencies the load resistance R_{load} is varying sinusoidal at the above mentioned frequencies. The electrical circuit of battery is implemented in PLECS, while the internal resistance computation is implemented in Matlab-Simulink.

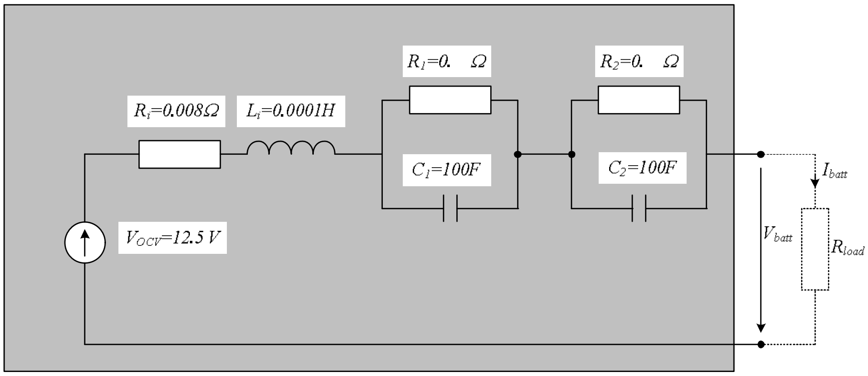

Fig. 2.11. Battery simulation model used for internal resistance estimation

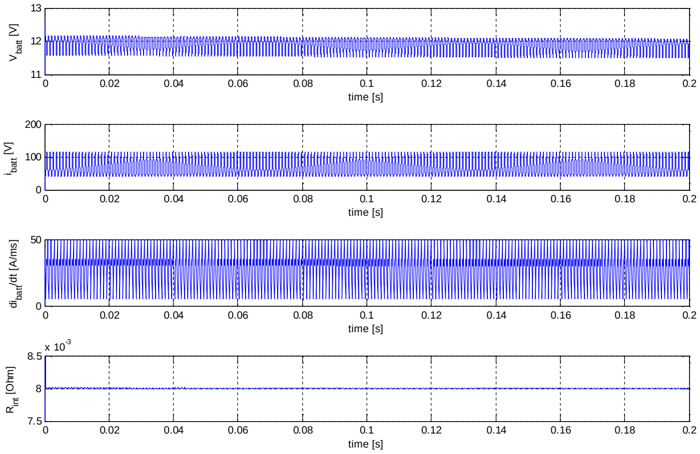

(a)

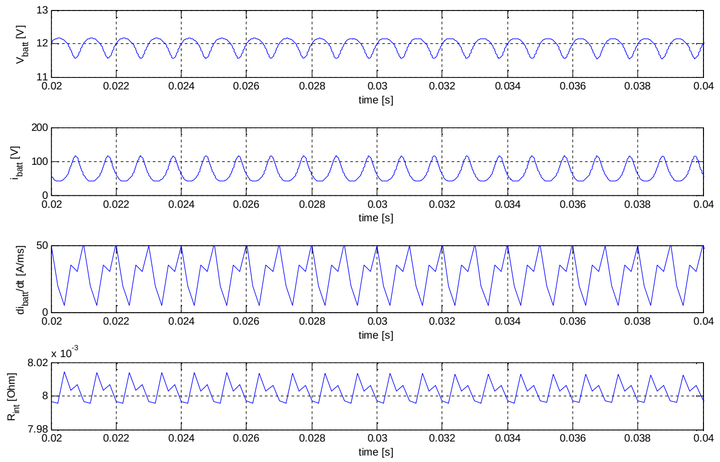
V_{batt} [V]
13
12
11
i_{batt} [V]
200
100
0
di_{batt}/dt [A/ms]
50
0
R_{int} [Ohm]
x 10^{-3}
8.02
8
7.98
0.02
0.022
0.024
0.026
0.028
0.03
0.032
0.034
0.036
0.038
0.04
time [s]

(b)

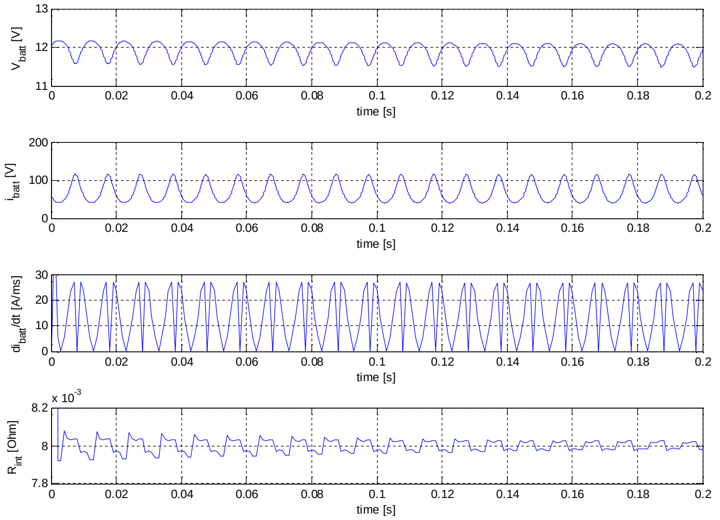
V_{batt} [V]
13
12
11
i_{batt} [V]
200
100
0
di_{batt}/dt [A/ms]
30
20
10
0
R_{int} [Ohm]
x 10^{-3}
8.2
8
7.8
0
0.02
0.04
0.06
0.08
0.1
0.12
0.14
0.16
0.18
0.2
time [s]

(c)

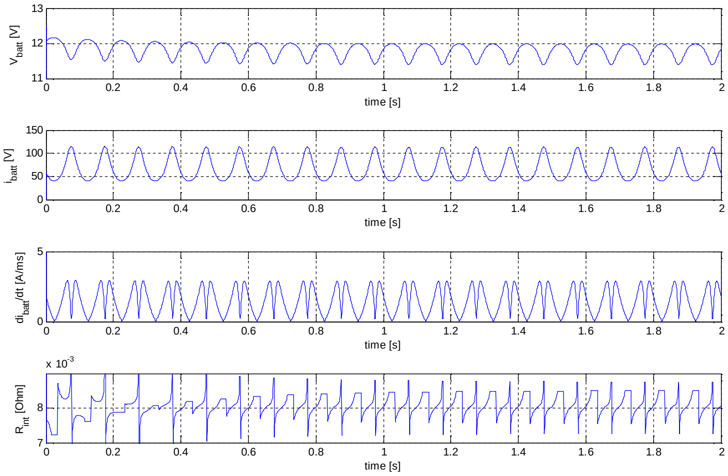

(d)

Fig. 2.12. Internal resistance estimation at a) 1000Hz, b) zoom on a), c) 100Hz, d) 10Hz

Only points where current variations higher than 2A/ms were evaluated for internal resistance estimation - for 1000Hz and 100Hz. For 10Hz, the points with di/dt>0.5A/ms were evaluated.

The analysis performed on the graphs from Fig. 2.12 gives us the following information:

- for 1000Hz, the accuracy of the internal resistance is ±0.19%.
- for 100Hz, the accuracy of the internal resistance is ±1.23%
- for 10Hz, the accuracy of the internal resistance is ±12.4%

Based on the above analysis we can conclude that the accuracy of internal resistance estimate is dependent on the frequency/slope of the battery current.

At very low and low frequencies the influence of *Rx*, *Cx* elements becomes very importance since the equivalent circuit battery is characterized by the equation (2.5):

$$R_i + (R_1 + R_2) = R_i + R = \frac{dv}{dt} \tag{2.7}$$

At high frequencies the R→0. Therefore the equivalent circuit is governed by the equation (2.8):

$$R_i = R_i = \frac{dv}{dt} \tag{2.8}$$

For impedances Z_1=Z_2=Rx || Cx – from Figure 2.4 – the impedance magnitude versus frequency is presented in Fig. 2.13.

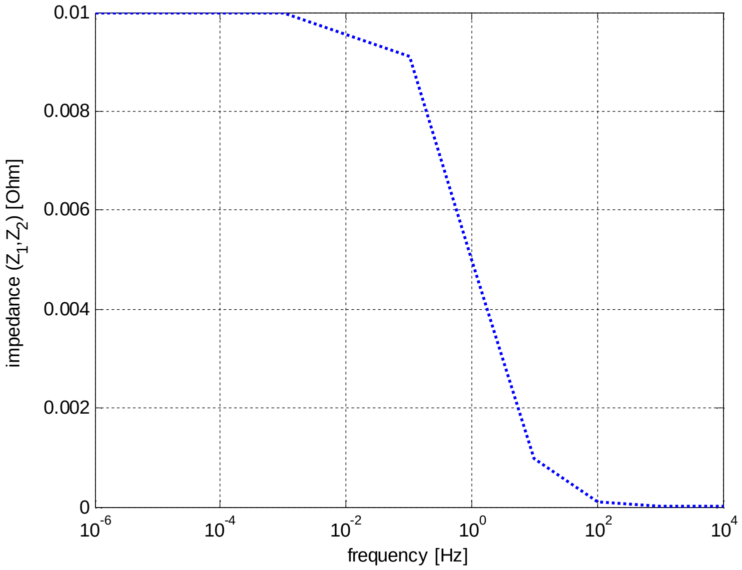

Fig. 2.13. Impedance Z_x versus frequency

According to Fig. 2.13. the impedance magnitude is lower than 0.0001Ω above 100Hz and lower than 0.000001Ω above 10000Hz. In fact the impedance magnitude is decreasing with the increase of the capacitance value, at the same frequency.

B Experimental results

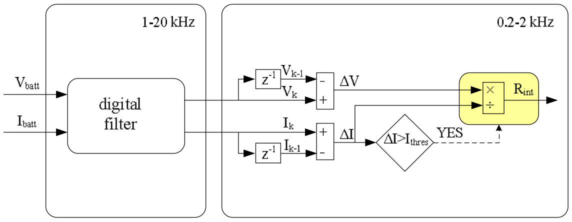

Fig .2.14. Block diagram of internal resistance on-line computation

The current and the voltage are acquired in a first phase at a high frequency of 20kHz. This frequency can be higher or lower than 20kHz. Then, the current and voltage are passed through a “low pass” filter with a cut-off-frequency of 1000Hz in order to remove the high frequency noise, characteristic to automotive environment. The filter has to be the same for the current and the voltage, otherwise the current or the voltage slope can be affected by delays and the results will be influenced by errors.

In a second phase, at a lower frequency, a computation algorithm is implemented for the internal resistance. This frequency has to be in the range of [0.2-2]kHz, for the reason that we shall explain later. In our case the frequency is 1 kHz. The voltage and current difference for 1ms period is then computed. The internal resistance computation is a valid operation if the condition $\Delta I > I_{thresh}$ is fulfilled. The value of $\Delta I > I_{thresh}$ is determined through experiments. For this reason a set of experiments was performed for this algorithm validation; the results are provided in Fig. 2.15.

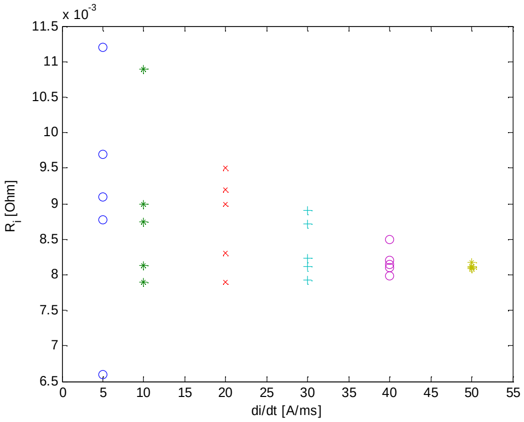

Fig. 2.15. Internal resistance computation as a function of di/dt at

1kHz computation frequency

Fig. 2.15 illustrates the values of internal resistance obtained for different values of di/dt. At lower values of *di/dt* the internal resistance cannot be considered valid because the estimation is affected by large errors. From Fig. 2.15, for *di/dt=5A/ms*, errors up to 35% in internal resistance estimation can be observed. The errors are decreasing at higher values of *di/dt*. At *di/dt=40A/ms*, errors up to 3.7% are obtained. A very good accuracy in the estimation of the internal resistance is achieved for *di/dt=50A/ms*. This is a valid value for Ithresh. An accuracy of 10-*40μΩ* can be obtained at high values of di/dt with the help of high-quality acquisition instruments (1mV precision for voltage and *50mA* precision for current).

The accuracy of internal resistance R_i vs I_{thresh} is illustrated in Fig. 2.16.

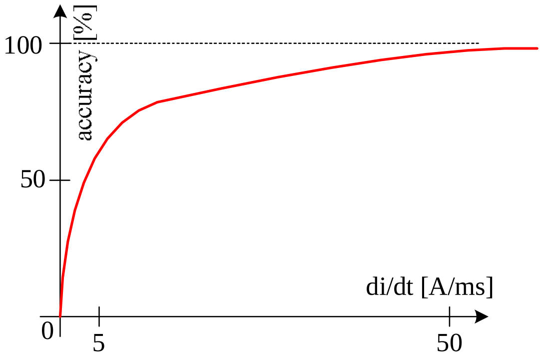

Fig. 2.16. Battery internal resistance accuracy as a function of dv/di

The internal resistance estimated is affected by the following errors:

- Resolution of current and voltage ADC (analog-to-digital converter). In industrial applications for such applications microcontrollers with maximum12-bit ADCs resolution are used. Considering a range of *[0-400]A* for battery current, an accuracy of $400A/212=0.1A$ is provided for current measurement. The quantization effect becomes more significant when points with low di/dt are used for internal resistance evaluation (e.g. $di/dt=2A/ms$). Similar explanations are valid for voltage measurement.
- Acquisition moment of voltage and current. It is known that in real applications it is very difficult to measure the current and voltage synchronous (exactly at the same time). In reality measurements are discrete-time event, but the problem is that during one acquisition sample the measurements are not synchronous. The explanation is in Fig. 2.17, where we supposed we have a constant di/dt at high frequency (di/dt, $dv/dt=const$). In the ideal case the distance (time) between two consecutive samples is constant (Δt), while in the real case this distance is not constant ($\Delta t_1 \neq \Delta t_2 \neq \Delta t_3 \neq \Delta t_4$)

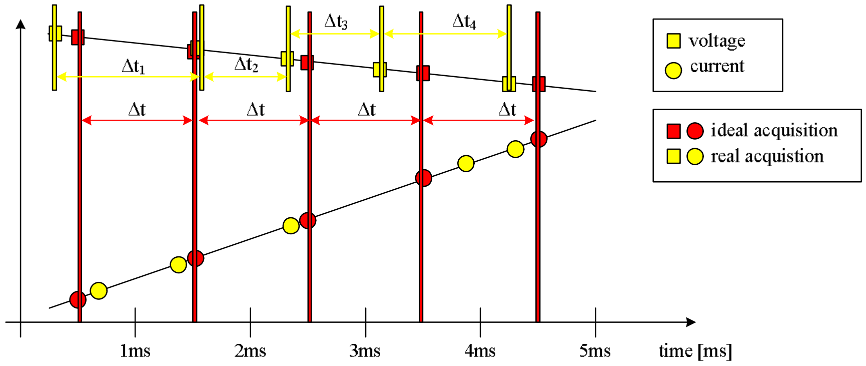

Figure 2.17. Ideal and real acquisition

- other errors

One application where the proposed method can be implemented is battery monitoring system used in HEV. This algorithm can provide good results in the estimation of the internal resistance of batteries, used in HEV, due to high values of di/dt that can be encountered, especially during the cranking of ICE. In Fig. 2.19, the current-time profile through a battery at a car starting is given.

In the discharging mode, the driver turns-on the key of automobile and the battery is discharging a constant current necessary for on-board systems (audio system, information system). Afterwards, the internal combustion engine is cranking and therefore, there are strong current variations (di/dt). It is in this mode that we have to measure the internal resistance of the battery. Black (circled) points are the selected points that meet the condition $di/dt>I_{threshold}$ and starting from these points the internal resistance is measured. Red (squared) points are not taken into account because they do not satisfy the above condition. A typical period for cranking mode is from 200 to 400 ms.

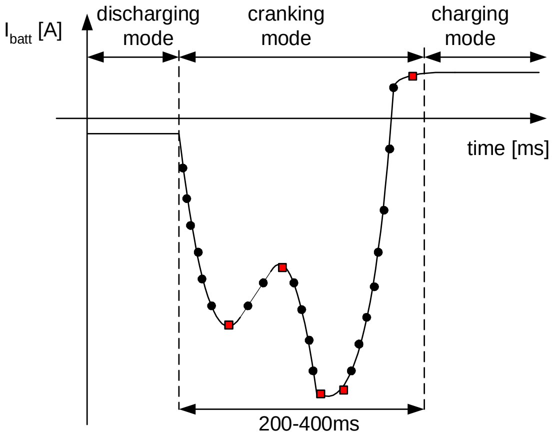

Fig. 2.19. Selected points for measurement of internal resistance in cranking mode used in HEV

Thus, it is very short and the polarization effect is avoided and only the effect of internal resistance can be seen. In the cranking mode, the shape of the voltage is the same as the shape of the current.
The most drastic regime for the battery is in ICE cranking mode, when values in the range of *[10-50]A/ms* can be encountered for the discharging current.
In Fig. 2.21 a few acquisition samples of battery voltage during discharging with current of 100A are presented. It can be easily observed from Fig. 2.21 that the slope of the battery voltage is the same during many acquisition samples. This means that the internal resistance is the same. The battery voltage at *di=0* (the OCV voltage) is not the same because the battery open circuit voltage has different values, due to the relaxation process of polarization voltage which is not finished.

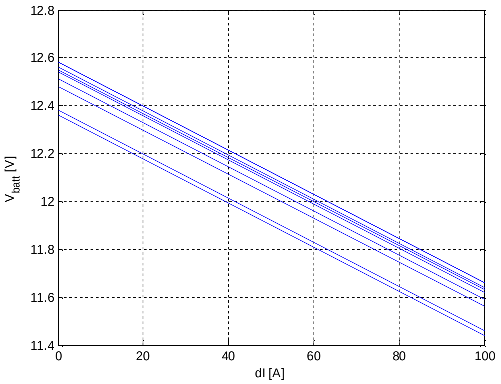

Fig. 2.21. Vbatt at Idisch=100 for successive measurement points of Rint

The estimated internal resistance of a BOSCH 12V, 55Ah, valve regulated lead-acid battery is shown in Fig. 2.22. As expected, the internal resistance increases with the state-of-charge decreasing and temperature decreasing.

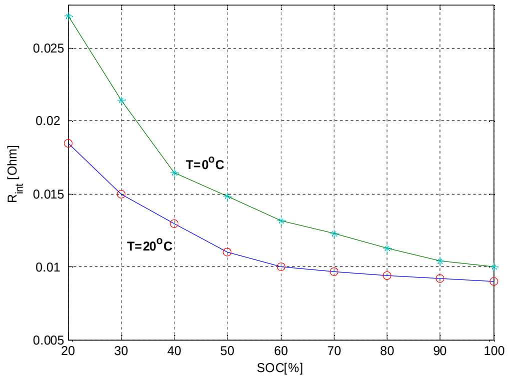

Fig. 2.22. Measured internal resistance as a function of state-of-charge for temperature of $T_{batt}=20^{o}C$ and $T_{batt}=0^{o}C$

2.2.3 Power discharge capability

The maximum discharged power from battery, at constant current I_{batt} , is:

$$P_{disch} = V_{batt} \cdot I_{batt} \tag{2.9}$$

On the other hand, the maximum discharge power after the battery voltage relaxation (or for fast discharge current transients is:

$$P_{disch} = \frac{V_{batt}{}^{2}}{R_{int}} \tag{2.10}$$

where V_{batt} is the actual voltage at battery terminals.
In hybrid electric vehicles it is important to know which is the minimum level of battery state-of-charge that can provide the power necessary for a safe cranking of internal combustion engine. The power discharged from the battery is influenced by the internal resistance at the same level of SOC.

Because of the unpredictable behavior of the internal resistance we have to develop a battery model that takes into account the internal resistance variation.
For this scope we developed a simple model that predicts the battery voltage at different levels of SOC and for different currents.

A. Battery voltage modeling

The battery model for steady-state we propose is shown in Fig 2.23.

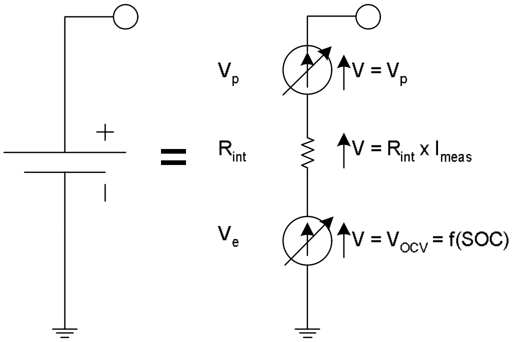

Fig. 2.23. Voltage model of lead-acid batteries

The corresponding equation for Fig. 2.23. is:

$$V_{batt} = V_{OCV} - R_{int} \cdot I_{batt} - V_p \tag{2.11}$$

The OCV represent the open circuit voltage of the battery. R_i- represents the internal resistance of the battery, V_p is the polarization voltage and V_{batt} is the voltage at battery terminals. The measured open circuit voltage (OCV) as a function of state-of-charge has been determined experimentally and it is shown in Fig. 2.24.

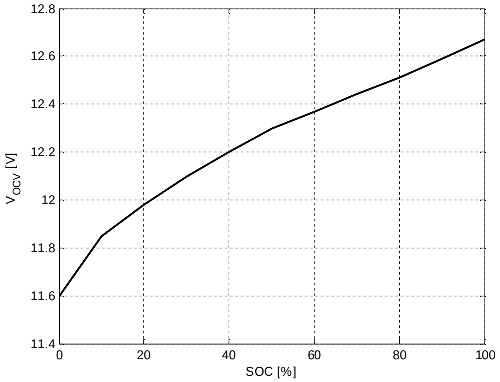

Fig. 2.24. Battery open circuit voltage (OCV) as a function of the state-of-charge

Polarization voltage is the voltage drop in a battery (or a cell) during discharge, due to the flow of an electrical current, and it is generated by the diffusion process, which opposes a barrier to the migration of ionic components across the acid solution. It depends on the state-of-charge and charge-discharge current. We should also mention that V_p has positive values for discharging and negative values for charging. The polarization voltage can be modeled by passive elements (combination of R,C elements) as indicated in Fig. 2.25.

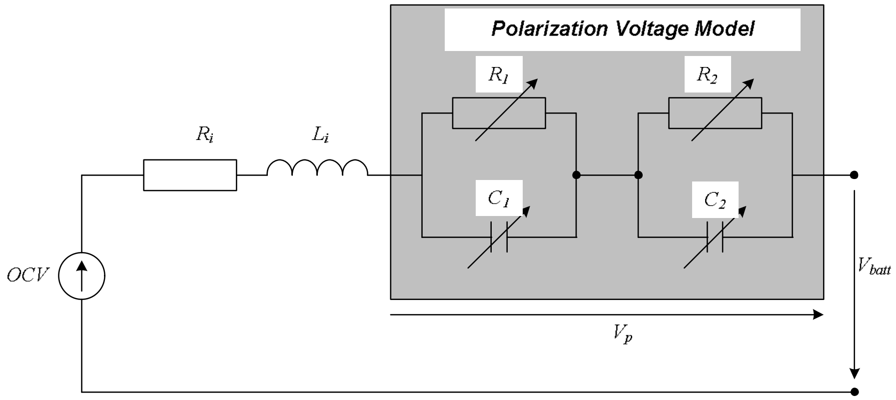

Fig. 2.25. Electrical circuit model for polarization voltage

Its steady state-value is given by the voltage drop on *R1* and *R2*, while *C1* and *C2* represent the transient behavior. The polarization voltage does not appear instantaneously, it requires some time until it gets to a steady-state value. The complete modeling of polarization voltage is beyond our scope here and a new paper will analyze it more profoundly.

The time constant for the polarization voltage is from a few milliseconds up to a few minutes. When it increases its variation is very fast and in a few seconds, it can get to the steady-state value for constant current-discharging. When it decreases, it converges to zero with a much slower time constant. Thus, if the measurement of internal resistance is done very quickly, the effect of polarization voltage does not appear. Typical values are in the range of zero and 4V(for currents of hundreds of Amps). For example, the polarization voltage at *200A* current discharging and *SOC=100%* the polarization voltage is $V_p=0.9V$. The greater the value of the current the greater the polarization voltage. Polarization voltage has practically no influence on battery's efficiency.
The behavior of the polarization voltage can be easily observed in Fig. 2.26.

In Fig. 2.26, the variation of the polarization voltage with the battery discharge current is given. The ratio of polarization voltage to the discharging current is higher at low current; this means that the polarization effect is more dominant at low current. For example while discharging the battery at *I=40A, SOC=100%*, we having stabilized the polarization voltage, the battery voltage drop is 0.702V. The polarization voltage is 0.311V while the voltage drop on internal resistance is 0.391V. For the same SOC and temperature at discharging current of I=200A, the polarization voltage is 0.908V, while the voltage drop on internal resistance is 1.96V. The zone unavailable due to Peukert effect is very dangerous for battery operation and therefore it should be avoided.

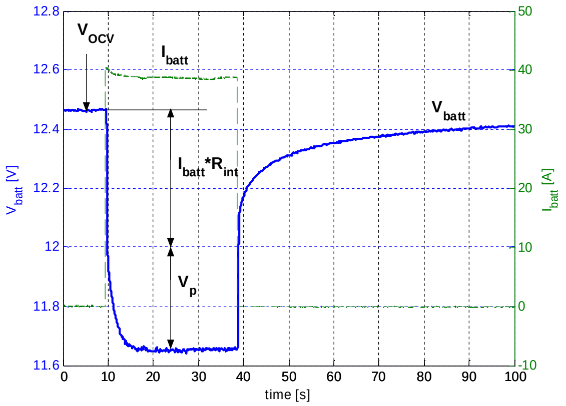

Fig. 2.26. Battery voltage at constant discharge current

The battery's operation in this zone is characterized by a very high voltage drop in battery voltage at high currents (for low SOC) and very high currents (at high SOC). The battery's lifetime is negatively affected if battery runs in that zone.

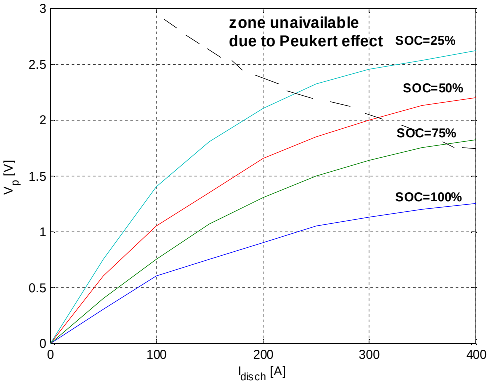

Fig. 2.27. Polarization voltage as a function of battery

2.2.4 Battery discharged power measurement

In many applications, the demands on batteries are not only to serve as an energy storage device, delivering moderate power for a long time, but also to deliver high power for short periods. Examples of such pulse power applications are boost mode for hybrid electric vehicles (HEVs), x-by-wire technologies, idle-stop mode for HEVs and cranking of a conventional motor vehicle.

It is therefore, essential to have a reliable prediction of batteries power capability. Based on this it is possible to decide whether the vehicle can operate in idle-stop mode or whether the engine has to keep on running to charge the battery safely.

In modern vehicles, these tasks are performed by intelligent energy management systems that monitor the behavior of the battery. State-of-charge, state-of-health, cranking capability, maximum discharge power (current), maximum charge (current) acceptance are the most important functionalities of an intelligent battery management system.

The maximum current extracted from battery in HEV is in cranking mode, however, the current is dependent on the shaft torque of integrated starter-alternator (ISA). Also, the ISA shaft torque is dependent on the load torque. The friction force of internal combustion engines, gives the load torque seen by ISA. In cranking the worst situation is at very low temperature. A temperature of -40oC is the minimum temperature for which a modern vehicle ought to be able to start. So, the lower the temperature, the greater the load torque for ISA system. For a good cranking of the internal combustion engine a high ISA torque is required. Values between 30-60Nm are typical for ISA load at cranking. Values of 1.5-3kW are typical values for the power discharged from battery at cranking. Again, for a safe cranking at -40^{o}C the battery has to be able to provide a power of 2.5kW and this is the value of power that should be provided by battery any time. This means a high power discharged from battery and not high current, because the voltage at battery terminals depends on its state-of-charge, temperature and current and is far from a constant value. There is one way to provide a good power discharge capability characterization and that is to plot the discharge power versus discharge current at different SOC and different temperatures. We see from Fig. 2.28 that the discharged power is dependent on the state-of-charge of battery, discharged current and temperature.

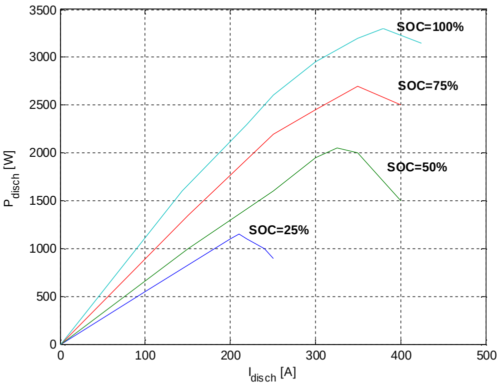

Fig. 2.28. Maximum discharge power (Pdisch) as a function of discharge current (I_{disch}) at different SOC; temperature: T=20^{o}C.

It can be observed in Fig. 2.28 that for every SOC value there is a maximum discharging power that is independent of discharging currents. The higher SOC the higher the maximum discharging power. The negative slope of the discharging power, after the maximum discharging power point, is encountered due to Peukert effect. These families of curves help us to derive the minimum level of battery SOC for operation, if it is known the necessary amount of power in an application.

The operation of the battery beyond the maximum discharging power point is not efficient and it should be avoided.

Starting from Fig. 2.28. it should be quite simple to derive the minimum SOC level at which we should maintain the battery, if we measured the power discharge capabilities at -40°C and if we know the maximum power of the ISA. Also, this could be used for state-of-health estimation of the battery if we knew with a good precision the battery state-of-charge and battery temperature. But if we take into account that the battery power discharge capability depends on state-of-health, we must also consider a greater SOC than calculated by the above algorithm. We store these curves into a look-up table (as a reference) and we compare the power discharge from battery with the reference. If the power discharge for a given SOC and temperature is two times lower than the reference value we strongly believe the battery should be replaced.

For battery protection it is recommended to identify a voltage threshold Vmin, so that for a pulse load power, the voltage at battery terminals should not drop below Vmin. A value of 7.5V for Vmin is practical.

For hybrid electric vehicles the most representative curve is the maximum discharged power (P_{max}) at -40°C. Due to some special equipment missing this curve is not presented in the paper.

The battery SOC and battery discharging power are affected by temperature. In Fig. 2.29 is given the influence of temperature on battery SOC.

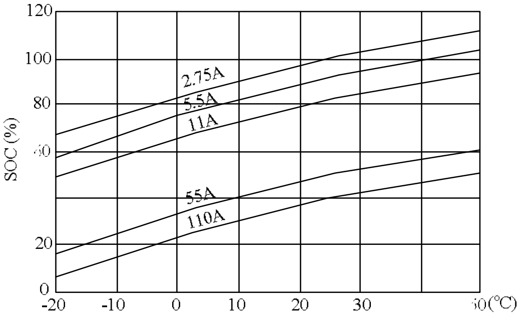

Fig. 2.29. SOC as a function of temperature

For instance, if we measure for a battery a SOC=80% at 20°C, at -20°C the SOC is around 50%. The rest of 80%-50%=30% in not lost and we say that it is “frozen”. Again if we bring the battery at a temperature of 20oC , the battery SOC is the same as initial, 80%. So the SOCs at temperature below 20oC are not real values of SOC, and we call this as apparent SOC. It is obvious from Fig. 2.29. that the dependency of SOC on temperature is the same for different initial values of SOC.

The relation between real SOC (SOC corresponding to T=20°C) and apparent SOC (SOC corresponding to a temperature T=x°C , that is different from 20°C) may be described by equation (2.12):

$$SOC_{T=x}(\%) = -0.0025 \cdot T^2 + 0.65 \cdot T - 14 + SOC_{T=20^oC} \quad (2.12)$$

This equation is easy to implement in simulation software. It is very useful in applications because it saves memory and requires less time for computation that a look-up table.

2.2.5 Battery state-of-health estimation

During the lifetime of batteries, their performance tends to decrease generally due to changes that take place in active material inside the batteries. This process is irreversible for batteries. The performance of batteries is decreasing with ageing but for conventional lead-acid batteries these could be improved by reconditioning the batteries. In case of VRLA batteries this is not possible. The process of decreasing of battery performance is called "ageing" and in literature is known as "state-of-health". The state-of-health (SOH) is a measurement that reflects the performance of a battery compared to a fresh battery for the same conditions (capacity, temperature, SOC).

Unlike the SOC that can be estimated by measuring the actual charge in the battery, the SOH has no clear definition. The SOH is defined by researchers according to their own rules. It is estimation rather than a measurement. Any parameter which changes significantly with age, such battery impedance, battery internal resistance, capacity, can be used as a basis for providing an indicator of the SOH of the battery.

Because the SOH estimation is relative to the condition of a new battery a set of experiments should be done to measure the parameters values, which constitute the SOH indicator.

Battery state-of-health estimation by internal resistance

The battery state-of-health is computed based on the internal resistance.
The algorithm proposed for state-of-health estimation is represented in Fig 2.30.
In the look-up table1 (LUT1) are stored the values of internal resistance determined experimentally for different levels of SOC and temperature in the range of [0-100]%, respectively [-40-60]^{o}C, when the battery is new. These values are considered as references value (Riref).
The estimation of real battery internal resistance (Ri) is computed by means of dv/di method. Normalized internal resistance, Rin, is the computed by dividing Ri by Riref.
The real battery state-of-health (SOH) is then obtained from look-up table2 (LUT2).
A three times increasing of internal resistance, decreases the power discharging from battery at half. In this case we consider the SOH is zero and the battery should be replaced.

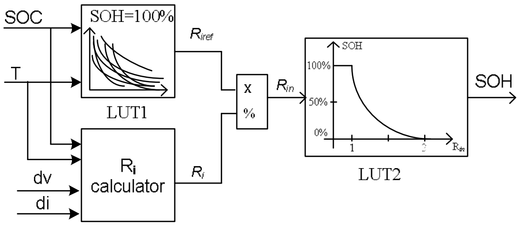

Fig. 2.30. SOH computation

2.3 Battery state-of-charge estimation

THE increasing demand to improve fuel economy and reduce emissions in present vehicles has led to the development of advanced hybrid vehicles. A hybrid electric vehicle (HEV) will operate with an electric motor running in conjunction with the internal combustion engine (ICE).

Batteries are important components of HEV systems as they provide the energy for the integrated starter-alternator (ISA) during ICE cranking, power boosting and to store the energy during regenerative braking. During urban driving, the ICE will be shut on and off frequently, according to driving conditions, causing the battery to be frequently charged and discharged by the ISA.

The reduction of fuel consumption HEV involves the knowledge of valve regulated lead acid batteries state of charge (SOC). A modern battery monitoring system used in HEVs should be able to provide for an intelligent energy management system based on the following information: (cold) cranking ability, maximum power discharge, maximum charge (current) acceptance during regenerative braking. Due to the non-linearity of the battery system, we need to identify a comprehensive state variable in regard to the definition of the above mentioned battery characteristics. This state variable is here the so called battery state-of-charge (SOC).

Battery state-of-charge identification with an error of 5% is one of the major requirements concerning battery monitoring systems used in HEV.

2.3.1 Review of battery state-of-charge estimation

Batteries state-of-charge is a chemical parameter of the batteries, which can not be directly measured with electric signals, and therefore it has to be estimated with the help of available electric signals such as voltage and current. Since the battery state-of-charge is affected by the temperature for a good estimation, the temperature has to be taken into consideration. In the literature there are many papers dealing with the battery state-of-charge estimation.

The most common methods involve the coulomb counting. The coulomb counting (or current integration) method measure the amount of charge (current) extracted or put into the battery in terms of ampere-hours. Only coulomb counting is not a reliable method, since the error is increasing with time and the current magnitude. In fact, the efficiency of the battery, which is very important at higher current, is not considered. The main problem for coulomb counting is that it requires an initial value and needs to be calibrated regularly to ensure an accurate SOC determination. Anyway it is inexpensive and reasonably accurate for short time intervals. Under steady state conditions there is almost a linear relationship between battery open-circuit voltage (OCV, EMF) and state-of-charge. In [2.14], [2.15] a method that incorporates battery impedance, current, and terminal voltage to predict the EMF voltage of the battery is proposed. The limitations of this solution are: EMF accuracy is low under high charge/discharge current rates; the battery impedance is affected by the temperature and battery state-of-health. Kalman filters are a well known technology used for dynamic and nonlinear systems states estimation such as tracking, navigation and batteries. Battery state-of-charge estimators using Kalman filters are proposed in [2.16], [2.17], [2.18], [2.19], [2.20]. One advantage of Kalman filter is that it optimally estimates states that are affected by a large band of noise contained in the system bandwidth. The main disadvantage of Kalman filter is that is requires high complex mathematical calculations. The gain of the filter is obtained in five steps of algorithm. There can be the possibility of divergence due to imperfect modeling [2.21]. The performance of the Kalman filter depends on the accuracy of the a priori assumptions. The performance can be less than impressive if the assumptions are erroneous. The Kalman filter performance is poor in transients and it needs longer time to adapt parameters in order to get small errors

Another method used for Li-Ion battery state-of-charge estimation is based on a nonlinear estimator [2.21]. The algorithm is based on a sliding mode observer. The performance of the observer is dependent on the switching gain. The magnitude of chattering is highly dependent on the observer gain. If the gain is very high, a large amount of ripples may result, leading to errors in estimation. On the other hand the stability of the observer has to be achieved. Therefore, the design of the observer gain is a tradeoff between the robustness and stability of the observer.

A fuzzy-logic based estimator for battery state-of-charge estimation is reported in [2.22]. The impedance measurement is performed, offline, using EIS method (described in Chapter 2.2.1). Then the battery impedance is measured, on-line, and the match between the on-line and offline measured impedance gives the battery state-of-charge. A good agreement between impedance measurement, using on-line and off-line method raise many questions. An algorithm for SOC estimation based on discharge time versus discharge rate data given in manufacture's data sheet, and current integration, without the need for battery voltage measurement during the equilibrium state is introduced in [2.23]. The test results have indicated an accuracy better that 3-4% for various charge-discharge strategies, with practical applicability for batteries used in telecommunication power supplies.

Unfortunately, the charging-discharging level periodicity is notably higher in EHV and thus a dedicated SOC estimation is required to match a good precision with realistic CPU time and hardware effort for it. An algorithm for NiMH battery SOC detection (applicable also for lead-acid batteries), based on a simple equivalent-circuit representation of the battery pack, with the parameters adapted by means of on-line least-squared regression is presented in [2.24]. The output of the algorithm is the SOC and the power capabilities for subsequent charge or discharge, are necessary for an efficient hybrid vehicle operation through optimal torque reference allocation. The behavior of the algorithm in terms of convergence, accuracy and robustness is examined. Other reported methods for estimating the battery state-of-charge are based on neural networks principles [2.25.], [2.26], [2.27]. Neural networks require high computational resources, which lead to problems for online implementation, but maybe in the near future, once he price of digital signal processing chips will decrease, these could be an alternative to the already known solutions.

2.3.2 Proposed algorithm for battery state-of-charge estimation

A schematic representation of inputs/outputs of the proposed battery state of charge (SOC) estimation algorithm is represented in Fig. 2.31. It consists of three main parts: Filter algorithm, that is the closest to the hardware level and is running at a frequency of 20 kHz. The second part is the Fast Speed algorithm which is running at 1kHz and provides the following signals: V_1mV (battery voltage with 1mV resolution), I_25mA (battery current with 25mA resolution), Rint (battery internal resistance), Ah_charged (battery charged current integration), Ah_discharged (battery discharged current integration), Ah_total (battery ah remaining) as inputs for Slow Speed part algorithm. The Slow Speed part, may be considered the core of the algorithm. The output of the Slow Speed algorithm is the battery state of charge (SOC).

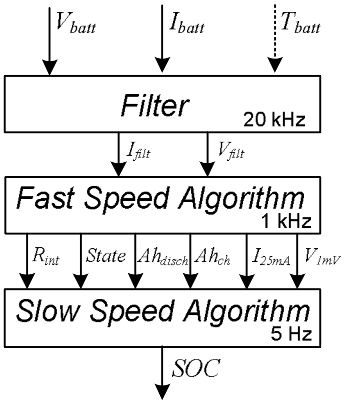

Fig. 2.31. Schematic block diagram of battery SOC estimator

A. Filter Algorithm

The filter part consists of two first order filters order that remove the high frequency noise inherent to automotive environment.
The discrete equation of the first order filter is:

$$y[t] = K \cdot (x[t] - y[t-1]) + y[t-1] \tag{2.13}$$

In our case for the voltage we have:

$$V_{filter}[t] = K_V \cdot (V_{batt}[t] - V_{filter}[t-1]) + V_{filter}[t-1] \tag{2.14}$$

and for the current:

$$I_{filter}[t] = K_I \cdot (I_{batt}[t] - I_{filter}[t-1]) + I_{filter}[t-1] \tag{2.15}$$

where K_V=0.005 and K_I=0.005 are calibration parameters derived experimentally.

B. Fast Speed Algorithm

The purpose of the fast speed algorithm is:

- to filter the voltage and current
- to count the Ah charged/discharged by current integration
- to estimate the internal resistance of the battery
- to calculate the battery efficiency
- to detect if the current is constant or not

All these quantities are given as inputs to the Slow Speed algorithm. The Fast Speed algorithm is running at a frequency of 1 kHz in order to detect with good precision the battery internal resistance and in order to measure accurately the current integration during transients (cranking, power boosting).

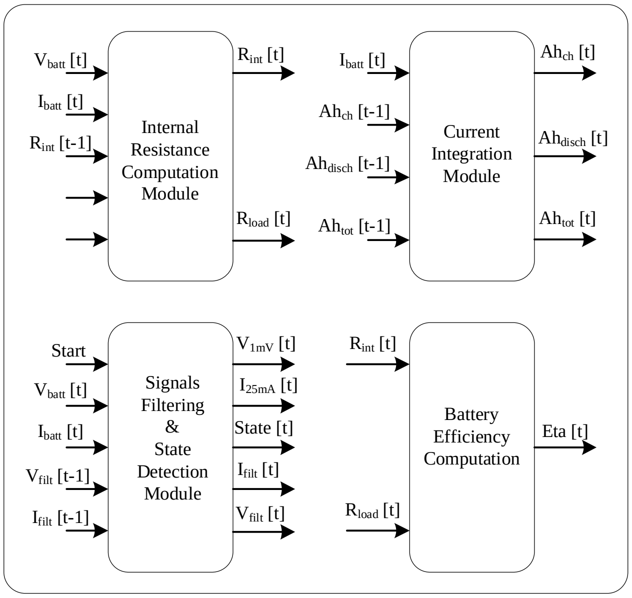

Fig. 2.32. Block diagram of the Fast Speed algorithm

A detailed description of Fast Speed algorithm components is presented below.

B.1. Internal Resistance Computation Module

The purpose of the internal resistance computation module is to estimate the battery internal resistance and also the load resistance.
The internal resistance is computed only during current gradients, based on equation (2.16):

$$R_{int} = \frac{dv}{di}, \quad if \quad d_i > K_{thresh} \tag{2.16}$$

where K_{tresh} is a calibration parameter derived experimentally, taking into consideration the remarks that follows.
In [2.19] an algorithm for internal resistance measurement is described. The accuracy of the internal resistance measurement is dependent on current variation (di/dt). At high current gradient (di/dt=40A/ms) the internal resistance is measured with a good accuracy, while at low current variations (di/dt=5A/ms) the accuracy is affected by errors of up to 35%.
The value of calibration parameter Kthresh can be derived if we take into account the vehicle drive cycle. In urban driving the number of start/stop cycles is relatively large. The starting mode of the vehicle means ICE cranking with very high current variations in a very short time. On the other hand, in high way mode the cranking scenarios are rare. In a real car on the highway, the battery state of charge variation is very slow because the electric loads (audio and information systems, water pump, lights) get the energy from the electric generator (if provided for). Thus we assume that the battery internal resistance is almost constant and there is

no need for estimation. The conclusion is that a value around 30 A for Kthresh , is practical.

B.2. Current Integration Module

The current integration module computes the charging, discharging Ah based on equations (5), (6):

$$Ah_{ch}[t] = \begin{Bmatrix} Ah_{ch}[t-1] + \dfrac{I_{batt} \cdot 0.001}{3600} & , \ I_{batt} > 0 \\ Ah_{ch}[t-1] \ , \ I_{batt} <= 0 & \end{Bmatrix} \tag{2.17}$$

$$Ah_{disch}[t] = \begin{Bmatrix} Ah_{disch}[t-1] + \dfrac{I_{batt} \cdot 0.001}{3600} & , \ I_{batt} < 0 \\ Ah_{disch}[t-1] \ , \ I_{batt} >= 0 & \end{Bmatrix} \tag{2.18}$$

For our case we consider the sign "+" for charging current and sign "-" for discharging current.

Signal Filtering and State Detection Module

Due to the noise presence in automotive environment the signal filtering operation is a must. The automotive noise is in order of 10-20mV. The requirement is that the current and voltage have to be filtered in such a way that noise is smaller than 1-2 mV. For example, 20mV error in battery voltage acquisition leads to an additional error of 2% in battery SOC estimation.

A good signal filtering, in our case, means to reduce to minimum the noise influence, and to maintain good dynamics (no propagation delays).

We can distinguish three phases, with different dynamics for current and voltage, in battery operation life, specific only to automotive batteries:

- high frequency , in cranking mode where large dv/dt and di/dt are encountered.
- moderate dv/dt and di/dt during engine running
- low frequency during the voltage recovery process where small dv/dt are encountered and zero frequency after the voltage is completely stabilized.

Taking all these into account implies identifying in which situation the battery is running and then filter the voltage and current with the right filter coefficients.

We define three states:

- ***CRANKING***: in this state the ICE is cranking. It is characterized by high current and high di/dt during a time of approximately 1s. A value of filter gain around 1 is required in order to avoid delays, and current and voltage slope modifications..
- ***RUNNING***: in this state the battery can be charged (with low current) or discharged with relative medium current (below 75A).
- ***STOP***: in this case the battery current is zero. In real cars the battery current is never zero due to supervisory systems that take from the battery a very small current, up to 200mA.

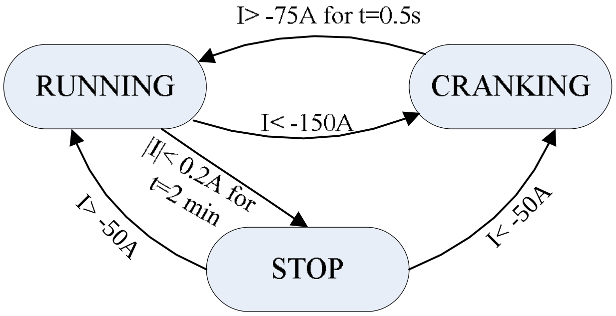

Fig. 2.33. Finite state machine for battery state detection

B.3. Constant Current Detection Module

The purpose of this module is to check for the Slow Speed algorithm, through a flag, if the battery current is constant or not during a period of time of 200ms. The algorithm is given in the statechart on Fig. 2.34.

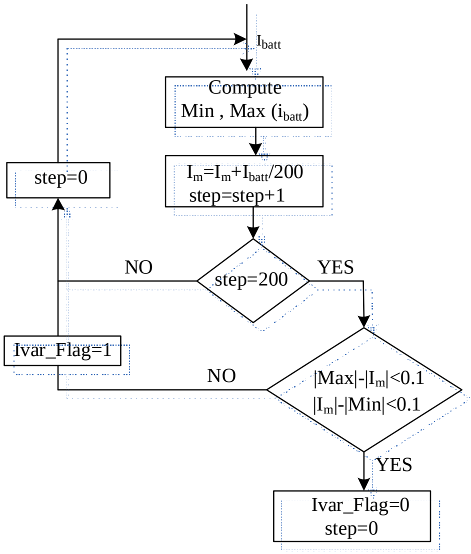

Fig. 2.34. Constant current detection statechart

B.4. Efficiency Computation Module

The battery efficiency, in conventional cars, is in general high because usually the battery operates at low discharge rates and only from time to time at high rates. In HEV high transients (especially in urban driving) are typical due to power boosting and frequent ICE cranking. In these cases, the SOC estimation, based on a simple current integration, leads, in time to significant errors. Therefore, in order to keep these errors small, we need to bring in some corrections. The correction we propose here takes into account the battery efficiency and we start from an equivalent circuit representation of the battery, illustrated in Fig. 2.35.

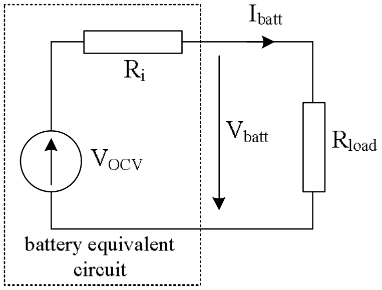

Fig. 2.35. Battery equivalent circuit representation

The battery efficiency is given by equation (2.19):

$$\eta_{batt} = \frac{R_{load}}{R_i + R_{load}} \tag{2.19}$$

where R_i has a range of [8-20mΩ] for a 55Ah, 12V, lead-acid battery.
Equation (2.19) shows that at low discharge rate (e.g. 12.5A), R_{load} is around 1Ω, which means an efficiency of 99.1%. In case of high loads (e.g. 200A) R_{load} is around 0.05Ω, which means an efficiency of 83.3%.
The efficiency of the battery decreases as the supplied current increases; however we can say that even at high loads the battery efficiency is still good.
The corrected value of the battery current (or discharged Ah) is:

$$I_{disch\_c} = \frac{I_{disch}}{\eta_{batt}} or Ah_{disch\_c} = \frac{Ah_{disch}}{\eta_{batt}} \tag{2.20}$$

Complex models for battery efficiency as a function of frequency, current level and initial voltage are presented in [2.35]. The battery is modeled as a series and parallel connection of impedances where each represent some characteristic phenomena such as double layer effect, mass transport limitation, diffusion effect and ohmic resistance.

C. Slow Speed Algorithm

The main idea behind the proposed algorithm is to recognize the battery operation and then to apply the estimation method that leads to minimum errors in the SOC estimation.
Seven battery operation modes, during an operation cycle, have been identified as follows:
- *constant current discharge* characterized by a constant current discharge and slow voltage variation for low discharge rates. In case of high discharge rates the voltage variations increase so that at medium to low SOC the voltage drop can reach values of 2V/Ah.

- *OCV relaxation* (after charge and after discharge): in these cases the battery current is very small (around zero) and voltage recovery takes place until the voltage reaches the equilibrium state.
- *cranking:* very high current is drawn from the battery, due to high torque necessary for ICE safe cranking.
- *variable current discharge*: during this state the current discharge is not constant and is not high.
- *constant current charging*: during this state the battery is charged at constant current. The current during charging can be 5A or 10A.
- *regenerative braking* is characterized by highly variable battery currents.

All these operation modes of the battery are illustrated in Fig. 2.36.

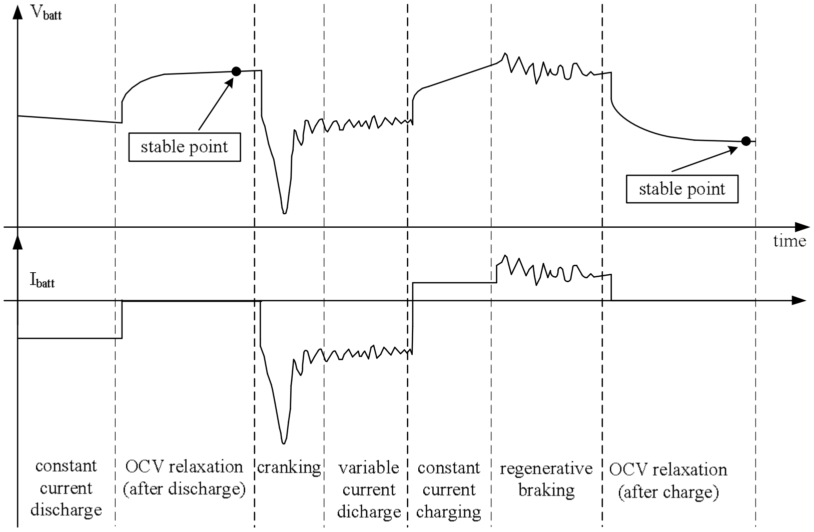

Fig. 2.36. Diagram of a typical HEV battery operation cycle

Every operation mode has its method for SOC estimation.
In Fig. 2.37. the battery SOC estimation methods for all battery operation modes are given.

For constant current discharge the SOC estimation is based on current integration. It is possible to store in a look-up table combinations of u and i for different SOC and from such a look-up table to estimate SOC. The inconvenience is that when the battery is ageing the internal resistance increases and the combination of u and I can not be considered valid. For the present algorithm, during battery constant current discharging the SOC estimation is based on current integration method.

During the OCV relaxation the OCV stable point is estimated and from the SOC vs. Vocv (open circuit voltage) look-up table (LUT) the estimated battery SOC is extracted. Stable OCV estimation is not difficult if the battery was previously discharged before due to a relatively low period of time (compared to the case when battery has been charged previously) necessary to get a stable point. During cranking, variable current discharge and regenerative breaking the OCV estimation is very difficult and even if this is possible the estimation is affected by unacceptable errors, which are propagated further in the SOC estimation process.

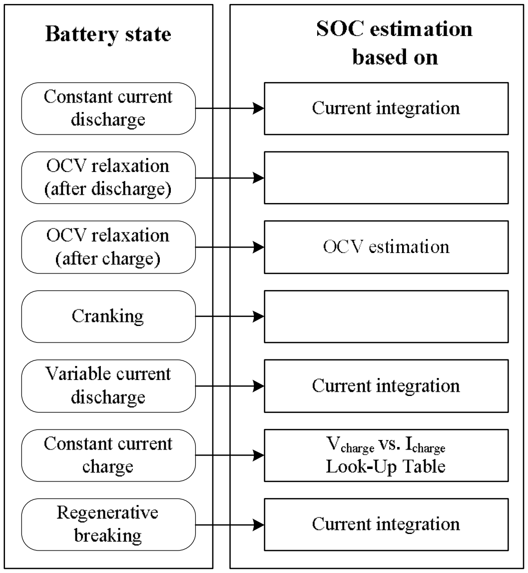

Fig. 2.37. Battery state and their SOC estimation method

Therefore, the preferred solution for this case is the one based on current integration. For constant charging, SOC estimation is based on the look-up table which stores the SOC versus battery voltage for different charging currents (5A and 10A).

The reconfiguration algorithm for battery state-of-charge is shown in Fig. 2.38. Each state is characterized by:

- Enable input
- Reset input
- State-of-charge output
- Confidence indicator (CI) output

Each state provides a more or less accurate SOC value. Each state has associated a confidence indicator that indicate how reliable is the SOC values. The selector decides which one of the inputs will be selected as an output of the switch. The Selector will detect which state has the highest confidence indicator, and that state will provide the value for the battery state-of-charge.

SOC estimation based on static (stable) OCV detection

By definition the open circuit voltage (OCV) is the battery voltage under the equilibrium conditions (no current is flowing through the battery). The open circuit voltage is a function of battery state-of-charge and is expected to remain the same during the life-time of the battery. In fact this is the key element of all state-of-charge estimators used in applications that use valve regulated lead-acid batteries.

Almost all other important parameters are changing during the battery life (e.g. battery capacity, internal resistance, state-of-health, etc). Also, battery open circuit voltage is temperature independent.

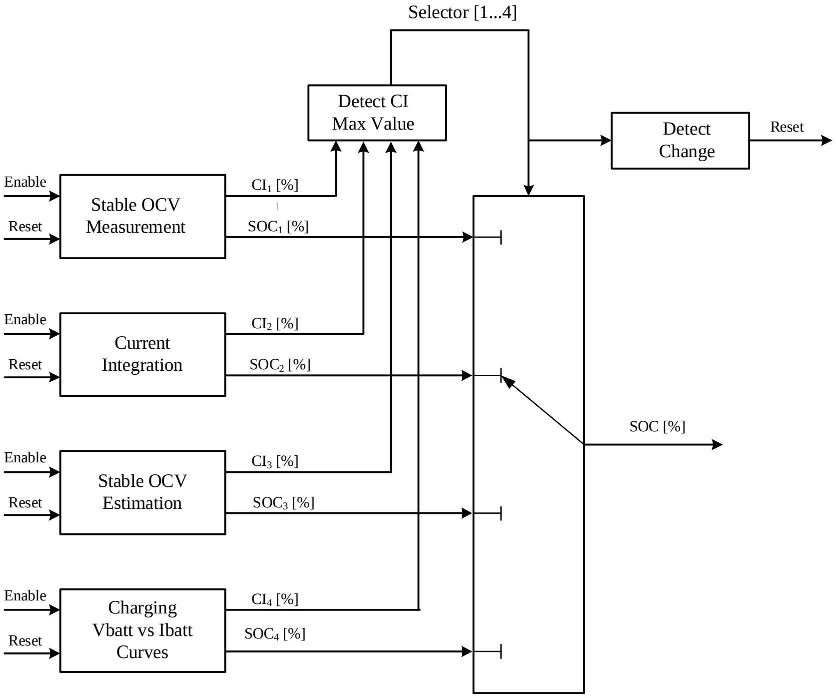

Fig. 2.38. Self-reconfigurable battery SOC estimator architecture

We consider that the battery SOC estimation based on the static OCV has a 100% confidence indicator. We define the static OCV as the battery voltage after the relaxation process is completely stabilized. The experiments revealed that the complete battery voltage relaxation process takes from tenth of minutes up to a few (2-3) days. The relaxation time if influenced by the battery state-of-charge, the amount of current charged/discharged, and the magnitude of the current, if the battery has been charged or discharged. Voltage relaxation after charging takes longer than after discharging, in almost similar conditions (same SOC, same Ah charged/discharged).

The measurements performed on a valve-regulated battery have shown that battery voltage needs around 8 hours to become completely stabilized after the discharging is off and more than 48 hours after the charging is off. For the first test the battery has been discharged 10 minutes at a constant current of 5A. After 10 minutes the discharging has been switched of and the battery voltage has been measured with a digital voltmeter from ten to ten minutes in the first hour and after that from hour to hour. Similar measurements have been performed for charging, in similar conditions.

The static OCV voltage represents the value of the voltage at battery terminals, measured after the complete relaxation of OCV. This is illustrated graphically in Fig. 2.39.

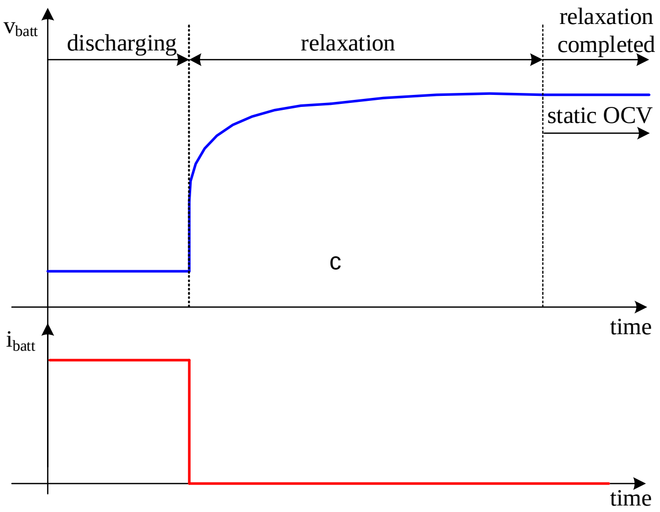

Fig. 2.39. Typical voltage and current waveform during and after constant current discharging

In Fig. 2.40. the static OCV vs SOC, derived from experiments is given.

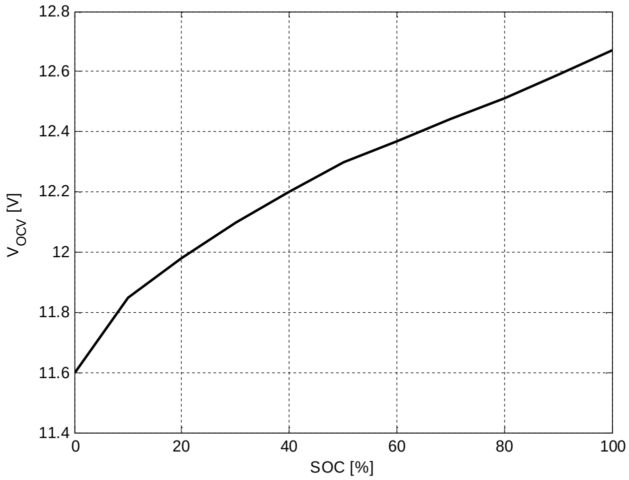

Fig. 2.40. Measured static OCV as a function of battery SOC (BOSCH VLRA battery, 12V, 55Ah)

In the range of [20-100]% SOC, that the curve is almost linear and a gradient of *17mV/[%]SOC* can be calculated. This means that any *17mV* error in OCV estimation will lead to 1% SOC error.

SOC estimation based on static OCV estimation

Looking at the diagram of a typical HEV battery voltage and current profile (Fig. 2.23), we see that there is a time when no current is flowing through the battery, but the battery open circuit voltage is still active, changing its value in time until it gets a constant value. As we have seen in the above paragraph, the battery voltage needs hours to reach the steady-state (constant) value. Now we have two options to estimate the battery state-of-charge:

a. to consider the actual battery voltage as an static OCV and based on the static OCV vs SOC look-up table to estimate SOC.

b. to consider the SOC the same as the estimated in the previous state (e.g. if previously the battery was discharged and the SOC was estimated at 80%, we consider the battery has 80% SOC, until the battery voltage reaches its static OCV and a new reevaluation of SOC is achieved)

The first option is totally unreliable in the first minutes and tenth of minutes due to the difference between OCV and static OCV. For example, let us analyze the values from Table 1. After 5 min the battery entered into the relaxation state the battery voltage is 12.540V, while the static OCV is 12.607 V. This means an error of 57mV which leads to an error around 4% which is acceptable, because it is within the range of 5%, the maximum acceptable error by the automotive manufacturers. A worst case is when the above mentioned fact occurs immediately (1-3 minutes) after the battery entered into the relaxation state. For example, after 3 minutes, the OCV is 12.430V. Now the voltage difference is 177mV, which is equivalent with an error of 10%, which is totally unacceptable. Such a situation could happen, even often, when the driver is at stop, the brake pedal is pressed, thermal engine is off, and electrical accessories are OFF.

The second option is also more or less reliable and the SOC accuracy depends on how accurate it was the SOC in the previous state. For example if in the previous state a big amount of current has been charged/discharge from the battery, and the current was non-linear the accuracy of the SOC became smaller (due to the current integration method). It might be happen that this accuracy to be lower that 5%, and this is not acceptable. The voltage relaxation after charging is lower (the gradient *dOCV/dt* is lower) and take longer time. In this case we expect higher errors for SOC estimation, than for discharging.

In the above mentioned explanation, it has been demonstrated that the a) and b) options are not reliable 100%, and could lead to error out of the range of [0-5]% for SOC.

Because the voltage relaxation needs so much time to stabilize, it is desired to estimate the SOC during this time. The solution proposed is to estimate the static OCV and further, based on *SOC vs* V_{ocv} look-up table to derive the estimated SOC.
The battery voltage relaxation process (for 4h) after battery discharging with a current around 85A for 60s is presented in Fig. 2.41.

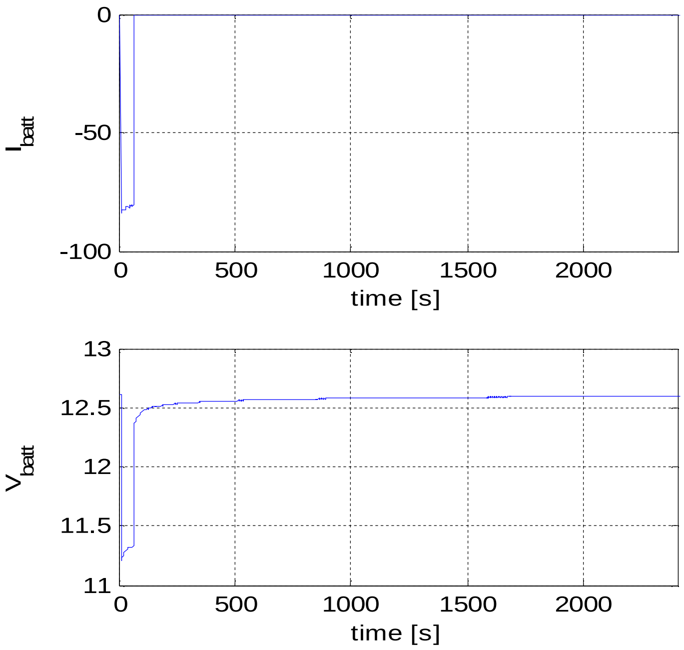

Fig. 2.41. Open Circuit Voltage variation after 60s of battery discharging at 85A.

For a better understanding of the battery's open circuit voltage dynamics (corresponding to Fig. 2.24.). Table 1 gives the battery open circuit voltage at different representative time moments.

Table 1. OCV corresponding to Fig. 2.42

time	battery voltage [V]
0 min	12.322
5 min	12.548
10 min	12.567
20 min	12.582
30 min	12.591
40 min	12.595
1h	12.600
2h	12.606
3h	12.6082
4h	12.6087
7h	12.6088
24h	12.609

From Fig. 2.42 we can see clearly that after the battery switches to rest, the voltage relaxation process is fast (*dv/dt≈40mV/min*) in the first minutes. In this case it is difficult to estimate the OCV within the specified limits. After approximately 5 minutes the relaxation process is getting slower and OCV can be estimated with a very good precision. These considerations are valid for the discharging process.

The battery voltage relaxation process is more complex when the battery switches from charging to rest due to the longer time (around 72h) required for a complete voltage stabilization (in a real car this situation can be encountered in weekends when the car is sleeping).

The predicted OCV is given by equation (2.21):

$$\hat{V}_{ocv} = V_{ocv|t} + \frac{V_{ocv|t+\Delta t} - V_{ocv|t}}{\Delta t} \cdot K = V_{ocv|t} + dv_{ocv} \cdot K \tag{2.21}$$

where $\widehat{V}_{ocv}$ is the battery estimated open circuit voltage, Δt- time interval (sampling time) in seconds, K is the gain derived experimentally and given in Fig. 2.42. Both K and Δt can be considered as calibrations.

The battery SOC error is calculated as:

$$error_{SOC}\,[\%] = \frac{V_{ocv} - \widehat{V}_{ocv}}{0.012} \tag{2.22}$$

where 0.012 is the voltage drop over 1% of SOC (100%=1.2V=12.7V-11.5V).

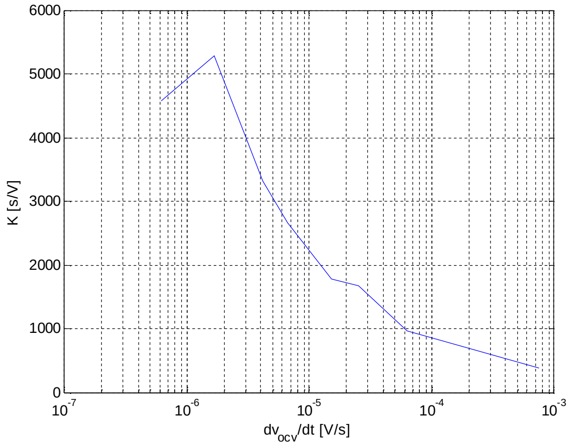

Fig. 2.42. Gain K as a function of open circuit voltage variation (dvocv/dt)

In the first step the algorithm detects the time moment when the battery enters in zero current state. In the next 5 minutes the algorithm checks if the battery current is zero. If YES then the OCV estimation process starts based on equation (2.21). The OCV estimation is finished when the battery voltage is completely stabilized.

The battery voltage is considered completely stabilized if the relationship given by (2.23) is true:

$$\frac{dv_{ocv}}{dt} \leq \frac{0.006}{3600} V / s \qquad (2.23)$$

Then the SOC estimation is performed by OCV vs. SOC look-up table. From experiments, we conclude that after 1h of voltage relaxation, the OCV estimation is not necessary, because the voltage variation is insignificant and SOC error is less than 5% if the SOC is estimated based on voltage reading from battery terminals.

The battery open circuit voltage estimate as well as the battery state-of-charge error based on this estimate for $\Delta t=dt_{est}=2.5min$ and $\Delta t=dt_{est}=5min$ is given in Fig. 2.43 and Fig. 2.44 respectively. We have to mention that the battery has been previously discharged and only after the algorithm detects zero battery current it is checked if the OCV estimation process can start.

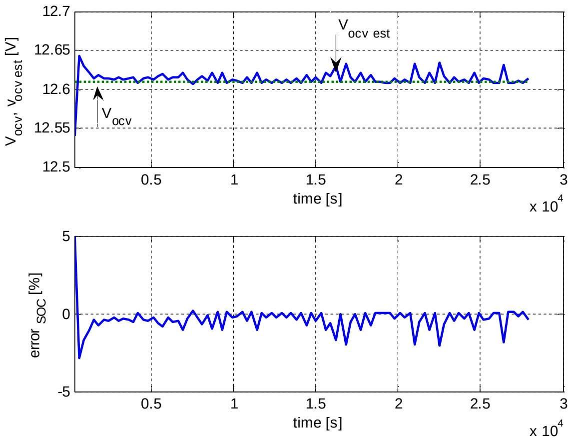

Fig. 2.43. a) Static OCV (Vocv) – dotted line - and estimated OCV (vocv est) –solid line -, b) SOC error for =3 min.

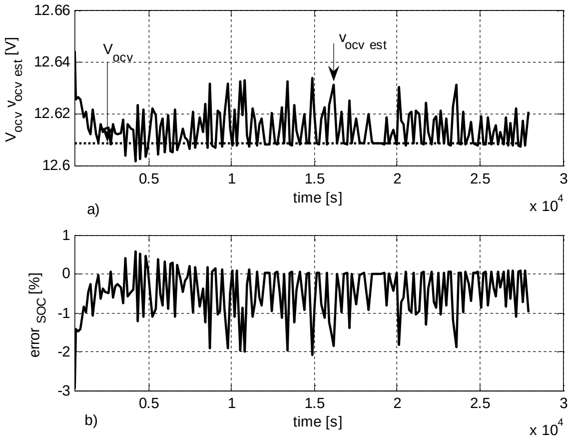

Fig. 2.44. a) Static OCV (Vocv) – dotted line - and estimated OCV (vocv est) –solid line -, b) SOC error for =2.5 min.

The results plotted in Fig. 2.43, 2.42. demonstrate the reliability, accuracy (average error is lower than 1%) and robustness of the proposed algorithm. In both cases the battery state-of-charge error is almost the same, within the specified limits (max 5% error). The great advantage of this method is that the OCV estimation is not dependent on one or more physical parameters of the battery. We have to notice that during the OCV estimation, the CPU load is reduced at minimum due to a very small computational effort (only a few arithmetic operations are necessary). Thus, we believe that this solution is low cost, accurate, reliable, and fast.

SOC estimation based on current integration Module

The battery state-of-charge estimation based on current integration is carried out when unstable conditions are detected and battery static OCV estimation is difficult. The SOC estimation is based on equation (2.24):

$$SOC = SOC_{ini} + Ah_{total} \qquad (2.24)$$

where Ah_{total} is the sum of Ah during charging and discharging, and is calculated by the Fast Speed algorithm. We have to mention that when the algorithm decides that SOC estimation needs to be estimated by current integration, the Ahtotal is reset.

However, the current integration method, in general, is affected by errors (offset, etc) and in time the error increases.
From experiments we propose a new formula for confidence indicator:

$$CI\,[\%] = CI_{ini}\,[\%] - \frac{0.1 \cdot Ah_{total}}{100} \qquad (2.25)$$

Equation (2.25) shows that for 100Ah the error can be maximum 5Ah (10%).

SOC estimation based on Look-Up Table during constant current charging

During charging (or) discharging, the battery voltage generally increases abruptly for a short period of time because of internal resistance and capacitive (polarization voltage) components of the battery. Therefore, an instantaneous measurement of the battery voltage does not accurately reflect the charge state of the battery while its capacitive component exists.
To acquire an accurate effective voltage for a battery, a minimum period of time must pass in order to allow the capacitive component of the battery to disappear. This allows for more stable and more accurate control of the battery and of the vehicle. This capacitive component is not an energy store component, but rather a component that rapidly responds mainly to a load. It is much more difficult to estimate the capacitive component of the battery in a HEV in which charging and discharging occur repeatedly.
In the proposed look-up table the curve from Fig. 2.45 is stored.

In Fig. 2.45 a representation of the battery voltage during charging (after capacitive effect disappeared) for a SOC range of 30%-90% is given. However, a typical SOC range for HEV is [50%-85%]. The upper level is limited around 85% in order to capture with high efficiency the energy during regenerative braking. The lower level is limited around 50% due to the low performance of battery (e.g. the maximum power during discharging decreases substantially, and thus cold cranking is not very safe).

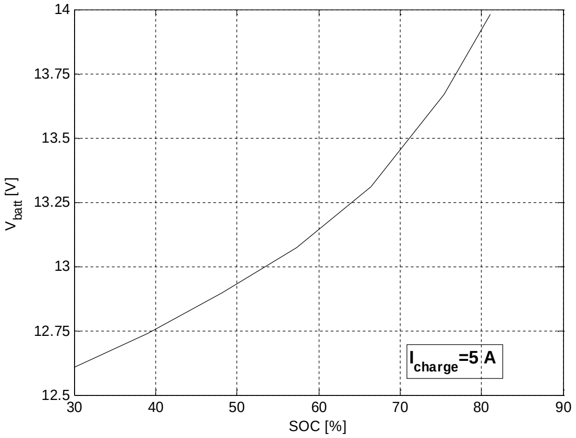

Fig. 2.45. Battery voltage as a function of SOC for constant charging current Icharge=5 A.

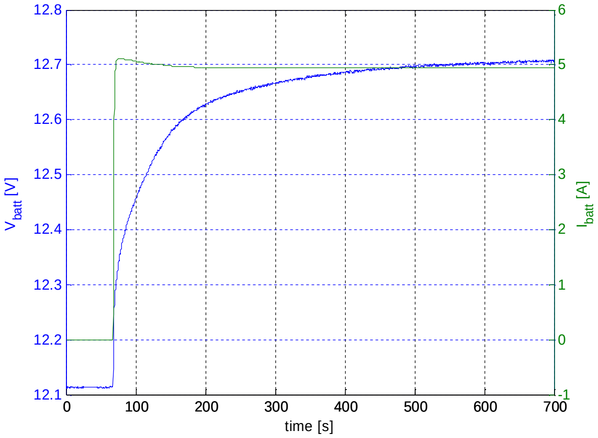

Fig. 2.46. Battery voltage and current during charging with Icharge=5A.

The capacitive component (effect) of the battery during charging can be easily observed in the Fig. 2.46. At time t=80s the charging process is initiated. Until the time t=400s the battery voltage is increasing and only after this time the effect disappears; that means dv/dt=0.155V/Ahcharged.

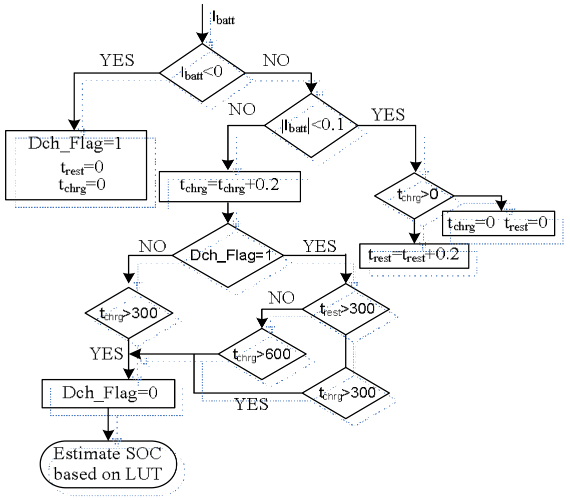

Fig. 2.47. SOC estimation flowchart during constant current charging

The SOC estimation flow chart during current charging is shown in Fig. 2.47.
The battery current is monitored permanently. If the battery is running in discharge mode we set to 1 the flag *Dch_Flag* and reset the timer trest and tchrg. Timers trest and tchrg measure the time when the battery is at rest and respectively, the time when the battery is charging. If the battery current is not negative, two cases are possible: (1) the battery is resting and (2) the battery is charging. If the battery switches directly from discharging to charging the counter tchrg is activated (is incremented by 0.2 because the algorithm is running at 0.2s). Further, the algorithm tests if the battery has been discharged before. If this is not true, the algorithm waits for 300s before the SOC estimation starts. If the condition is true and the battery has not been rested then the algorithm waits for 600s, and then the estimation begins. If the battery has been rested for more than 300s (time when the battery voltage recovery happened) additional 300s of charging are necessary until SOC estimation is active. In both cases the flag *Dch_Flag* is set to zero, and this means that the discharging influence disappears completely.
The *Dch_Flag* is set to zero because, after 300s of charging, the effect of discharging disappears completely. If the battery switches from charging to rest, both counters are reset and the algorithm starts to count the resting time of the battery.
The battery SOC estimation based on LUT has a confidence indicator of 98%; that means possible maximum deviation of 2%.

SUMMARY

This chapter introduces and documents the dv/di method to estimate on-line through experiments, the VRLA battery internal resistance and then applies it for on-line quick estimation of state-of-charge, for HEV where the battery undergoes frequent heavy transients. The results are deemed useful for on-line practical battery SOC estimation so necessary for starter-alternator torque contribution wise constraining to avoid battery early ageing.

The advantages of dv/di method over impedance spectroscopy for HEV applications are: easy on-line implementation, potential good accuracy in internal resistance estimation. A simple and accurate model for the estimation of power discharge from the battery is also, proposed in the paper. A new and very simple procedure for battery state-of-health estimation based on internal resistance estimation with practical application was proposed and developed. It can be very easy implemented in industry and is reliable. Then, a novel, on-line, battery state-of-charge (SOC) estimation algorithm, that might be used for battery (energy) management algorithm, on board HEV, is proposed. Based on current-voltage profile of the battery, the algorithm selects one of the four methods which provide the best accuracy in the battery state-of-charge estimation. The experiments, done on a 48Vdc 55Ah (four battery pack), proved that the algorithm fulfills the criteria of 5% maximum error in battery SOC. The advantages of this algorithm are thought to be: good precision, small computation effort, reliability and quickness in SOC estimation.

REFERENCES

[2.1] http://data.energizer.com/PDFs/BatteryIR.pdf
[2.2] A. Kalfelz, "Battery Monitoring Condiderations for Hybrid Vehicles and Other Battery Systems with Dynamic Duty Loads", Journal of Battery Power Products and Technology, Vol. 10, Issue 3, may/June 2006
[2.3] I. Buchmann, "Does internal resistance reveal battery capacity?"
[2.4] H. Shih, T. C. Lo, "Electrochemical Impedance Spectroscopy for Battery Research and Development – Technical Report", http://www.solartronanalytical.com/downloads/technotes/technote31.pdf
[2.5] J. A. Tinnemeyer, "Multiple Model Impedance Spectroscopy Techniques for Testing Electrochemical Systems", Journal of Power Sources, Vol. 136, Issue 2, October 2004
[2.6] S. K. Martha, K. Shukla, " Monitoring Sealed Automotive Lead-Acid Batteries by Sparse-Impedance Spectroscopy", Proceedings of Indian Academy Science, October-December 2003
[2.7] A. Teno, “Modeling and Evaluation of Valve-Regulated Lead-Acid Batteries, Helsinki University of Technology, Espoo 2004, Finland
[2.8] O. Bahlen, S. Buller, R. W. De Doncker, M. Gelbke, R. Naumann, “Impedance base battery diagnosis for automotive applications”, PESC 2005, Aachen, Germany
[2.9] S. Buller, M. Thele, R. W. De Doncker, E. Karden, “Impedance based simulation models”, IEEE Industry Application Magazine, pp. 740–741, April 2005.
[2.10] E. Karden, “Using low frequency impedance spectroscopy for characterization, monitoring and modeling of industrial batteries”, Ph. D. Thesis, 2001
[2.11] N. S. Z. Hai, M. W. Li, W. L.Wang, D. L. Zhang, D. G. Xu, "Aapplication of the EIS in Li-Ion Batteries Measurement"
[2.12] S. Buller, E. Karden, D. Kok, R. W. De Doncker, “Modeling the Dynamic Behavior Supercapacitors Using Impedance Spectroscopy”, IAS 2001
[2.13] W. Merida, D. Harington, G. McLean, N. Djilali, "Hardware Development for Impedance Spectroscopy on a 4-Cell PEMCF Stack Under Load"
[2.14] M. Coleman, C. K. Lee, C. Zhu, W. G. Hurley,” State-of-Charge Determination from EMF Voltage Estimation: Using Impedance, Terminal

Voltage, and Current for Lead-Acid and Lithium-Ion Batteries”, IEEE Trans. IE, Vol. 4, No. 5, Oct. 2007

[2.15] C. B. Zhu, M. Coleman, W. G. Hurley, "State-of-Charge Determination in a Lead-Acid Battery: Combined EMF Estimation and Ah-Balance Approach", IEEE Power Electronics Specialists Conference, Aachen, 2004, pp. 1908-1914

[2.16] G. Plett, “Extended Kalman Filtering for Battery Management Systems of LiPb-based HEV Battery Packs: Part 1. Background“, Journal of Power Sources, No. 134, 2004, pp. 252-261

[2.17] G. Plett, “Extended Kalman Filtering for Battery Management Systems of LiPb-based HEV Battery Packs: Part 2. Modeling and identification“, Journal of Power Sources, No. 134, 2004, pp. 262-276

[2.18] G. Plett, “Extended Kalman Filtering for Battery Management Systems of LiPb-based HEV Battery Packs: Part 3. State and Parameter Estimation“, Journal of Power Sources, No. 134, 2004, pp. 277-292

[2.19] G. L. Plett, "Dual and Joint EKF for Simulatneous SOC and SOH Estimation"

[2.20] B. S. Bhangu, P. Bentley, D. A. Stone, C. M. Bingham, "Nonlinear Observers for Predicting State-of-Charge and State-of-Health of Lead-Acid Batteries for Hybrid-Electric Vehicles", IEEE Trans. Veh. Technol., Vol. 54, No. 3, pp. 783-794, May 2005

[2.21] I. S. Kim, "Nonlinear State-of-Charge Estimator for Hybrid Electric Vehicle Battery", IEEE Trans. Power Electron., Vol. 23, No. 4, pp. 2027-2034, July 2008

[2.22] P. Singh, D. R. Eisner, "Development of Fuzzy Logic-Based Lead Acid Battery Management Techniques with Applications to 42V Systems"

[2.23] K. Kutluay, Y. Cadirci, Y. Ozkazanc, I. Cadirci, “A New Online State-of-Charge Estimation and Monitoring System for Sealed Lead-Acid Batteries in Telecommunication Power Supplies”, IEEE Transactions on Industrial Electronics, Vol.52, No. 5, October, 2005

[2.24] M. Verbrugge, E. Tate, “Adaptive State-of-Charge Algorithm for NiMH Batteries Including Hysteresis Phenomena”, Journal of Power Sources, No. 126, 2004, pp. 236-249

[2.25] C. C. Chan, E. W. C. lo, S. Weixiang, “The Available Capacity Computation Model Based on Artificical Neural Networks for Lead Acid Batteries in Electric Vehicles”, Journal of Power Sources, Vol. 87, pp. 201-204, 2000

[2.26] Affanni, A. Bellini, A. Concari, C. Franceschini, G. Lorenzani, E. Tassoni, C., “EV battery state of charge: neural network based estimation”, Vol. 2, pp.684-688, IEMDC, 2003

[2.27] G. O. Patilon, J. N. d’Alche-Buc, “Neural Networks Adaptive Modeling of Battery Discharge Behaviour”

[2.28] K. Kutluay, Y. Cadirci, Y. Ozkazanc, I. Cadirci, “A New Online State-of-Charge Estimation and Monitoring System for Sealed Lead-Acid Batteries in Telecommunication Power Supplies”, IEEE Transactions on Industrial Electronics, Vol.52, No. 5, October, 2005

[2.29] M. M. D. Ross, "A Simple but Comprehensive Lead-Acid Battery Model for Hybrid System Simulation"

[2.30] P. M. Hunter, A. H. Anbuky, “VRLA Battery Virtual Reference Electrode: Battery Float Charge Analysis”, IEEE Trans. On EC, Vol. 23, No. 3, Sep. 2008

[2.31] M. Coleman, W. G. Hurley, C. K. Lee, “An Improved Battery Characterization Method Using a Two-Pulse Load Test”, IEEE Trans. On EC, Vol. 23, No. 2, June 2008

[2.32] S. Barsali, M. Ceraolo, “Dynamical Models of Lead-Acid Batteries: Implementation Issues”, IEEE Transactions on Energy Conversion, Vol. 17, No. 1, March 2002

[2.33] M. Chen, G. A. Rincon, "An Accurate Electrical Battery Model Capable of Predicting Runtime and I-V Performance"

[2.34] S. Buller, M. Thele, E. Karden, R. W. De Doncker, "Impedance-Based Non-Linear Dynamic Battery Modeling for Automotive Applications", Journal of Power Sources, No. 113, 2003, pp. 422-430

[2.35] M. F. de Koning, A. Veltman, Paul P. J. van den Bosch, “Modeling Battery Efficiency with Parallel Branches”, IEEE-PESC, 2004, Aachen, Germany

[2.36] V. Coroban, I Boldea, “Valve-Regulated Lead-Acid. Batteries Characterization for Hybrid Electric Vehicles”, in Proc. 10th Int. Conf. on Optimization of Electrical and Electronic Equipment OPTIM 2006, 18- 19 May, Brasov 2006, Romania

[2.37] V. Coroban, I. Boldea, F. Blaabjerg, “A novel on-line state-of-charge estimator algorithm for Valve regulated lead-acid batteries used in hybrid electric vehicles”, Proc. ACEMP’07 & Electromotion’07, Bodrum, Turkey, pp.39-47, Sept. 2007.

3. BEGA – MATHEMATICAL MODEL AND SIMULATION RESULTS

3.1. Introduction

Se Integrated starter/alternator (ISA) systems combined with power electronics converters make the main difference between the powertrain architecture of the conventional automobiles and hybrid electric vehicles (HEV). Except for cruising control, ISA requires basically torque-control, not speed-control for vehicle propulsion. When the electric motor drives the air-conditioner, with the engine idle in traffic jams or at stoplights, a speed control may be needed. The motoring and generating torque/speed reference in HEV require large constant power speed range (CPSR) (up to 10:1) for most cases. Such a challenging requirement implies both electric machine and converter over-sizing. The induction machine, claw-pole alternator, permanent magnet synchronous machine, switched reluctance machine and the newest proposed solution called biaxial excitation generator for automobiles (BEGA) are briefly analyzed and compared for ISA. The induction machine (IM) was the first brushless machine proposed for ISA. The reliability, low cost, low maintenance and ability to operate in hostile environment are the main IM advantages. Despite of these advantages, IM has serious drawbacks, which limit its investigations to theoretical analysis and laboratory tests. Notable rotor losses and limited flux-weakening capability, which leads to low CPSR up to maximum 4:1, are the main drawbacks [3.1]. At higher speeds the rotor and core losses increase dramatically and this leads to a reduction in efficiency. Also, the power factor decreases at higher speeds and, combined with a lower efficiency, it means a diminished inverter capability usage (low kW/kVA ratio). The equality between d and q-axis flux, for maximum flux/torque control, reduces the voltage availability at higher speeds and limits the power delivery by induction ISA [3.2]. A method to improve the voltage availability is to switch the stator winding from Y to Δ connection above the rated speed. A considerable improvement in the field weakening capability can be done by using a dual-inverter control strategy reported in [3.3], but with additional cost of a second inverter. The second inverter action starts only beyond the rated speed and it cancels out the voltage drop described by the term jωeσLsis, which considerably increases at higher speeds. The switched reluctance machine (SRM) fulfills more easily a criterion imposed by high performance ISA: simple and rugged construction, ability of extremely high-speed operation, and hazard free operation, represent a few advantages. In contrast to IM, the well-designed SRM has a larger CPSR up to 7 [3.4]. The design constraints, which have direct influence on SRM performances, are: number of stator-rotor poles and width of poles. A low number of stator-rotor poles increase CPSR, while the torque is lower. For the same number of stator-rotor poles, the CPSR is larger for narrowest rotor pole and the rated torque is minimum. For the widest rotor poles, CPRS decreases with the benefit of increasing rated torque value. The efficiency for SRM is around 90% over entire speed range. Although the SRM suffers due to a lower power factor at lower speed, this difficulty is overcome at higher speeds, facts that lead to a slightly better utilization of inverter (kW/kVA ratio increases). Noise and vibrations are known SRM problems. The permanent magnet (PM) synchronous machine is built in three main configurations: surface mounted PM synchronous machine (SPMSM), interior PM synchronous machine (IPMSM), and PM assisted reluctance synchronous machine (PM-RSM).

SPMSM has a compact design and high efficiency due to the lack of excitation in the rotor, but have poor CPSR [3.5]. A major barrier in achieving a wider CPSR is the limited voltage availability at higher speeds due to the induced EMF that is proportional to speed. The IPMSM has similar features, but the major benefit is the higher torque density due to additional reluctance torque produced by the difference in d, q axis inductance: larger difference between d and q axis inductance, larger power (torque) density for the same PM flux. PM-RSM has the largest CPSR. A lower value of PM flux on q axis gives the possibility to cancel the flux linkage in q axis. In this case, the total flux is equal to d axis flux that is controlled easily by d-axis current. Also the power factor is higher, which means that PM-RSM performs better in terms of peak kVA. Efficiency beyond 90% between 3000-6000 rpm is reported in [3.7]. The consequent pole permanent magnet machine (CPPM) presented in [3.8] comes as an alternative solution to the limited constant power speed range of the above presented solutions. This combines the fixed PMs flux with variable flux given by a field winding. Despite its advantages such as: wide range of air-gap flux control, larger CPSR, PMs lower demagnetization possibility, CPPM has some limitations: the q-axis flux never reaches zero value, the dc winding capability is not used at maximum [3.9]. BEGA is one of most recent radial electric machine proposed for ISA systems (Fig. 3.1). Efficiency around 80%, unity power factor operation, very large constant power speed range 10:1, zero (and negative) q axis flux operation, a reduced rated kVA of the inverter are a few advantages specific to BEGA. Papers [3.9], [3.10] provide a comprehensive characterization of BEGA. On the other hand, it still has brushes for low power rotor dc field winding with additional cost for its dc-dc converter. In terms of torque/kg the various solutions that can accommodate the given rather large maximum speed (15000rpm), which excludes the transverse flux PM machine because the fundamental frequency is to high, all solutions analyzed here including BEGA rely on about the same air-gap density and current loading (to secure about the same heat transfer capacity, through the frame) and thus a pretty much equivalent at peak torque which dictate the size of the machine, but they are different in how they handle the capacity of CPSR required in the sense that they demand more or less machine or converter oversizing for the scope.

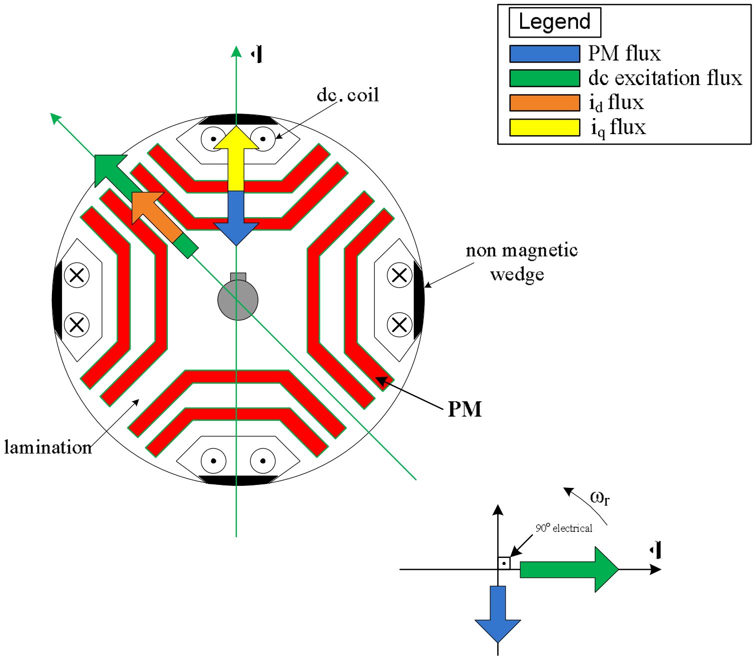

Fig. 3.1. BEGA rotor cross-section

3.2. BEGA - mathematical model

BEGA has a typical uniformly slotted stator with a three-phase ac winding, with a rotor with multiple flux barriers filled partially with PMs to reduce q axis armature flux, and along d axis (of higher inductance) a dc field winding supplied through slip rings and brushes.

Detailed modeling of BEGA is required for proper simulation of the system. The dq model has been developed in rotor reference frame.

Voltage equations are given by:

$$V_d = R_s I_d - \omega_r \Psi_q + \frac{d\Psi_d}{dt} \tag{3.1}$$

$$V_q = R_s I_q - \omega_r \Psi_d + \frac{d\Psi_q}{dt} \tag{3.2}$$

$$V_f = R_f I_f + \frac{d\Psi_f}{dt} \tag{3.3}$$

Flux linkages are given by:

$$\Psi_d = L_d I_d + L_{mf} I_f \tag{3.4}$$

$$\Psi_q = L_q I_q - \Psi_{PM} \tag{3.5}$$

$$\Psi_f = L_{mf} I_d + L_f I_f \tag{3.6}$$

Substituting equations (3.4) and (3.5) into (3.1) and (3.2) yields:

$$V_d = R_s I_d - \omega_r \left(L_q I_q - \Psi_{PM}\right) + \frac{d\Psi_d}{dt} \tag{3.7}$$

$$V_q = R_s I_q - \omega_r \left(L_d I_d - L_{mf} I_f\right) + \frac{d\Psi_q}{dt} \tag{3.8}$$

$$V_f = R_f I_f + \frac{d\Psi_f}{dt} \tag{3.9}$$

The electromagnetic torque is given by:

$$\begin{aligned} T_e &= \frac{3}{2} p_1 \left(\Psi_d I_q - \Psi_d I_q\right) \\ T_e &= \frac{3}{2} p_1 \left(L_{mf} I_f I_q + \left(L_d - L_q\right) I_d I_q + \Psi_{PM} I_d\right) \end{aligned} \tag{3.10}$$

The mechanical torque equation is:

$$T_e - T_L = J \frac{d\omega_r}{dt} + B\omega_r \tag{3.11}$$

and

$$\omega_r = \frac{\omega_{re}}{p} \tag{3.12}$$

where: V_s, I_s - are the stator voltage and current vector respectively, Ψ_s is the stator flux linkage vector, R_s is the stator resistance, ω_r is the electrical rotor speed, ω_{re} is the mechanical rotor speed, L_d, L_q are the d, q axis inductance, L_{mf} is the mutual field-armature inductance, Ψ_{PM} is the PM flux on q axis, and p is the pole pair.

Park transformation

Converting the variable x_{abc} to variables x_{dq0} in rotor reference frame the following equations are obtained:

$$\begin{bmatrix} x_d \\ x_q \\ x_0 \end{bmatrix} = \begin{bmatrix} \sin\theta_r & \sin\left(\theta_r - \frac{2\pi}{3}\right) & \sin\left(\theta_r + \frac{2\pi}{3}\right) \\ \cos\theta_r & \cos\left(\theta_r - \frac{2\pi}{3}\right) & \cos\left(\theta_r + \frac{2\pi}{3}\right) \\ 1/2 & 1/2 & 1/2 \end{bmatrix} \cdot \begin{bmatrix} x_a \\ x_b \\ x_c \end{bmatrix} \tag{3.13}$$

Converting the variable x_{dq0} to variables x_{abc}:

$$\begin{bmatrix} x_a \\ x_b \\ x_c \end{bmatrix} = \begin{bmatrix} \sin\theta_r & \cos\theta_r & 1 \\ \sin\left(\theta_r - \frac{2\pi}{3}\right) & \cos\left(\theta_r - \frac{2\pi}{3}\right) & 1 \\ \cos\left(\theta_r + \frac{2\pi}{3}\right) & \cos\left(\theta_r + \frac{2\pi}{3}\right) & 1 \end{bmatrix} \cdot \begin{bmatrix} x_d \\ x_q \\ x_0 \end{bmatrix} \tag{3.14}$$

The BEGA parameters are given in Table I. The saturation effect for the mutual inductance L_{mf} is taking into account and it is illustrated in Fig. 3.2.

TABLE I
BEGA PARAMETERS

Rated power (PN)	1 kW
Rated phase voltage (Vs)	22 V (rms)
Rated phase current (Is)	67 A (rms)
Rated field current (If)	4 A
Rated battery voltage (Vbatt)	48 V
Rated torque (TN)	6.15 Nm
Rated speed (nN)	1500 rpm
Number of pole pairs (p)	2
Stator phase resistance (Rs)	0.05 Ω
q axis inductance (Lq)	0.38 mH
D axis inductance (Ld)	1.8 mH
PM flux (ΨPM)	0.013 Wb
Field winding resistance (Rf)	6.5 Ω
Field winding inductance (Lf)	0.407 H
Mutual field-armature inductance (Lmf)	18 mH
Moment of inertia (J)	16e-3 kg•m2
Viscous friction coefficient (B)	1e-4

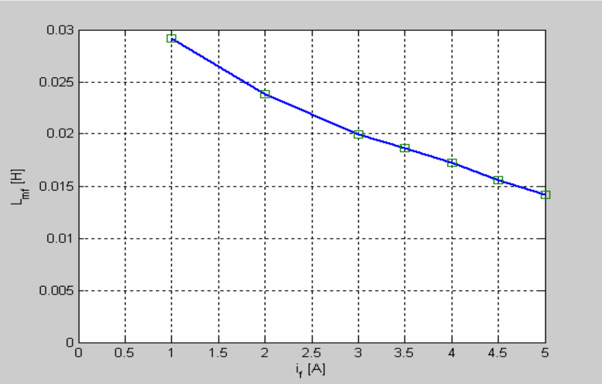

Fig. 3.2. L_{mf} vs i_f

3.3 MATLAB-Simulink Simulation environment of BEGA

In order to investigate the performance of BEGA, a Matlab-Simulink® model has been developed. The main parts of the model are: i) machine mode, ii) three-phase inverter model and iii) vector control algorithm. The machine parameters used in the model has been previously experimentally measured, and are shown in Table 1.

The target of the simulation model was to simulate the system as close as possible to the reality. A continuous time event is a succession of discrete time events executed with an infinitesimal step time. Therefore the BEGA model is running at *100ns* sampling time. In modern control system microcontrollers and digital signal processors with a clock frequency of *20MHz* are used. This means that *50ns* is the time base for PWM signal generation. In order to be close to the reality the simulation step of *100ns* was chosen for three-phase inverter simulation. It was also possible to choose *50ns* but due to intensive computations the simulation time would be at least doubled. The control algorithm is running at *100us*, as in the real dSpace system. The switching frequency of the inverter is chosen the same as control algorithm, *10kHz*. In this way, results closer to reality can be obtained.

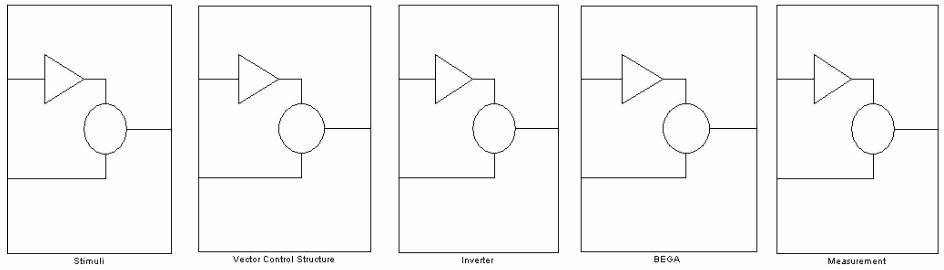

Fig. 3.3. The components of the Matlab-Simulink model for BEGA vector control implementation.

The main simulation subsystems are:

- *Stimuli* – basically, it contains the profiles of the reference speed and load torque
- *Vector control structure* – it contains the implementation of BEGA vector control in the same way as in the dSpace rapid prototyping system. The complete vector control structure (subsystem is running at 100us). The advantage of this structure is that it allows the user to copy it directly in the dSpace environment without any adaptation. In other words any change done in simulation model can be easily implemented in dSpace by simply copy and paste. The vice-versa is also possible. This way the time consuming for real-hardware implementation can be reduced at minimum with a good agreement between simulation and reality.
- *Inverter* – provides the phase voltages at BEGA terminals. In order to obtain simulation results closer to the experimental results a simulation model of the inverter is developed. This model in fact is an emulation of the real hardware. The working principles of the inverter in the simulation are

exactly the same as behind dSpace platform. For example, the duty cycles for the inverter MOSFETs are generated exactly like in dSpace.

- *BEGA* – contains the d-q model of the machine.
- *Measurements* – allows the user to see any signal waveform in the simulation. Also here are implemented mathematical calculation like active and reactive power, power factor angle, etc.

The advantage of such in details implementation of the complete system is that the simulation results are close to the reality and furthermore the simulation can be used as a basis for a preliminary investigation and validation of different controls solutions for BEGA.

A more in detail description of the simulation subsystems follows.

A. BEGA model

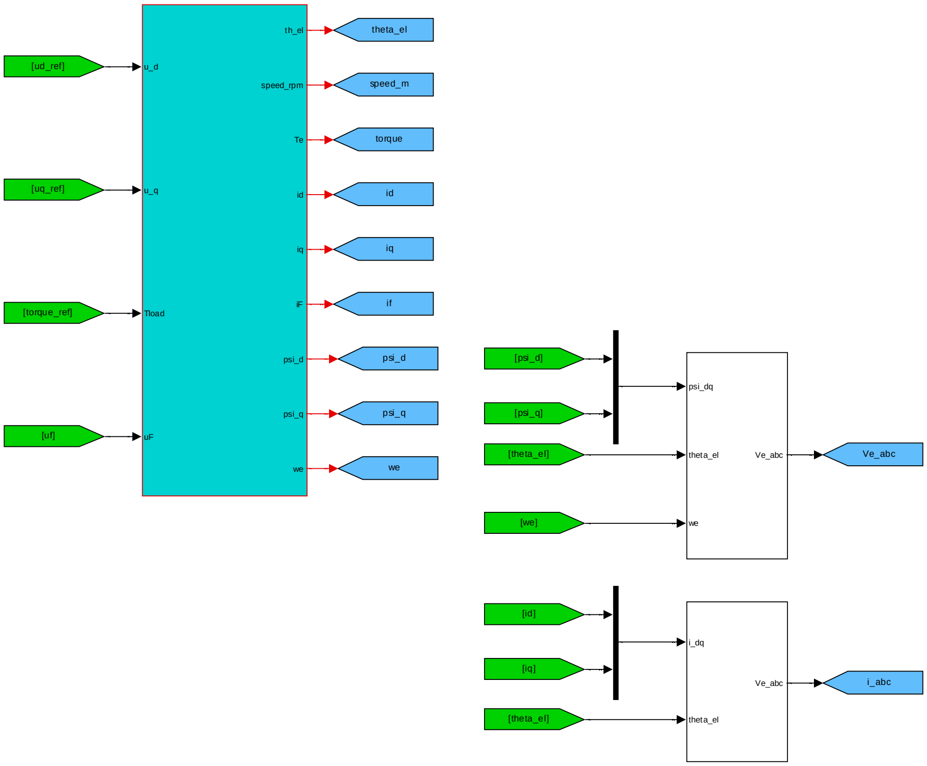

Figure. 3.4. BEGA Subsystem overview

The inputs of the BEGA model are the reference d-q voltages, load torque and the dc excitation reference voltage.

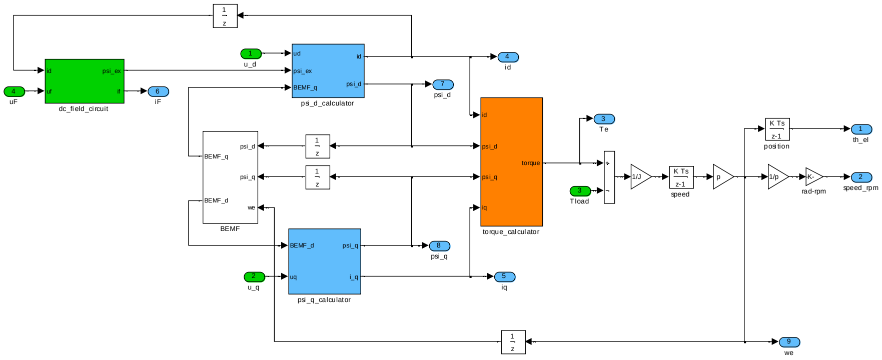

Figure 3.5. BEGA d-q model

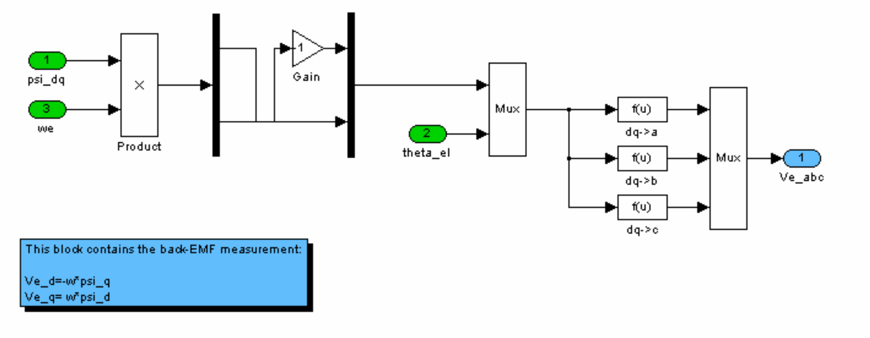

Figure 3.6 Phase Back-EMF calculation block

B. *Three Phase Voltage Source Inverter Model*

The structure of the basic three-phase voltage source inverter, with MOSFET transistors as switching devices, is shown in Fig. 3.7. The three-phase inverter contains three legs a,b,c and each leg consists of two switching power devices and two diodes for current return. The diodes allow the current to flow when the power devices are turned off.

For the inverter model implemented in Matlab-Simulink the following hypothesis are assumed:

- The dc link voltage V_{dc} is considered constant
- The power switching devices are assumed to be identical. The turn-on Ton and turn-off time Toff are the same for each device and are zero.
- The dead time is the same for each device.
- The voltage drop on the power semiconductors is the same and is modeled like in the Fig. 3.10.

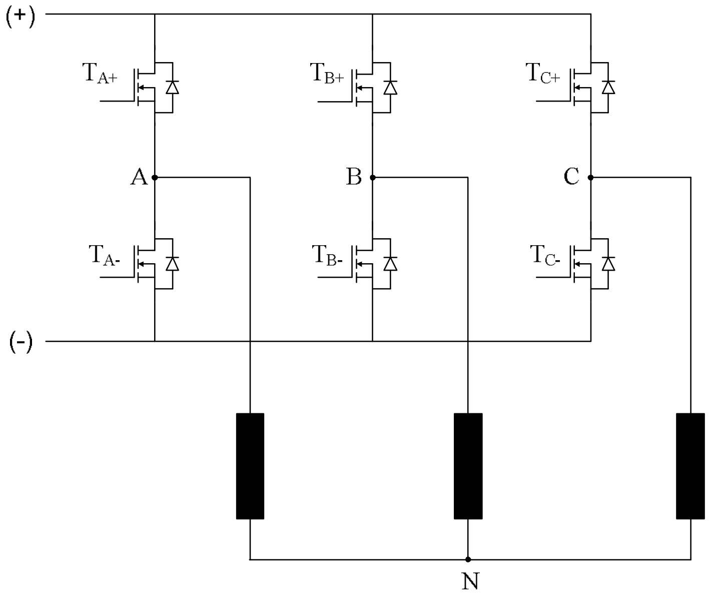

Fig. 3.7 Three phase inverter

The instantaneous phase voltages of the BEGA are:

$$V_{an} = \frac{V_{dc}}{3} \cdot \left(-2S_a + S_b + S_c \right) \tag{3.15}$$

$$V_{bn} = \frac{V_{dc}}{3} \cdot \left(S_a - 2S_b + S_c \right) \tag{3.16}$$

$$V_{ac} = \frac{V_{dc}}{3} \cdot \left(S_a + S_b - 2S_c \right) \tag{3.17}$$

where S_x is defined as the switching signal for the leg “x”. $S_x=1$ if the upper transistor on leg “x” is on (TA+, TB+, TC+) and Sx=0 if the upper transistor is off (TA-, TB-, TC-).

Since each switching device can assume two states, the three-phase inverter can assume eight distinct and independent states. When all switching signals have the same values (0,0,0) or (1,1,1) the output voltage is zero and the two associated vectors V0 and V7 are called zero vectors. In the remaining six modes, the instantaneous output of the inverter consists of six active vectors. The angle between vectors is sixty degrees and all vectors have the same amplitude $2V_{dc}/3$.
In complex notation, the six active vectors are:

$$\underline{V}_k = \frac{2}{3} V_{dc} \cdot e^{j(k-1)\frac{\pi}{3}} \tag{3.18}$$

where k is the vector number. The basic voltage vectors, identified as $V_k\ (S_a, S_b, S_c)$ are illustrated in Fig. 3.8.

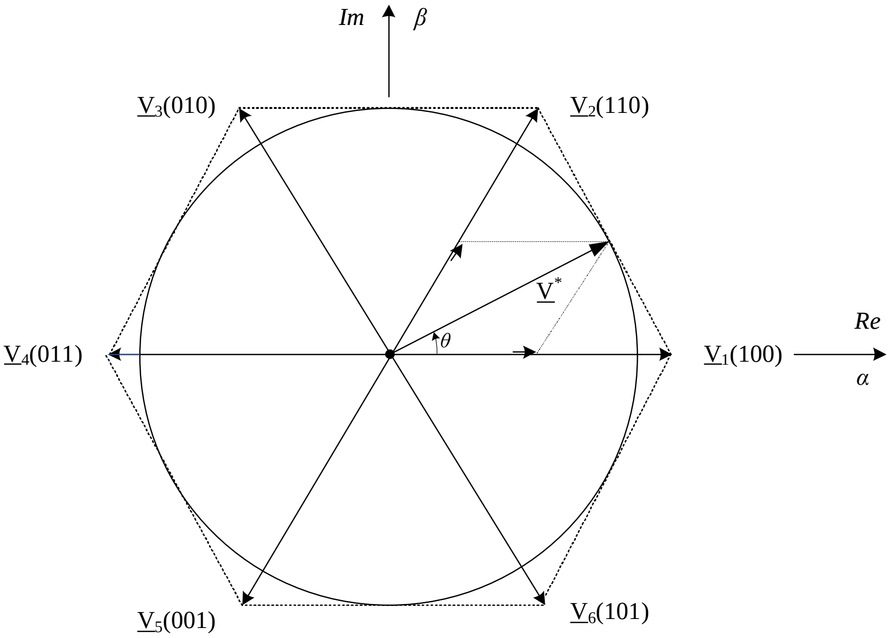

Fig. 3.8 Basic voltage vectors of the source inverter

To guarantee that both power devices in an inverter leg never conduct simultaneously, a small delay time, Td, called dead time, is added to the gate signal of the turning-on device, Fig. 3.9. This delay introduces some distortions in the output voltage. Since the delay occurs in every PWM cycle, the magnitude of distortion grows in inverse proportion to the fundamental frequency. The voltage distortion increases with switching frequency also. The Matlab-Simulink implementation of dead time is shown in Fig. 3.19-3.20.

The voltage drop across the power devices, transistors or diodes, is another source of voltage distortion. Depending on the current polarity, the voltage drop on the power devices will add or subtract to the output voltage, Fig. 3.11.
The inverter phase voltage on phase “a”, taking into account the voltage drop, is:

$$\begin{aligned} v_{an} &= v_{aN}^{*} - v_T \quad if \quad v_{aN}^{*} \neq 0 \\ v_{an} &= v_{aN}^{*} + v_D \quad if \quad v_{aN}^{*} = 0 \end{aligned} \tag{3.19}$$

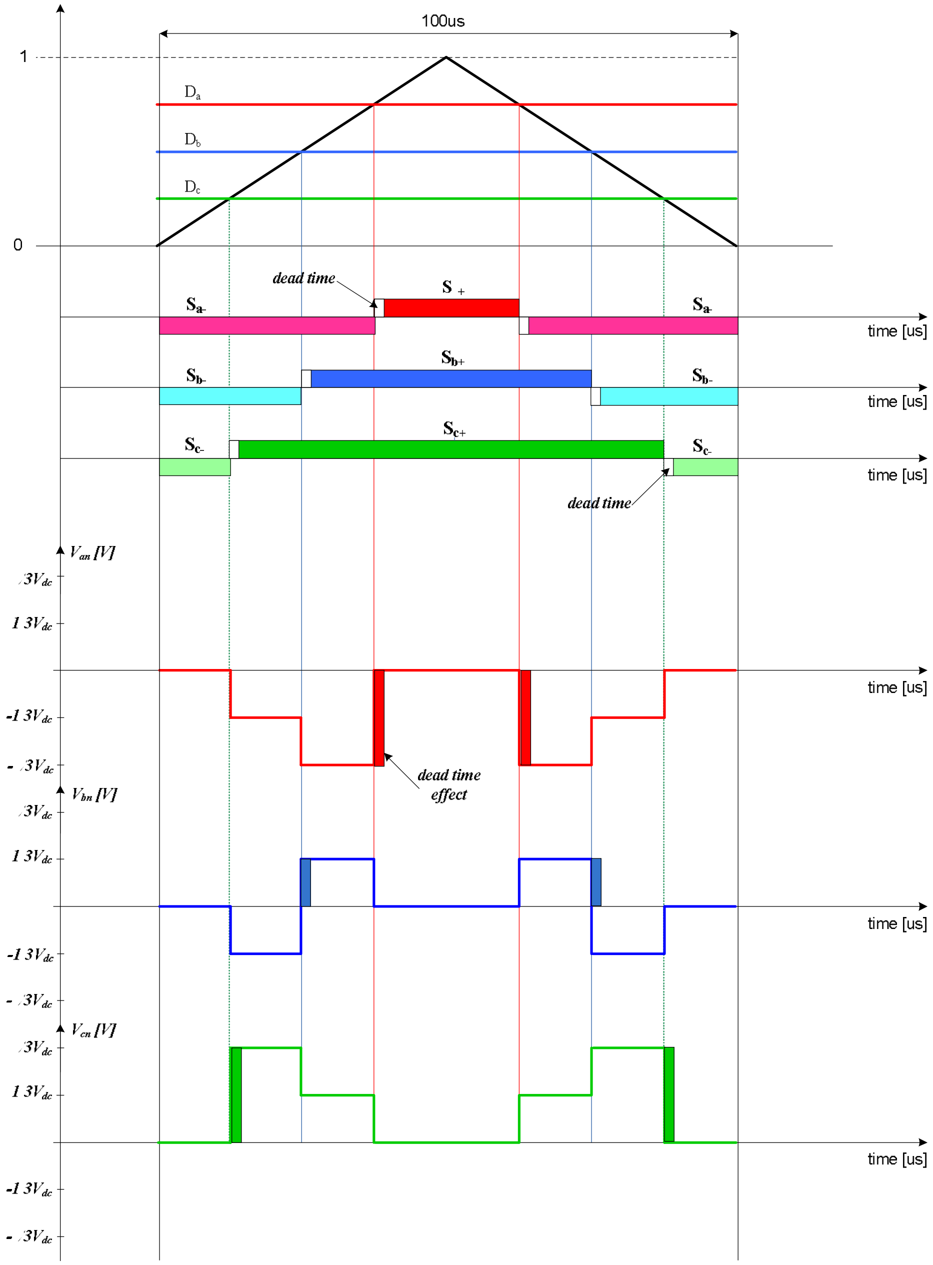

Fig. 3.9 Space vector modulation switching sequence for sector S4 and dead time effect on switching signals and phase voltages

where v_T and v_D are the voltage drops across the transistor and the diode, respectively.

$$v_T = v_{Tth} + r_{ds} \cdot |i_a| \tag{3.20}$$

$$v_D = v_{Dth} + r_{ds} \cdot |i_a| \tag{3.21}$$

where v_{Tth} and v_{Dth} are the threshold voltages and vds and vd are the drain-to-source resistance and diode resistance during on-state, respectively.

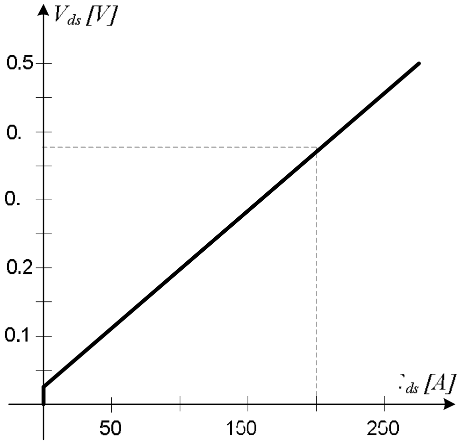

Fig. 3.10 FM200TU-2A (200A, 100V) MOSFET characteristic [3.12]

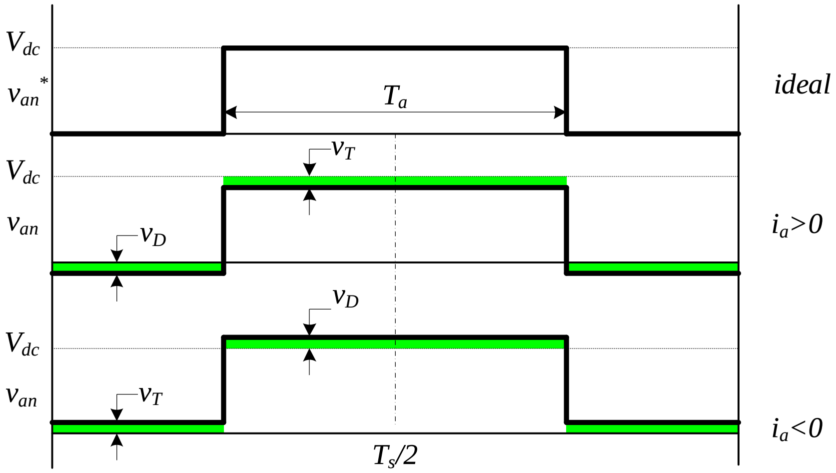

Fig. 3.11 Ideal phase voltage v_{an}^* and real phase voltage van, for $i_a>0$ and $i_a<0$, taking into account the power devices voltage drop, v_T and v_D

The influence on the dead time over the current distortion is shown in Figs. 3.12-3.15. The load consists of BEGA (with rotor blocked) circuit having the stator resistance *R=1Ω*. The input voltages are $v_{d\_ref}=2V$, $v_{q\_ref}=0V$ for the first case and for the second case $v_{d\_ref}=20V$, $v_{q\_ref}=0V$. The simulation results, clearly, illustrates that the voltage/current distortion is high at low reference voltages. For the second case the, where the current magnitude is “high”, the current distortion is not obvious. In conclusion the current distortions increase with reference voltage decreasing, dead-time increasing and switching frequency increasing.

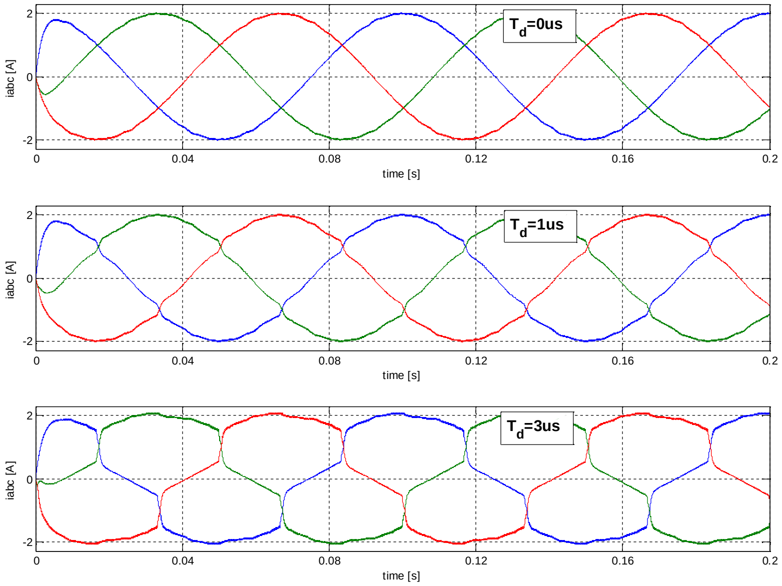

Fig. 3.12 Dead time effect on the phase currents waveform (v_d^*=2V, v_q^*=0V, rs=1Ω) - from top to bottom: T_d=0, T_d=1us, T_d=3us

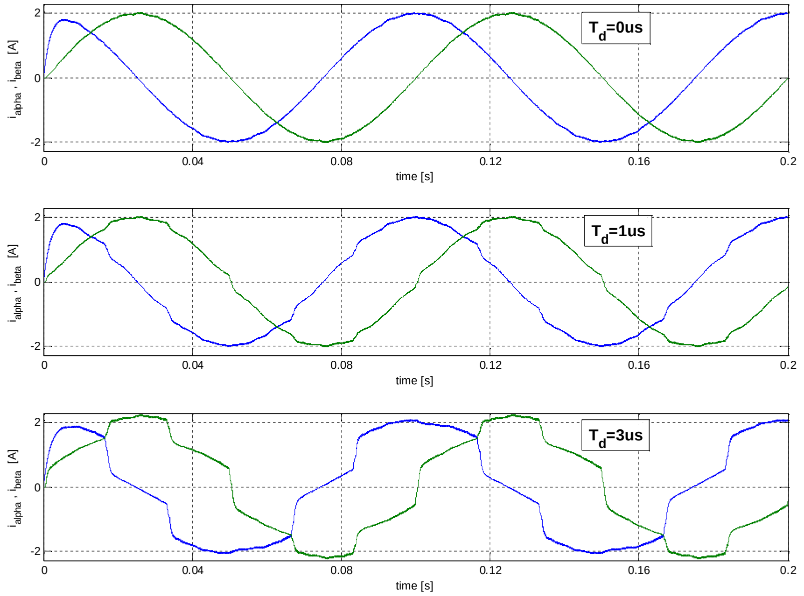

Fig. 3.13 Dead time effect on the current vector components (i_α, i_β) waveform ($v_d^*=2V$, $v_q^*=0V$, , $r_s=1\Omega$) - from top to bottom: $T_d=0$, $T_d=1us$, $T_d=3us$

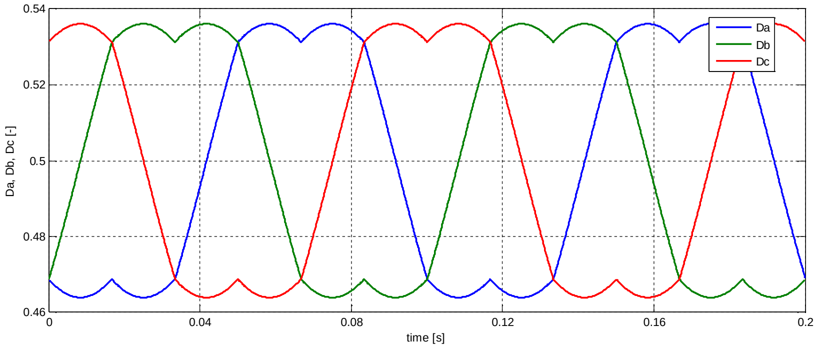

Fig. 3.14 D_a, D_b, D_c for simulation results shown in Fig. 3.13, Fig. 3.14

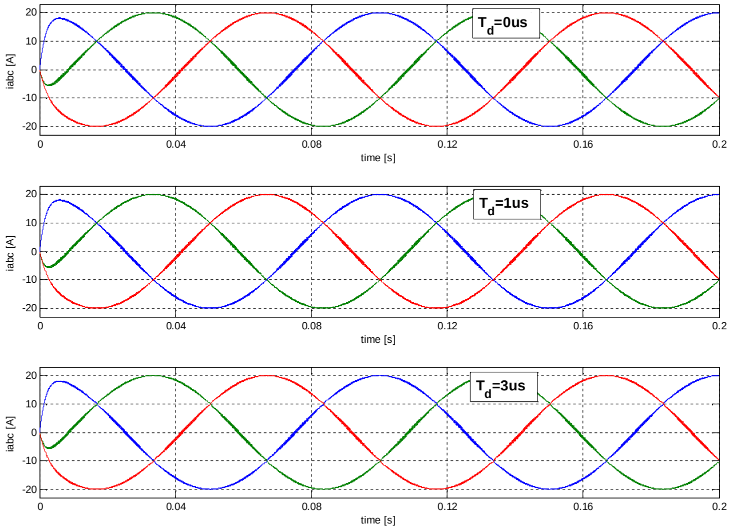

Fig. 3.15 Dead time effect on the phase currents waveform ($v_d^*=20V$, $v_q^*=0V$, , $r_s=1\Omega$) - from top to bottom: $T_d=0$, $T_d=1us$, $T_d=3us$

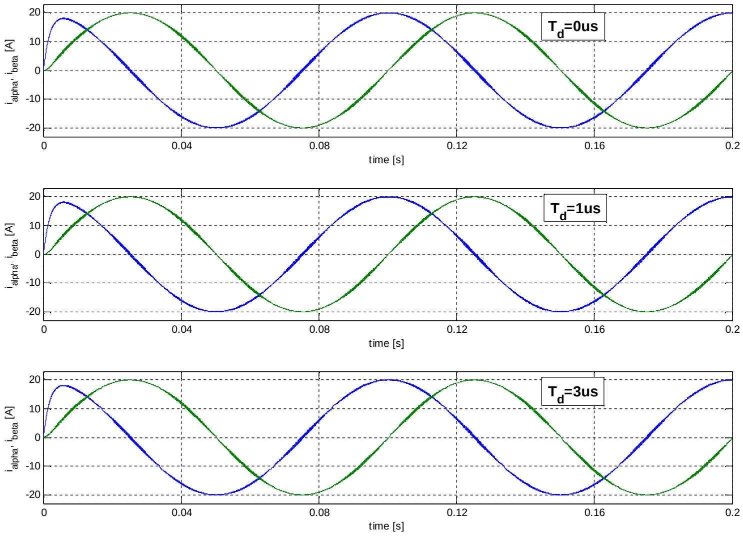

Fig. 3.16 Dead time effect on the current vector components (i_α, i_β) waveform ($v_d^*=20V$, $v_q^*=0V$, , $r_s=1\Omega$) - from top to bottom: $T_d=0$, $T_d=1us$, $T_d=3us$

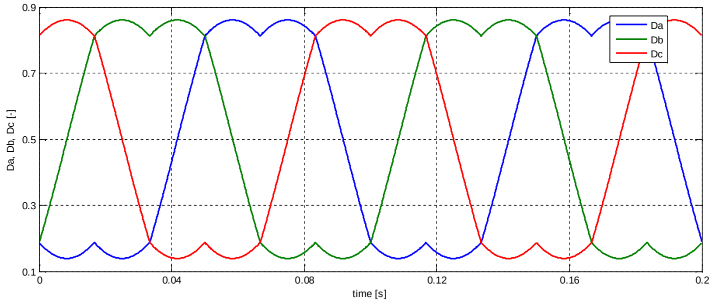

Fig. 3.17 D_a, D_b, D_c for simulation results shown in Fig. 3.14, Fig. 3.15

In Fig. 3.18 is presented a top view of the inverter model. The inputs are v_d, v_q and rotor electrical position, dc-link voltage and the outputs are the phase voltages v_a, v_b, v_c and their correspondences in rotor reference frame. Electrical position is needed only for coordinate's transformation. The space vector modulation block input are the stator voltage in stator coordinates and the outputs are the duty cycle D_a, D_b, D_c.

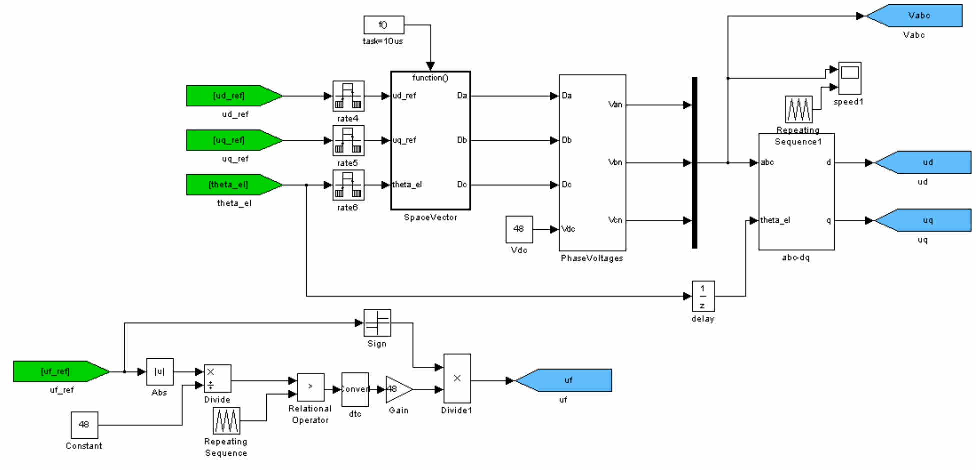

Figure. 3.18. Overview of the inverter model implementation

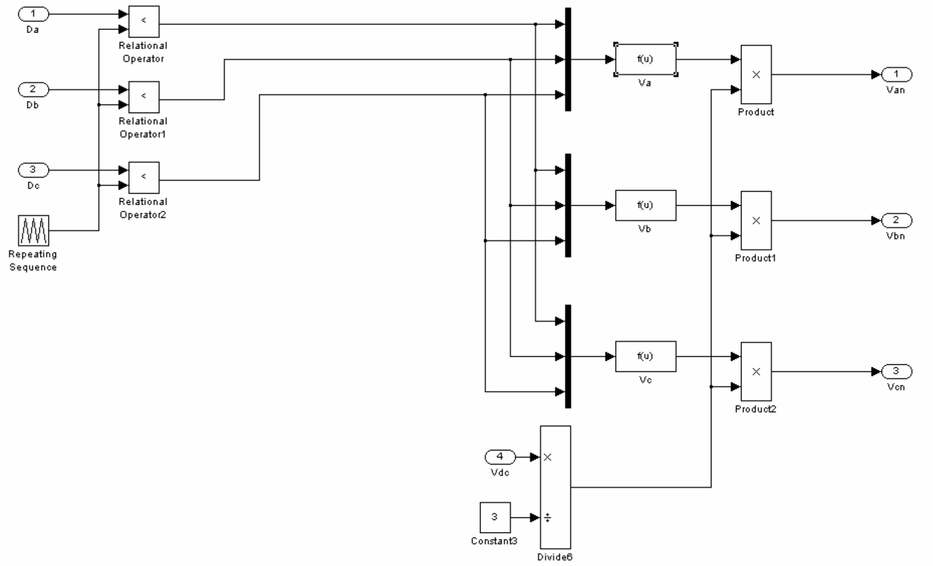

Figure. 3.19. Phase voltage generation from duty cycles

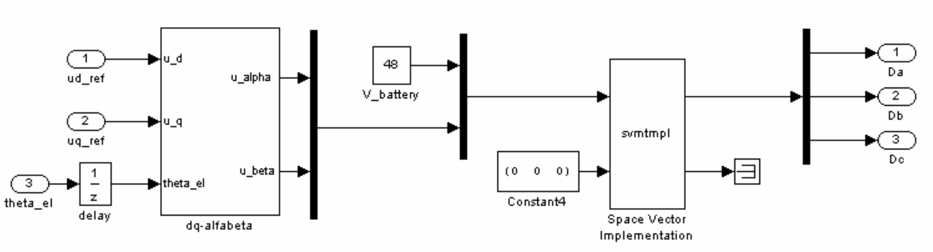

Figure 3.20. Space vector implementation

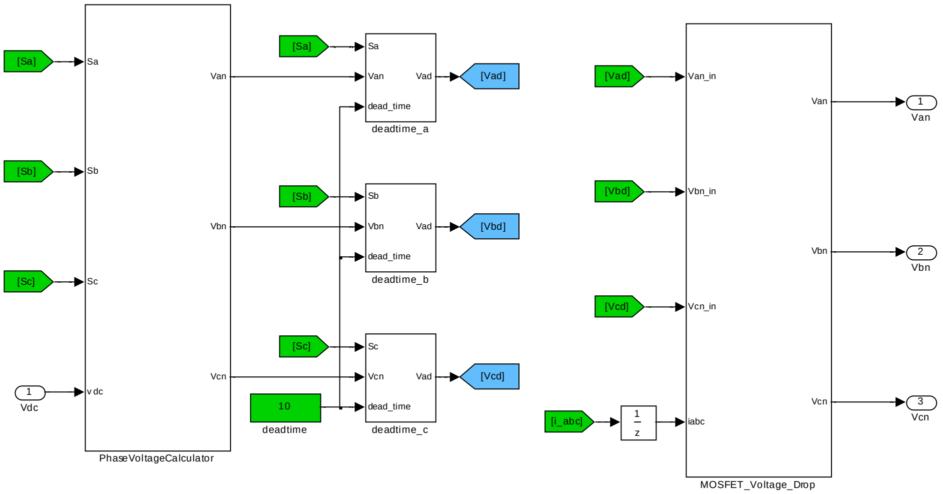

Fig. 3.21. Inputs/outputs of dead time and MOSFET voltage drop model

In Fig. 3.21 the dead time is expressed in microsecond multiplied by a factor of 10 due to *100ns* simulation step (*1us=10x100ns*).

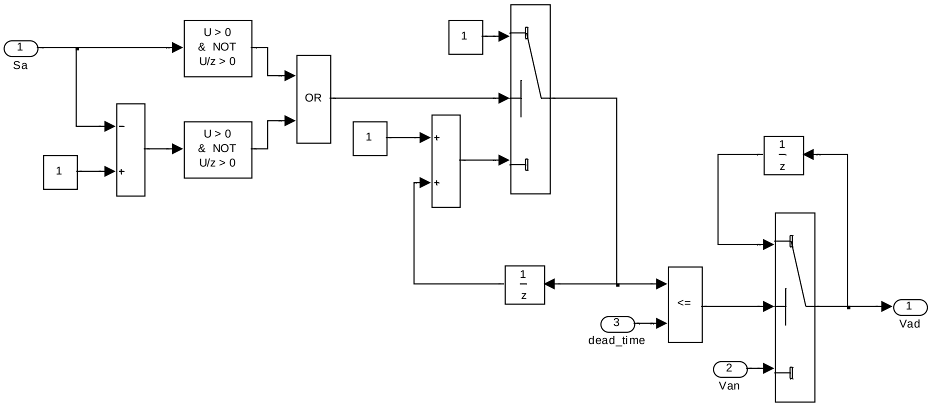

Fig. 3.22 Dead time implementation model for phase "a"

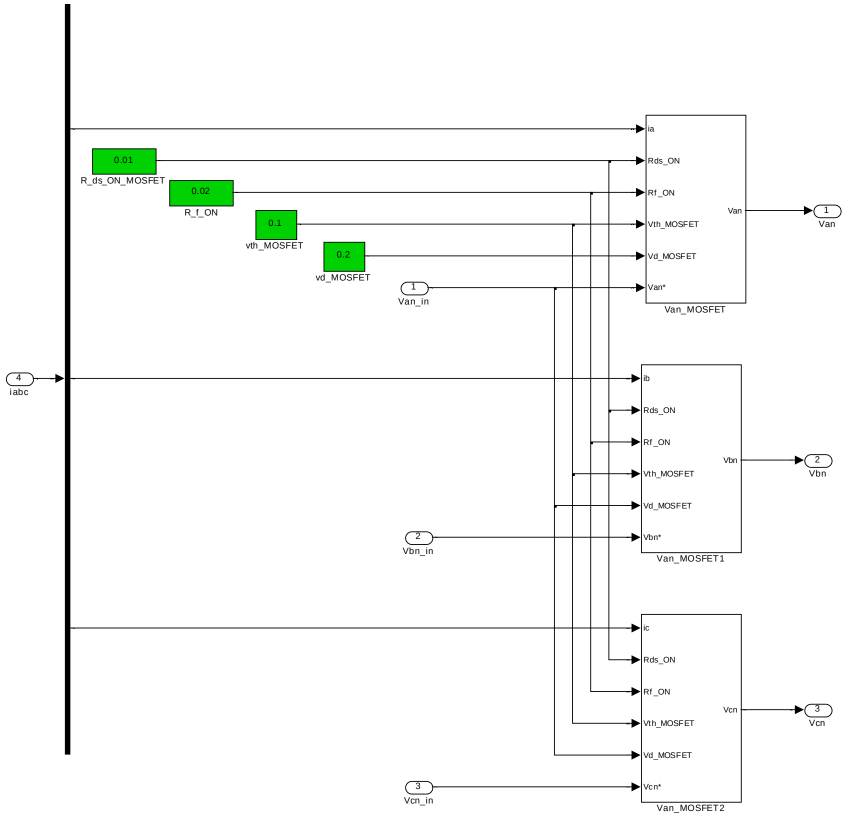

Fig. 3.23. Inputs/outputs of MOSFET voltage drop model

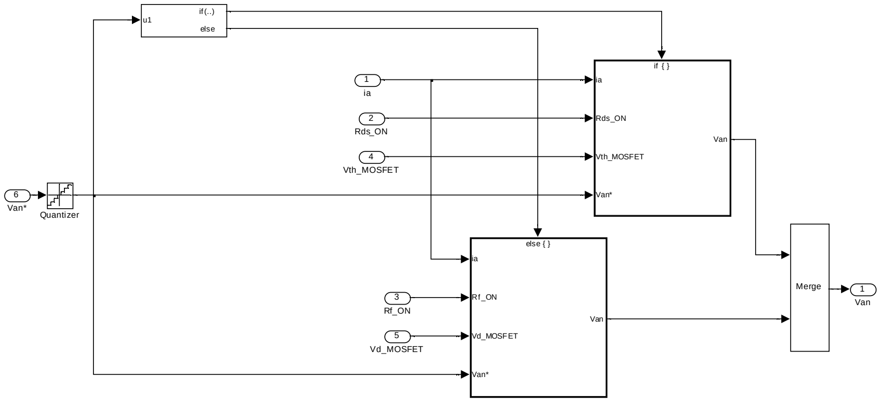

Fig. 3.24. Voltage drop on MOSFET calculator – first level of view

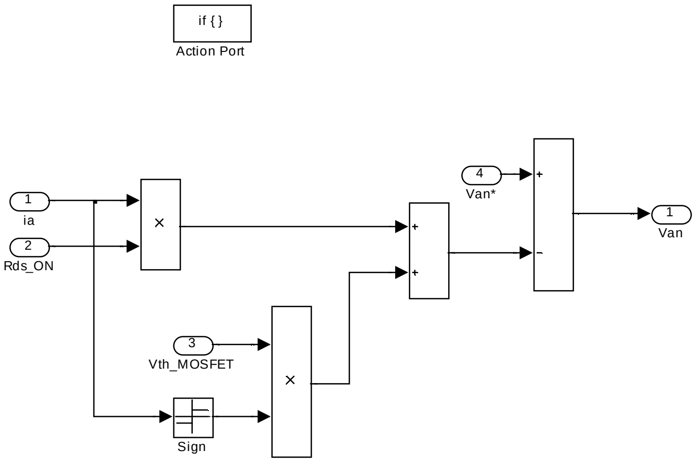

Fig. 3.25. Voltage drop on MOSFET calculator – second level of view ($v_{an}^{*}<>0$)

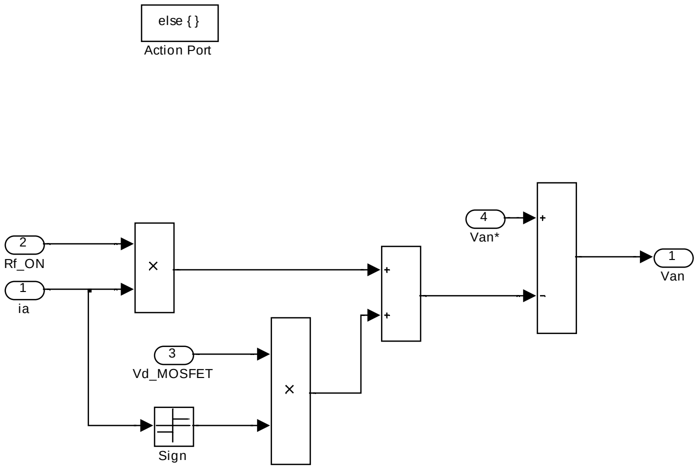

Fig. 3.26. Voltage drop on MOSFET calculator – second level of view ($v_{an}^{*}=0$)

The maximum sinusoidal phase voltage is given by the equation (3.22):

$$v_1 = \frac{2}{3} V_{dc} \qquad (3.22)$$

The maximum sinusoidal phase voltage is given by the equation (3.23):

$$V_{s\_peak} = \frac{\sqrt{3}}{2} V_1 = \frac{\sqrt{3}}{2} \cdot \frac{2}{3} V_{dc} \tag{3.23}$$

In the linear modulation range, the RMS phase voltage is:

$$V_{s\_RMS} = \frac{1}{\sqrt{3}} \cdot \frac{1}{\sqrt{2}} V_{dc} = \frac{1}{\sqrt{6}} V_{dc} \tag{3.24}$$

For a value of 48Vdc for dc-link voltage the phase voltage for sinusoidal voltage (current) the peak value is 27.71V, while the RMS value is $V_{s\_RMS}=19.6V$.
The relationship between V_d, V_q and V_s is:

$$V_s = V_{s\_peak} = \sqrt{V_d^2 + V_q^2} \tag{3.25}$$

To validate the inverter model, a simulation was run. The inputs of the systems were v_d and v_q voltage. The stator resistance of BEGA was set to 1Ω in order to have a ratio of 1 between phase voltage and phase current. The reference peak voltage was set of $V_s=25V$ $(V_d=25V,\ V_q=0V)$, $30V$ $(V_d=30V,\ V_q=0V)$, $35V$ $(V_d=35V,\ V_q=0V)$. The simulation results, showing the phase currents, duty cycle and reference voltage, are presented in Fig. 3.27. It is obvious, from Fig. 3.27, that for 25V (<27.71V) the phase current are sinusoidal. For 30V (>27.71V) reference voltage, the currents waveform distortion is visible, while for 35V the currents distortion is more significant.

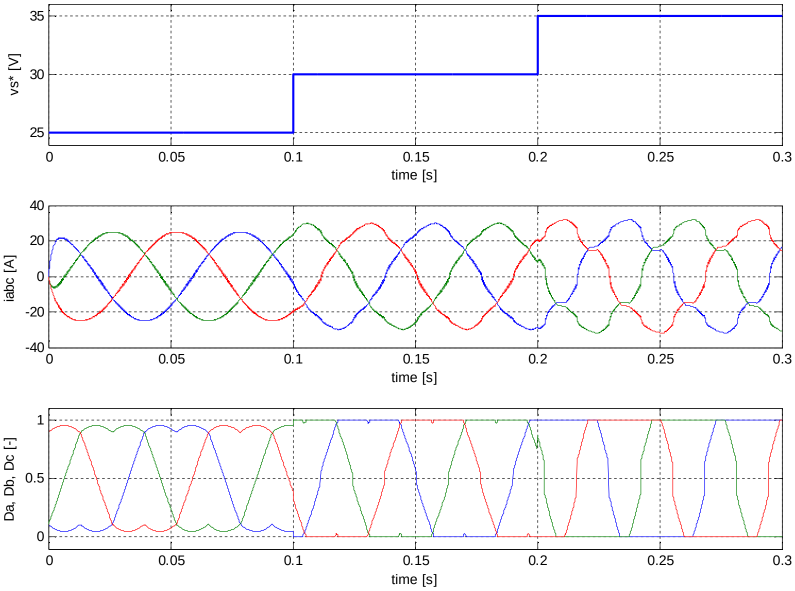

Fig. 3.27. Phase currents and duty cycle waveform for phase voltage reference $v_s^*=25V$, $v_s^*=30V$, $v_s^*=35V$

C. BEGA DC-DC Converter model

The converter used to supply BEGA dc excitation is a four quadrant dc-dc converter (Fig. 3.28). In general the converter operates in I and III quadrant, when $i_f>0$ and the total voltage on the excitation is lower than dc voltage and when $i_f<0$ and the total voltage on the excitation is lower than dc voltage, respectively. Sometimes it might be that the induce voltage is high enough that the dc excitation current flows back into the battery. This way the converter will operate in II and IV quadrant.

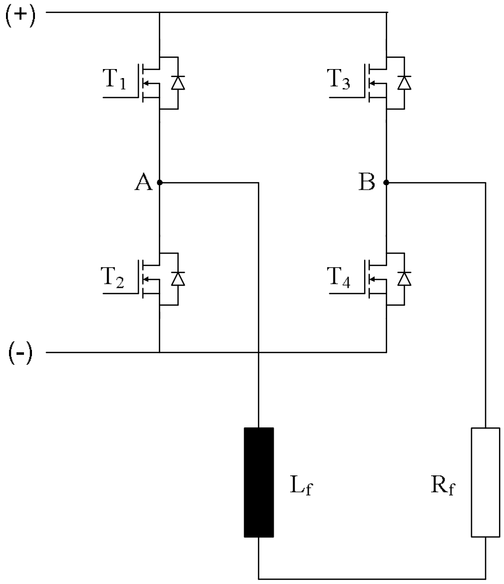

Fig. 3.28. 4-Quadrant DC-DC excitation converter

The operating principle of the converter is shown in Fig. 3.29. Over one switching period all the MOSFET are conducting, but only one pair of MOSFETs are open at a certain time. For positive voltage T1,T4 are open and for negative voltage T2,T3 are open. The dc excitation voltage is the average between positive and negative voltages that supplies the excitation. For zero reference voltage each MOSFETs pair is conduction 50% of the switching period. For fully positive voltage only T1,T4 are conducting over one cycle. For fully negative voltage only T2,T3 are conducting. Consequently, the relationship between the commanded dc excitation voltage and duty cycle is not proportional, but it is linear and symmetric in respect of the half of period.

The relationship between reference dc excitation voltage (v_f^*), duty cycle (D_x) and dc-link voltage (Vdc) is:

$$v_f^* = D_x \cdot V_{dc} + (1 - D_x) \cdot (-V_{dc}) = V_{dc} \cdot (2D_x - 1) \qquad (3.26)$$

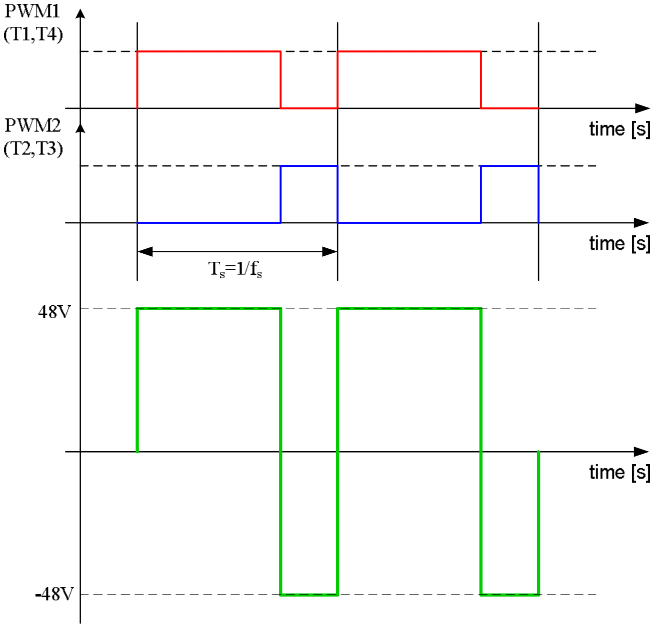

Fig. 3.29. DC-DC converter voltage synthesis (duty cycle=70%)

The duty cycle necessary to achieve the reference voltage (v_f^*) becomes:

$$D_x = \frac{v_f^* + V_{dc}}{2 \cdot V_{dc}} \tag{3.27}$$

The Matlab-Simulink implementation of the dc-dc converter is given in Fig. 3.30. The duty cycle is calculated according equation (3.27) and the compared with a triangular signal. For values of duty cycle higher than the triangular signal the output of the converter is the positive dc voltage (+V_{dc}), while for lower values of duty cycle the output of the converter is negative dc voltage (-Vdc).

In contrast to the three-phase converter model, the dead time and voltage drop on the power devices are not modeled, since their effect is not significant, taking into account a switching period of *500us* for dc-dc converter. During dc current regulation the converter voltage nonlinearities does not affect the current waveform – the only thing is that the reference voltage will be a bit higher/smaller than the ideal case.

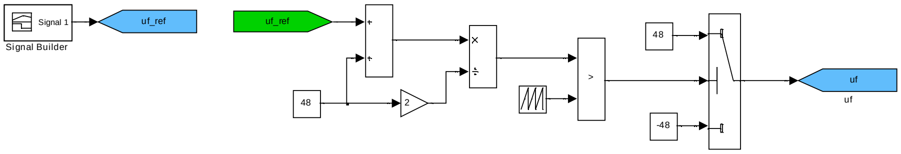

Fig. 3.30. DC-DC excitation converter model

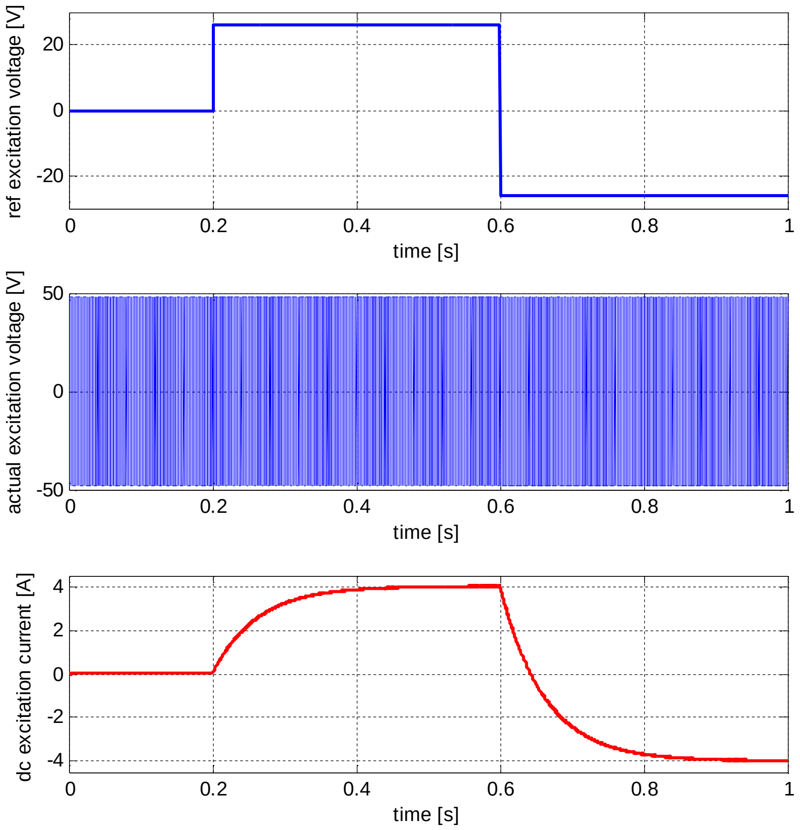

Fig. 3.31. Simulation results for $v_f^*=0$ (time<0.2s), $v_f^*=26V$ (0.2s<time<0.6s), $v_f^*=-26V$ (time>0.6s)

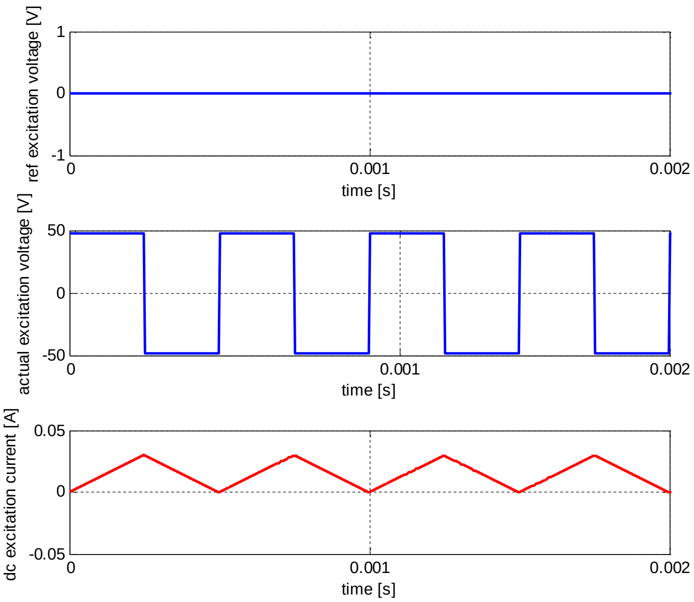

Fig. 3.32. Zoom on Fig. 3.4

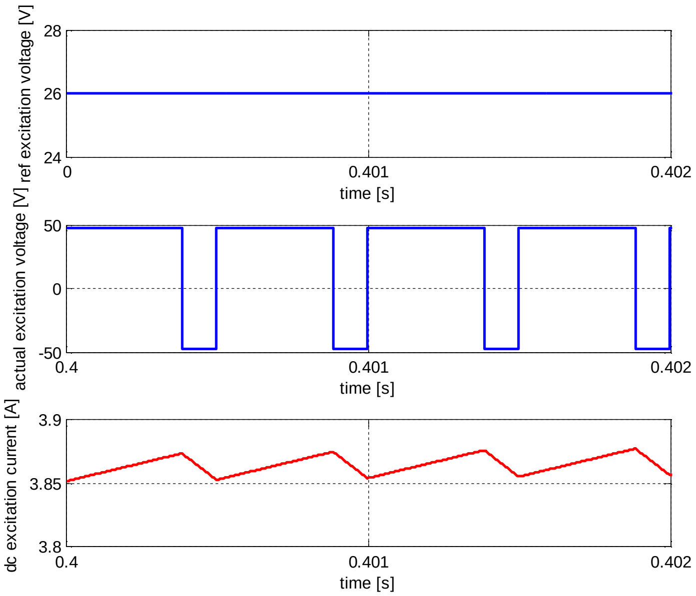

Fig. 3.33. Zoom on Fig. 3.31

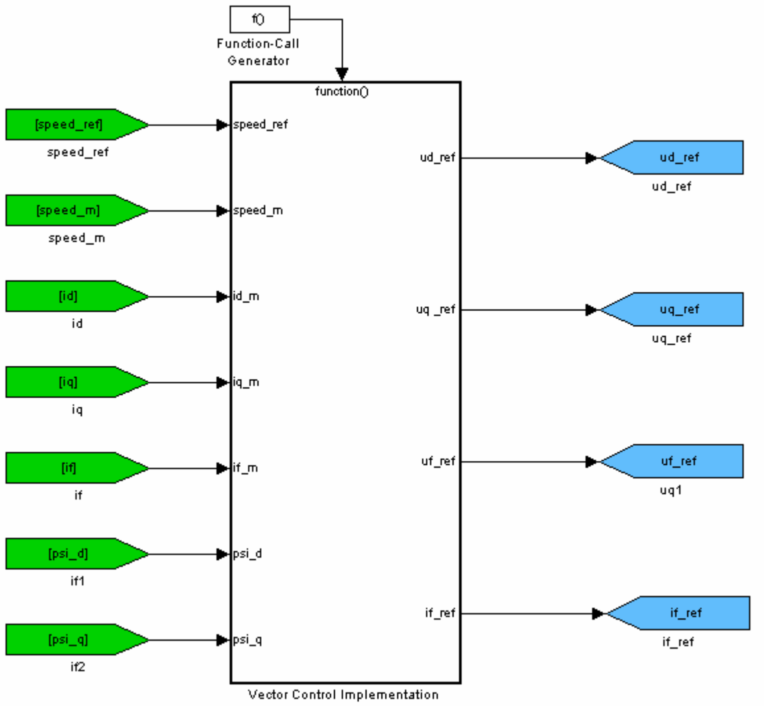

Fig. 3.34. Vector Control overview – inputs and outputs

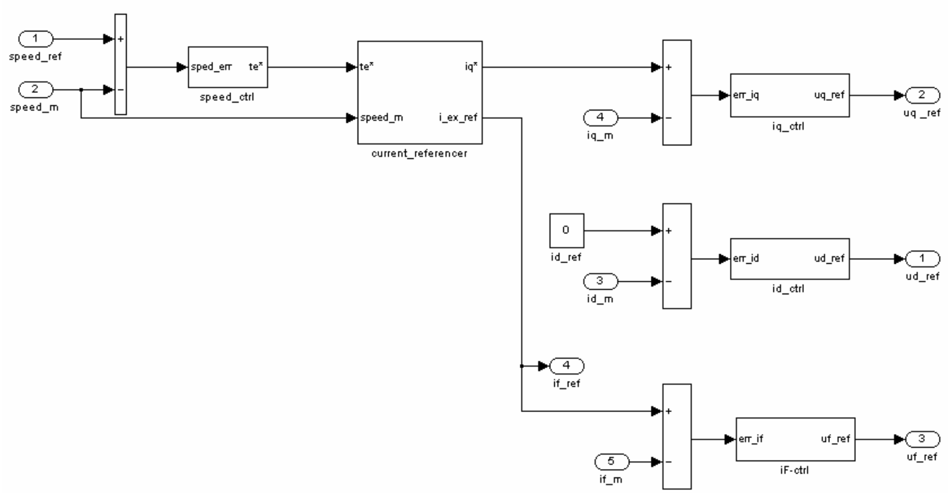

Figure 3.35 Vector Control structure

D. Stimuli

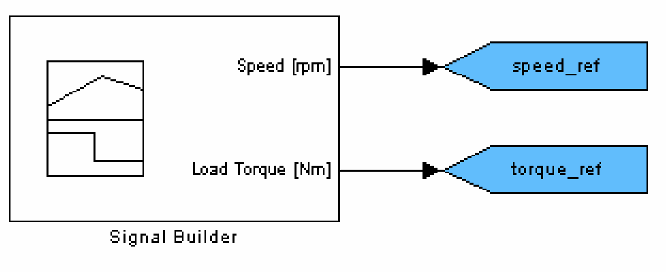

Fig. 3.36. The content of stimuli block

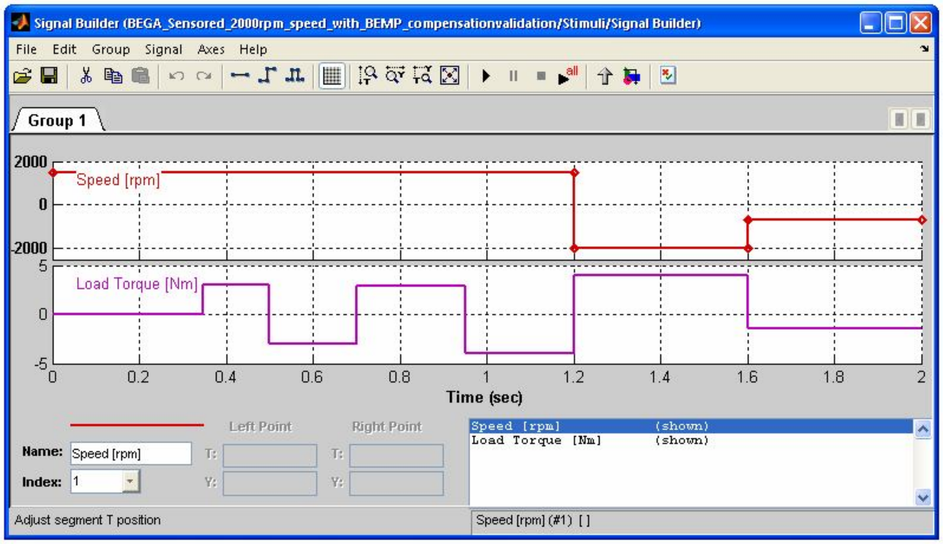

Name: Speed [rpm]

Index: 1

```
Speed [rpm]          (shown)
Load Torque [Nm]     (shown)
```

Adjust segment T position

Speed [rpm] (#1) [ ]

Fig. 3.37. The content of Signal Builder from stimuli block

3.4 Simulation results

3.4.1 Current controller's validation

After implementation and validation of BEGA dq model and three-phase inverter model, the validation of i_d, i_q and i_f current controllers is performed. All three controllers are PI controllers having the structure from Fig. 3.38 and the transfer function given by the equation (3.28):

$$H(s) = K_p \cdot \left(1 + \frac{K_i}{s}\right) = K_p \cdot \left(1 + \frac{1}{sT_i}\right) \qquad (3.28)$$

The i_d, i_q current controllers are implemented in rotor coordinates reference frame. For validation of current controllers design and parameters, the step response is analyzed. The complete speed/position loop is disabled (rotor blocked), so that no disturbance affects the system behavior. The current responses for all three current controllers are shown in Fig. 3.39. The values of PI controller parameters, for the responses shown in Fig. 3.39 are: $K_{p\_id}=2$, $T_{i\_id}= 0.05$; $K_{p\_iq}=2$, $T_{i\_iq}= 0.0167$; $K_{p\_if}=20$, $T_{i\_if}= 0.1$. The controller's parameters values are similar to those used in the experimental setup.

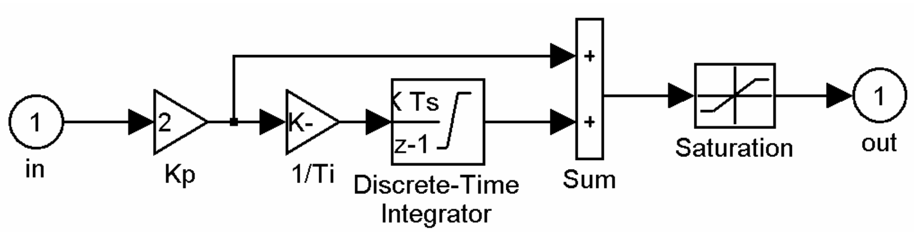

Fig. 3.38. Matlab-Simulink implementation of current controllers

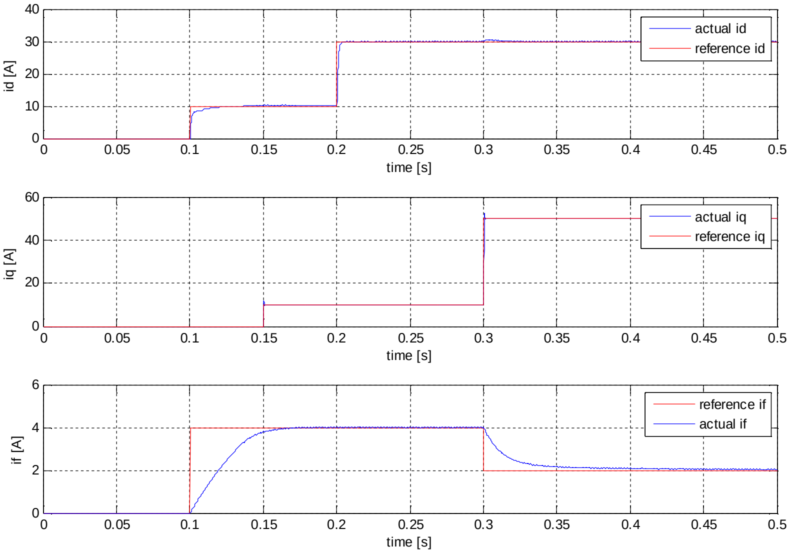

Fig. 3.39. Simulation of id, iq and if current response

3.4.2 Speed controller validation

The speed controller is a PI type with anti-windup loop. The Simulink implementation is shown in Fig. 3.40. For speed controller validation a set of simulations with different speed and load profiles has been run. Based on simulation results the following values of the controller parameter are considered to be valid: $K_{p\_w}=0.03$, $T_{i\_w}= 0.077$; $K_{AW\_w}=120$. The first criterion for speed controller was that no overshoot is desired. This condition was entirely fulfilled since no speed overshoot is recorded in the simulation results. The parameters are a good compromise between no overshoot, time response and disturbance rejection. Note that for speed controller validation no back-EMF compensation is used.

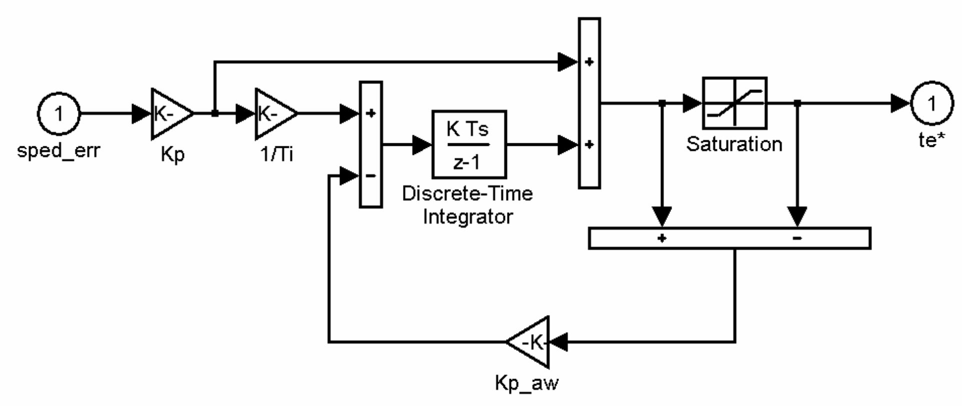

Fig. 3.40. Matlab-Simulink implementation of speed controller

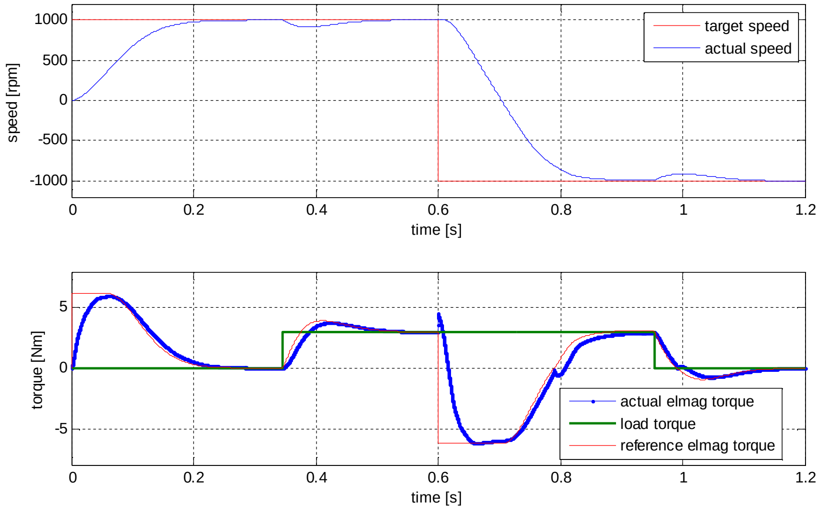

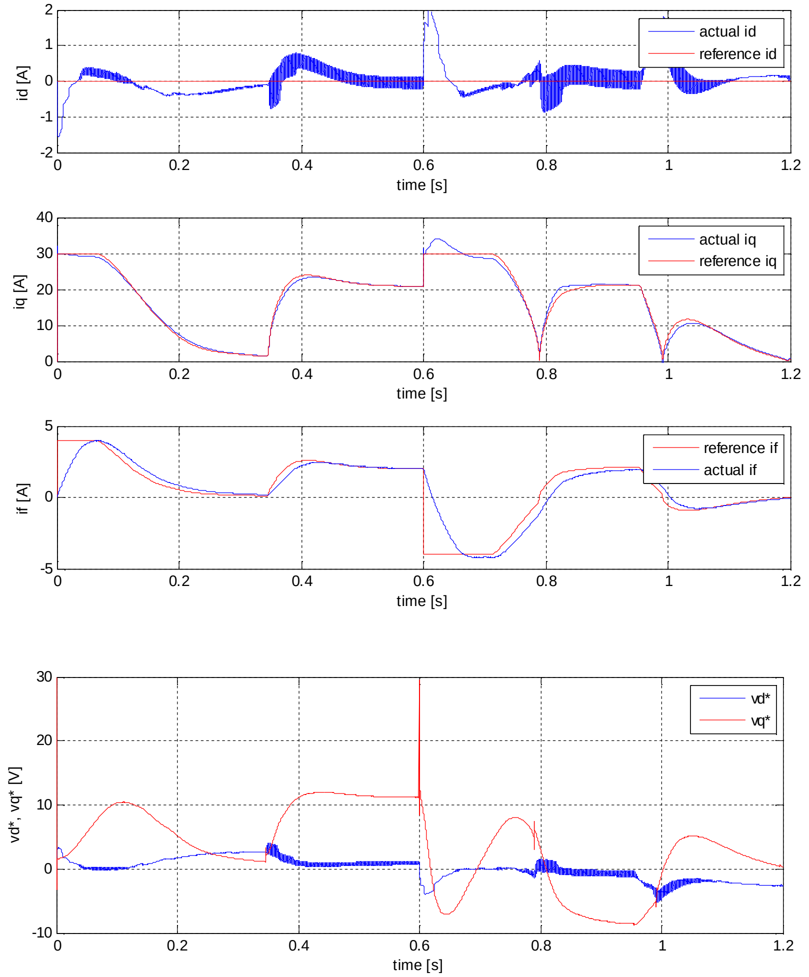

Fig. 3.41. Simulation of speed step response with/without load –from top to bottom: a) reference and actual mechanical speed, b) reference, load and electromagnetic torque, c) i_d, i_q, i_f currents, d) v_d^*, v_q^*

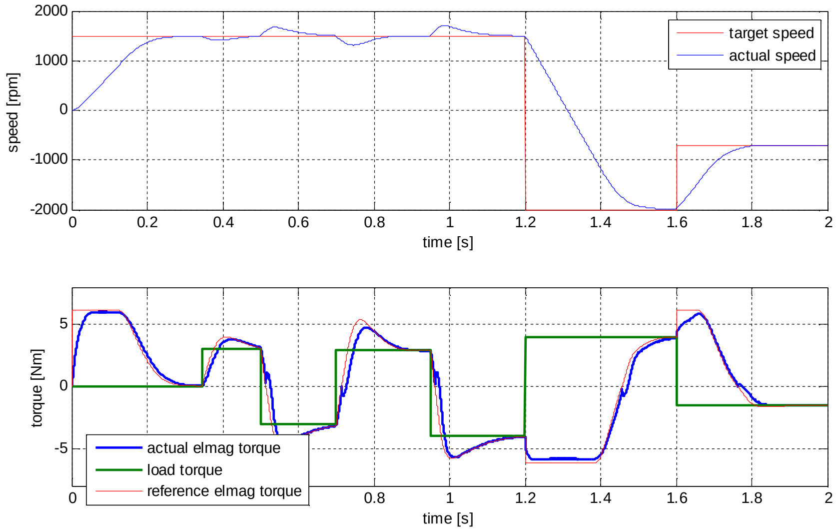
speed [rpm]
2000
1000
0
-1000
-2000
target speed
actual speed
0
0.2
0.4
0.6
0.8
1
1.2
1.4
1.6
1.8
2
time [s]
torque [Nm]
5
0
-5
actual elmag torque
load torque
reference elmag torque
0
0.8
1
1.2
1.4
1.6
1.8
2
time [s]

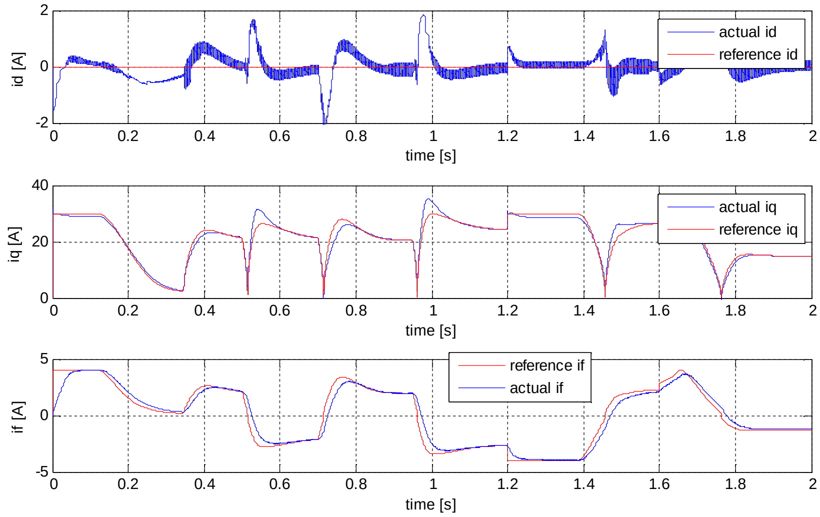
id [A]
2
0
-2
actual id
reference id
0
0.2
0.4
0.6
0.8
1
1.2
1.4
1.6
1.8
2
time [s]
iq [A]
40
20
0
actual iq
reference iq
0
0.2
0.4
0.6
0.8
1
1.2
1.4
1.6
1.8
2
time [s]
if [A]
5
0
-5
reference if
actual if
0
0.2
0.4
0.6
0.8
1
1.2
1.4
1.6
1.8
2
time [s]

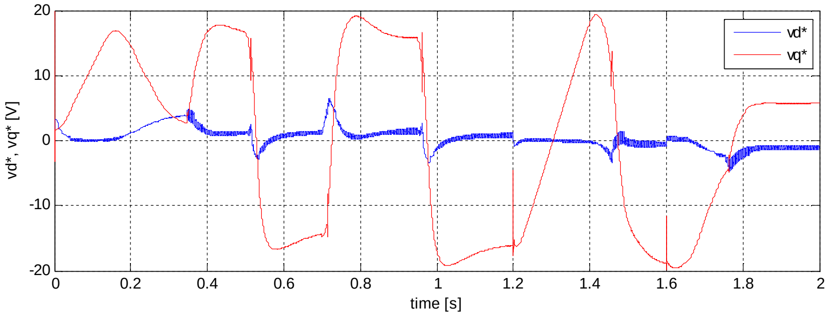

Fig. 3.42. Simulation of speed step response with/without load –from top to bottom: a) reference and actual mechanical speed, b) reference, load and electromagnetic torque, c) i_d, i_q, i_f currents, d) v_d^*, v_q^*

3.4.3 Back-EMF compensation

After the speed controller validation the back-EMF compensation loop has been added. The scope of the back-EMF compensation is to assure better regulation of the machine currents. With back-EMF compensation the voltage decoupling of d,q circuits is assured. For compensation the electromagnetic machine parameters and dq currents information is needed. In the simulation model, the back-EMF is calculated as a multiplication of electrical rotor speed and dq fluxes “measured” in the machine (instead of calculation the dq fluxes based on measured current and electromagnetic parameters of the machine) – this way the computation time is reduced a bit.

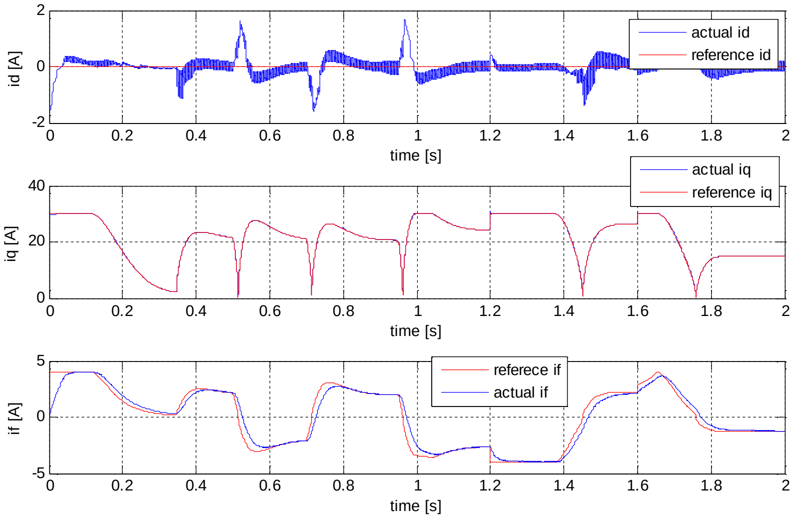

Fig. 3.43. Reference and actual id, iq, if currents with back-EMF compensation

Simulation results for the speed/torque profile from Fig. 3.42 are shown in Fig. 3.43 only dq current are shown since the influence on the machine dynamic is minimum for the given profile. The highest impact of back-EMF compensation is on iq current, while for id current the effect is not so visible. To see the effect i_d, i_q currents from Fig. 3.42 and Fig. 3.43 has to be compared. It is obvious from Fig. 3.43 that the actual iq current follows very well its reference demonstrating the effectiveness of back-EMF loop on current regulation.

3.4.4 Unity power factor operation

Unity power factor operation of electrical machines (used in HEV) is desired since it has a direct impact over the three-phase inverter design (lower cost, lower volume, etc). With conventional vector control permanent magnet synchronous machine can operate at unity power factor operation only in arbitrary operating points. Induction machine requires reactive power for operation – thus its power factor is inherently poor. Doubly-fed induction machine can operate at unity power factor if it is magnetized from the rotor with a second converter (source voltage). BEGA has the unique property of being capable of unity power factor operation over the whole speed/torque range for both motoring and generating. Two conditions must be fulfilled: $i_d=0$ and $\psi q=L_q i_q-\psi_{PM}=0$. The consequence of these two conditions is that the iq current has to be maintain at the critical value I_{qk} and the dc field current to be controlled. The vector control structure for unity power factor operation is shown in Fig. 3.44. The simulation results are given in Fig. 3.45. A target speed of 100rpm is set for a time period of 1.2s. The load torque is increased step by step to 1Nm (time=0.35s), 3Nm (time=0.5s), 5Nm (time=0.7s). After 1.2s until 1.6s the target speed is set to 3000rpm. After time=1.6s the reference speed is set to 700rpm and the load torque is -2Nm. With such profile the whole torque and speed range is almost covered for both motoring and generating. It is obvious from the Fig. 3.45 the unity power factor operation is achieved. During transients the power factor is very slightly below unity due to non-zero id current.

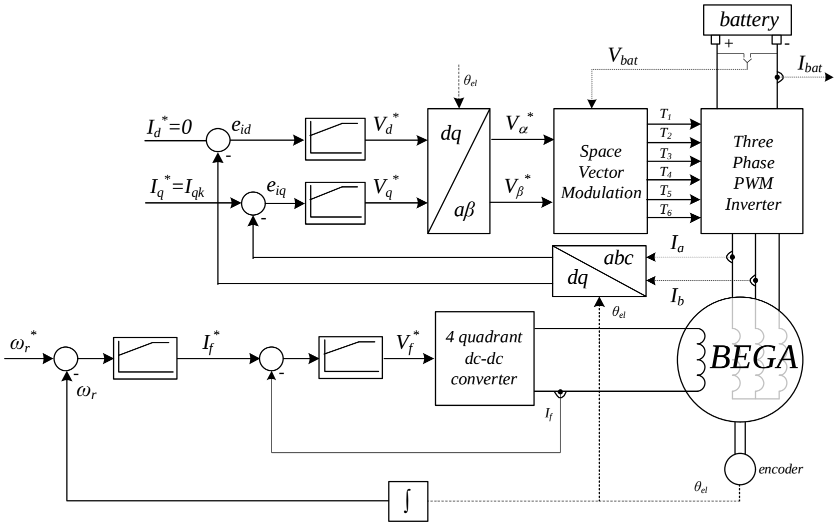

Fig. 3.44. BEGA vector control structure at unity power factor operation

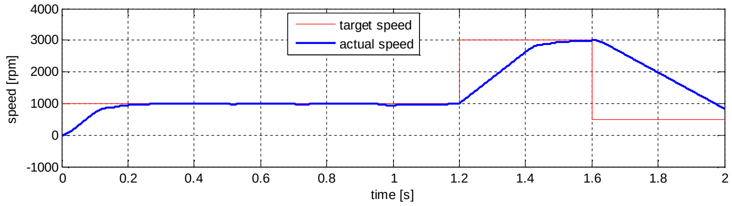
target speed
actual speed
speed [rpm]
4000
3000
2000
1000
0
-1000
0
0.2
0.4
0.6
0.8
1
1.2
1.4
1.6
1.8
2
time [s]

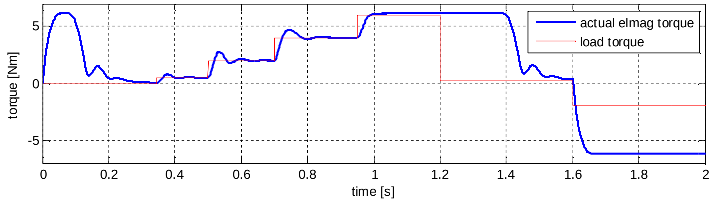
actual elmag torque
load torque
torque [Nm]
5
0
-5
0
0.2
0.4
0.6
0.8
1
1.2
1.4
1.6
1.8
2
time [s]

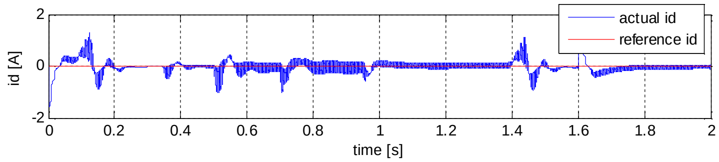
actual id
reference id
id [A]
2
0
-2
0
0.2
0.4
0.6
0.8
1
1.2
1.4
1.6
1.8
2
time [s]

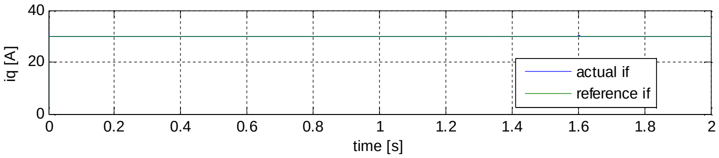
actual if
reference if
iq [A]
40
20
0
0
0.2
0.4
0.6
0.8
1
1.2
1.4
1.6
1.8
2
time [s]

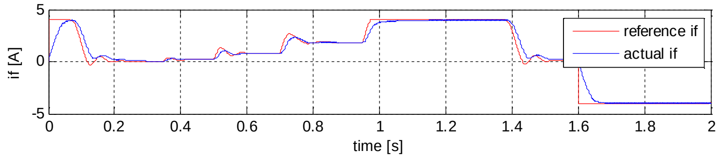
reference if
actual if
if [A]
5
0
-5
0
0.2
0.4
0.6
0.8
1
1.2
1.4
1.6
1.8
2
time [s]

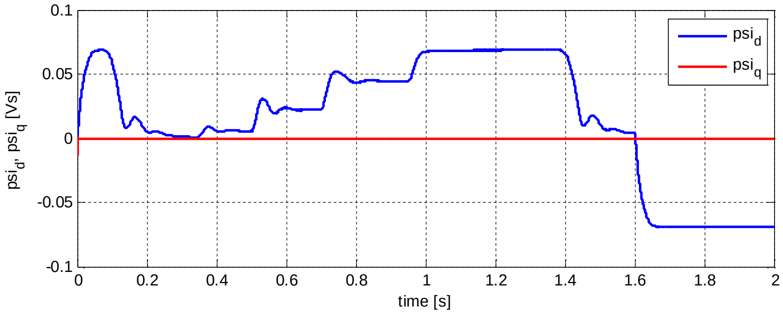
psi_d
psi_q
psi_d, psi_q [Vs]
0.1
0.05
0
-0.05
-0.1
0
0.2
0.4
0.6
0.8
1
1.2
1.4
1.6
1.8
2
time [s]

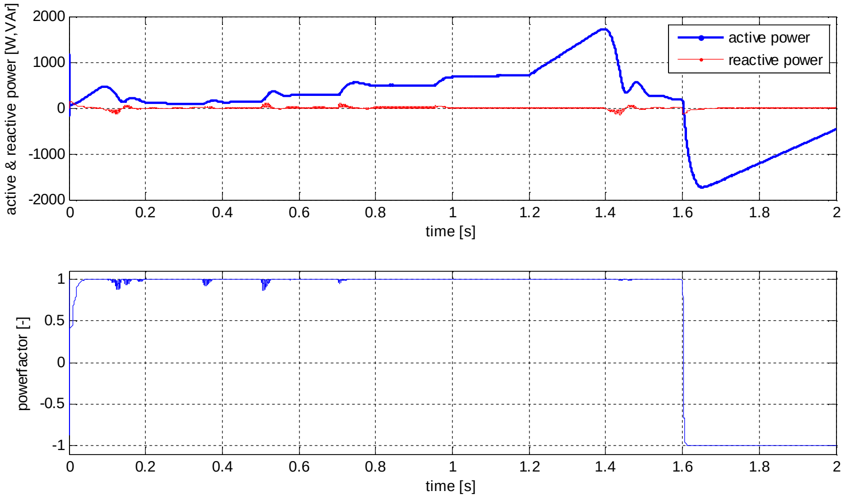

Fig. 3.45. Simulation of BEGA at unity power factor operation – from top to bottom: target and actual speed, load and electromagnetic torque, i_d, i_q, i_f currents, d,q axis flux (Ψ_{dq}), active and reactive power, power factor

SUMMARY

This chapter deals with the development of a detailed Matlab-Simulink simulation environment for BEGA operation investigation. A simulation model for BEGA, three-phase inverter, dc-dc converter and control algorithm has been built. BEGA simulation model is based on dq equations. The three-phase inverter model takes into account the dead time effect and voltage drop on the transistors. Simulation results are given to see the effect of dead time over the phase currents distortions. The speed and current controllers tuning based on simulation results. The benefit of back-emf compensation and unity power factor operation are analyzed through simulations.

REFERENCES

[3.1] W. L. Soong, N. Ertugrul, E. C. Lovelace, and T. M. Jahns, “Investigation of interior permanent magnet offset-coupled automotive integrated starter/alternator,” in Conf. Rec. 2001 IEEEIAS Annu. Meating, Chicago, IL, Oct. 2001, vol. 1, pp. 429–436.

[3.2] I. Boldea, “Starter/alternator systems for HEV and their control: A review,” KIEE Int. Trans. on Electrical Machinery and Energy Conversion Systems, vol. 4-B, no. 4, pp. 157–169, Dec. 2004.

[3.3] J. Kim, J. Jung, and K. Nam, “Dual-inverter control strategy for high-speed operation of EV induction motors,” IEEE Trans. Ind. Electron., vol. 51, no. 2, pp. 312–320, Apr. 2004.

[3.4] K. M. Rahman, B. Fahimi, G. Sureh, A. V. Rajarathnam, and M. Ehsani, “Advantages of switched reluctance motor applications to EV and HEV: Design and control issues,” in Conf. Rec. 1998 IEEE-IAS Annu. Meating, St. Louis, MO, Oct. 1998, vol. 1, pp. 327–334.

[3.5] W. Cai, “Comparison and review of electric machines for integrated starter alternator applications,” in Conf. Rec. 2004 IEEE-IAS Annu. Meating, Seattle, WA, Oct. 2004, vol. 1, pp. 3–7.

[3.6] C. I. Pitic, L. Tutelea, I. Boldea, and F. Blaajberg, “The PM-assisted reluctance synchronous starter/generator (PM-RSM): Generator experimental characterization,” in Proc. OPTIM 2004,Brasov, Romania, May 2004, vol. 2, pp. 275–282.

[3.7] I. Boldea, L. Tutelea, and C. I. Pitic, ”PM-assisted reluctance synchronous motor/generator (PM-RSM) for mild hybrid vehicles: Electromagnetic design,” IEEE Trans. Ind. Appl., vol. 40, no. 2, pp. 492–498, Mar./Apr. 2004.

[3.8] J. A. Tapia, F. Leonardi, and T. A. Lipo, “Consequent-pole permanent-magnet machine with field-weakening capability”, IEEE Trans. Ind. Appl., vol. 39, no. 6, pp. 1704–1709, Nov./Dec.2003.

[3.9] S. Scridon, I. Boldea, L. Tutelea, F. Blaabjerg, and E. Ritchie, “BEGA-A biaxial excitation generator for automobiles: Comprehensive characterization and test results,” IEEE Trans.Ind. Appl., vol. 41, no. 4, pp. 935–944, Jul./Aug. 2005.

[3.10] I. Boldea, E. Ritchie, F. Blaabjerg, S. Scridon, and L. Tutelea, “Characterization of biaxial excitation generator for automobiles,”in Proc. OPTIM 2002, Brasov, Romania, May 2002, vol. 2, pp.371–376.

[3.11] S. Scridon, “BEGA – biaxial excitation generator for automobile”, Ph. D. Thesis, Timisoara, 2002

[3.12] http://www.mitsubishielectric-mesh.com/mesh/power/select%20table/datasheet/MOSFET%20Module/fm200tu-2a_e.pdf

[3.13] J. Holtz, “Pulsewidth Modulation for Power Electronics Conversion”, Proceedings of IEEE, vol. 82, no. 8, Agust 1994, pp 1194-1214.

[3.14] J. Holtz, “Pulsewitdh Modulation – A Survey”, IEEE Transactions on Industrial Electronics, vol. 39, no. 5, Dec. 1992, pp. 410-420.

[3.15] D. Leggate, R. J. Kerkman, “Pulse-Based Dead-Time Compensator for PWM voltage Inverters”, IEEE Trans. On Industrial Electronics, vol. 44, no. 2, April 1997, pp. 191-197

[3.16] A. R. Munroz, T. A. Lipo, “On-Line Dead-Time Compensation Technique for Open Loop PWM-VSI Drives”, IEEE Trans. on Power Electronics, vol. 14, no. 4, July 1999, pp. 683-689

[3.17] J. W. Choi, S. K. Sul, “Inverter Output Voltage Synthesis Using Novel Dead Time Compensation”, IEEE Trans. on Power Electronics, vol. 11, no. 2, March 1996, pp. 221-227

4. BEGA – MOTOR/GENERATOR OPERATION AT UNITY POWER FACTOR

4.1. Introduction

The integrated starter-alternators are being proposed for more electric vehicles [4.1], [4.2] in different configurations: induction-type [4.3], IPM-synchronous type [4.4], [4.5], [4.12] surface PM synchronous type with fractionary stator winding [4.23], PM transverse flux synchronous type [4.24], [4.25] and switched reluctance machine type [4.15]. Besides, the standard claw-pole alternator has been applied on the first commercial mild hybrid automobile (Prius by Toyota) [4.1].

The electric motoring and generating on hybrid-electric vehicles is defined via torque versus speed referencers, triggered by the acceleration/brake paddle driver expectations tempered with the battery state-of-charge. Minimum fuel consumption or minimum pollution optimization criteria may be added to adapt torque-speed referencers to vehicle needs.

Except for cruising control, starter/alternators require basically torque-control and not speed control for vehicle propulsion. When the electric motor drives the air-conditioner, with the engine idle in traffic jams or at stop lights, speed close loop control may be needed. But then, an external speed loop is added. The motoring and generating torque/speed referencers in HEV are characterized by unusually large constant power speed range requirements (up to 10:1) for most cases.

Such a challenging requirement implies both electric machine and inverter oversizing in relation to machine constant power speed range (CPSR). The higher the more the electric machine with multiple flux barrier rotor (high saliency) has been found very suitable for the scope [4.2,4.4,4.5] though the single flux-barrier IPM rotor (low saliency) synchronous machine is used on the main commercial HEV (Toyota Prius 4). The claw-pole alternators has been used for the first commercial mild-HEV [4.1] as it is proven technology (and fits mechanically under the hood) and, for peak stall torque with full magnetization from excitation (rotor), it reduces the peak current by as much as 30%. This way the inverter costs is reduced proportionally. However, the rather high (transverse) inductance of the claw-pole machine reduces its natural constant power speed range.

In an effort to combine the IPM-SM wide constant power speed range ability with the claw-pole machine lower peak current for peak stall torque, the BEGA (biaxial excitation generator for automobiles) has been introduced by these authors [4.17,4.18]. The stator of BEGA is standard-with uniform slots and a three phase winding – while the rotor cross section (Fig. 4.1) is characterized by:

- Salient laminated rotor poles
- Heteropolar d.c. excitation winding (in axis d)
- Multiple flux-barriers in the rotor poles
- Lower cost PMs located in the flux barriers (in axis q)

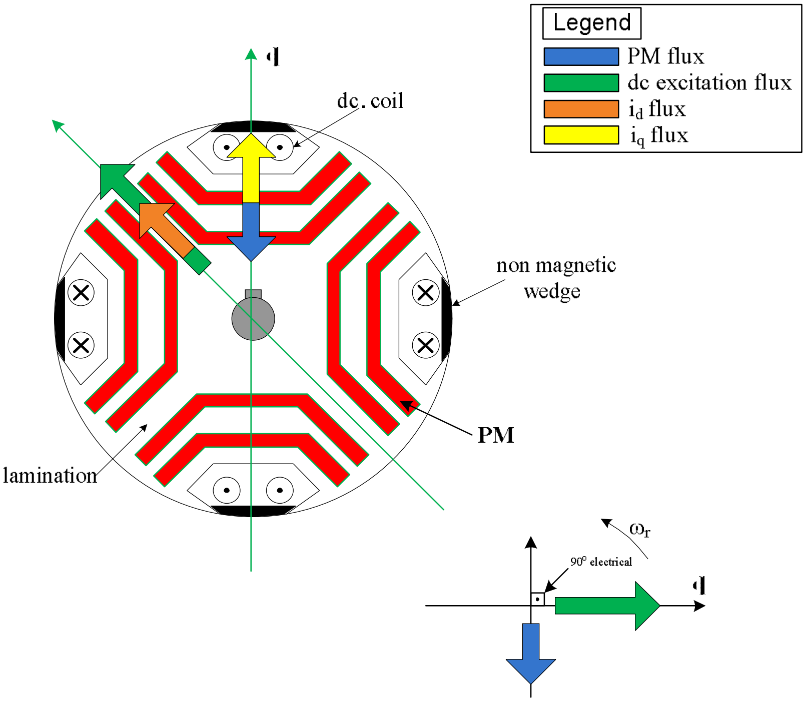

Fig. 4.1. BEGA rotor cross-section

In [4.20], [4.21], [4.22] synchronous machines with permanent magnets and dc excitation along the same axis, in the rotor, were proposed as integrated starter-alternator systems for hybrid electric vehicle. This kind of machines will be called in what follows as hybrid synchronous machines (HSM). The fundamental difference between BEGA and HSM is that BEGA has the permanent magnets and dc excitation at 90 electrical degrees. This will have a great impact over the constant power speed range of these two types of machine. In HSM the dc excitation is used to amplify/destroy the PM flux. Too high negative current in dc excitation could destroy the PM.

In BEGA the PM are used:

1) to destroy, partially, the q-axis flux produced by the stator current
2) to fully cancel the q-axis flux when unity (or high) power factor is required
3) to produced torque during transients (or steady-state) if the machine is driven with non-zero id (id☐0)

The dc excitation requires a four quadrant dc-dc converter. The rated power of dc-dc converter is approximately 5% of the rated power of the machine.

4.2. BEGA mathematical model at unity power factor

BEGA has a typical uniformly slotted stator with a three-phase ac winding, with a rotor with multiple flux barriers filled partially with PMs to reduce q axis armature flux, and along d axis (of higher inductance) a dc field winding supplied through slip rings and brushes.

The BEGA transient equations in d-q reference frame are:

$$\overline{V}_s = R_s \overline{I}_s + \frac{d\overline{\Psi}_s}{dt} + j\omega_r \overline{\Psi}_s \tag{4.1}$$

$$\overline{V}_s = V_d + jV_q \quad , \quad \overline{I}_s = I_d + jI_q \ , \ \overline{\Psi}_s = \Psi_d + j\Psi_q \tag{4.2}$$

$$\Psi_d = L_d I_d + L_{mf} I_f \quad , \ \Psi_q = L_q I_q - \Psi_{PM} \tag{4.3}$$

$$\begin{aligned} T_e &= \frac{3}{2} p_1 \left(\Psi_d I_q - \Psi_d I_q\right) \\ T_e &= \frac{3}{2} p_1 \left(L_{mf} I_f I_q + \left(L_d - L_q\right) I_d I_q + \Psi_{PM} I_d\right) \end{aligned} \tag{4.4}$$

$$V_f = R_f I_f + \frac{d\Psi_f}{dt} \quad , \quad \Psi_f = L_{mf} I_d + L_f I_f \tag{4.5}$$

where V_s and I_s are the stator voltage and current vector respectively, Ψ_s is the stator flux linkage vector, R_s is the stator resistance, ω_r is the electrical rotor speed, L_d, L_q are the d, q axis inductance, L_{mf} is the mutual field-armature inductance, Ψ_{PM} is the PM flux on q axis, and p is the pole pair. Equation (4.5) characterizes the dc field (excitation) circuit, where, V_f and I_f is the field voltage and current respectively, Ψ_f is the field flux, and R_f, L_f are the field winding resistance and inductance respectively.

The equivalent circuit of BEGA, based on d-q model is presented in Fig. 4.2.

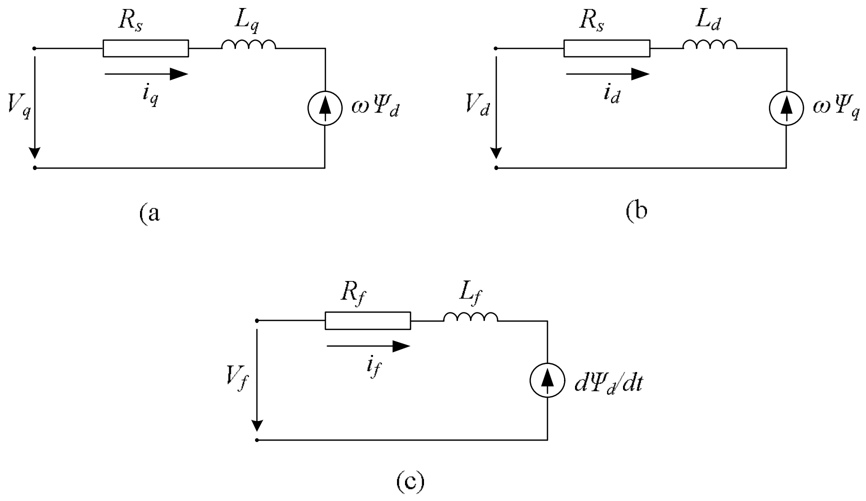

(a

(b

(c)

Figure 4.2. Equivalent circuit of BEGA

During the unity power factor operation (with zero id and zero), the steady-state dq equations of BEGA are:

$$\overline{V}_s = R_s I_q + \omega_r L_{mf} I_f \quad , \quad \overline{I}_s = jI_q = const \tag{4.6}$$

$$T_e = \frac{3}{2} p_1 \left(L_{mf} I_f I_q \right) \qquad (4.7)$$

At unity power factor operation the torque of the machine is controlled only from the rotor, through the dc excitation current. Switching from motoring to generating forces the dc current to change its sign.

The equivalent circuit of BEGA , at unity power factor operation, at steady state, is shown in Fig. 4.3.

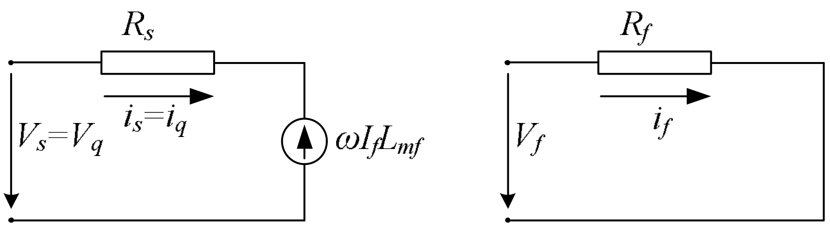

Figure 4.3. Equivalent circuit of BEGA at unity power factor operation

The stator supply voltage ($V_s=V_q$, $V_d=0$) covers the voltage drop on the stator resistance and induced voltage due to dc excitation flux. This way, BEGA behaves like a truly separately excited dc machine, without stator inductance.

Remark: with zero id and zero (iq=Iqk) the machine is operating over the entire speed/torque range at unity power factor operation, both for motoring and generating, as shown in Figure 4.4.

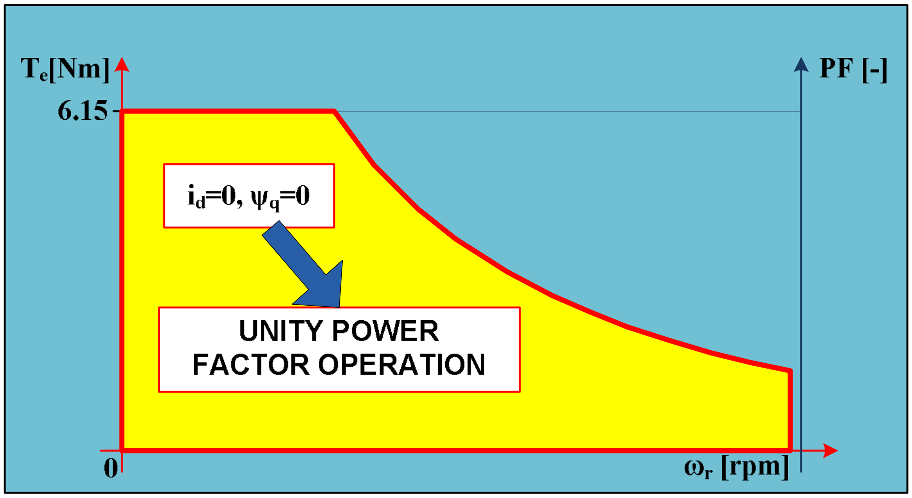

Figure 4.4. BEGA operation at unity power factor

The vector diagram illustrates the unity power factor operation at steady state (Fig. 4.5).

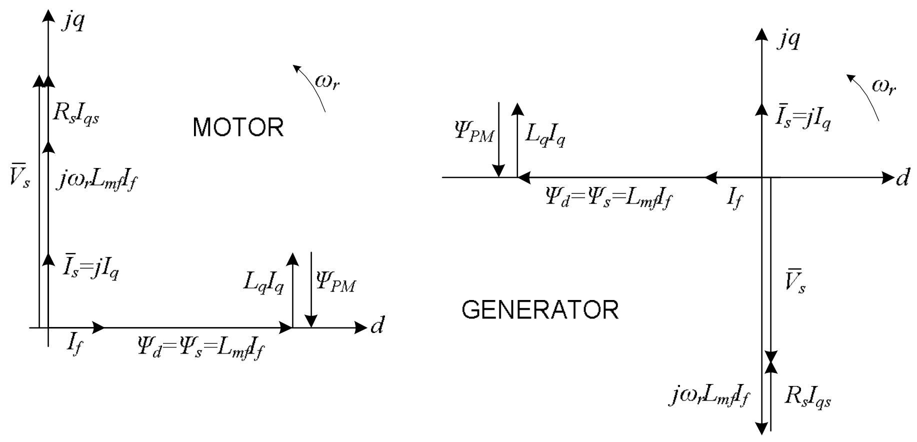

a) b)

Figure 4.5. BEGA steady state vector diagram at unity power factor a) motoring mode b) generating mode

The vector control structure for BEGA operation at unity power factor, over the whole torque/speed range is depicted in Fig. 4.6. With the proposed vector control structure, we measure the torque/speed envelope that will be used, later, in another vector control structure.

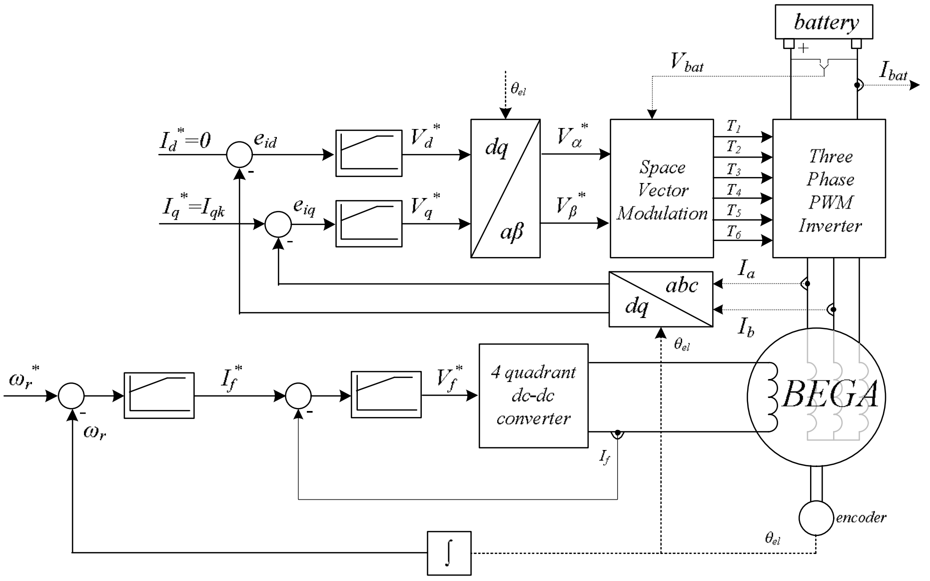

Fig. 4.6. BEGA vector control structure at unity power factor operation

The BEGA prototype parameters are given in Table I.

TABLE I. BEGA Parameters

Rated power (PN)	1 kW
Rated phase voltage (Vs)	15 V (rms)
Rated phase current (Is)	22 A (rms)
Rated field current (If)	4 A
Rated battery voltage (Vbatt)	48 V
Rated torque (TN)	6.15 Nm
Rated speed (nN)	1500 rpm
Number of pole pairs (p)	2
Stator phase resistance (Rs)	0.037 Ω
q axis inductance (Lq)	0.455 mH
D axis inductance (Ld)	1.8 mH
PM flux (ΨPM)	0.0136 Wb
Field winding resistance (Rf)	6.58 Ω
Field winding inductance (Lf)	0.407 H
Mutual field-armature inductance (Lmf)	47.7 mH
Moment of inertia (J)	16e-3 kg•m2
Viscous friction coefficient (B)	1e-4

4.3. DC excitation induced voltage

According to equation (4.5) any variation of id current will produce an induced voltage in the dc field winding according to the following relationship:

$$V_e = \frac{d\left(L_{mf} I_d\right)}{dt} \tag{4.9}$$

The equivalent dc excitation circuit, during id transients and steady-state, is illustrated in Figure 4.7.

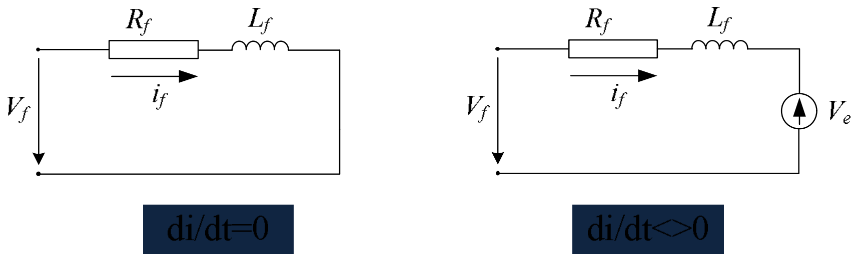

Figure 4.7. The equivalent circuit of dc field excitation: with did/dt=0 (left side) and did/dt#0 (right side)

In order to prove this, an i_d current with 100Hz frequency and 4V reference magnitude has been injected in the stator at standstill. The induced voltage has been measured at dc excitation terminal. The results are presented in Figure 4.8. For 100Hz, the magnitude of id current is 3.5V, while for the induced voltage is 18V. Consequently the relationship between the id current and induced voltage Ve is:

$$\begin{gathered} V_e = j \cdot k \frac{di_d}{dt} = j \cdot k \cdot 2.19 \frac{A}{ms} = 11.23V \\ \Rightarrow k = \frac{11.23}{2.19} = 5.12 \Rightarrow V_e = j \cdot 5.12 \cdot \frac{di_d[A]}{dt[ms]} \end{gathered} \tag{4.10}$$

The induced voltage is expressed as variation of i_d current expresses in [A/ms] because during vector control operation the variation of i_d current can be easily measured without significant noise distortion.

The induced voltage will act as a disturbance in the dc field excitation, increasing/decreasing the if current. On the other hand any dc field current variation will be reflected on the induced voltage due to excitation, affecting the stator current control. More precisely, any i_d stator current variation will be reflected on iq stator current.

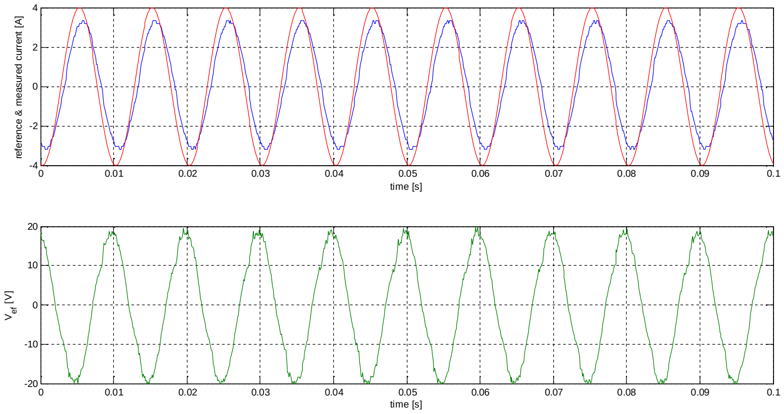

Fig. 4.8. Induced voltage at dc excitation terminal (fid=100Hz)

4.4. BEGA energy conversion

The energy flow and losses during BEGA operation in motoring and generating is shown in Fig. 4.9.

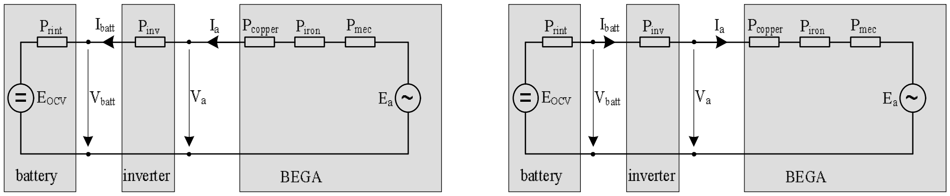

a) generator mode b) motor mode

Fig. 4.9. Power flow during a) motor operation, b) generator operation

The electromagnetic power at unity power factor is given by the equation (4.11):

$$P_{elm} = 3 \cdot E_{a(rms)} \cdot I_{a(rms)} \tag{4.11}$$

where $E_{a(rms)}$ is the rms value of phase back EMF voltage and $I_{a(rms)}$ is the rms value of phase current.

The electromagnetic power for motoring mode can be expressed as:

$$P_{elm} = P_{batt} - P_{conv} - P_{copper} - P_{iron} - P_{mec} \tag{4.12}$$

where: is the (active) power at battery terminals, are the three phase converter losses, are the copper losses in the stator windings, are the iron losses and are the mechanical losses.

The power at the battery terminals is:

$$P_{batt} = V_{batt} \cdot I_{batt} \tag{4.13}$$

The copper losses are expressed as follow:

$$P_{copper} = 3 \cdot I^2_{a(rms)} \cdot R_S \tag{4.14}$$

The electromagnetic power for generating mode can be expressed as:

$$P_{elm} = P_{batt} + P_{conv} + P_{copper} + P_{iron} + P_{mec} \tag{4.15}$$

The efficiency of the system (converter+machine), neglecting dc. excitation losses, is as follow:

$$\eta_{mot(gen)} = \frac{p_{elm(batt)}}{p_{batt(elm)}} \tag{4.16}$$

In our case, we measure only battery power (p_{batt}), while the electromagnetic power can be easily estimated knowing the motor speed and the dc excitation current.

For motor/generator mode we can simply estimate the system efficiency knowing the electromagnetic power and battery power during discharging/charging.

4.5 Experimental platform and test results

A set of experiments were carried out to prove the validity of the proposed solution. The structure of experimental platform is shown in Fig. 4.10.

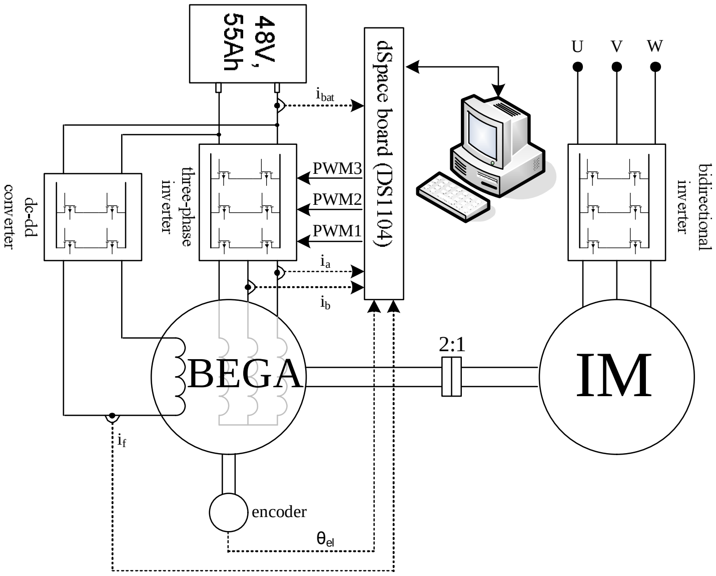

Fig. 4.10. Experimental platform for BEGA control

BEGA is fed through a 48Vdc, 350A Sauer-Danfoss three phase inverter from a 48V, 55Ah valve regulated lead-acid battery pack. The BEGA was linked with a three phase induction machine (IM) via a transmission belt (nIM/nBEGA=1/2). The IM was driven by an ABB ACS600 bidirectional converter. The rated of IM was 5.5kW at n=2945 rpm, enough to load the BEGA at maximum load. A four quadrant dc-dc converter with was used for current control in the dc. field winding. An incremental encoder, Telemecanique XCC-1510PR50R, 5000ppr was used for BEGA position and speed measurement.

The control algorithm has been developed in Matlab-Simulink and implemented on a dSpace 1104 Real Time System (RTI) used for rapid prototyping. The following signals were measured using dSpace acquisition board: phase currents, battery current, dc field current, phase voltages, battery voltage and BEGA position.

4.6. Proposed vector control scheme at unity power factor

Fig. 4.11 shows the proposed system configuration for controlling the BEGA, where the stator current is controlled in the rotor reference frame, and the dc field current (rotor current) is controlled by a feedback current loop independent of stator current loop. However, both current commands for the stator and rotor current loops are produced simultaneously. The system command is given by the speed, but can be torque or power, as well. The speed error is reflected in the reference electromagnetic torque (t_e^*) through the speed controller. A limitation (saturation) of reference electromagnetic torque is necessary due to computation performed inside the current referencer. The limitation block is a two-dimensional look-up table that contains the torque/speed enveloped determined at unity power factor operation. The current referencer computes simultaneously the reference q-axis current (i_q^*) and the reference dc field current (i_f^*). Further the iq and id current controllers adjust the d-q reference voltage (V_d^*, V_q^*) to minimize the d-q reference current errors. Space vector modulation block calculates the duty cycle for each transistor of the inverter, based on the measured battery voltage and α-β voltage components.

The current referencer (see Fig. 4.12.) calculates the i_q^* and i_f^*, based on reference electromagnetic torque (t_e^*) and measured (or estimated) rotor speed (ω_r), using a simple loss minimization principle given by the equation (4.17). So, the scope of the current referencer is to enhance the machine efficiency, by minimizing the copper losses in the machine.

As it is clearly shown in equation (4.7) the same torque can be produced by a variety of stator and rotor currents. The main problem of the current control system for BEGA is how to determine a stator/rotor current command, from the torque command, that will lead to a reducing of copper losses.

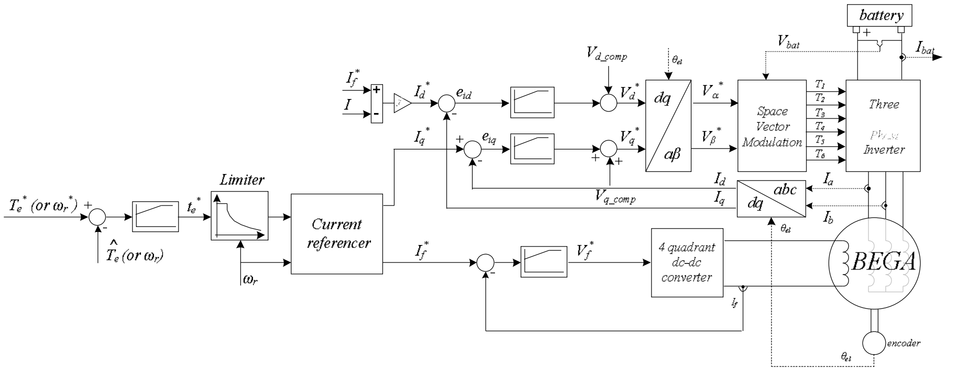

Figure 4.11. BEGA vector control structure

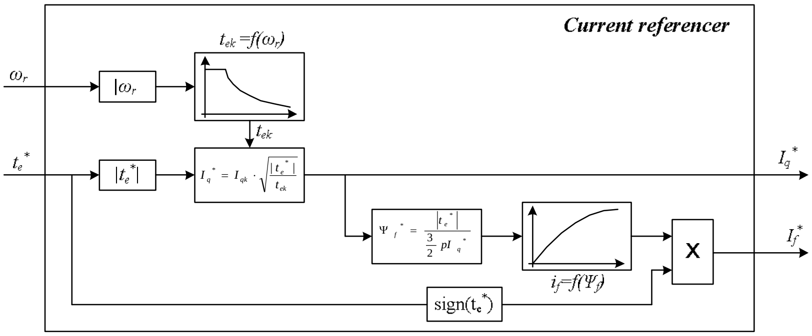

Figure 4.12. Current referencer structure

For $i_d^* = 0$, the instantaneous reference values of i_q^* and i_f^* to build the required torque t_e^*, are given by the current referencer (see Fig. 4.11.) as function of the rotor speed ωr and reference torque t_e^*. The peak torque (t_{ek}^*) is constant bellow rated speed, while the peak power is constant above rated speed. When $t_e^* < t_{ek}(\omega_r)$, then the condition $\Psi_q = 0$ is relaxed, in order to reduce the overall copper losses. In this respect we use the relationships given by equation (4.17).

$$i_q^* = I_{qk}\sqrt{\frac{\left|t_e^*\right|}{\left|t_{ek}(\omega_r)\right|}} \quad , \quad i_f^* = \frac{2t_e}{3i_q L_{mf}(i_f)i_f} \tag{4.17}$$

Once i_q^* is determined, is obtained and after that i_f^* is specified using the nonlinear dependence . It is essential to observe that Iqk decides the influence of I_f and Iq on the torque.

Since the dc field winding inductance Lf is large in (4.5), a very fast (few miliseconds) dc field current response is very difficult. This means that the single way to provide fast torque response is to control during transients the id current, while the converter voltage is not saturated. The algorithm is:

$$i_d^* = k \cdot \left(i_f^* - i_f\right) \tag{4.18}$$

where the gain k=5, experimentally derived. This way the contribution of reluctance and PM torque is employed.

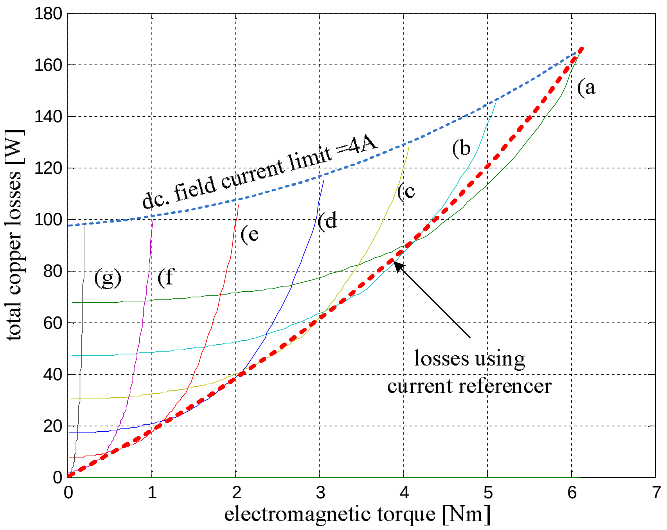

Fig. 4.13. Total copper losses vs torque for iq=30A (a), 25A (b), 20A (c), 15A (d), 10A (e), 5A (f), 1A (g).

The total copper losses vs electromagnetic torque at $i_d=0$ and different i_q^* values, taking into account the saturation effect in d axis, are represented in Fig. 4.11. The total copper losses in the machine are expressed as follows:

$$P_{copper} = 3I_q^2 R_s + I_f^2 R_f = I_q^2 R_s + \left(\frac{T_e}{3L_{mf}(i_f)I_q}\right)^2 R_f \tag{4.19}$$

Figure 4.13. demonstrates that the proposed simplified current referencer reduces the total copper losses at minimum. The dotted red line in Figure 4.9 represents the minimum losses that can be achieved using the proposed current referencer (4.17).

A theoretical analysis of the effect of the current referencer on the BEGA power factor during operation is done in what follows.
For peak torque values ( ), during BEGA operation, unity power factor is achieved. Also, for low and very low torque levels, the unity power factor operation is possible, but with the efficiency penalty. Using the current referencer (4.17), for lower torque levels, the unity power factor can not be maintained anymore, but we are interested to see how much the power factor degradation is.
The BEGA power factor angle, at id=0, is expressed:

$$PF = \cos \qquad (4.20)$$

At id=0, from Fig. 4.14, the power factor angle becomes:

$$= \prec\left(\bar{I}_s, \bar{V}_s\right) = \prec\left(\bar{V}_q, \bar{V}_s\right) \qquad (4.21)$$

$$\varphi = a\sin\left(\frac{V_q}{V_s}\right) = a\sin\left(\frac{V_q}{\sqrt{V_d^2 + V_q^2}}\right) = a\sin\left(\frac{\omega_r\left(L_q I_q - \Psi_{PM}\right)}{\sqrt{\left[\omega_r\left(L_q I_q - \Psi_{PM}\right)\right]^2 + \left[\left(R_s I_q + \omega_r L_{mf} I_f\right)\right]^2}}\right)$$

(4.22)

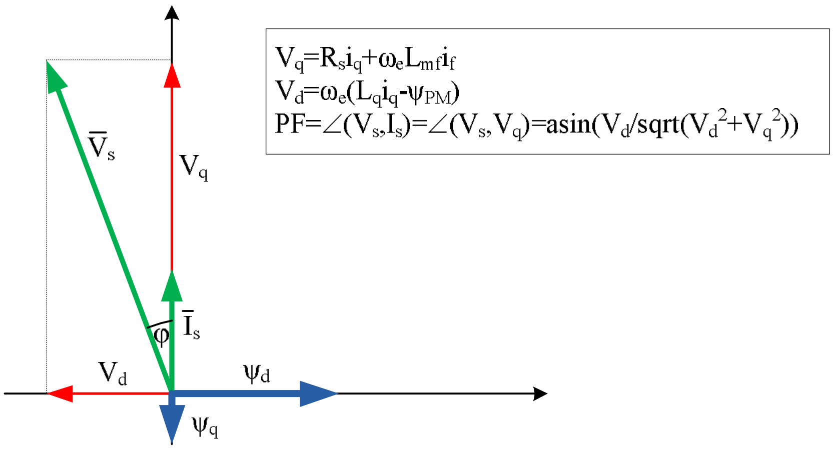

Figure 4.14. BEGA vector control diagram with id=0

The power factor angle vs speed, for different torque levels, for 0...1500rpm speed range, using the proposed loss minimization strategy is illustrated in Fig. 4.15. For a speed range of 0-1500rpm and a torque range of 0.5-6.12Nm the power factor is over 0.9. Above the rated speed, for the same electromagnetic torque level, the power factor is expected to increase, due to the fact that the peak torques (Tek) decreases, which furthermore determines an increasing of Iq close to Iqk. As closer Iq to Iqk, as higher the power factor. Consequently, above the rated speed the power factor tends to increase. The results from Fig. 4.15 shows that for 8% (0.5Nm) of rated load the power factor is 0.9, which is quite a good power factor for such a low load. In Fig. 4.16 a graphical representation of the power factor behavior for a large speed range, is shown. Below the rated speed, for the same torque value, the power factor is exponentially decreasing from unity to minimum value which occurs at rated speed.

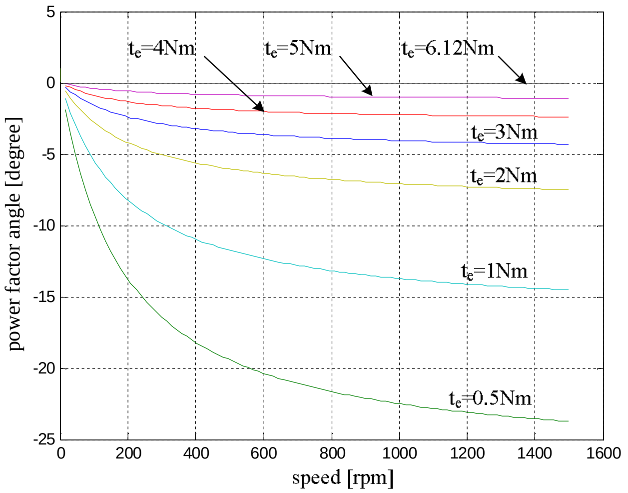

Figure. 4.15. Power factor angle vs. speed for different lower torque values

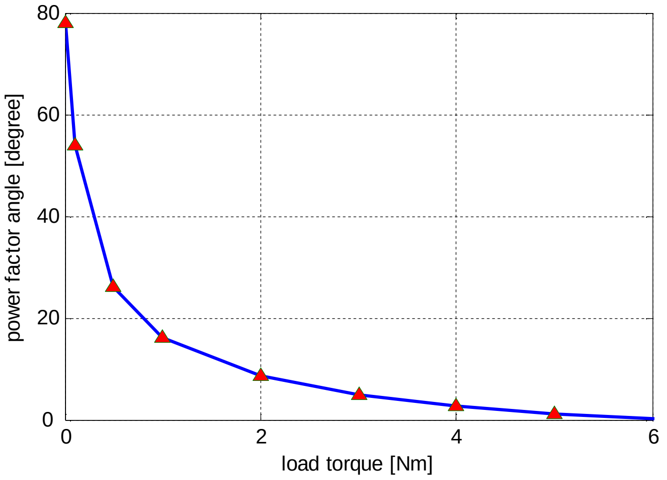

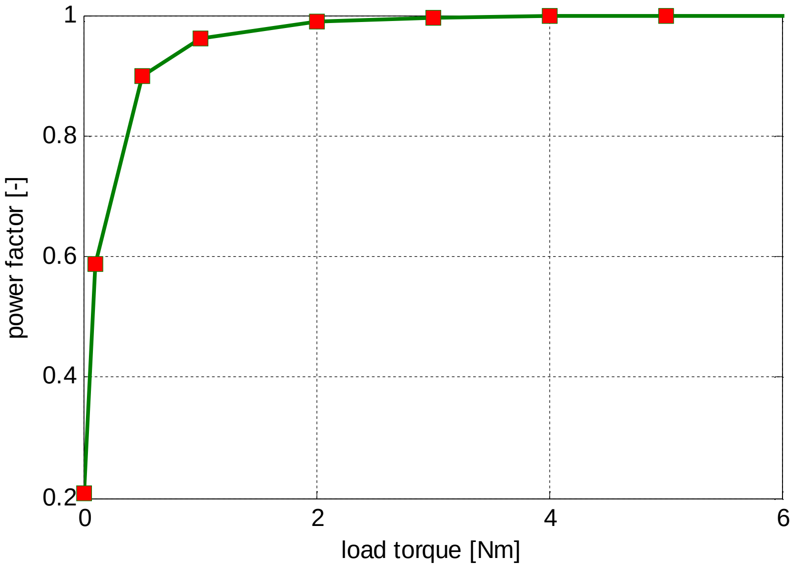

Figure 4. 16. Power factor angle (top) and power factor (bottom) vs. load torque at rated speed

Above the rated speed the power factor is increasing to unity value which occurs when the machine operates on the toque/speed envelope (rated/maximum power). The power factor angle and power factor for a range of zero to rated torque, for 1500rpm (rated speed) is shown in Fig. 4.16.

4.6.1 Back-EMF Compensation

In order to assure a better current regulation the back-emf compensation is necessary. Back-emf compensation means to add to the output of the current controller the term that contains the back-emf. Also, this way the voltage decoupling can be achieved. Current compensation is important during high current transients, especially when the voltage reserve is low (at high speed) . Though back-emf compensation we have the guaranteed the reference current is achieved in high dynamic transients. One meaning of the back-emf compensation is that the reference voltage from the current controller(s) has smaller variations due to the fact that the back-emf compensation term aim is to assure the zero value of the current during any condition.

In Fig. 4.17 it is illustrated the back-emf compensation effect. The machine is running as motoring at half from the rated load and suddenly the load changes its sign. The d-axis flux is forces to change its sign, also, but this way the back-emf travels from high positive values to high negative value. So, the back-emf voltage excursion is high. In order to be sure that the reference current is achieved the output of the current controller should be faster than the back-emf variation.

It can be easily observed that with back-emf compensation the target current is achieved, even in high transients, while without back-emf compensation there is time when the current can not be easily controlled.

$$V_d^* = \left(k_{pid} + \frac{k_{iid}}{s}\right) \cdot e_{id} + V_{d\_comp} = \left(k_{pid} + \frac{k_{iid}}{s}\right) \cdot e_{id} - \omega_e \cdot \left(L_q I_q - \Psi_{PM}\right) \quad (4.23)$$

$$V_q^* = \left(k_{piq} + \frac{k_{iiq}}{s}\right) \cdot e_{iq} + V_{q\_comp} = \left(k_{piq} + \frac{k_{iiq}}{s}\right) \cdot e_{iq} + \omega_e \cdot \left(L_d I_d + L_{mf} I_f\right) \quad (4.24)$$

The i_d, i_q current regulation with and without back-emf compensation is illustrated, through simulations, in Fig. 4.17.

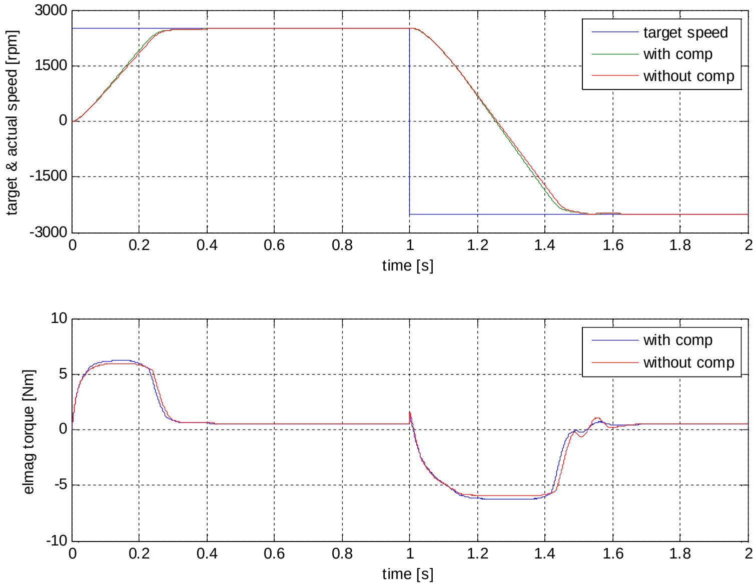

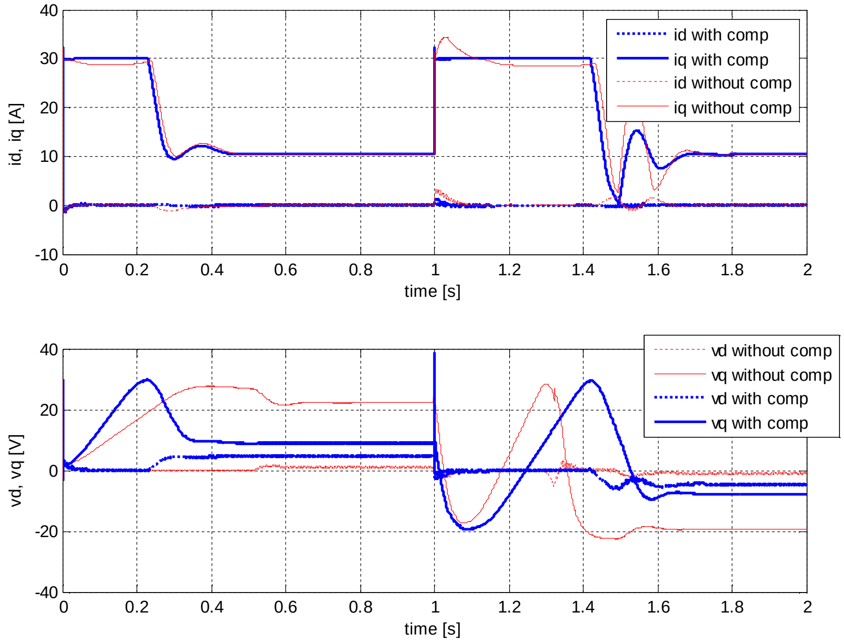

Fig. 4.17. id, iq current response with/without back-emf compensation

4.7. Simulation results

Extensive simulations have been performed in order to determine the BEGA performance under transients and stead-state.

In the first experiment carried out, the speed response for a target speed of 1500rpm is investigated. While the machine is running in steady-state (speed is constant) the load torque changes, suddenly, its sign, the torque value remaining the same. The simulations results are presented in Fig. 4.15. Very fast response of iq current is achieved. During acceleration the current iq reaches the critical value Iqk, canceling the q-axis flux. The torque response is not very fast, due to the slow response of dc field current if. The torque shape, during acceleration, is the same as the dc. field current, iq current being constant. A significant error between the reference and measured dc currents is observed. Insignificant errors in the id current, during transients, can be seen in Fig. 4.15.d. Because the id current is zero (or very close to zero) the d-axis flux is proportional with the field current, considering the saturation of dc excitation circuit is neglected.

In the first 50ms, the power factor is rapidly increasing, while during steady-state value over 0.98 for power factor are guaranteed even if the load is half of the rated value. As a first consequence, we could say that at rated speed, with the load higher than half of the rated value, BEGA is operating at unity power factor. The phase currents and the total induced voltage are shown in Fig. 4.18.h. Fig. 4.18.i. (a zoom on Fig. 4.18.h during motoring) proves the unity power factor operation of BEGA. The angle between total induced voltage and phase current is zero, suggesting that BEGA is similar with a separate excited dc current machine, without inductance. Similar with a dc excited machine BEGA is switching from motoring to generating by changing the current direction in the dc. excitation. The active power changes also its sign during generating.

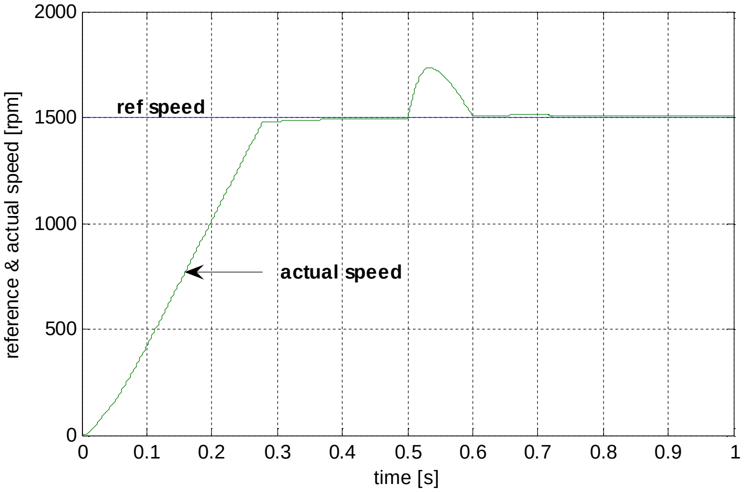

a)

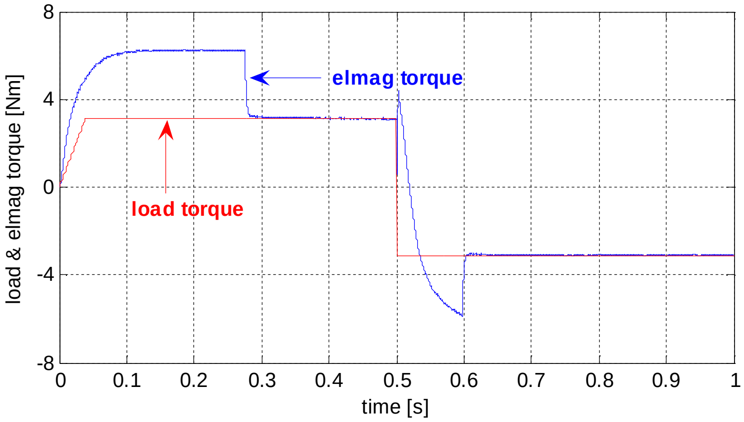

b)

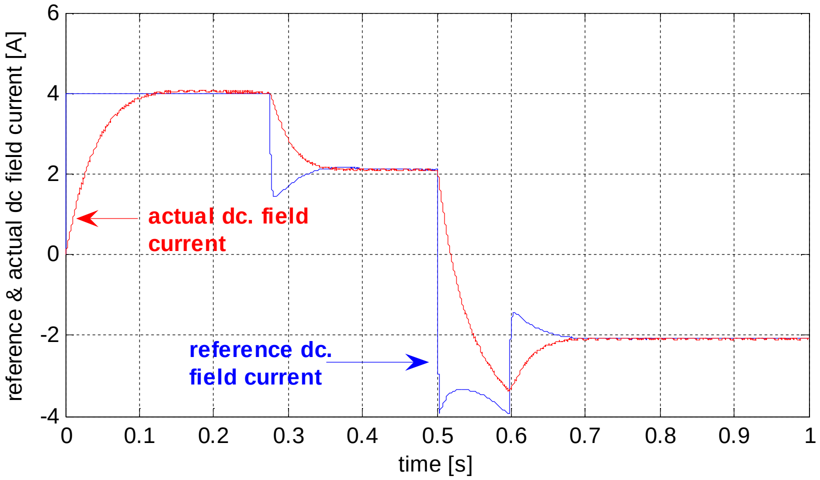
6
4
2
0
-2
-4
reference & actual dc field current [A]
actual dc. field current
reference dc. field current
0
0.1
0.2
0.3
0.4
0.5
0.6
0.7
0.8
0.9
1
time [s]

c)

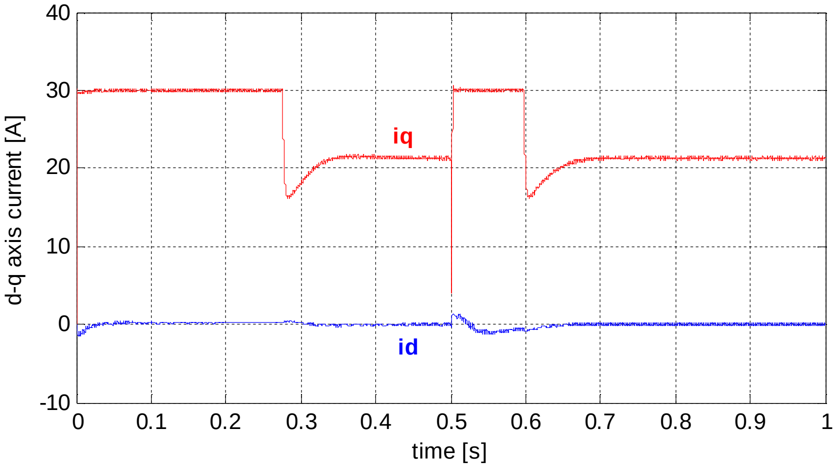
40
30
20
10
0
-10
d-q axis current [A]
iq
id
0
0.1
0.2
0.3
0.4
0.5
0.6
0.7
0.8
0.9
1
time [s]

d)

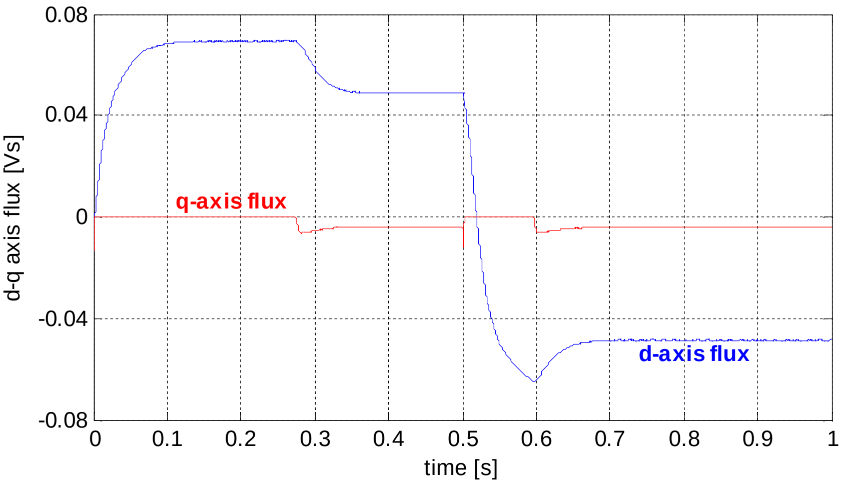
0.08
0.04
0
-0.04
-0.08
d-q axis flux [Vs]
q-axis flux
d-axis flux
0
0.1
0.2
0.3
0.4
0.5
0.6
0.7
0.8
0.9
1
time [s]

e)

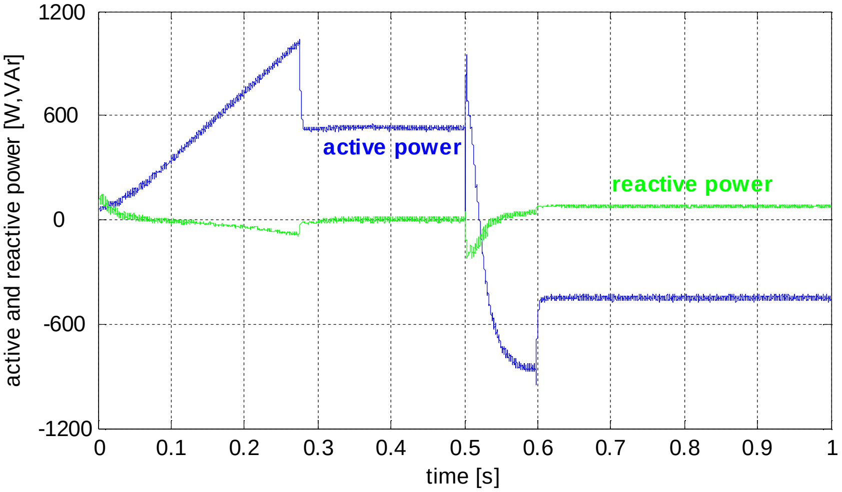
1200
600
0
-600
-1200
active and reactive power [W,VAr]
active power
reactive power
0
0.1
0.2
0.3
0.4
0.5
0.6
0.7
0.8
0.9
1
time [s]

f)

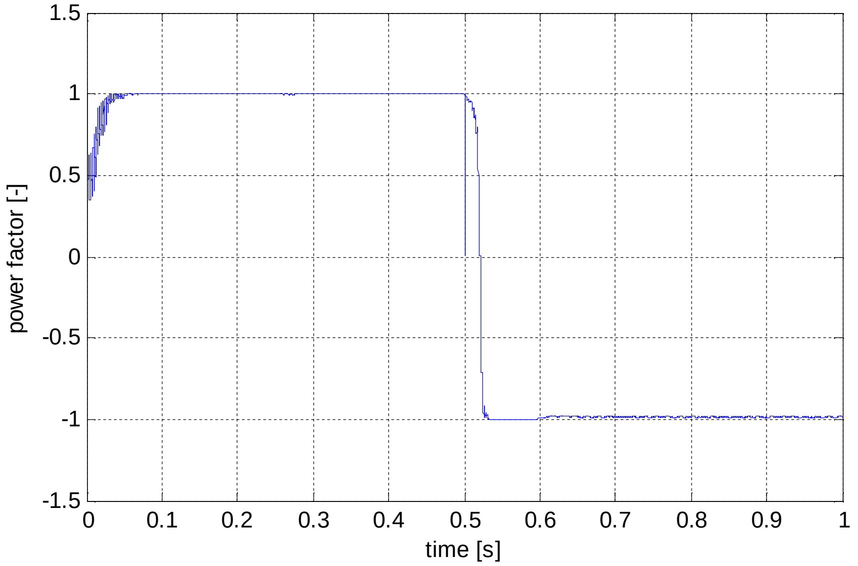
1.5
1
0.5
0
-0.5
-1
-1.5
power factor [-]
0
0.1
0.2
0.3
0.4
0.5
0.6
0.7
0.8
0.9
1
time [s]

g)

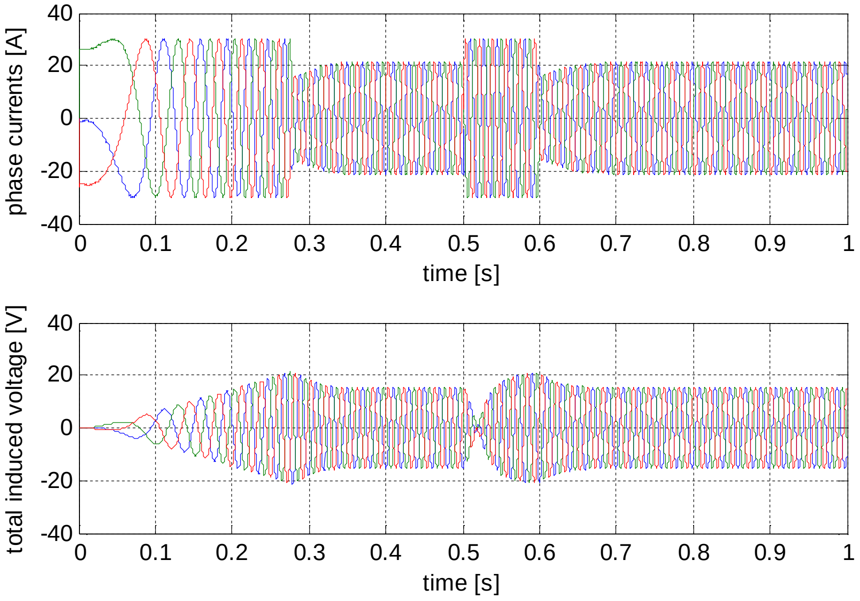
40
20
0
-20
-40
phase currents [A]
0
0.1
0.2
0.3
0.4
0.5
0.6
0.7
0.8
0.9
1
time [s]
40
20
0
-20
-40
total induced voltage [V]
0
0.1
0.2
0.3
0.4
0.5
0.6
0.7
0.8
0.9
1
time [s]

h)

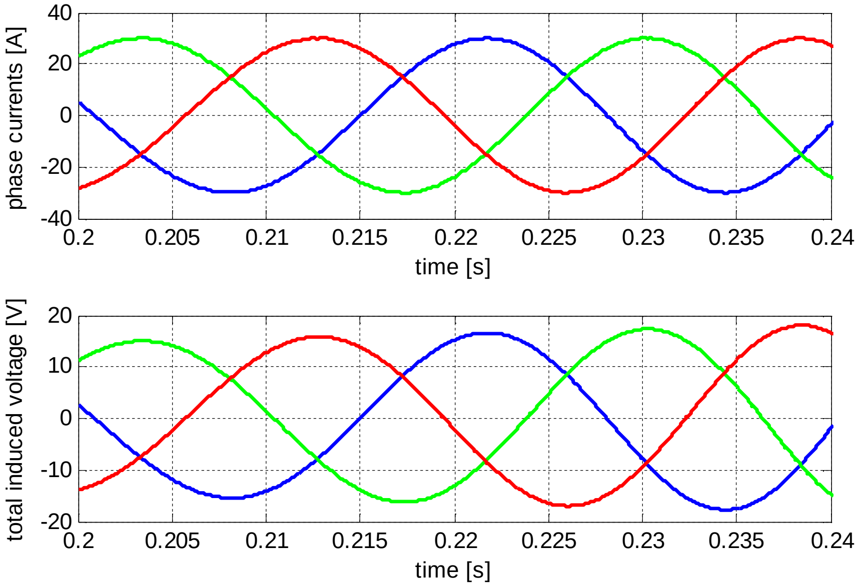

h)

Fig. 4.18. BEGA measurements at unity power factor operation: a) reference and actual speed, b) load and electromagnetic torque, c) reference and actual dc field current, d) d-q axis currents, e) d-q axis flux, f) power factor, g) active and reactive power, h) phase currents and total induced voltage, i) zoom on h)

In a second simulation BEGA behavior is investigation during speed reversal at constant torque. During speed reversal (braking) the machine switches from motoring to generating by forcing the dc. field current to change its sign as well as the electromagnetic torque. Over the entire speed range (including the transients), the power factor is over 0.98. The reactive power is fluctuating around zero due to id=0 and q-axis flux value close to zero. Higher values, for the active power, could be observed during stead-state motoring in comparison with generating, due to the additional losses on the stator resistance. Fig. 4.19.i (a zoom on Fig. 4.19.h) shows the BEGA unity power factor operation during generating. During generating, an angle of 180o between the total induced voltage and the phase currents can be easily observed in Fig. 4.19.i. This way the unity power factor during generating is guaranteed and proved. In contrast to the previous case, where during generating the dc field current changed its sign, now even if the machine is running in generating, the dc. field current keeps its positive sign. This is normal considering that in this case the torque remains positive, while the speed changes the sign. However, in both (and all) cases, the dc. field current sign follows the torque sign, according to the equation (4.2).

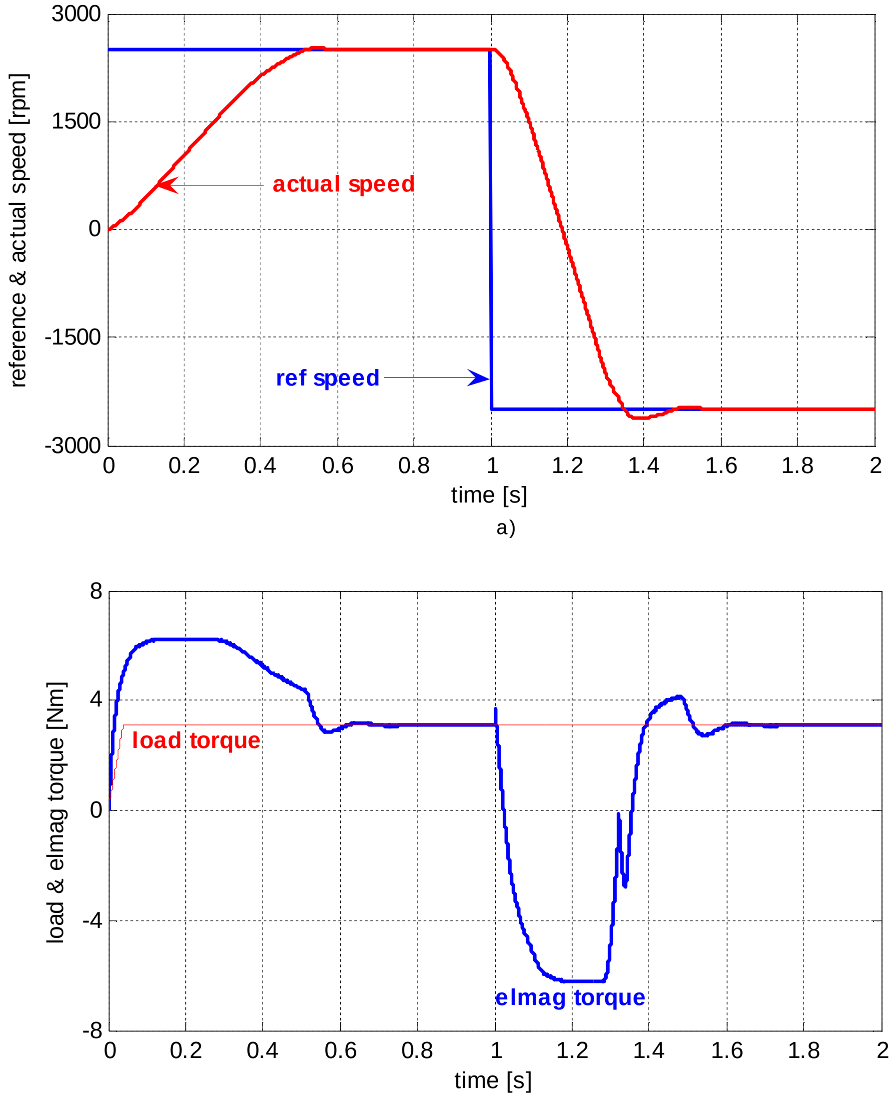
3000
1500
0
-1500
-3000
reference & actual speed [rpm]
actual speed
ref speed
0
0.2
0.4
0.6
0.8
1
1.2
1.4
1.6
1.8
2
time [s]
8
4
0
-4
-8
load & elmag torque [Nm]
load torque
elmag torque
0
0.2
0.4
0.6
0.8
1
1.2
1.4
1.6
1.8
2
time [s]

a)

b)

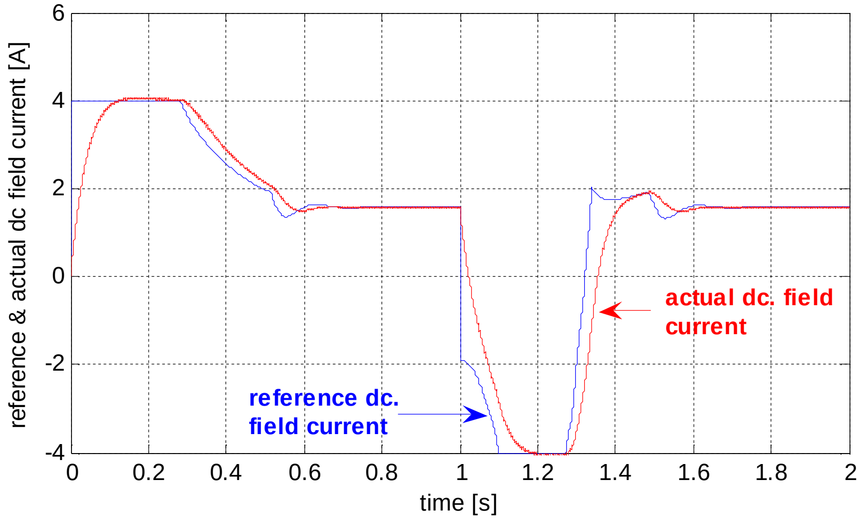
reference & actual dc field current [A]
6
4
2
0
-2
-4
0
0.2
0.4
0.6
0.8
1
1.2
1.4
1.6
1.8
2
time [s]
actual dc. field current
reference dc. field current

c)

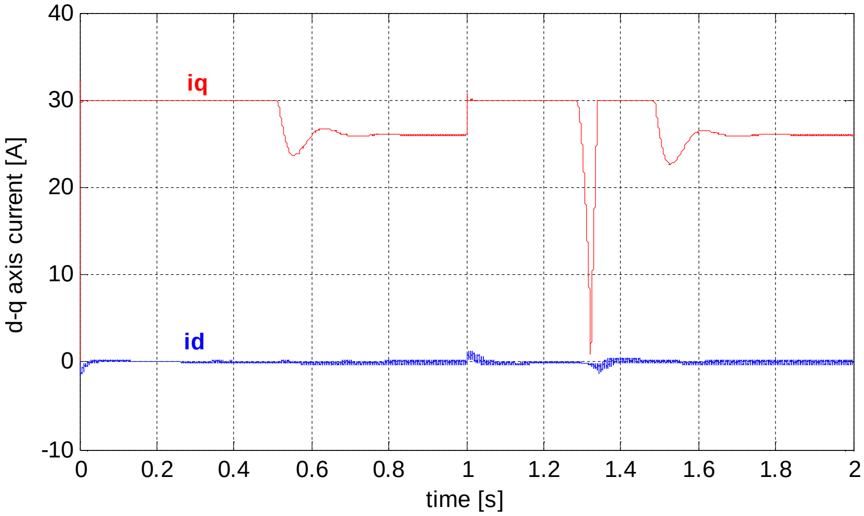
d-q axis current [A]
40
30
20
10
0
-10
iq
id
0
0.2
0.4
0.6
0.8
1
1.2
1.4
1.6
1.8
2
time [s]

d)

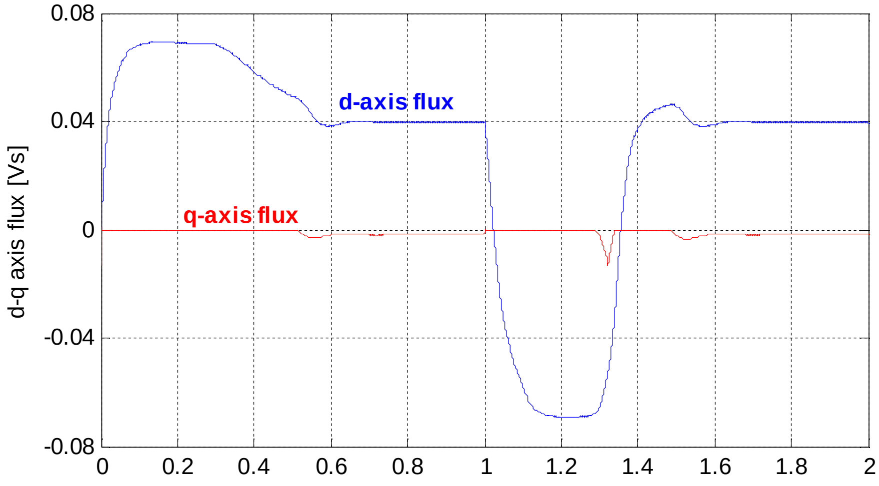
0.08
0.04
0
-0.04
-0.08
d-q axis flux [Vs]
d-axis flux
q-axis flux
0
0.2
0.4
0.6
0.8
1
1.2
1.4
1.6
1.8
2
time [s]

e)

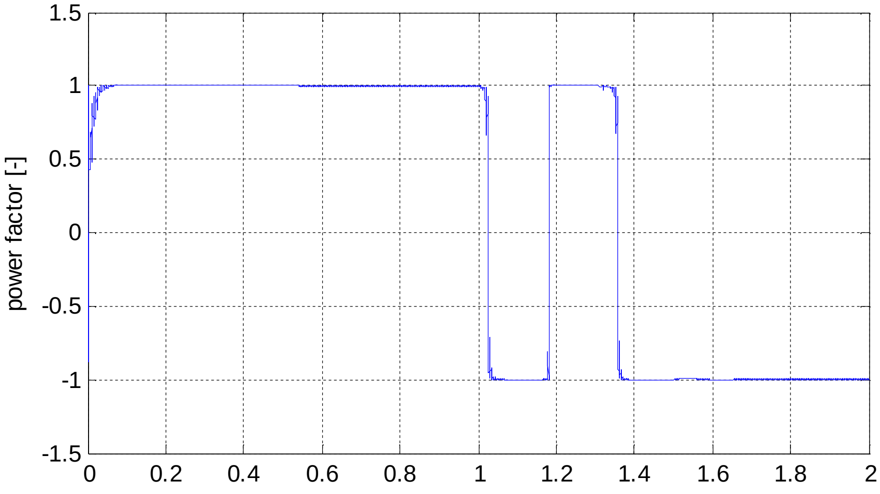
1.5
1
0.5
0
-0.5
-1
-1.5
power factor [-]
0
0.2
0.4
0.6
0.8
1
1.2
1.4
1.6
1.8
2
time [s]

f)

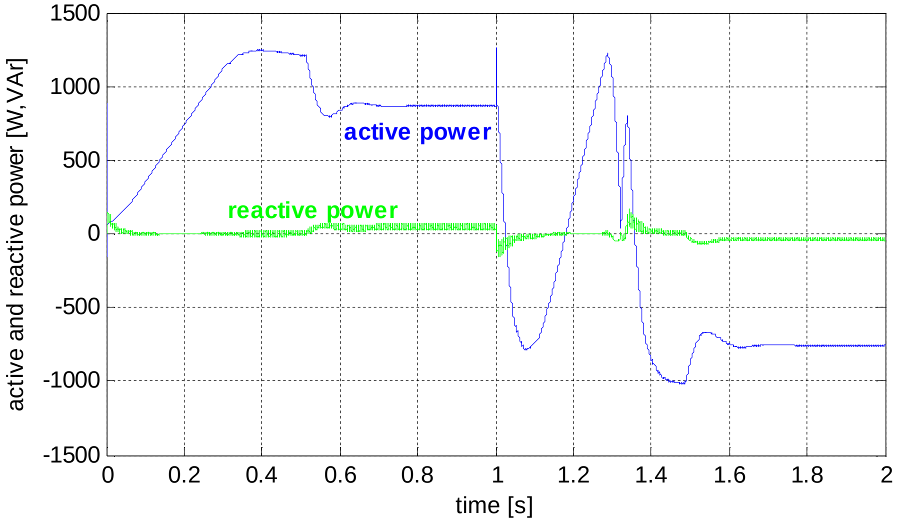
1500
1000
500
0
-500
-1000
-1500
active and reactive power [W,VAr]
active power
reactive power
0
0.2
0.4
0.6
0.8
1
1.2
1.4
1.6
1.8
2
time [s]

g)

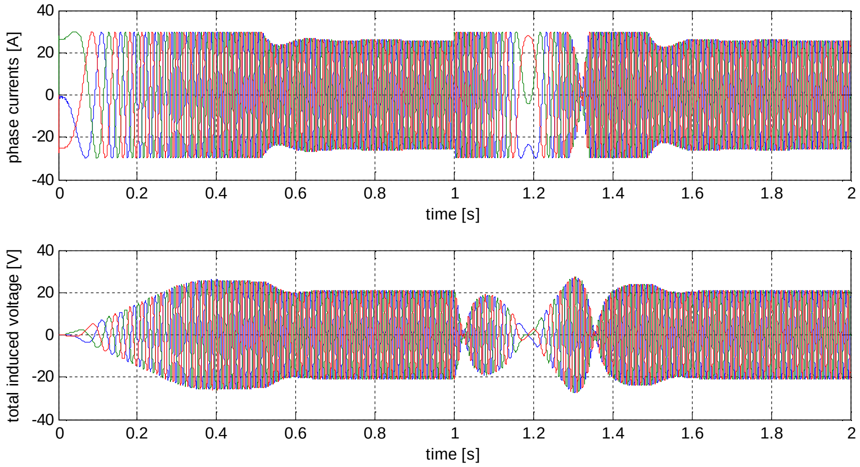
40
20
0
-20
-40
phase currents [A]
0
0.2
0.4
0.6
0.8
1
1.2
1.4
1.6
1.8
2
time [s]
40
20
0
-20
-40
total induced voltage [V]
0
0.2
0.4
0.6
0.8
1
1.2
1.4
1.6
1.8
2
time [s]

h)

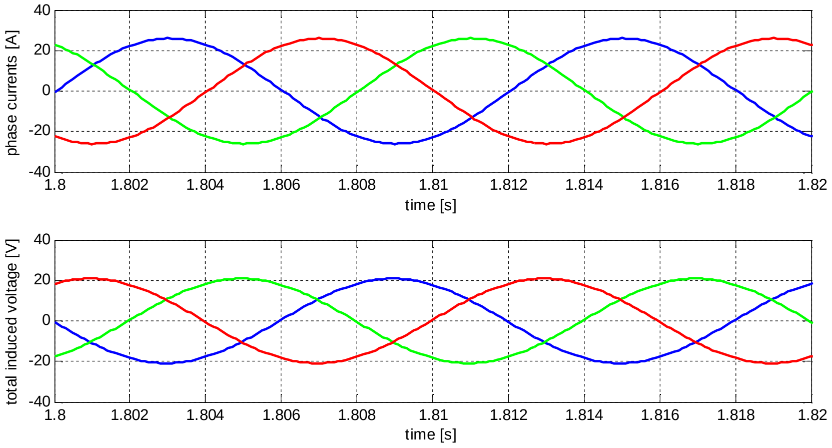

i)

Figure 4.19. BEGA measurements at unity power factor operation: a) reference and actual speed, b) load and electromagnetic torque, c) reference and actual dc field current, d) d-q axis currents, e) d-q axis flux, f) power factor, g) active and reactive power, h) phase currents and total induced voltage, i) zoom on h)

The third experiment is an acceleration from zero to 3000rpm, under no-load (Fig. 4.20). This time a high power factor is achieved only during acceleration. The power factor decreases as the electromagnetic torque decreases. The current referencer set, a low value for the iq current, while the dc. field current is higher. For the same torque a second solution would be to have a high iq current (enough to fully cancel the q-axis flux) and a lower value for the dc current – this way the unity power factor would be, again, achieved.

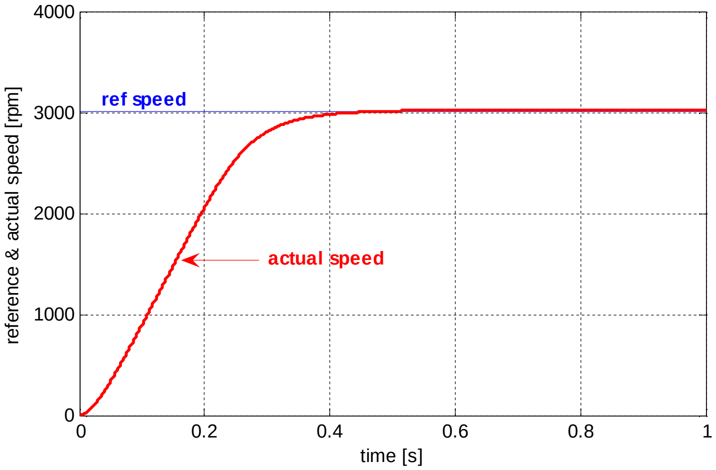

a)

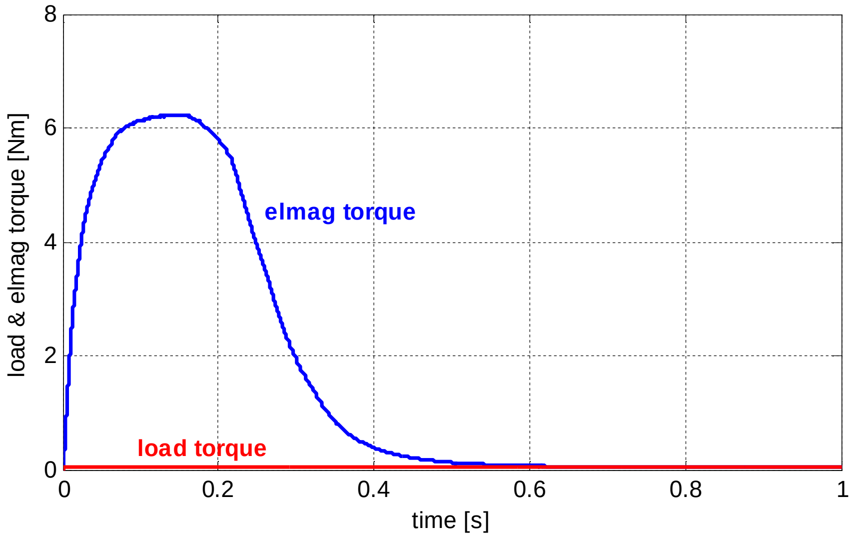
load & elmag torque [Nm]
8
6
4
2
0
elmag torque
load torque
0
0.2
0.4
0.6
0.8
1
time [s]

b)

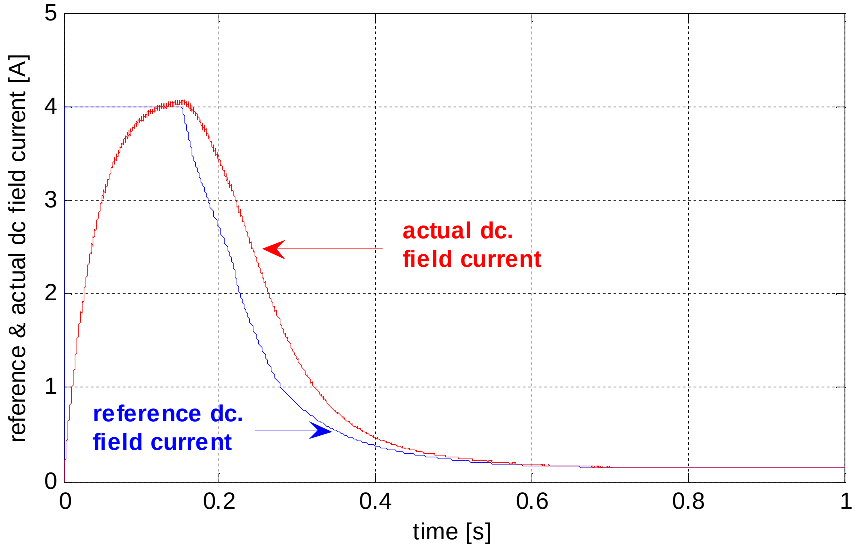
reference & actual dc field current [A]
5
4
3
2
1
0
actual dc.
field current
reference dc.
field current
0
0.2
0.4
0.6
0.8
1
time [s]

c)

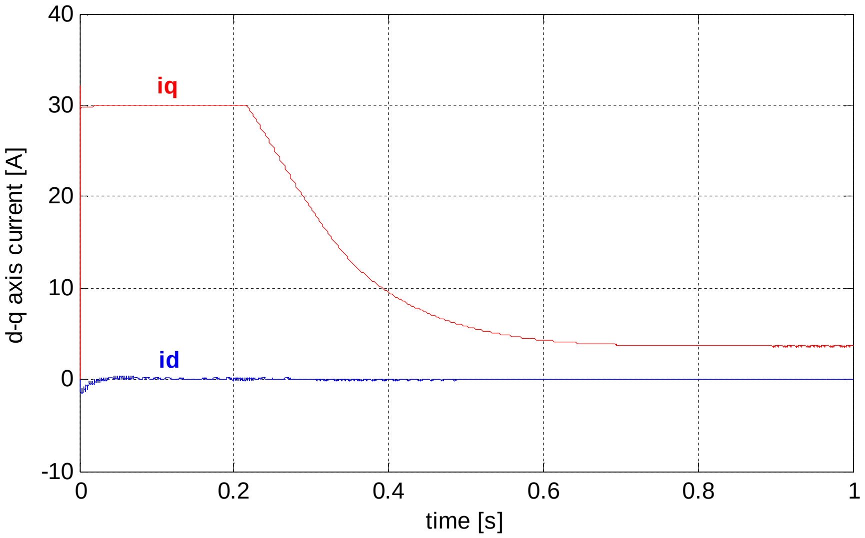
40
30
20
10
0
-10
0
0.2
0.4
0.6
0.8
1
iq
id
d-q axis current [A]
time [s]

d)

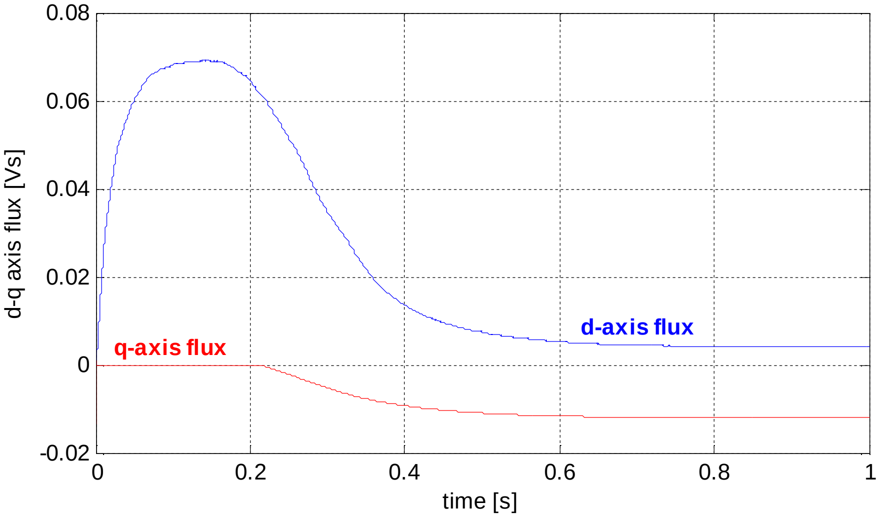
0.08
0.06
0.04
0.02
0
-0.02
0
0.2
0.4
0.6
0.8
1
d-axis flux
q-axis flux
d-q axis flux [Vs]
time [s]

e)

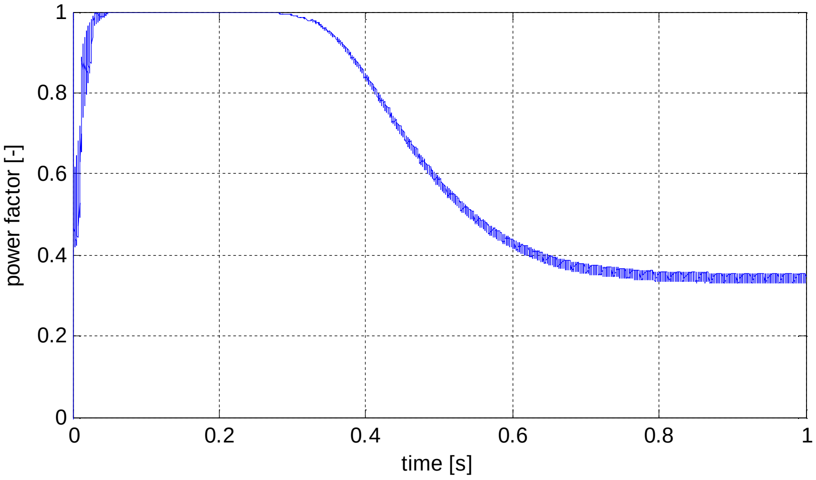
power factor [-]
1
0.8
0.6
0.4
0.2
0
0
0.2
0.4
0.6
0.8
1
time [s]

f)

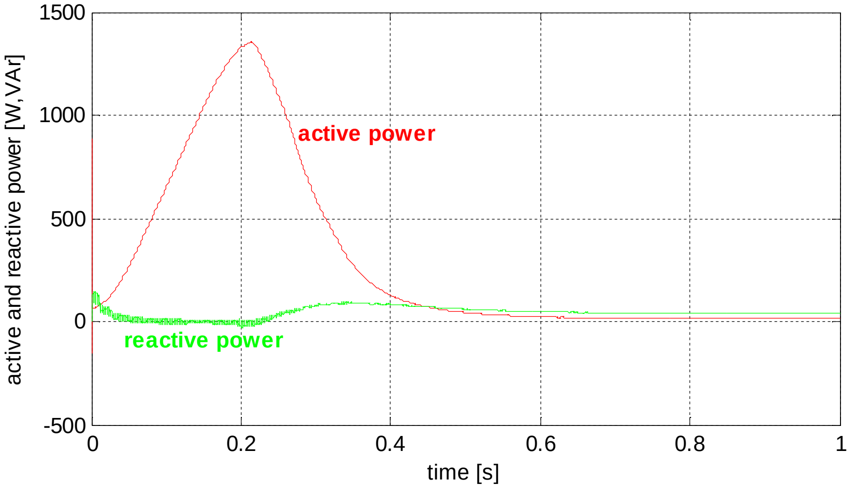
active and reactive power [W,VAr]
1500
1000
500
0
-500
0
0.2
0.4
0.6
0.8
1
time [s]
active power
reactive power

g)

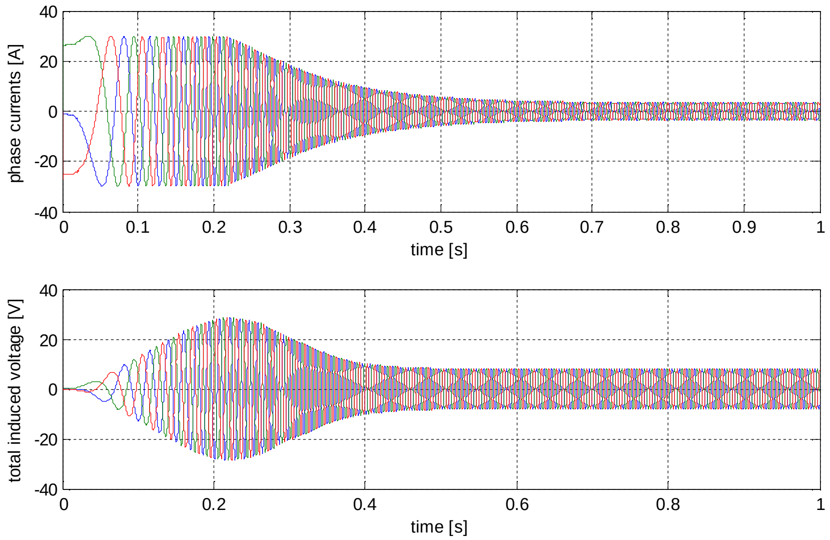

h)

Figure 4.20. BEGA measurements at unity power factor operation: a) reference and actual speed, b) load and electromagnetic torque, c) reference and actual dc field current, d) d-q axis currents, e) d-q axis flux, f) power factor, g) active and reactive power, h) phase currents and total induced voltage

As we mentioned, in the beginning, for light loads the target is to minimize the losses. For light loads, the unity power factor is not a priority due to that fact that, the apparent power (KVA) of the inverter is anyway bellow the rated value. In other words, we could say, that during light load the target is that BEGA to be more efficient and not to operate at unity power factor. In fact, for higher loads, the current referencer achieves in the same time, very well, two goals: i) unity power factor operation, ii) minimum copper losses.

4.8. Torque response improvement

The torque response improvement strategy employs non-zero id current during transients when non-zero error in dc. field current error occurs. The reference id current is given by equation (4.25).

$$i_d^* = k \cdot \left(i_f^* - i_f\right) \tag{4.25}$$

Where if* is the reference dc field current, if is the measured dc field current and k is the gain. Using equation (4), the contribution of reluctance and permanent magnet torque is employed.

$$T_e = \frac{3}{2} p_1 \left(L_{mf} I_f I_q + \left(L_d - L_q \right) I_d I_q + \Psi_{PM} I_d \right) \tag{4.26}$$

The equation (4.26) shows:

- The contribution of reluctance torque is higher for higher motor load
- The permanent magnet torque contribution is iq current independent and is proportional with the dc field current error.
- A significant contribution of permanent magnet torque is expected for high dc field current excursions.

Taking into account that three currents are controlled in the same time the voltage decoupling is mandatory in order to avoid speed oscillations.

The consequences of equation (4.26) are:

- As long as the dc field current exists the unity power factor can not be achieved
- Fast torque response can be achieved and consequently the speed response is faster

The simulation results for k=0 (id*=0) and k=6 are presented in Fig. 4.21. The torque response for k=6 is almost instantaneous since the id current response is very fast due to small d-axis inductance.

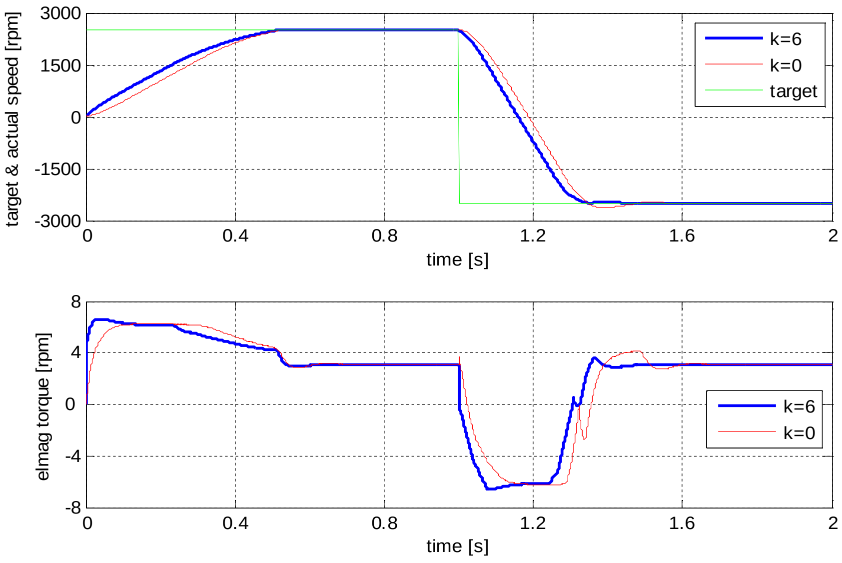

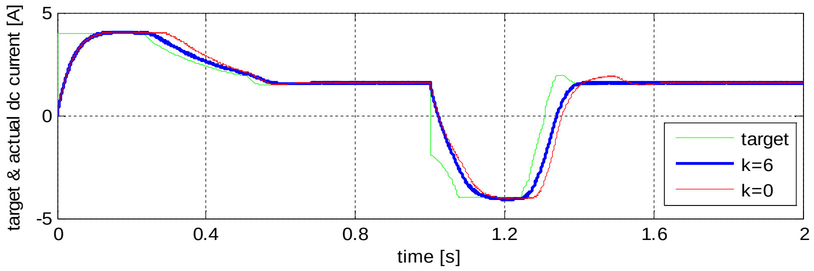
target & actual dc current [A]
5
0
-5
0
0.4
0.8
1.2
1.6
2
time [s]
target
k=6
k=0

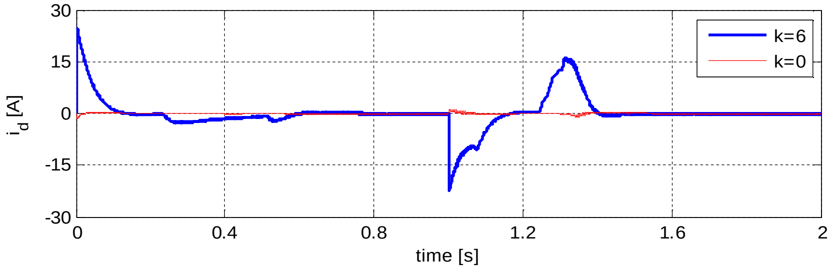
i_d [A]
30
15
0
-15
-30
0
0.4
0.8
1.2
1.6
2
time [s]
k=6
k=0

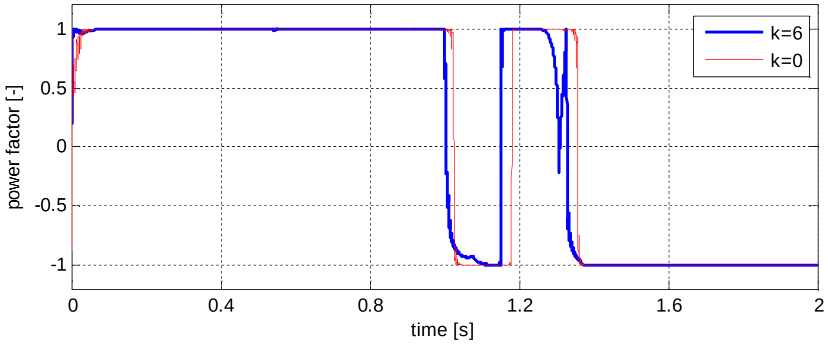
power factor [-]
1
0.5
0
-0.5
-1
0
0.4
0.8
1.2
1.6
2
time [s]
k=6
k=0

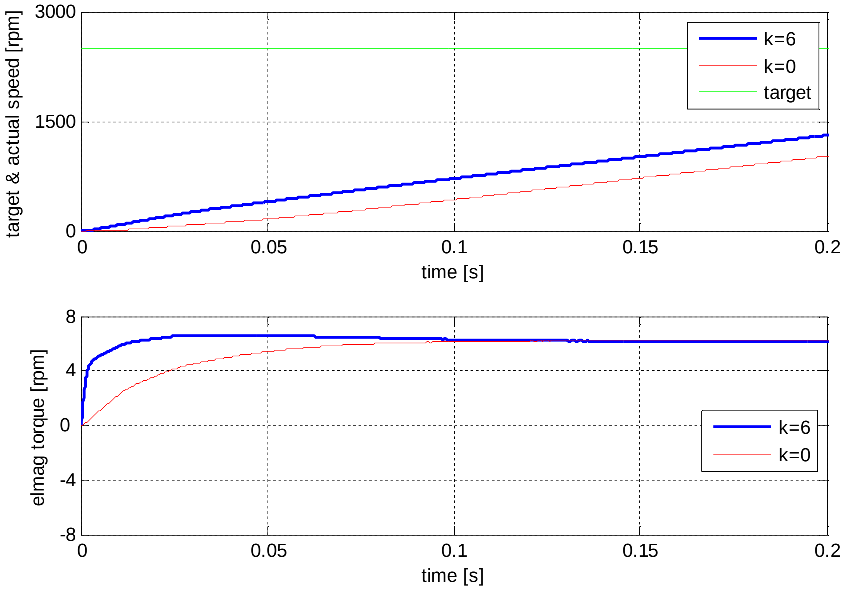

Fig. 4.21. The effect of zero and non-zero id during transients (from top to bottom): target and actual speed, electromagnetic torque, id and if currents, power factor, zoom in on speed and electromagnetic torque (k=0□ id*=0; k=6□ id*□0 during transients)

4.9. Experimental results

A. PEAK ACTIVE POWER vs SPEED at UNITY POWER FACTOR OPERATION

In order to confirm the very large constant power speed range of BEGA, at unity and high power factor operation, a set of experiments have been carried out, both for motoring and generating. The dc link voltage is 48V (12 x 4 valve regulated lead acid batteries connected in series). The rated speed of BEGA is 1500rpm. The Iqk current is 20A, experimentally derived. The maximum dc current is considered 5A, but for experiments a value of 4A is used due to strong machine core saturation above 4A. In the same time a value of 4.1A provide an efficiency increase of the machine due to dc field copper losses reduction from 163W (at if=5A) to 109W (at if=4A).

BEGA operation is divided in two regions (Fig. 4.22): a) constant torque region and b) constant power region. In constant torque region the desired torque can be produced without any voltage limitation due to the relatively low speed. In constant power region the peak torque can no longer be produced due to voltage limitation, but also due to the losses that increase over the limits, leading to the machine damage. As a consequence we are forced to operate at constant power over the rated speed. The constant power speed range is defined by equation (4.27):

$$CPRS = \frac{\omega_{r|p\_rated}}{\omega_{r\_rated}} \tag{4.27}$$

where is the maximum speed where the rated active power can be achieved, and is the machine rated speed.

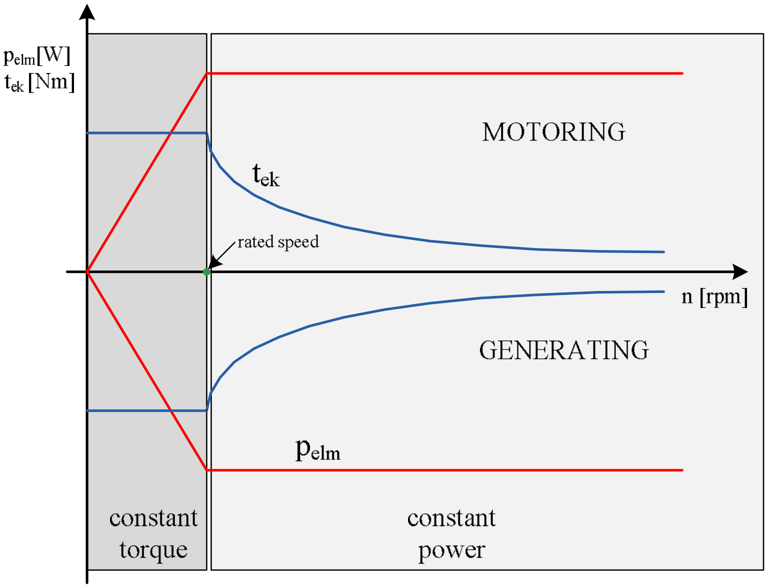

Fig. 4.22. Behavior of peak torque (tek) and peak power (pelm) vs rotor speed for wide speed range operation in motoring and generating

The measurement of BEGA active power vs speed envelope is performed over a speed range of 0-3000rpm, both for motoring and generating. Over the entire speed range the iq* current is kept constant at a value of 20A. Below the rated speed the field current, is also kept constant, in order to assure a constant electromagnetic torque below the rated speed. Over the rated speed the field current is decreasing slowly, while the power at battery terminals (motor terminals) is constant. The experimental results are shown in Fig. 4.23. Two ways were used for active power measurement: i) we measured the active power at the battery terminals using equation (4.10) and ii) we estimated the active power at machine terminals based on d-q machine model using equation (4.28)

$$P_{elm} = V_d I_d + V_q I_q \tag{4.28}$$

There is small difference between the measured active power at battery terminals and the estimated active power due to the inverter losses. On the other hand the accuracy of active power estimation at low power level is not so accurate. That is why for simplicity we considered in the experiments the active power of the motor the same as the power at the battery terminals.

For the same stator and rotor currents, the active power during motoring is lower than in generating mode, while the electromagnetic power is constant.

For motoring and generating, the active power is expressed as:

$$\begin{aligned} P_{mot} &\cong P_{batt} = P_{elm} + \Sigma P \quad , \text{ for motoring} \\ P_{gen} &\cong P_{batt} = P_{elm} - \Sigma P \quad , \text{ for generating} \end{aligned} \tag{4.29}$$

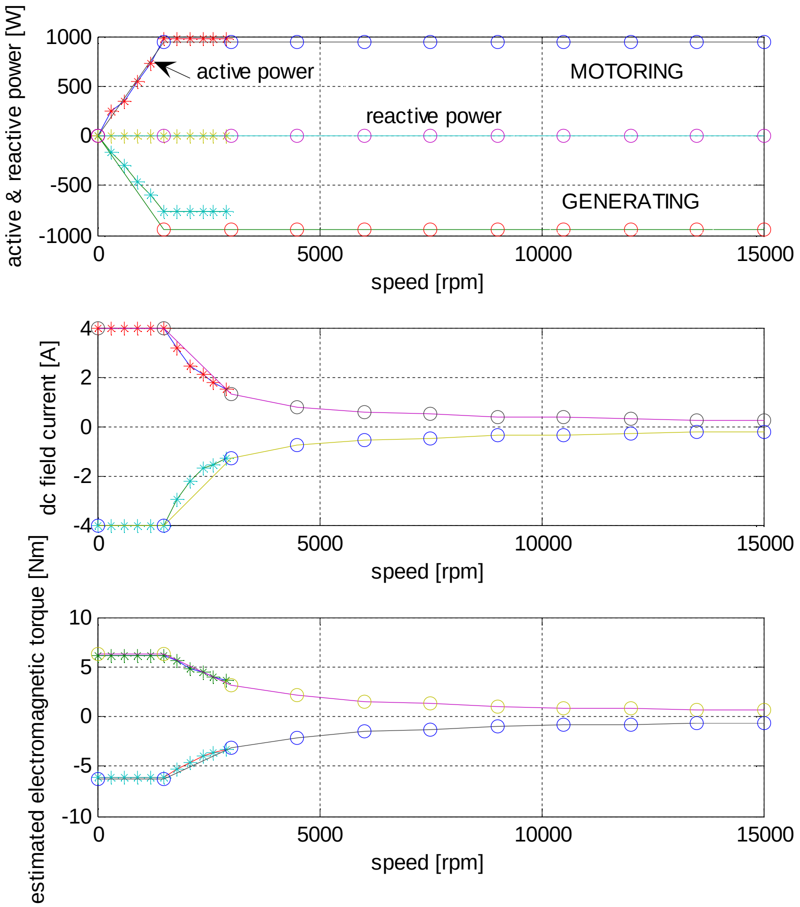

Figure 4. 23. BEGA measurements at unity power factor operation: a) active power during motoring (positive) and during generating (negative), b) dc. field current, c) estimated electromagnetic torque ('*'- measurements, 'o'-simulations)

It is clear from equation (4.29) that the deference between active power of BEGA during motoring and generating is two time the total losses in the machine.

$$P_{mot} - P_{gen} = P_{elm} + \Sigma P - \left(P_{elm} - \Sigma P\right) = 2 \cdot \Sigma P \qquad (4.30)$$

Since with the experimental results plotted in Fig. 4.23, the CPSR is 2, another experiment was carried out to demonstrate a CPRS of 8. For this the battery voltage was set to 12V (1/4 of rated dc voltage) and the rated speed was considered 375rpm (1/4 of rated speed). Now the rated power of the machine is considered that one obtained at 375rpm, which is, almost, 1/4 of the rated power (calculated for 1500rpm). The simulation and experimental results are shown in Fig. 4.24.

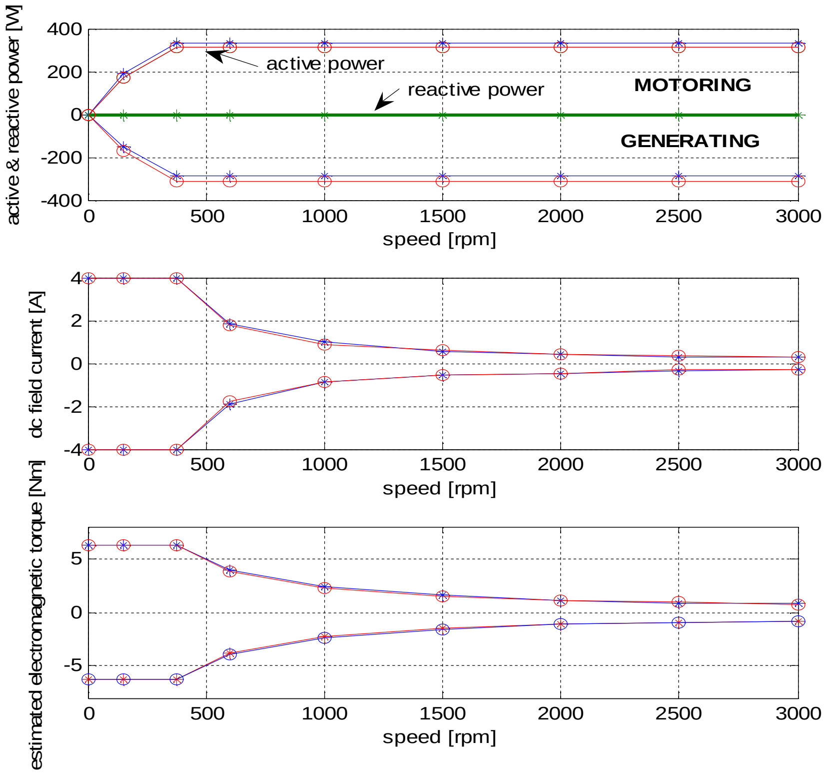

Fig. 4.24. BEGA measurements at unity power factor operation-12Vdc: a) active power during motoring (positive) and during generating (negative), b) dc. field current, c) estimated electromagnetic torque ('*'- measurements, 'o'-simulations)

Fig. 4.23. and Fig. 4.24. prove that BEGA has a very large constant power speed range (theoretically infinite) similar to dc machine with separate excitation. In Figure 4.24 it is shown the active power, battery current and dc field current, measured at rated speed (1500rpm) during BEGA operation in motoring mode, at unity power factor.

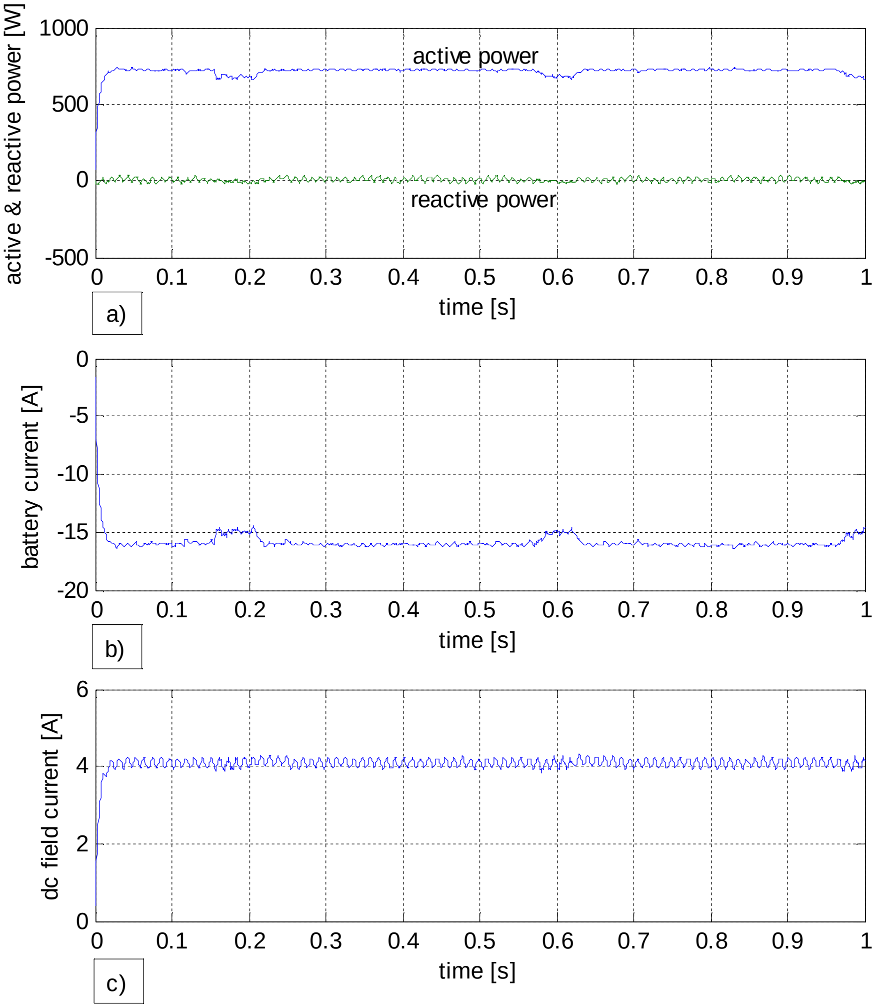

Figure 4.24. BEGA measurements at 1500rpm during motoring: a) active and reactive power, b) battery current c) dc. field current

Figure 4.25. proves that BEGA has the capability to operate over a very large constant power speed range, similar to the dc machine with separate excitation. Note that during acceleration, the machine is operating at unity power factor, also.
To investigate the BEGA operation during unity power factor operation and to characterize the steady-state and transient behavior, several additional experimental tests have been carried out.

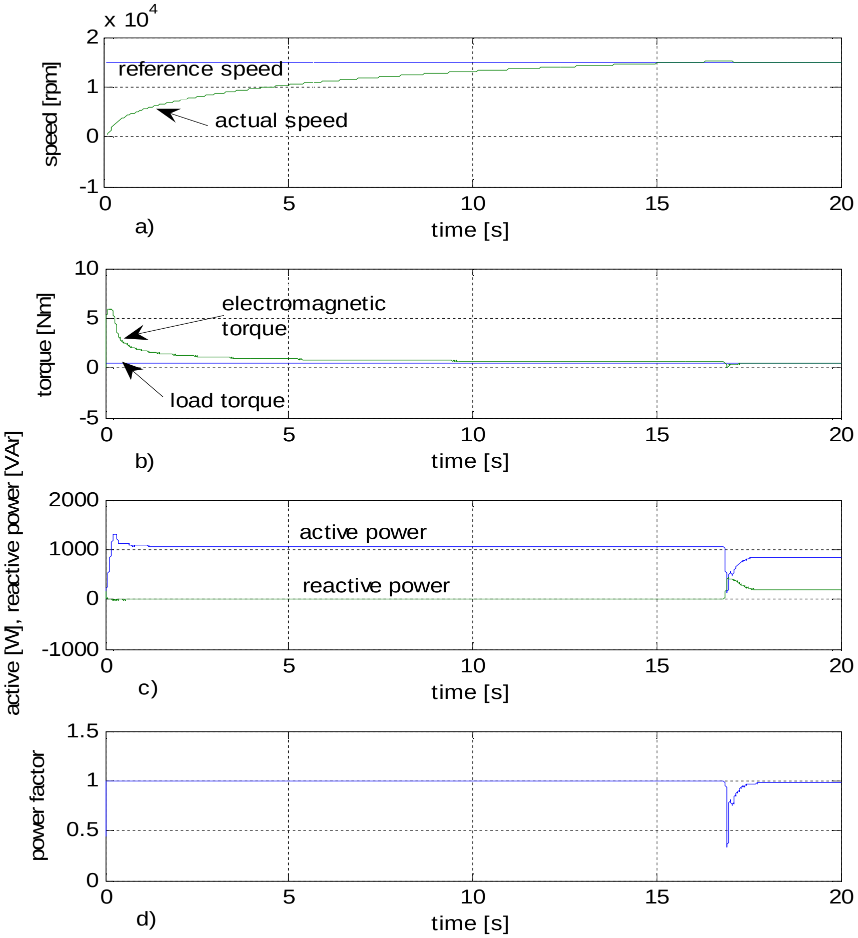

Figure 4.25. BEGA simulation results – reference speed =15000rpm: a) reference and actual speed, b) load and electromagnetic torque, c) active and reactive power, d) power factor

B. BEGA MOTOR/GENERATOR VECTOR CONTROLLED at (and near) UNITY POWER FACTOR OPERATION

Motor operation involves torque control or speed control close loop control. In HEVs the starter-alternator systems provide additional torque to the ICE torque to improve the overall efficiency of the vehicle as well as to allow fast vehicle acceleration.

BEGA capabilities (performance) at unity power factor operation are tested through experiments and the results are described in what follows.
The first experiment performed was the speed response from 0 to 1500rpm at constant load.

Switching from motor to generator at constant speed

The first dynamic experiment performed has been the switching from motoring to generating at constant speed. The reference speed is set constant at 2500rpm. Before time=1.5s, the torque is positive, and then it changes its sign becoming negative (see Fig. 4.26. d.). In this case, the machine is switching from motoring to generating. The dc field current (Fig. 4.26.c) changes its sign according to the torque sign, becoming negative. Some torque (and speed) oscillations occur, due to the vector controller of IM load drive that is switching from generating to motoring.

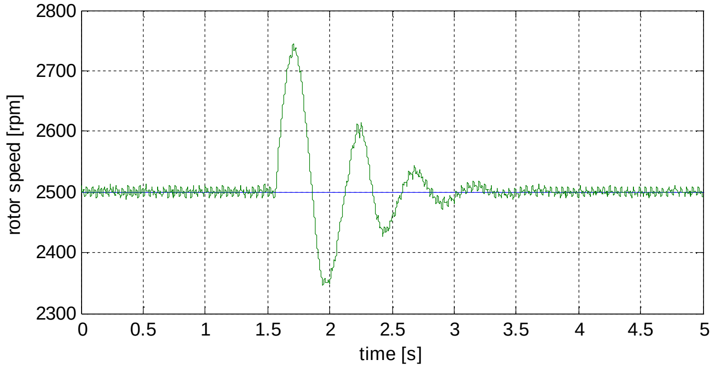

a)

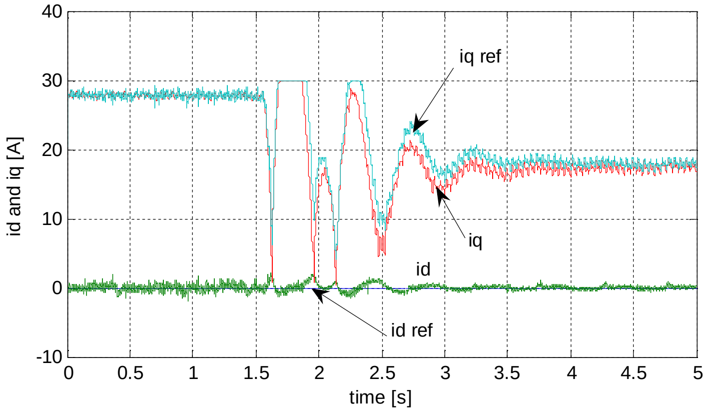

b)

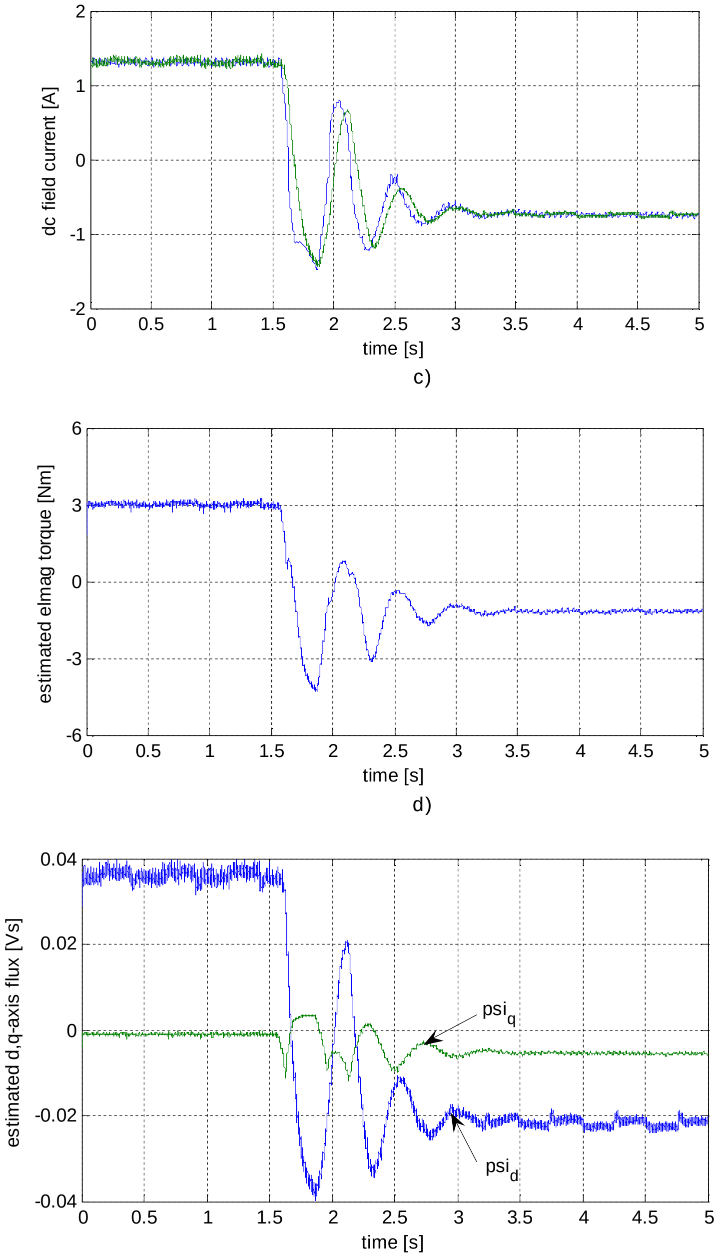

c)

d)

e)

Figure 4.26. Switching from motoring to generating a) reference and measured speed, b) reference and measured iq and id current c) reference and measured field current d) estimated electromagnetic torque, e) estimated d,q-axis flux

During motoring the unity power factor is achieved ( ), while during generating the power factor slightly decreased to the value of 0.95.
Speed reversal at constant load torque

The second experiment is a speed reversal from -2500rpm to 2500rpm. The experimental results are plotted in Fig. 4.27. Initially, the machine is running as a generator, charging the batteries (seen Fig. 4.27. g.), while at time=2.25s the speed reference changes its sign forcing the machine to operate as a motor. The deceleration is obtained by increasing the braking torque generated by BEGA still operating as a generator. The braking torque creates a high power pulse (three times in comparison with steady state) immediately after the changing of speed command (see Fig. 4.27. e.).

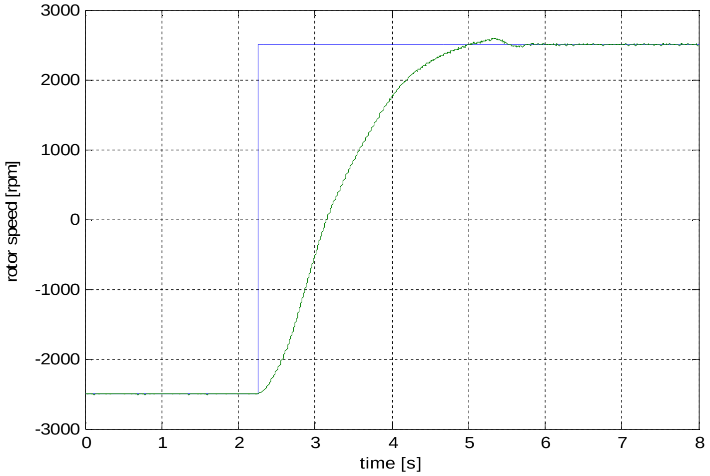

a)

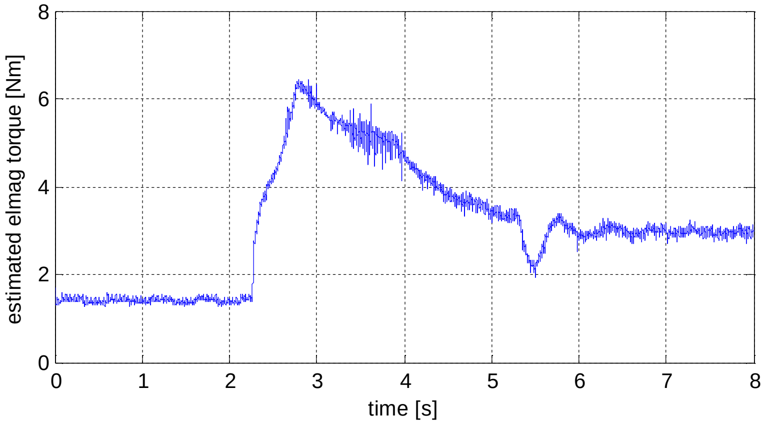

b)

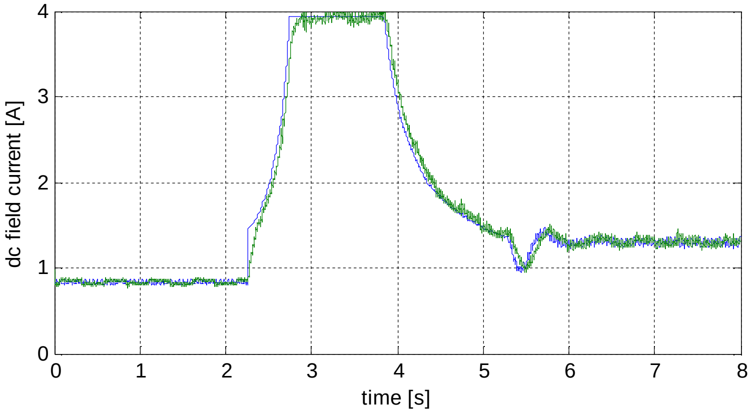

dc field current [A]
4
3
2
1
0
0
1
2
3
4
5
6
7
8
time [s]

c)

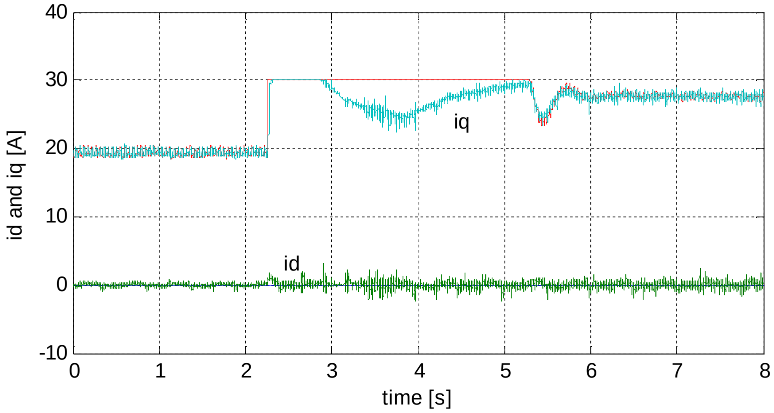

id and iq [A]
40
30
20
10
0
-10
iq
id
0
1
2
3
4
5
6
7
8
time [s]

d)

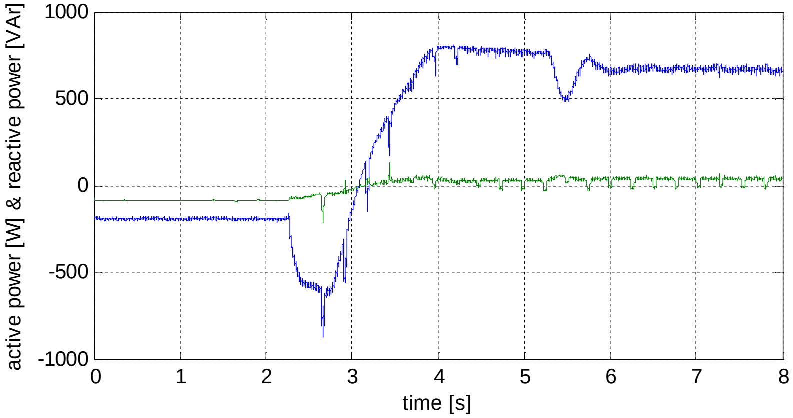

active power [W] & reactive power [VAr]
1000
500
0
-500
-1000
0
1
2
3
4
5
6
7
8
time [s]

e)

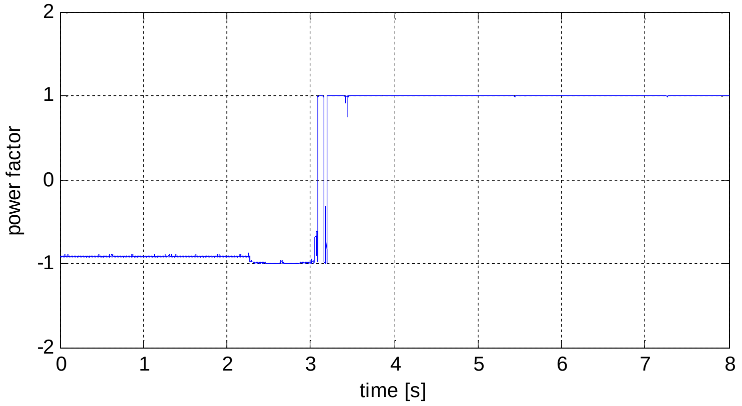

f)

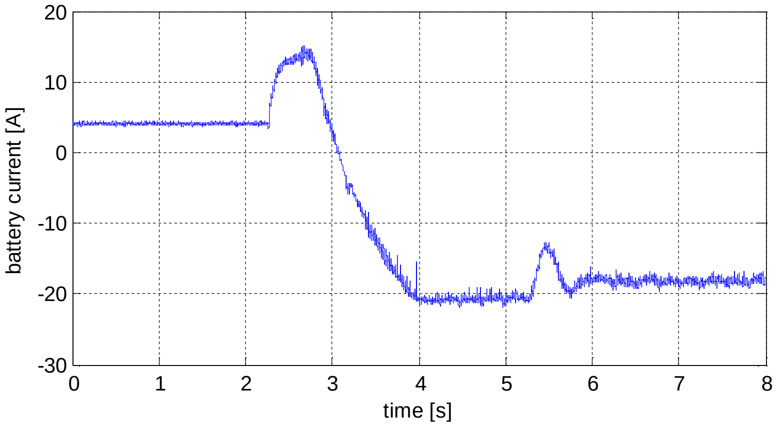

g)

Fig. 4.27. Speed step response a) reference and actual speed, b) estimated electromagnetic torque, c) reference and measured dc field current, d) reference and measured id , iq currents, e) active and reactive power f) power factor, g) battery current

It is worth noting that the dc. field current does not change its sign, even if the machine switches from generating to motoring. This is due to the fact that both power and speed change its sign in the same time (forcing the torque to remain positive as well as the dc field current). This is in contrast to the previous experiment (Fig. 4.26)) where the power (and torque and dc field current) changed its sign, while the speed remained positive. The iq current is not constant during motoring and generating due to the load (Fig. 4.27. d.) which is different.
Acceleration from zero to 3000rpm at no-load

The third experiment performed is an acceleration test from zero to 3000rpm. The experimental results are represented in Fig. 4.28. Below rated speed the dc field current is constant and closer to the maximum limit (4A), while the iq current is Iqk=30A, at the value required to cancel the q-axis flux. The unity power factor operation during acceleration is proved in Fig. 4.28.d. Above the rated speed (1500rpm) the current referencer automatically reduces the dc current reference (Fig. 4.28.c) and proportionally the electromagnetic torque (Fig. 4.28.b).

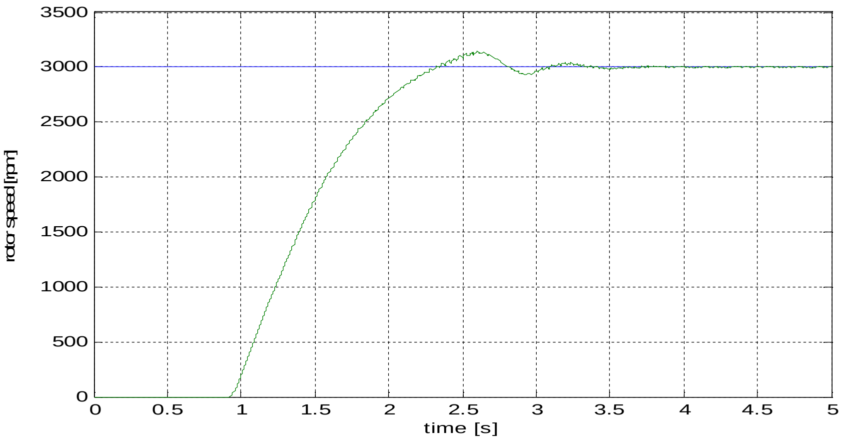

a)

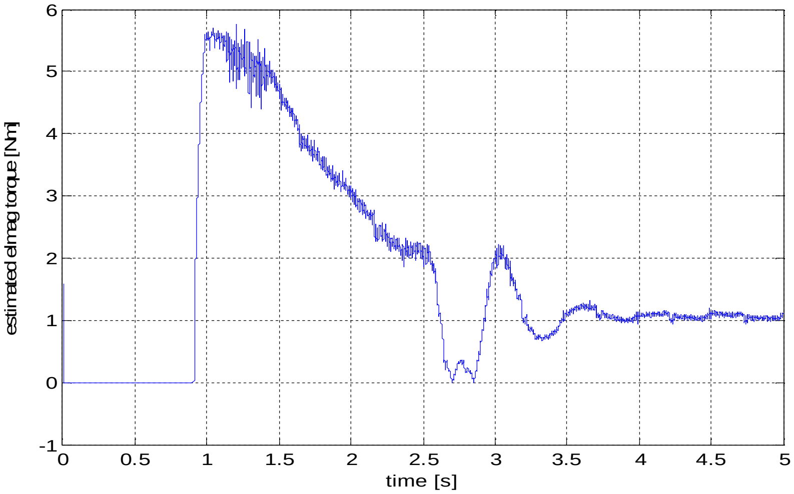

b)

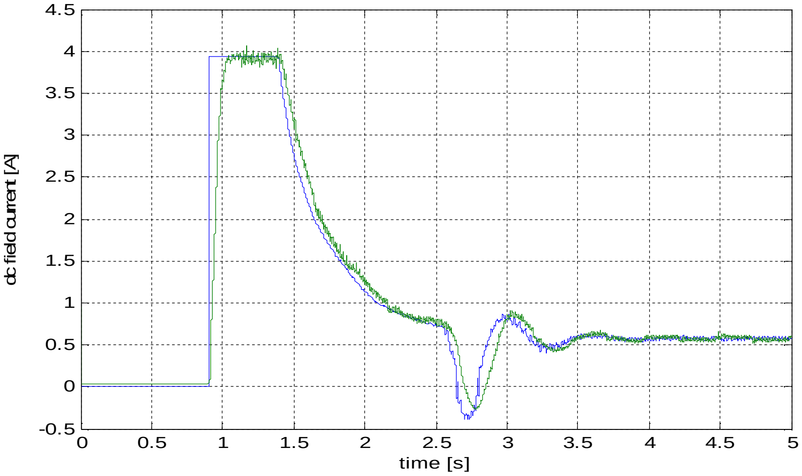

c)

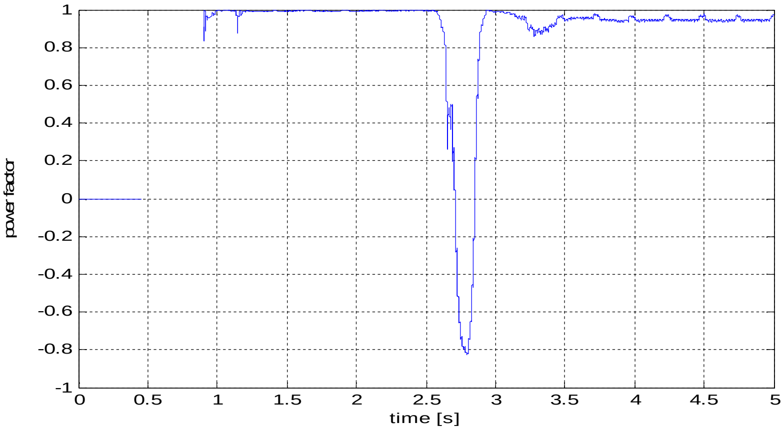

d)

Fig. 4.24. Acceleration from zero to 3000rpm: a) reference and measured speed, b) estimated electromagnetic torque c) reference and measured field current d) power factor

SUMMARY

In this chapter a vector control structure for BEGA operation at unity and high power factor operation, both for motoring and generating, was proposed. The control structure includes a current referencer (calculator) which computes, on-line, the reference current iq* and if*, in order to minimize the copper losses of BEGA, for lower torque levels. The very high constant power speed range of BEGA is demonstrated by experiments and digital simulations. In order to increase the torque response a simple solution has been proposed based on the dc field current error during transients.

REFERENCES

[4.1] T. Teratani, K. Kuramochi, H. Nakao, T. Tachibana, K. Yagi, S. Abou, "Development of Toyota mild-hybrid systems (THS-M) with 42V power net", Record of IEEE-IEMDC-2003, Madison, WU, 2003, pp. 3-10

[4.2] A. Vagati, A. Frata, P. Gugliehni, G. Franchi, F. Villata, "Comparison of ac motor based drives for electric vehicle applications", Record of PCIM-1999 Europe, Vol. IM, pp. 173-181

[4.3] E. C. Lovelace, T. Keim, J. H. Lang, T. M. Jahns, D. D. Wentzloff, J. Wai, P. McCleer, "Design and experimental verification of a direct-driven IPMSM using saturable parameter model", Record of IEEE-IAS-2002, vol. 4, pp. 2486-2492

[4.4] J. T. A. Jahns, "Component rating requirements for vehicle constant power operation of IPMSM", Record of IEEE-IAS-2000, Rome, pp. 1697-1704

[4.5] W. L. Soong, M. Ertugrul, E.C. Lovelace, T.M. Jahns, "Investigation of IPMSM offset coupled automotive integrated starter/alternator", Record of IEEE-IAS-2001

[4.6] I. Boldea, L. Tutelea, C. I. Pitic, "PM-assisted reluctance synchronous motor/generator (PM-RSM) for mild-hybrid vehicles: electromagnetic design", IEEE Trans. Ind. Appl., vol. 40, no. 2, pp. 492-498

[4.7] S. Chen, B. Lequesne, R. R. Henry, Y. Xao, J. Ronning, "Design and testing of a belt driven induction starter/generator", IEEE Trans. Ind. Appl., vol. 38, no. 6, 2002, pp. 1525-1532

[4.8] J. M. Miller, V. Stefanovic, V. Ostrovic, J. Kelly, "Design considerations for automotive integrated starter/generator with pole-phase modulation", Record of IEEE-IAS-2001, vol. 4, pp. 2366-2373

[4.9] A. Lange, W. R. Conders, F. Laube, H. Mosebach, "Comparison of different drive systems for a 75 KW electrical vehicle drive", Record of ICEM-2000, Vol. 2, pp.1308-1312

[4.10] J. M. Miller, V. R. Stefanovic, D. Kak, D. Delergus, “Progress for starter-alternator systems in Automotive Applications, Record of EPE-PEMC-2002, Dubrovnik&Cavtat, Croatia

[4.11] J. A. Tapia, F. Leonardi, T. A. Lipo, "Consequent pole permanent magnet machine with field weakening capability", IEEE Trans. Ind. Appl., vol. 39, no. 6, pp. 1704-1709, Nov./Dec. 2003.

[4.12] E. C. Lovelace. T. M. Jahns, J. L. Kirtley, J. M. Lang, “An interior PM starter-alternator for automotive application”, Record of ICEM-1998, Instambul, Vol. 3, pp. 1802-1808

[4.13] A. Emadi, M. Ehsani, J. Miller, “Vehicular Electric Power System”, book, Marcel Dekker Inc, New York, 2004

[4.14] H. Bausch, A. Grief, K. kamelis, A. Milke, “Torque control of battery supplied switched reluctance motor drives for electric vehicle”, Record of ICEM-1998, Instambul, Vol. 1, pp. 229-239

[4.15] R. B. Inderka, R. De Doncker, “Control of switched reluctance drives for electric vehicle applications”, IEEE Trans. Vol. IE-49, no. 1, 2002, pp. 48-53

[4.16] I. Boldea, S. Scridon, L. Tutelea, “BEGA-a biaxial excitation generator for automobiles”, Record of OPTIM-2000, Poiana Brasov, Romania, vol

[4.17] S. Scridon, I. Boldea, L. Tutelea, F. Blaabjerg, E. Ritchie, “BEGA: Comprehensive characterization and test results ”, Record of IEEE-IAS-2004, Seattle, USA

[4.18] S. Scridon, I. Boldea, L. Tutelea, F. Blaajberg, A. E. Ritchie, “BEGA – A Biaxial Excitation Generator for Automobiles: Comprehensive Characterization and Test Results”, IEEE Trans. Vol. IA-41, no. 4, 2005, pp. 935-945

[4.19] V. Coroban, I. Boldea, G. D. Andreescu, F. Blaajberg, “BEGA – Motor/Generator Vector Control for Wide Constant Power Speed Range”, Record of OPTIM2006, Brasov, Romania

[4.20] D. Fodorean, A. Djerdir, I. A. Viorel, A. Miraoui, “A Double Excited Synchronous Machine for Direct Drive Application – Design and Prototype Tests”, IEEE Trans. Vol. EC-22, no. 3, 2007, pp. 656-665

[4.21] D. Fodorean, I. A. Viorel, A. Djerdir, A. Miraoui, "Double-Excited Synchronous Motor with Wide Speed Range: Numerical and Experimental Results", Iranian Journal of Electrical and Computer Engineering, Vol. 5, No. 1, Winter-Spring 2006

[4.22] D. Fodorean, A. Djerdir, A. Miraoui, and I. A. Viorel, "Flux. Weakening Performances for a Double-Excited Machine", ICEM 2004

[4.23] Y. Dai, L. Song, S. Cui, "Development of PMSM Drives for Hybrid Electric Car Applications", IEEE Trans. on. Magnetics, Vol. 43, No. 1, January 2007

[4.24] M. R. Dubois, N. Dehlinger, H. Polinder, D. Massicotte, "Clawpole Transverse Flux Machine with Hybrid Stator"

[4.25] A. Masmoudi, A. Njeh, A. Mansouri, H. Trabelsi, "Optimizing the Overlap Between the Stator Teeth of a Claw Pole Transverse-Flux Permanent-Magnet Machine", IEEE Trans. on Magnetics, 2004

[4.26] V. Coroban, I. Boldea, G.D. Andreescu, F. Blaabjerg, “BEGA - Motor/generator vector control for wide constant power speed range”, in Proc. 10th Int. Conf. on Optimization of Electrical and Electronic Equipment OPTIM 2006, Brasov, 18-19 May, 2006

5. ACTIVE-FLUX STATE OBSERVER FOR BIAXIAL EXCITATION GENERATOR FOR AUTOMOBILES (BEGA) VECTOR CONTROL

5.1. Introduction

Permanent magnet synchronous motors are a good solution for integrated starter-alternator systems for hybrid electric vehicles due to their high power density, high efficiency, high torque/power density, low inertia. Synchronous machines as starter-alternators are proposed in several configurations: interior permanent magnet synchronous motors (IPMSM), surface permanent magnets synchronous motors (SPMSM), permanent-magnet assisted synchronous reluctance motors (PM-RSM), and hybrid excited synchronous motors (HESM). High control performance (fast torque response, very good speed regulation, very low speed control) can be achieved with permanent magnet synchronous motor equipped with position sensor. In hybrid electric vehicle applications, the elimination of position/speed sensors is desired because of mounting difficulties, cost reasons, EMC. Consequently, the benefits of position sensor missing are: reduced hardware complexity and lower cost, reduced size of the drives, elimination of the sensor cables, better noise immunity and less maintenance.
In hybrid electric vehicles the electric machine has to operate in a very large speed range from a few rpm up to the maximum speed. Also, fast torque response is requested for vehicle acceleration and internal combustion engine cranking (e.g. when the vehicle is at stop light). Therefore high performance and robust control algorithms for the electric machine is a must.

In the past different sensorless control methods have been proposed. These methods are open loop structures (estimators) or close loop structures (observers). In what follows, an attempt to provide a short overview of the existing sensorless control methods for permanent magnet synchronous machines is tried.

5.1.1 Method based on stator inductance calculation

For interior permanent magnet synchronous motor the stator phase inductance is a function of rotor position θ_r and it varies twice with the motor electrical frequency/position. Consequently, if the stator phase inductance is known, the motor position is known. Based on this property of the machine, in [5.1] is proposed a method to calculate the motor rotor position using the measured stator phase currents and voltage. For example the inductance of the phase “a” is calculated as follows:

$$L_{sa} = \frac{v_a - e_a - r_s i_a}{\frac{di_a}{dt}} \qquad (5.1)$$

The back-EMF value is calculated based on the last two calculated position samplings. There is a proportional relationship between the position derivative (speed) and back-EMF. Some problems could raise in transients when the calculation of the back-EMF is not very precisely and when the rotor temperature is varying, because the permanent magnet flux is also affected by the temperature.
The reference stator inductance values, that are stored in a look-up-table, are measured off-line, in advance, more accurate. The on-line estimated values of the inductances are compared with those stored in the look-up-tables and then the estimated rotor position is derived. For the same position, the variation of inductance with the stator flux, due to saturation, raises additional problems, also. Anyway, this is an open loop method and a high accuracy of the rotor position, can not be guaranteed.

5.1.2 Back-EMF integration

Rotor position estimation based on voltage integration is proposed in [5.2]. In steady state, the stator flux and rotor flux are rotating synchronous. The angle difference between these two flux vectors is the load angle. If the stator flux vector is known, then the rotor flux angle can be calculated. The rotor position is given by the rotor (permanent magnet) flux angle. The stator flux can be obtained by voltage integration:

$$\Psi_{ds} = \int (v_{ds} - r_s i_{ds}) \quad ; \quad \Psi_{qs} = \int (v_{qs} - r_s i_{qs}) \tag{5.2}$$

The angle of stator flux vector is:

$$\theta_{\Psi s} = arctan\left(\frac{\Psi_{ds}}{\Psi_{qs}}\right) \tag{5.3}$$

For surface permanent magnet synchronous machine, where the stator inductance is not varying, the rotor flux can be calculated:

$$\overline{\Psi}_r = \overline{\Psi}_s - L_s \overline{I}_s \tag{5.4}$$

This method provides good results only at higher speeds, while at low and very low speeds it fails. The stator resistance R_s plays an important role in the equation since it is affected by the temperature – which most of the cases is not known. The voltage drops on the stator resistance dominates the integrator input at low speeds, when the supply voltage vs is low, also. For better results the initial value of the integrators are important. Pure integration (which leads to drifts in the estimated flux) and sensitivity of the model to the stator resistance variation constitute major problems regarding the reliability and robustness of this method. In [5.3] is proposed a programmable low-pass filter to solve the dc-drift problems associated to the pure integrator. The particularity of this solution is that the gain of the filter is speed dependent and it is decreased with the increase of the motor speed.

5.1.3 Extended electromotive force (EMF)

In [5.4], [5.5], [5.6], [5.7] are proposed sensorless control strategies for IPMSM. The speed and position are obtained based on extended EMF. The extended EMF is obtained by a least-order observer and the furthermore the estimated position error is obtained from EMF. The speed and position are then corrected so that the position and speed error becomes zero.

Taking into account the extended EMF, the mathematical model for IPMSM is expressed:

$$\begin{bmatrix} v_d \\ v_q \end{bmatrix} = \begin{bmatrix} R_s + sL_d & \omega_e L_d \\ \omega_e L_q & R_s + sL_q \end{bmatrix} \begin{bmatrix} i_d \\ i_q \end{bmatrix} + \begin{bmatrix} 0 \\ (L_d - L_q)(\omega_e i_d - s i_q) + \omega_e \Psi_{PM} \end{bmatrix} \quad (5.5)$$

Where the extended EMF is defines as:

$$E_{ex} = (L_d - L_q)(\omega_e i_d - s i_q) + \omega_e \Psi_{PM} \quad (5.6)$$

In this way, the voltage equation is identical with that of SMPM. The problem is that the extended EMF is influenced by the stator currents id and iq, which are varying during transients. Also, the inductances Ld or Lq are affected by the saturation, therefore a knowledge of their variation with the currents will help for better results at lower speeds. In the low speed range this solution is not reliable and robust. To overcome these drawbacks, in [5.7] is proposed a combined solution that uses extended EMF method for high speed and INFORM method for low speed operation.

5.1.4 Extended Kalman Filter (EKF)

The EKF based observers are a good alternative to estimate the rotor speed and position [5.8]-[5.14]. An advantage of EKF is that it is less influenced by the measurement noise, and parameters inaccuracy is not so critical that in conventional back EMF estimation methods.
A standard EKF observer contains three steps [5.10]:

1) Prediction step

$$xe_{k|k-1} = xe_{k|k-1} + \left[F\left(xe_{k-1|k-1}\right)xe_{k-1|k-1} + B\left(u_{k-1}\right)\right]T_c$$

$$P_{k|k-1} = P_{k|k-1} + \left(F_{k-1}P_{k-1|k-1} + P_{k-1|k-1}F'_{k-1}\right)T_c + Q_d$$

2) Innovation step

$$xe_{k|k} = xe_{k|k-1} + K_k\left(y_k - h\left(xe_{k|k-1}\right)\right)$$

$$P_{k|k-1} = P_{k|k-1} + \left(F_{k-1}P_{k-1|k-1} + P_{k-1|k-1}F'_{k-1}\right)T_c + Q_d$$

3) Kalman gain

$$K_k = P_{k|k-1}H'_k\left(HP_{k|k-1}H'_k + R\right)^{-1}$$

where: x - system state vector, xe - estimated state vector, u - system input vector, y - system output vector, H - system output matrix, K - Kalman gain matrix, P - state error covariance matrix, Q - model noise covariance matrix, R - measurement noise covariance matrix, F - Jacobian of system state functional.
Choosing different state variables leads to different EKF observers:

$$x = \left\lfloor i_\alpha \; i_\beta \; \omega_r \; \theta \right\rfloor$$

$$x = \left\lfloor i_d \; i_q \; \omega_r \; \theta \right\rfloor$$

A crucial step in Kalman filter design is the choice of the elements of the covariance matrices Q and R, since they influenced the performance, convergence and stability. R is related to the measurement noise. Increasing the value of R will assume that the measured current is affected by noise, and is not so reliable. Consequently, the filter gain K will decrease, resulting in a poorer response during transients. Q is related to the parameter uncertainties. High values for Q means higher parameters uncertainties. An increase of Q will result in faster filter dynamics but poor performance during steady state.

Kalman filter based algorithms are computationally intensive and time consuming. Heavy computational load from variance matrix makes EKF difficult to apply in industry. A reduced-order Linear Kalman Filter for PMSM estimation is presented in [5.12]. A detailed description of an EKF implementation can be found in [5.14].

5.1.5 Model Reference Adaptive System (MRAS)

The MRAS principle is that the error between the real measured signal and estimated signal from the machine model is in a relationship with the estimated signal. A PI mechanism is used to obtain the estimated speed. As the error signal becomes minimized by the PI, the tuning signal ω approaches the actual speed ω of the machine.

Based on MRAS principle in [5.15] is proposed a speed observer that uses voltage model and current model to calculate the stator flux. The error between these two fluxes is used to estimate the rotor speed. The estimated speed depends greatly on the motor parameter accuracy. In order to overcome this problem, in [5.16], [5.17] a combined method is suggested. The idea comes from high frequency injection method. In the proposed method a calibration signal ☐ containing estimated angle error is used for the calculation of the stator flux using voltage model. The authors claim that the proposed solution have good steady state accuracy and good dynamic properties over a wide speed range. A MRAS method based on stator current is presented in [5.18]. The speed is estimated using a PI integration of the current error between the measured (id, iq) and estimated currents ( ) from the machine model. The stability of the system is guaranteed by the Popov stability theory.

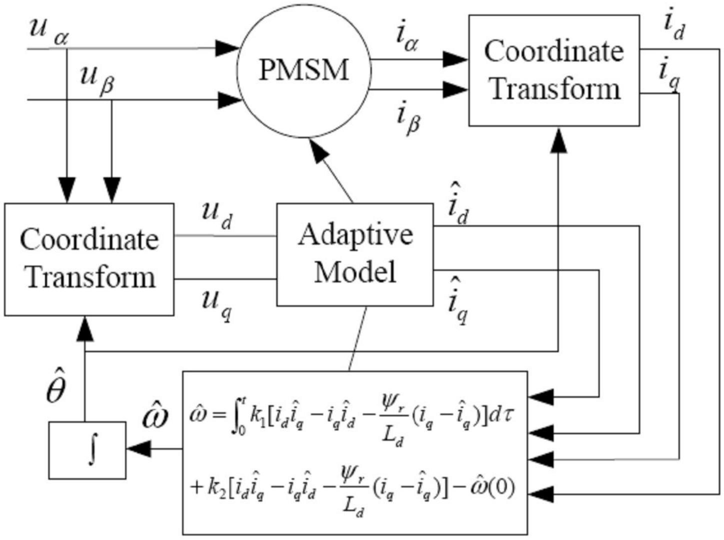

Fig.2 MRAS based on stator current

Figure 5.1. MRAS based on stator current

5.1.6 Sliding Mode Observer

A number of estimation techniques have been developed to achieve speed and position sensorless PMSM drives. Most of them suffer from variation of motor parameters such as the stator resistance, stator inductance and torque constant. Also, it is known that conventional linear estimators are not adaptive to variations of the operating point in a nonlinear system. Sliding mode observer illustrates the idea to construct a speed observer based on motor equations but not merely confined to the basic structure [5.19]-[5.28]. In SMO, the current error vector ΔIs is used to define the sliding hyperplane of the sliding mode compensator [5.19][5.20]. The magnitude of the estimation error ΔIs is forced to the vicinity of zero by a high-frequency nonlinear switching controller. The switched complex signal is directly used to exert a compensating influence on the machine model. The robustness of the sliding mode approach ensures zero error of the estimated stator current.

SMO and the estimated back EMF:

$$\begin{aligned}
\frac{di_\alpha}{dt} &= -\frac{R}{L}i_\alpha+\frac{1}{L}e_\alpha-\frac{l_1}{L}sign(i_\alpha)\\
\frac{di_\beta}{dt} &= -\frac{R}{L}i_\beta+\frac{1}{L}e_\beta-\frac{l_1}{L}sign(i_\beta)\\
\hat{e}_\alpha &= k\cdot sign(\hat{i}_\alpha-i_\alpha)\cdot\frac{\omega_c}{s+\omega_c}\\
\hat{e}_\beta &= k\cdot sign(\hat{i}_\beta-i_\beta)\cdot\frac{\omega_c}{s+\omega_c}
\end{aligned} \tag{5.7}$$

Using the reconstructed back EMF, the rotor position and motor speed is estimated:

$$\hat{\theta}_r = a\tan\left(\frac{\hat{e}_\alpha}{\hat{e}_\beta}\right) \tag{5.8}$$

Paper [5.21] proposed a new SMO method by properly choosing gain coefficient, aiming at full speed range operation especially for improving low speed range performance. But in the low speed range only 20% of rated speed was tested. The nearly zero speed range is still unverified. In [5.22] another sliding mode control method is proposed. In this method, not only the speed, but also stator resistor is online estimated using SMO. SMO doesn't need coordinate transformation, thus it won't introduce error due to position estimation transient deviation. By comparing the real and the estimated stator current, it is simple and to ensure the accuracy speed estimation comparing to other methods where coordination transformation is involved. The sufficient high switching gain satisfies the necessary condition for SMO convergence in the high speed range. This gain of the error compensator increases when a sliding mode controller is employed for observer tuning. The problem is, good steady state result versus fast convergence rate is a conflict. In order to get accurate speed estimation result, the convergence rate cannot be properly assured, especially for wide speed range operation. In principal the sliding model observer is always switching due to the existence of sliding surface. This will introduce error to the estimated value in the steady state. Finally, in low speed range there will be big error in the back EMF estimation, because the back EMF is a normally small value at low speed.

5.1.7 High frequency signal injection

The main problem of the electric machines is that the accuracy of rotor position estimation is dependent on the magnitude of the back-EMF voltage, which is proportional with the rotor speed. The performance is degraded significantly in the low speed region, where the magnitude of the back-EMF voltage is small. As a consequence, the permanent magnet motors have to be started open loop with an arbitrary voltage sequence and brought to a speed good enough for back-EMF detection. Such an approach has limited starting torque capability. Also, this method does not guarantee that the motor will start from the beginning in the right direction. This two criteria which are enough to claim that other solutions has to be find and implemented for low speed, where the starter-alternators system can operates frequently (especially in urban driving cycle).

To overcome these drawbacks high frequency signal injection based methods have been proposed [5.27] – [5.53]. This method is based on the magnetic saliency properties. By injecting voltage or current signals having higher frequencies than the fundamental, the response signal can be used to detect the rotor position. There are two forms of carriers signal injection techniques:

- Rotating vector [5.29], [5.30]
- Pulsating vector

Rotating vector techniques inject a balanced three-phase voltage or current carrier signal to form a rotating excitation vector. The machine response signals are modulated by the magnetic saliency position. Rotor position is estimated from the phase modulated response.

When a rotating carrier voltage vector is applied, the resulting high frequency current vector consists of two components. The first term on right-hand side of the current does not have any position-related information, whereas the second term is phase modulated by the angular position, θe, of the saliency, and can therefore be used to estimate the saliency position.

$$\begin{aligned} v^{s}_{dq\_c} &= V_c e^{j\theta_c} \approx L^{s}_{dq} \frac{di^{s}_{dq\_c}}{dt} \\ i^{s}_{dq\_c} &= -jI_{cp} e^{j\omega_c t} - jI_{cn} e^{j\omega_c t \pm h\theta_e} \end{aligned} \tag{5.9}$$

Pulsating vector techniques inject a voltage or current along the d or q axis. Position is estimated by minimization of the amplitude modulated carrier frequency response signal measured along the axis orthogonal to the injection axis. An advantage of the pulsating vector injection is that, since the carrier current in d-axis does not affect torque production, significantly higher amplitudes can be used for magnet polarity estimation in a two step process [5.35].

In both cases, the voltage injection is usually preferred, which results in carrier current which is measured and processes to estimate the rotor position.

If a pulsating carrier voltage signal injected in d-axis, the resulting current vector signal in the rotor reference frame is shown below. The first term in the right-hand side of the current does not contain any position related information, whereas the second one is phase modulated by the angular position of the saliency.

$$\begin{aligned} v^{r'}_{dq\_c} &= V_c \cos(\omega_c t) \approx L^{r'}_{dq} \frac{di^{r'}_{dq\_c}}{dt} \\ i^{r'}_{dq\_c} &= \left(I_{cp} + jI_{cn} e^{j(\pm h\theta_e)} \right) \sin(\omega_c t) \end{aligned} \tag{5.10}$$

Block diagrams of the basic signal processing and estimation schemes proposed in [5.34] are shown in Fig. 5.2

Carrier signal injection – based techniques are affected by the dead-time and other inverter nonlinearities [5.31], [5.32]. The effect of parasitic capacitances of the power devices during the dead-time has been found to be the main contributor to carrier-signal distortion. In [5.33], [5.34], a comparative analysis of pulsating versus rotating vector carrier signal injection techniques is performed. It was found that the accuracy of the two methods is the same, but pulsating carrier method is potentially less sensitive to the dead-time, but additional investigations are required to confirm. Differences in accuracy between the two methods have to be found in electromagnetic noise. Carrier voltage phase distortion due to inverter dead time is affecting both types of carrier excitation equally.

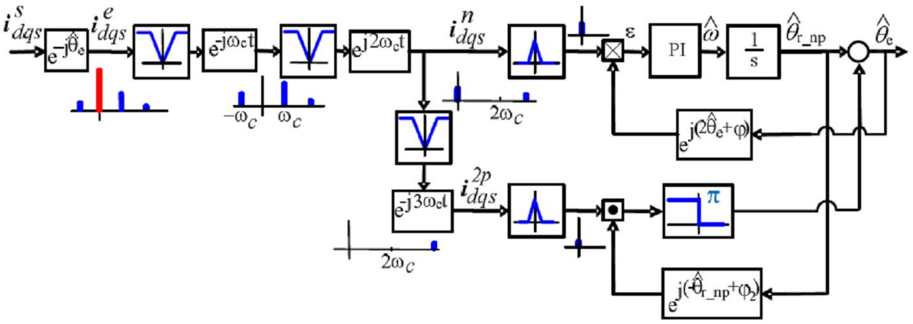

a) Rotating vector injection-based position tracking

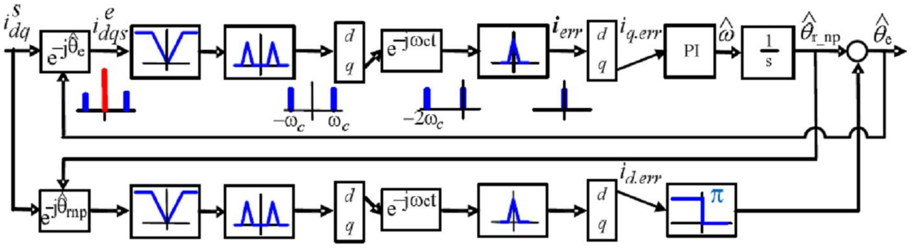

b) Pulsating vector injection-based position tracking

Fig. 5.2. Position estimation scheme using a) rotating vector injection and b) pulsating vector injection [5.34]

5.1.8 Low frequency signal injection

LF injection [5.54] is another method for motor speed estimation in the low speed range. In the proposed method, low frequency current is injected into the reference d-axis. The injected current will cause speed transient variation (due to torque oscillation) which indicates a speed estimation error. This error is then used to form a speed calibration value, and finally to estimate rotor position:

$$\hat{e}_{cq} = \cos\tilde{\theta}\,\sin\tilde{\theta}\,\frac{3p^2\psi_m^2 I_c}{J\omega_c} \approx \tilde{\theta}\,\frac{3p^2\psi_m^2 I_c}{J\omega_c}\sin(\omega_c t) \qquad (5.11)$$

LF injection method is originally designed for the speed estimation of IPM motor at low speed. The saliency of the motor is a distortion for this method. Thus the basic idea is quite different from the high frequency methods, where the saliency is a necessary condition for the estimator. Typical injection frequency is between a few Hz to a few hundred Hz according to the ratio of p2/J. The position error signal is dependent on motor mechanical parameter J. If J is too high this estimator method cannot be applied. In most cases, no accurate value of J can be acquired; this will cause trouble to the observer. The slow dynamic response is another drawback of this estimator.

5.1.9 INFORM

Rotor position estimation of permanent magnet synchronous machines (PMSM) at low speeds and standstill can be realized by utilizing position dependent inductance values of the stator windings which may be caused by saturation and/or reluctance effects. One of the methods is the so-called INFORM (“Indirect Flux detection by On-line Reactance Measurement”) [5.55]-[5.60]. This method is first introduced in [5.56]. The basic idea of INFORM is to measure the current response, which is evoked by voltage space vectors applied in different directions, and using this current to identify inductance variation. In detail, a sequence of voltage space vectors is applied to the motor via the inverter and the current reaction is measured [5.56]. The author defines the INFORM inductance as follows:

$$l_{INFORM} = \frac{\bar{u}_S}{d\bar{i}_S / dt} \tag{5.12}$$

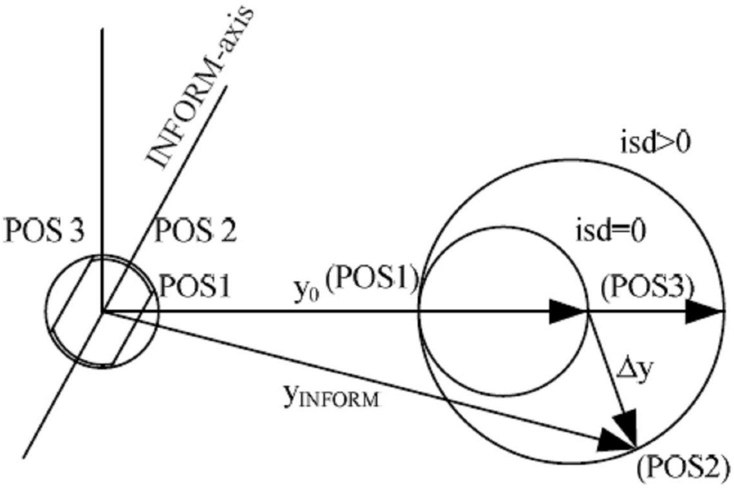

Fig. 5.3 Complex function yINFORM

The parameter lINFORM is the so called p.u. complex INFORM reactance containing the desired dependence on the rotor position:

$$l_{INFORM} = l_{INFORM}\left(2\gamma_m - 2\gamma_u\right) \tag{5.13}$$

l_{INFORM} is an 180° periodic function periodically changing with motor position. Its calculation is simple and no need to use motor equations. Thus this method is parameter insensitive. Yet the calculation is based on the assumption that motor flux is sinusoidally distributed, so a flux distortion will cause speed estimation error, and the influence needs to be further checked. Another disadvantage is that in the steady state the applied testing voltages will cause current ripple. This is the biggest disadvantage of this method. In Fig. 5.4 is depicted the inductance calculated on one phase using INFORM method and the ideal inductance.

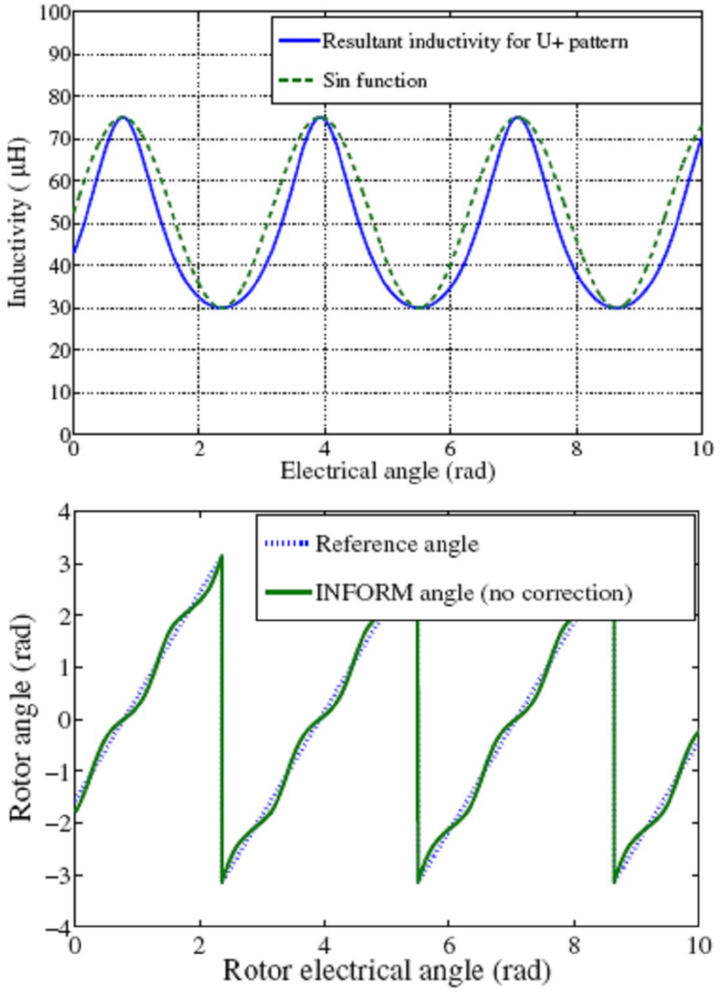

Fig.5.4 Top: resultant inductivity (Lu(v,w)) of the machine compared with a sinus signal [5.60], bottom: reference rotor angle and INFORM angle on PMSM

5.1.10 Adaptive control

In [5.61] a simple adaptive control method is proposed. For known magnitude of the permanent magnet $\psi_{PMref} = \psi_{PM}$, the observer (Fig.5.5) can be seen as a rotor field angle observer.

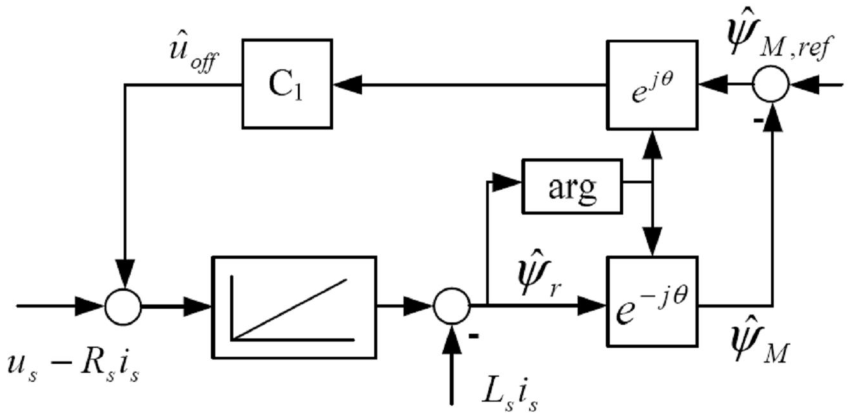

Fig. 5.5. Signal flow graph for adaptive control

Its advantage is that this method concerns compensating voltage offset (uoff), and a calibration loop (with rotor flux) is introduced, which makes the estimation somewhat more accurate. Yet the proposed method is based on motor fundamental equations, so it's dependent on parameter accuracy. Its performance cannot be guaranteed for wide speed range operation, especially in low speed region.

5.2. Active flux concept

The "active flux" concept proposed in [5.63] turns all salient-pole rotor ac machines into virtually nonsalient-pole machine, such that the rotor position and speed estimation becomes simpler. The active flux is aligned to the rotor d-axis. Consequently, the position of the active flux vector will be expressed in relationship with d-axis. The active flux concept has been already implemented and tested for interior permanent magnet synchronous machines [5.63]-[5.65] and reluctance synchronous machines [5.66]. Since active flux was introduced in [5.63] as a general concept for all types of synchronous and induction machines, now this will be in details investigated for BEGA.
For the beginning let us start with the BEGA mathematical model.

The BEGA transient equations in d-q reference frame are:

$$\overline{V}_S = R_S \overline{I}_S + \frac{d\overline{\Psi}_S}{dt} + j\omega_r \overline{\Psi}_S \tag{5.14}$$

$$\overline{V}_S = V_d + jV_q \quad , \quad \overline{I}_S = I_d + jI_q \ , \ \overline{\Psi}_S = \Psi_d + j\Psi_q \tag{5.15}$$

$$\Psi_d = L_d I_d + L_{mf} I_f \quad , \ \Psi_q = L_q I_q - \Psi_{PM} \tag{5.16}$$

$$\begin{gathered} T_e = \frac{3}{2} p_1 \left(\Psi_d I_q - \Psi_d I_q\right) \\ T_e = \frac{3}{2} p_1 \left(L_{mf} I_f I_q + \left(L_d - L_q\right) I_d I_q + \Psi_{PM} I_d\right) \end{gathered} \tag{5.17}$$

$$V_f = R_f I_f + \frac{d\Psi_f}{dt} \quad , \quad \Psi_f = L_{mf} I_d + L_f I_f \tag{5.18}$$

where V_s, I_s are the stator voltage and current vector respectively, Ψs is the stator flux linkage vector, R_s is the stator resistance, ωr is the electrical rotor speed, $L_{d,q}$ are the d, q axis inductance, L_{mf} is the mutual field-armature inductance, Ψ_{PM} is the PM flux on q axis, and p is the pole pair. Equation (5.18) characterizes the dc field (excitation) circuit, where V_f and I_f is the field voltage and current respectively, Ψ_f is the field flux, and R_f, L_f are the field winding resistance and inductance respectively.

In our approach the active flux will be investigated for BEGA, considering zero i_d current ($i_d=0$). Equations (5.14)-(5.18), in steady state, become:

$$\overline{V}_S = R_S \overline{I}_S + \frac{d\overline{\Psi}_S}{dt} + j\omega_r \overline{\Psi}_S \tag{5.19}$$

$$\overline{V}_S = V_d + jV_q \quad , \quad \overline{I}_S = jI_q \ , \ \overline{\Psi}_S = \Psi_d + j\Psi_q \tag{5.20}$$

$$\Psi_d = L_{mf} I_f \quad , \ \Psi_q = L_q I_q - \Psi_{PM} \tag{5.21}$$

$$T_e = \frac{3}{2} p_1 \left(\Psi_d I_q\right) = \frac{3}{2} p_1 \left(L_{mf} I_f I_q\right) \tag{5.22}$$

$$V_f = R_f I_f + \frac{d\Psi_f}{dt} \quad , \quad \Psi_f = L_f I_f \tag{5.23}$$

For BEGA the active flux is expressed as:

$$\begin{gathered} \overline{\Psi}_d^a = \overline{\Psi}_S - L_q I_S = L_{mf} I_f + j\left(L_q I_q - \Psi_{PM}\right) - L_q I_q \\ \overline{\Psi}_d^a = \overline{\Psi}_S - L_q I_S = L_{mf} I_f - j\Psi_{PM} \end{gathered} \tag{5.24}$$

The stator voltage model of BEGA in stator coordinates is:

$$\overline{V}_S = R_S \overline{I}_S + \frac{d\overline{\Psi}_S}{dt} \tag{5.25}$$

The stator voltage model, taking into account the active flux, becomes:

$$\overline{V}_S = R_S \overline{I}_S + \left(s + j\omega_r\right) L_q \overline{I}_S + + \left(s + j\omega_r\right) \overline{\Psi}_d^a \tag{5.26}$$

The vector diagram of equation (5.26) is illustrated in Fig. 5.6.

The active flux observer, in stator coordinates, is:

$$\overline{\Psi}_d^a = \left(\overline{V}_S - R_S \overline{I}_S + V_{comp}\right) - L_q \overline{I}_S \tag{5.27}$$

where:

$$\begin{gathered} \overline{\Psi}_d^a = \Psi_d^a \cos\left(\theta_{er} - \gamma\right) + \Psi_d^a \sin\left(\theta_{er} - \gamma\right) = \\ \overline{\Psi}_d^a = \Psi_d^a \cos\left(\theta_{\Psi_d^a}\right) + \Psi_d^a \sin\left(\theta_{\Psi_d^a}\right) = \Psi_{d\alpha}^a + \Psi_{d\beta}^a \end{gathered} \tag{5.28}$$

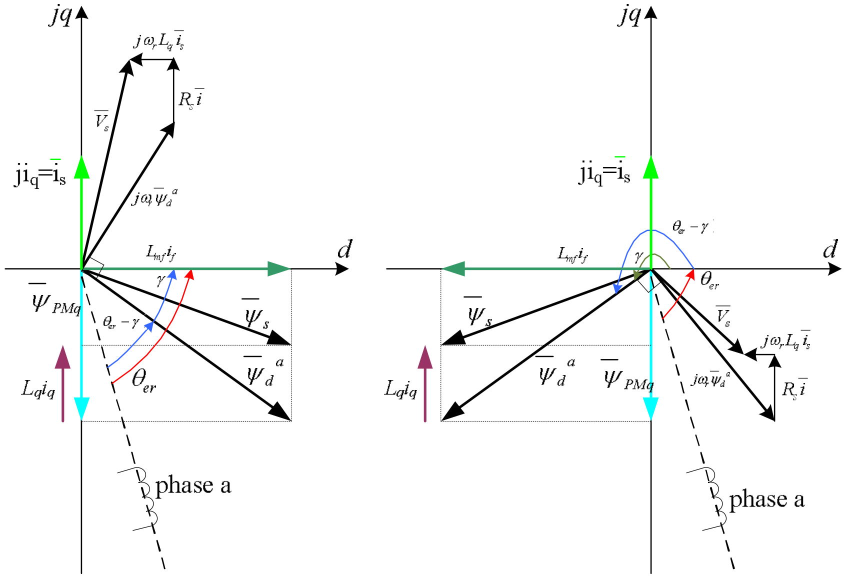

a) b)

Fig. 5.6. BEGA and its vector diagram pointing out the active flux , for a) motoring and b)generating

NOTE: 1) let us note the *active flux angle* as being the angle between the rotor electrical angle and the position of the active flux vector. 2) let us note the torque angle as being the angle between active flux vector position and d-axis.

$$\begin{aligned} &\text{active flux angle : } \theta_{\Psi_d^a} = \prec\left(\theta_{er}, \overline{\Psi}_d^a\right) \\ &\text{torque angle : } \gamma = \prec\left(d, \overline{\Psi}_d^a\right) \end{aligned} \tag{5.29}$$

Equation (5.27) indicates that if the active flux angle is known, the position of the rotor can be easily calculated, by adding the torque angle to the active flux angle.

$$\theta_{er} = \theta_{\Psi_d^a} + \gamma \tag{5.30}$$

Therefore our target is to estimate the active flux angle as good as possible.

The torque angle (δ) is varying between [0...atan(Ψ_{PM}/Ψ_{ex})] for positive dc field current and between [π ...π+atan(-Ψ_{PM}/Ψ_{ex})] for negative dc field current (see Fig. 5.7). The full range of torque angle is 0...180 electrical degrees.

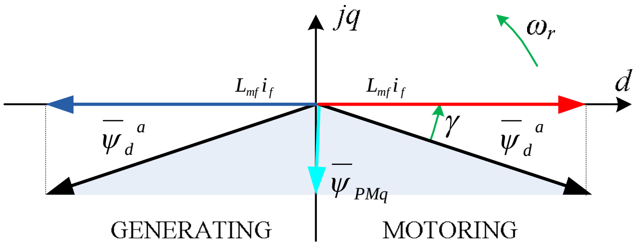

Fig. 5.7. Torque angle during motoring and generating

For validation of theoretical considerations of the active flux concept, a Matlab-Simulink simulation model has been built and run. Of interest has been the validity of relationship (5.30). The simulation results are shown in Fig. 5.8 – Fig. 5.10.
The target speed of the motor has been set to 1000rpm until time=0.4s when the reference speed is changed to -1000rpm. The purpose of this experiment is to validate the concept of "active flux" for motoring and generating. Changing the speed sign involve the operation of BEGA in generating for more than 150ms.

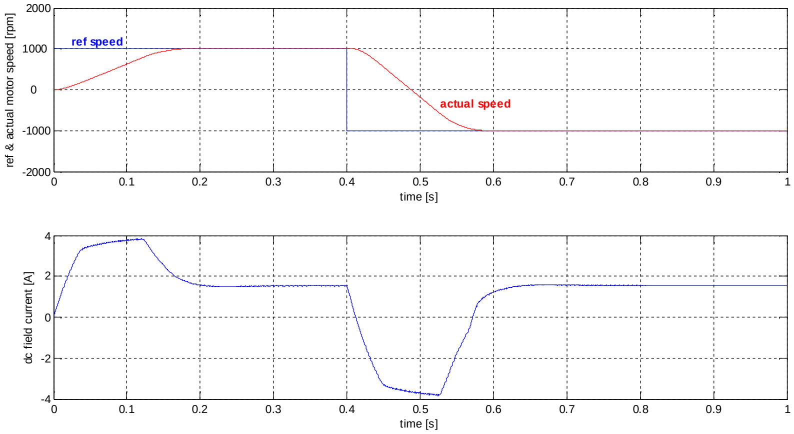

Fig. 5.8. BEGA reference and actual speed (upper side) and dc field current (lower side)

The machine was closed loop speed controlled with position and speed sensor. The active flux magnitude and angle were calculated based on the fluxes “measured” in the machine. The torque angle was calculated based on equation (5.35). The sum of the two angles (torque and active flux) is the actual rotor position. In Fig. 5.9 are shown the actual rotor position, active flux position and torque angle. In Fig. 5.10 it is shown only the actual and calculated rotor position using the sum of active flux position and torque angle. It can be easily seen that the two (actual and calculated) angles are overlapped – this proves the validity of the active flux concept. Note that for negative dc field current ☐ should be added to the torque angle to get the correct value of the torque angle.

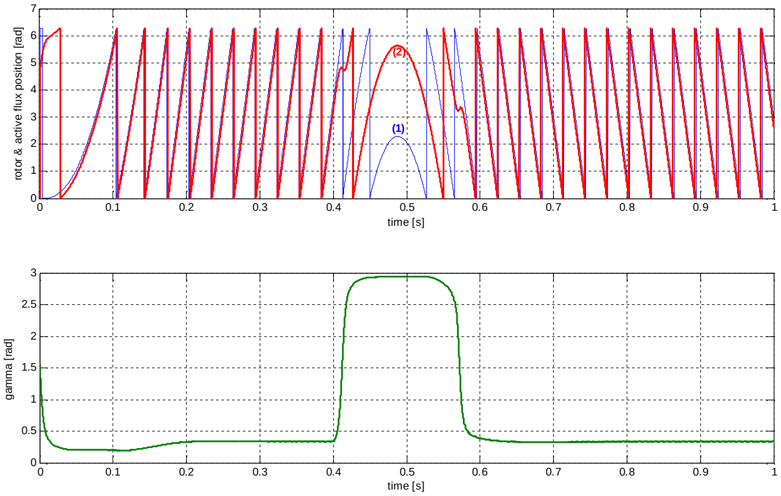

Fig. 5.9 Actual BEGA rotor position (1) and active flux position (2) – upper side – and torque angle – lower side –

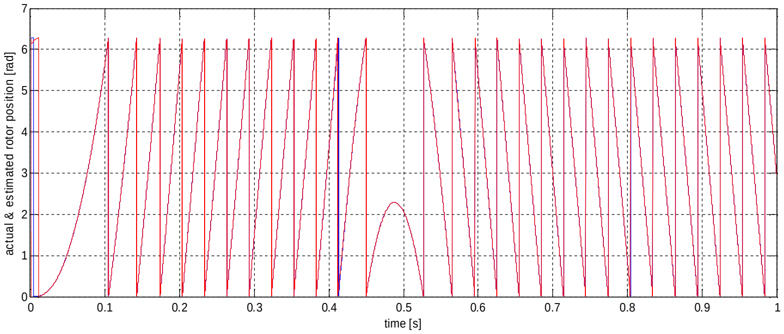

Fig. 5.10. BEGA rotor position: actual and calculated using active flux concept

This way all assumptions made in equations (5.29), (5.30) and (5.36), based on vector diagram in Fig. 5.6 are considered valid. The next step is the implementation of the position and speed estimator based on active flux observer.

5.3. Active flux observer

The BEGA proposed vector control system employs speed mechanical rotor speed, ωr, (as a feedback for the reference) and electrical rotor position, θer, necessary for coordinate's transformation in rotor reference frame. Since, no rotor position and speed is available from a position sensor the only chance is to estimate both of them. For this purpose an observer is proposed for rotor position and speed estimation. Mainly, the observer is divided into two major parts: i) active flux observer and ii) position and speed observer.

A. Active Flux Observer

The scope of the active flux observer is to estimate the magnitude and angle of the active flux components in stator coordinates.

The operating principle of the proposed observer is to extract the active flux using the measured stator current, dc. field current and the estimated stator voltage. The stator voltage is estimated based on the measured dc-link (battery) voltage and the switching states.

The signal flow diagram of active flux observer is shown in Fig. 5.11. It is based on a combined voltage-current model from which the Lq is term is substracted.

The stator flux observer combines advantages of the current-model estimator in rotor reference at low speed, with the voltage-model estimator in stator reference at medium high speed, using a dynamic PI compensator (5.13).

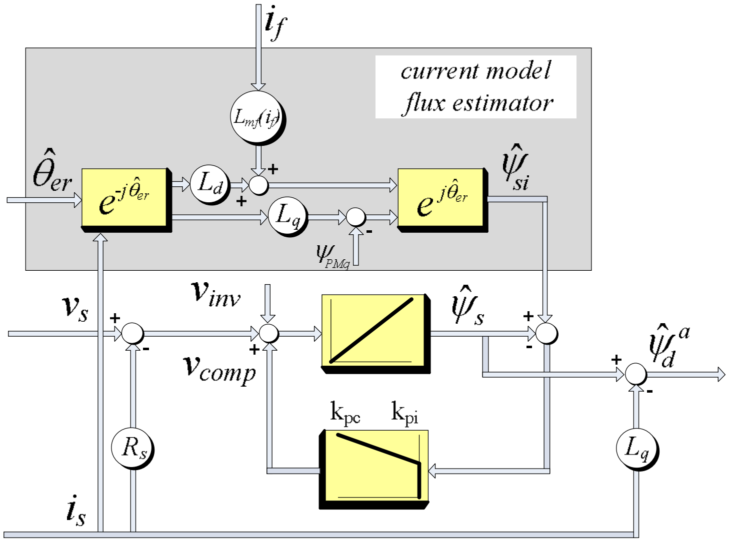

Fig. 5.11. Active flux observer

The supply stator voltage is the estimated one from space vector modulation block. The inverter nonlinearities are compensated by vinv, based on the method proposed in [5.67]:

$$v_{inv} = \frac{4}{3} v_{th} - sec(i_s) - r_d i_s \tag{5.31}$$

kpc and kic are the proportional and integral gains of the PI compensator that gives the compensation voltage vcomp.

decide the speed range where the current model (or voltage model) prevails.

$$v_{comp} = \left(k_{pc} + \frac{k_{ic}}{s}\right)\left(\hat{\Psi}_{si} - \hat{\Psi}_{su}\right) \tag{5.32}$$

where and are the stator flux estimated based on current model and respectively voltage model.
The design of PI parameters kpc and kic is based on the pole placement method:

$$k_{pc} = \omega_1 + \omega_2 k_{ic} = \omega_1 \cdot \omega_2 \tag{5.33}$$

where ω_1, ω_2 are the desired poles with $\omega_2 > \omega_1$. For low speed range the current model prevails, while for high speed range the voltage model prevails. Another advantage of this compensator is that the dc offset and drifts from the measured current are rejected.

B. Position and Speed Estimator

The rotor position estimator implementation is presented in Fig. 5.12. To extract the rotor position and speed from the active flux vector, a PLL (phase-locked-loop) state-observer is employed. The output of the PLL is the estimated position of the active flux ( ). To obtain the estimated position of the rotor the angle is added to the estimated position of active flux (see Fig. 5.6):

$$\hat{\theta}_{er} = \left(\hat{\theta}_{er} - \gamma\right) + \gamma \tag{5.34}$$

where $\left(\hat{\theta}_{er} - \gamma\right)$ is the active flux angle estimated by the active flux PLL, and γ is the torque angle.

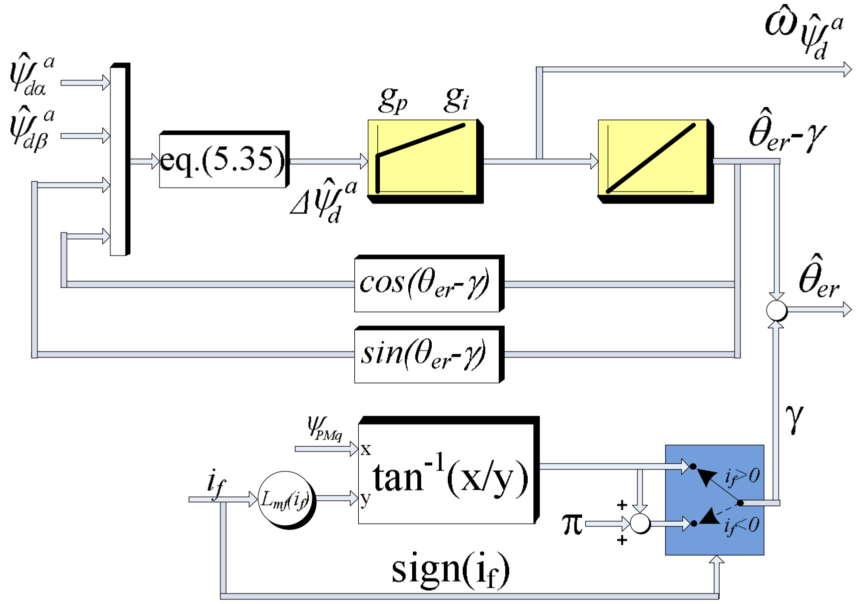

Fig. 5.12. Rotor position and speed estimator

$$\Delta\hat{\theta}_{\Psi_d^a} = -\hat{\Psi}_{d\alpha}^a \sin\left(\hat{\theta}_{er} - \gamma\right) + \hat{\Psi}_{d\beta}^a \cos\left(\hat{\theta}_{er} - \gamma\right) =$$

$$\Delta\hat{\theta}_{\Psi_d^a} = -\hat{\Psi}_{d\alpha}^a \sin\left(\hat{\theta}_{\Psi_d^a}\right) + \hat{\Psi}_{d\beta}^a \cos\left(\hat{\theta}_{\Psi_d^a}\right) \qquad (5.35)$$

The angle ☐ can be very precisely estimated due to accurate knowledge of and obtained from experiments.

$$\gamma = \begin{cases} \tan^{-1}\left(\Psi_{PM} / L_{mf} I_f\right) & , \quad for I_f > 0 \\ \tan^{-1}\left(\Psi_{PM} / L_{mf} I_f\right) + \pi & , \quad for I_f < 0 \end{cases} \qquad (5.36)$$

Note that important is the angle value and not the magnitude/amplitude of the active flux components.

Since the torque angle γ is easily and accurate calculated, the accuracy of the estimated position depends on the performance of the active flux observer.

The electrical rotor speed can be estimated using equation (5.37) if the rotor electrical position is known:

$$\hat{\omega}_{er} = \frac{d\hat{\theta}_{er}}{dt} \qquad (5.37)$$

Replacing θ_{er} in equation (5.37) with equation (5.34), it yields:

$$\hat{\omega}_{er} = \frac{d\left(\left(\hat{\theta}_{er} - \gamma\right) + \gamma\right)}{dt} = \frac{d\left(\hat{\theta}_{er} - \gamma\right)}{dt} + \frac{d\gamma}{dt} = \hat{\omega}_{\hat{\Psi}_d^a} + \hat{\omega}_{\gamma} \qquad (5.38)$$

According to equation (5.38) the rotor electrical speed is expressed as a sum of two components: i) active flux speed and ii) gamma speed.

The active flux speed estimation is based on derivatives of active flux components ( ) as follow:

$$\hat{\omega}_r = \frac{\frac{d\hat{\Psi}_{d\alpha}^a}{dt}\hat{\psi}_{d\alpha}^a - \frac{d\hat{\Psi}_{d\beta}^a}{dt}\hat{\psi}_{d\beta}^a}{\left(\hat{\psi}_d^a\right)^2} \quad , \quad \left(\hat{\Psi}_d^a\right)^2 = \left(\hat{\Psi}_{d\alpha}^a\right)^2 + \left(\hat{\Psi}_{d\beta}^a\right)^2 \qquad (5.39)$$

A second solution for the speed estimation is given by equation (5.38):

$$\hat{\omega}_r = \frac{\frac{d \sin\left(\hat{\theta}_{er}\right)}{dt}\cos\left(\hat{\theta}_{er}\right) - \frac{d \cos\left(\hat{\theta}_{er}\right)}{dt}\sin\left(\hat{\theta}_{er}\right)}{\left|\sin^2\left(\hat{\theta}_{er}\right) + \cos^2\left(\hat{\theta}_{er}\right)\right|} \qquad (5.40)$$

where Δt is the sampling time of rotor speed evaluation.

To remove the high frequency noise from the estimated speed a first-order low pass filter is used:

$$\hat{\omega}_r[t] = k \cdot \left(\hat{\omega}_r[t] - \hat{\omega}_r[t-1]\right) + \hat{\omega}_r[t-1] \qquad (5.41)$$

5.4 Bega vector control system

The proposed BEGA control strategy is the same as that one described in Chapter 4. The difference is that here the rotor position and speed are the outputs from an observer, not being measured using a position sensor, like in the experiments performed in Chapter 4.

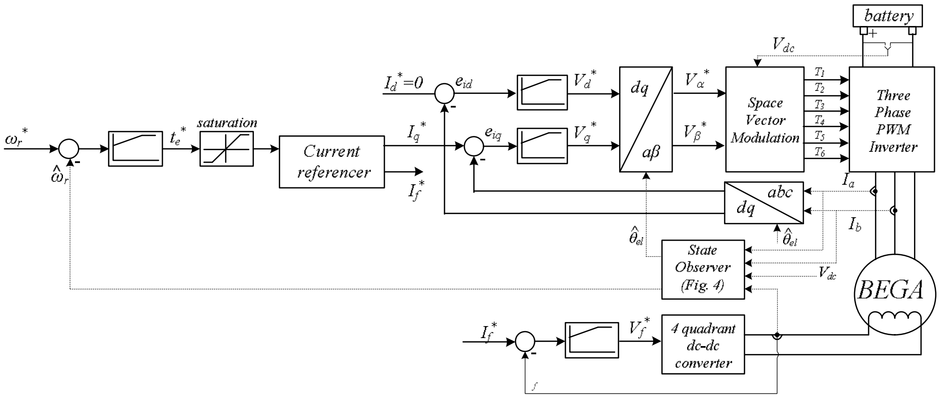

Fig. 5.13. BEGA Vector Control Structure

In order to find out the performance of speed estimation based on eq. (5.38) and eq. (5.40) a set of simulations has been run. One of the simulation results is presented in Fig. 5.14 – Fig. 5. 16.

In Fig. 5.14.a, it is shown the reference, actual and estimated rotor speed using equation (5.38) – method 1– and equation (5.40) – method 2. In Fig. 5.14.b it is shown only the estimated speed using the two methods. The conclusion is that the methods are equivalent.

In Fig. 5.15 is illustrated the estimated speed using method 1 and the two components of the estimated speed: active flux angle speed ( ) and torque angle speed ( ). Simulation results shows that one cancels the other during transients so that the estimated speed is close to the estimated speed, during transients, also. For high dc field current variations the accuracy of the estimated rotor speed is decreasing significantly.

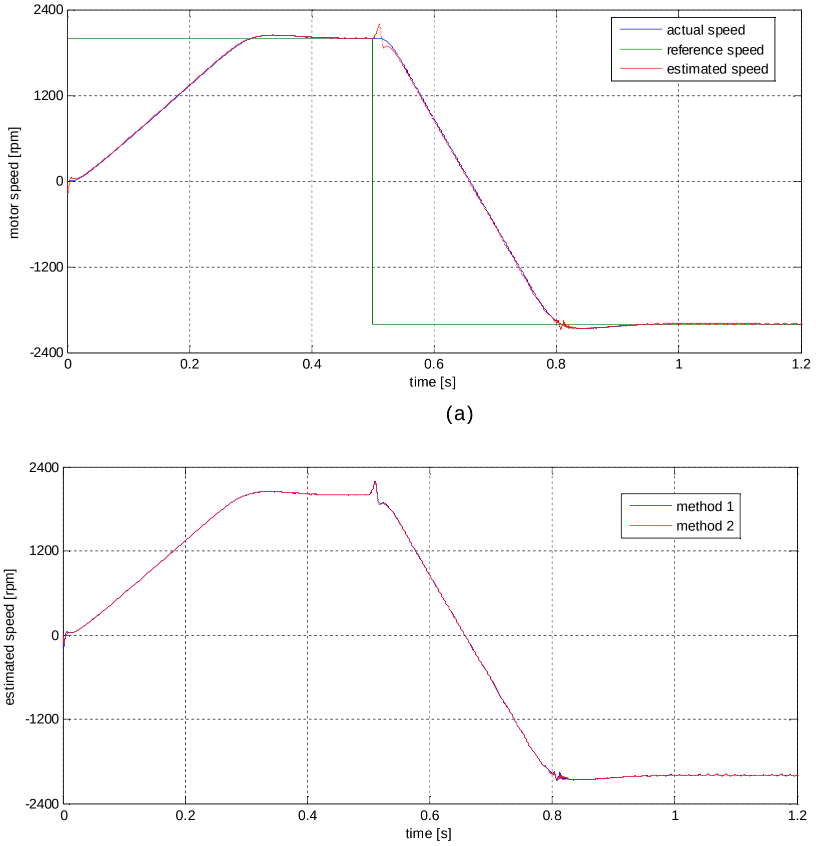

(a)

(b)

Fig. 5.14. a) Reference, actual and estimated speed, b) estimated rotor speed using method 1 and method 2

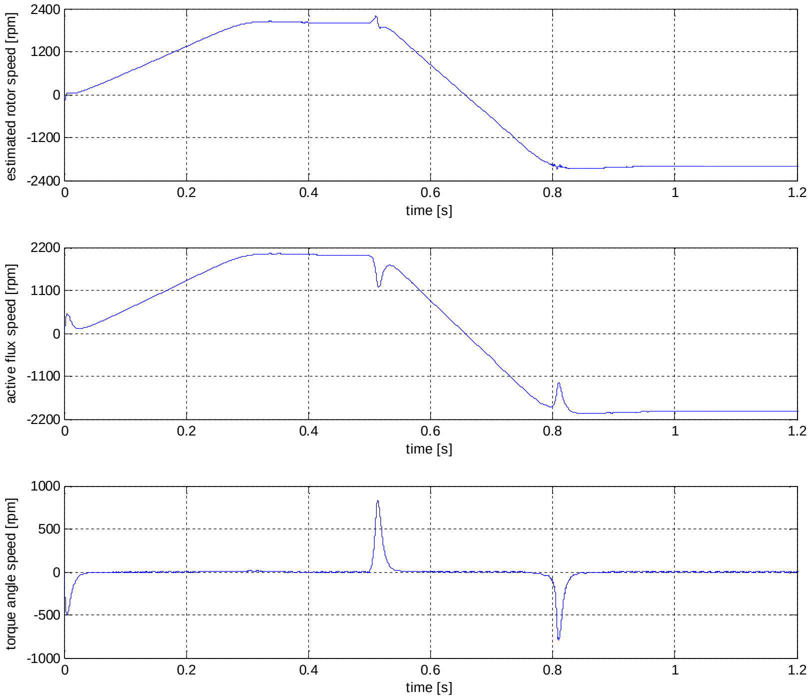

Fig. 5.15. Estimated rotor speed using method1 and its components: active flux speed and torque angle speed

5.5. Digital simulation results

One scope of this chapter is to establish a guideline for active flux observer, position and speed estimator tuning. In order to define such rules a set of digital simulations has been run and based on the conclusion from simulation results, the set of rules is presented. In general for motion sensorless control, where observers and estimators are employed, besides the tuning of observers and estimators parameters is important to know also the influence of machine parameters. Therefore in what follows will be investigated the way how the calibrations of the observers and machine parameters affects the performance of the estimated position and speed, will be investigated. The stator flux estimator is that shown in Fig. 5.16. The scheme has also an offset input in order to study how the offset affects the observer performance. The effect of the following parameters will be also investigated:

- Machine parameters: rs, ld, lq, lmf, ☐PM
- Active flux observers parameters: kp_ad, ki_ad
- PLL parameters: kp_pll, ki_pll

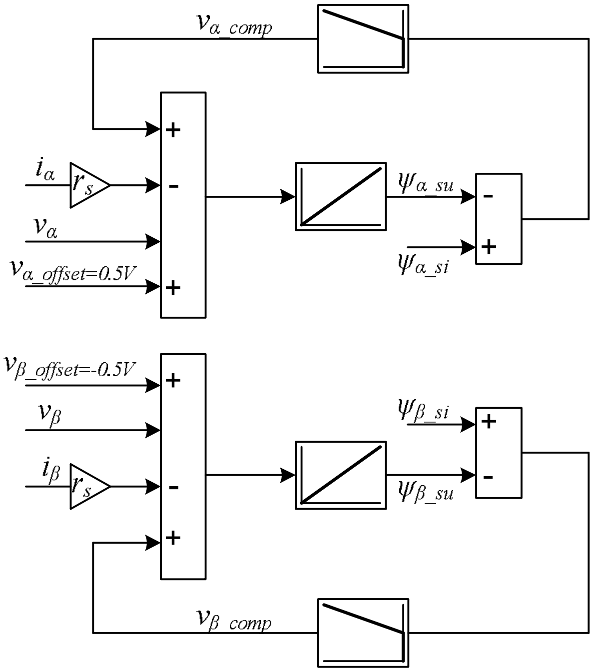

Fig. 5.16. Stator flux estimator structure

Rule 1: Initial condition on voltage integrator (if the initial position is known):

Case 1: Speed: 500rpm; Conditions: voltage offset: no voltage offset; Compensator parameters : kp_ad=10, kp_ad=20; Estimated voltage(vα, vβ) = measured (real) voltage

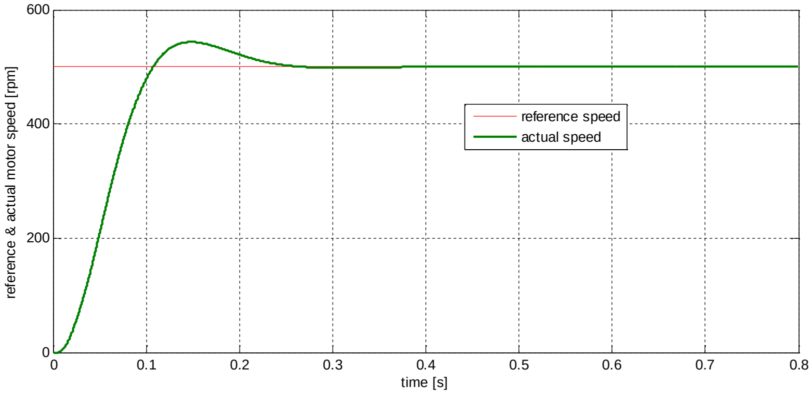

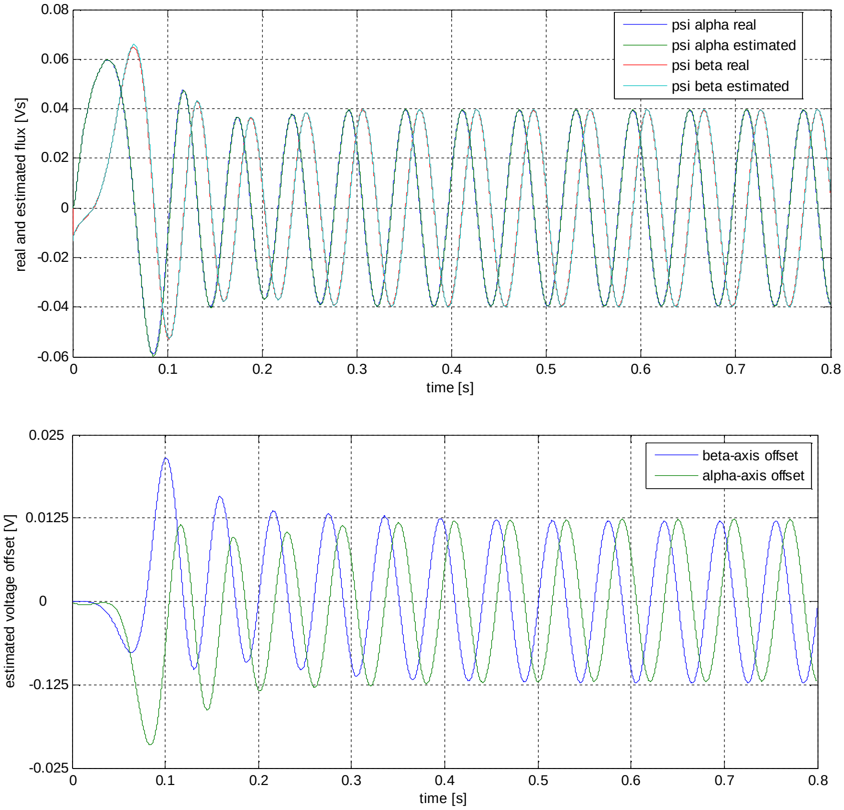

Fig. 5.17 Simulation results (from top to bottom): reference and actual motor speed, measured and estimated stator flux ( ), estimation offset voltage ( )

The simulation results plotted in Fig. 5.17 demonstrates that, if the initial conditions of the integrators are respected and no offset exists in the voltage measurement and machine parameters have the correct values, the stator flux estimation is very accurate from the begining.

Case 2: Speed: 2000rpm; Conditions: voltage offset: vα_offset=0.5V, vβ_offset=-0.5V; Compensator parameters : kp_ad=10, kp_ad=20;

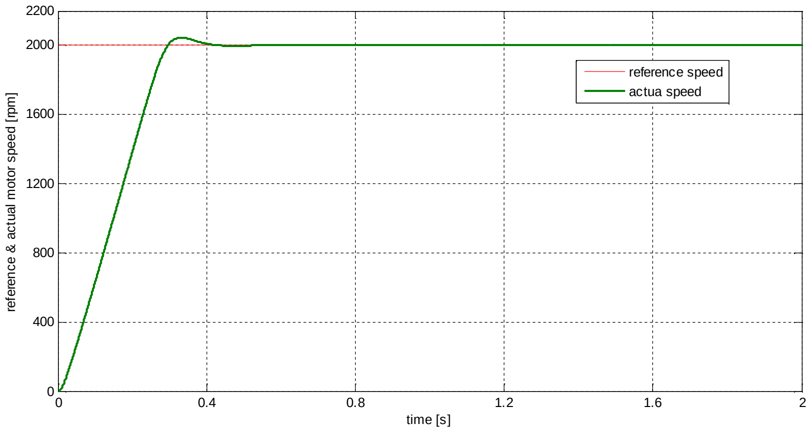
reference & actual motor speed [rpm]
2200
2000
1600
1200
800
400
0
0
0.4
0.8
1.2
1.6
2
time [s]
reference speed
actua speed

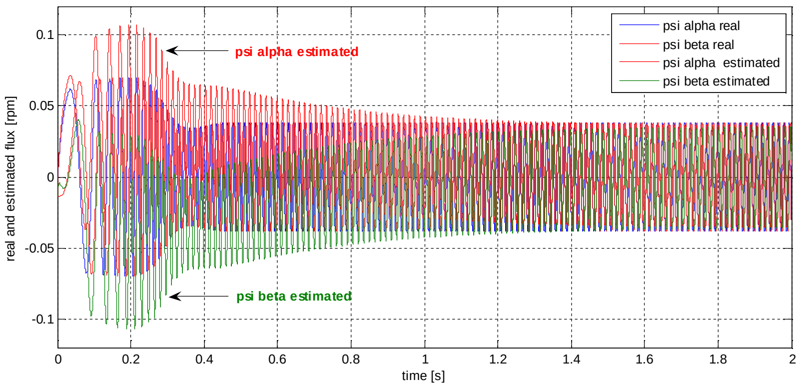
real and estimated flux [rpm]
0.1
0.05
0
-0.05
-0.1
0
0.2
0.4
0.6
0.8
1
1.2
1.4
1.6
1.8
2
time [s]
psi alpha real
psi beta real
psi alpha estimated
psi beta estimated
psi alpha estimated
psi beta estimated

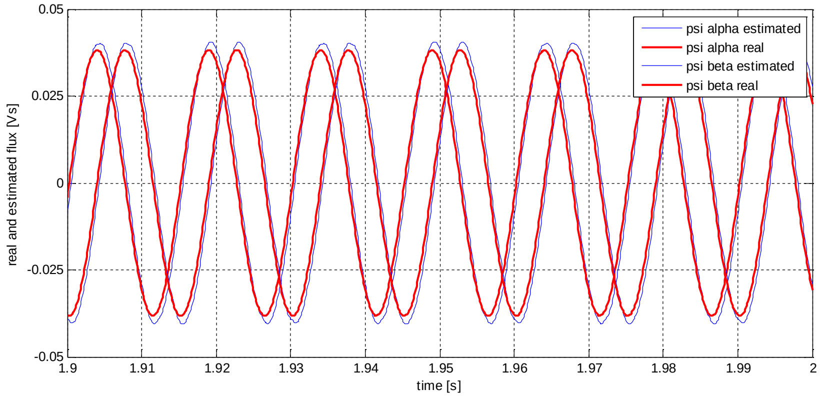
real and estimated flux [Vs]
0.05
0.025
0
-0.025
-0.05
1.9
1.91
1.92
1.93
1.94
1.95
1.96
1.97
1.98
1.99
2
time [s]
psi alpha estimated
psi alpha real
psi beta estimated
psi beta real

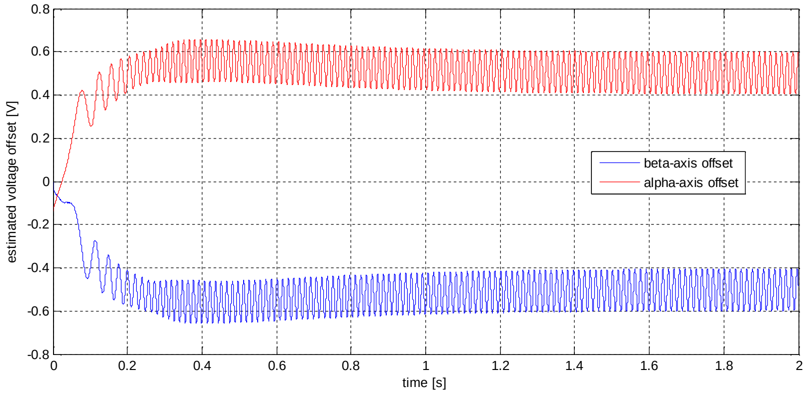

Fig. 5.18. Simulation results (from top to bottom): reference and actual motor speed, measured and estimated stator flux ( ), actual and estimated stator, zoom on actual and estimated stator flux, estimation offset voltage ( )- outputs of compensator

Simulation results shows that the voltage offset is fully compensated by the PI compensator. The magnitude of the PI compensator output defines the voltage offset, in steady state. The sign of the offset can be determined by the sign of the flux deviation (offset). If in the voltage will be a positive offset the estimated flux will be shifted with a positive offset (only in transients). Negative offset in the voltage will affect the estimated flux with a negative drift during transients.

Case 3: Speed: 2000rpm; Conditions: voltage offset: vα_offset=0.5V, vβ_offset=-0.5V; Stator resistance: rs=3*rsn; Compensator parameters : kp_ad=10, kp_ad=20;

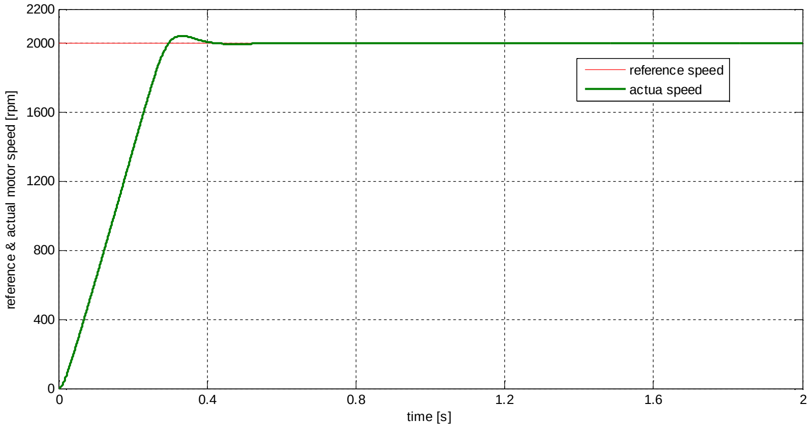

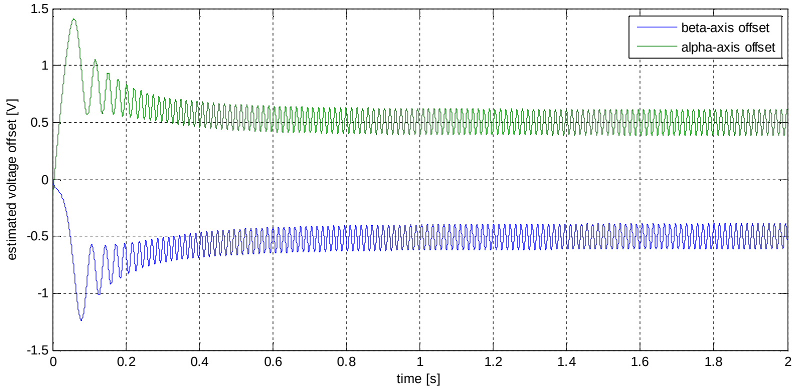
1.5
1
0.5
0
-0.5
-1
-1.5
estimated voltage offset [V]
0
0.2
0.4
0.6
0.8
1
1.2
1.4
1.6
1.8
2
time [s]
beta-axis offset
alpha-axis offset

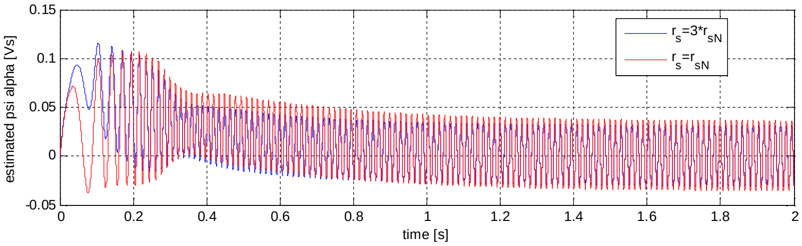
0.15
0.1
0.05
0
-0.05
estimated psi alpha [Vs]
0
0.2
0.4
0.6
0.8
1
1.2
1.4
1.6
1.8
2
time [s]
$r_s=3*r_{sN}$
$r_s=r_{sN}$

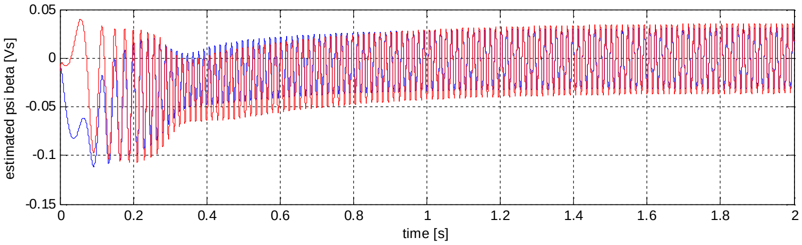
0.05
0
-0.05
-0.1
-0.15
estimated psi beta [Vs]
0
0.2
0.4
0.6
0.8
1
1.2
1.4
1.6
1.8
2
time [s]

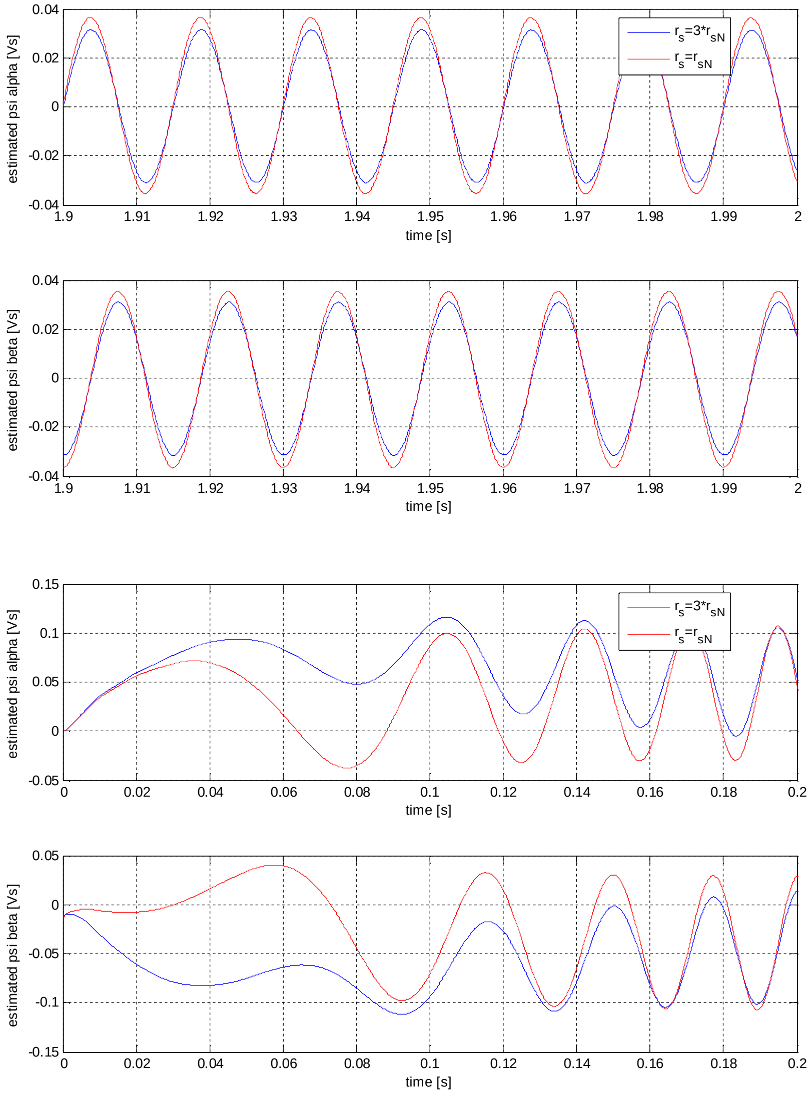

Fig. 5.19 Simulation results (from top to bottom): reference and actual motor speed, estimation offset voltage – outputs of PI compensator ( ), estimated stator flux components , measured and estimated stator flux ( ), zoom on ( )

Simulation results shows that a mismatch of the stator resistance value in the flux estimator affects only the magnitude of the flux (and not flux angle), during transients and steady state. The value of the resistance has no effect on the magnitude of the voltage offset during steady state, but during transient it has. So the compensator does not compensate for the stator resistance mismatch. The magnitude of the flux is affected by the stator resistance mismatch as equation (5.42) shows [5.67]:

$$\Delta\Psi_S = \hat{\Psi}_S - \Psi_S = \Delta R_S \int i_S dt \qquad (5.42)$$

Case 4: Speed: 200rpm; Conditions: voltage offset: vα_offset=0.5V, vβ_offset=-0.5V; Compensator parameters : kp_ad=10, kp_ad=20;

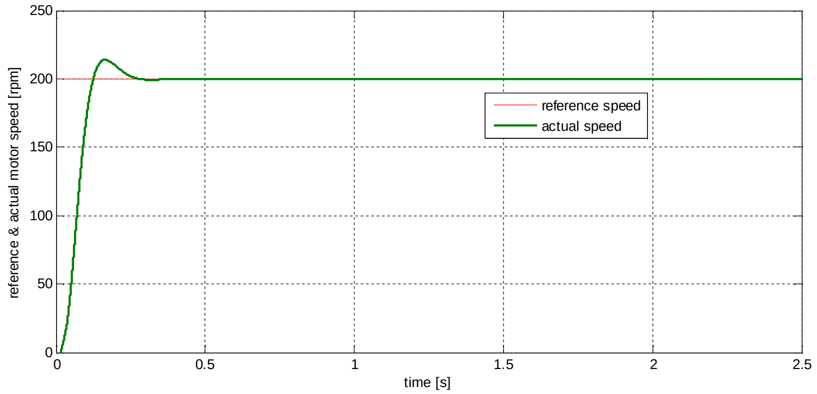

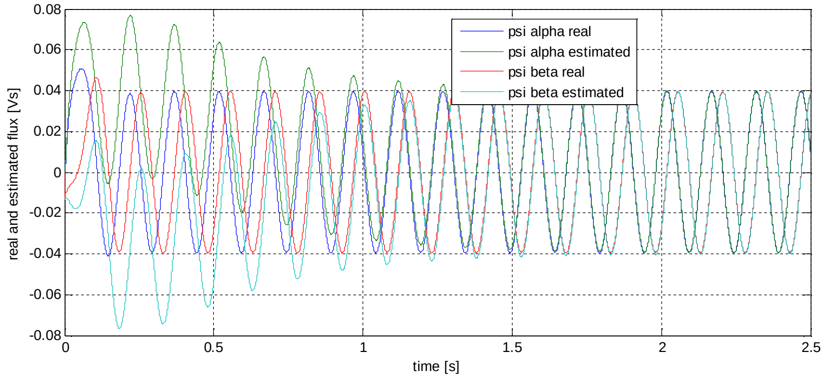

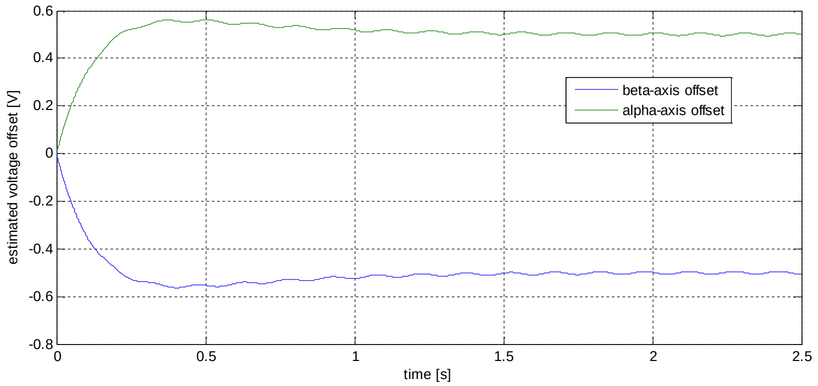

Fig. 5.20 Simulation results (from top to bottom): reference and actual motor speed, actual and estimated stator flux ( ), estimation offset voltage ( )

Case 5: Speed: 20rpm; Conditions: voltage offset: vα_offset=0.5V, vβ_offset=-0.5V; Compensator parameters : kp_ad=10, kp_ad=20;

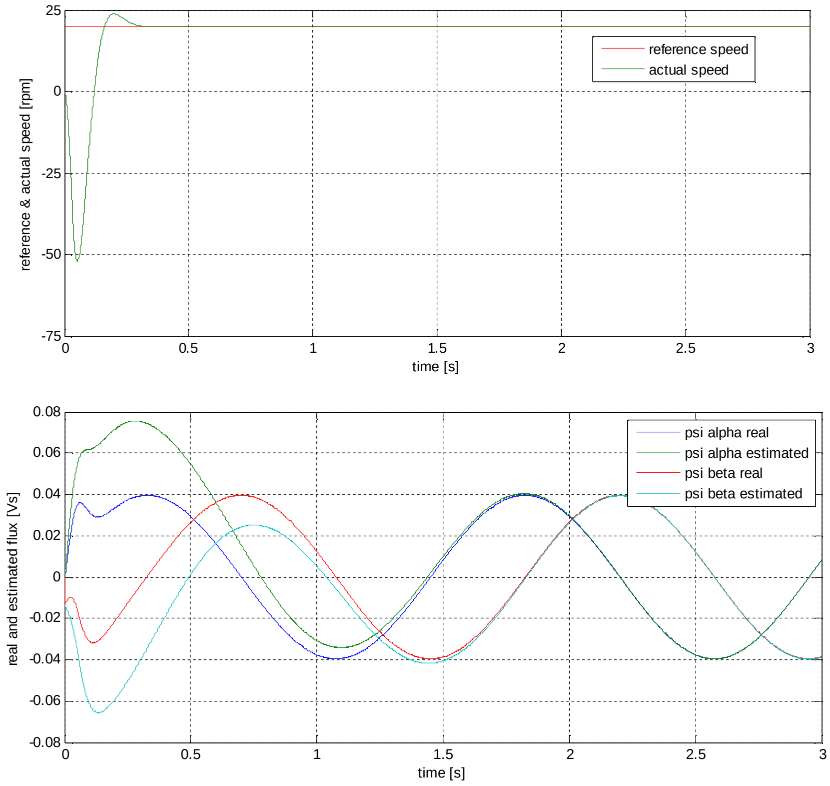

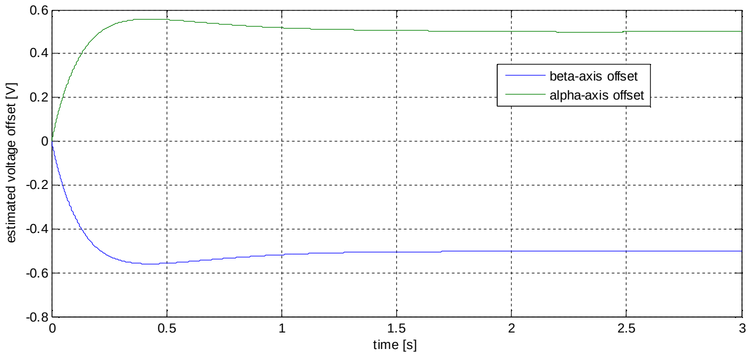

Fig. 5.21 Simulation results (from top to bottom): reference and actual motor speed, actual and estimated stator flux ( ), estimation offset voltage ( )

Case 6: Speed: 20rpm; Conditions: voltage offset: vα_offset=0.5V, vβ_offset=-0.5V; Compensator parameters : kp_ad=200, kp_ad=400;

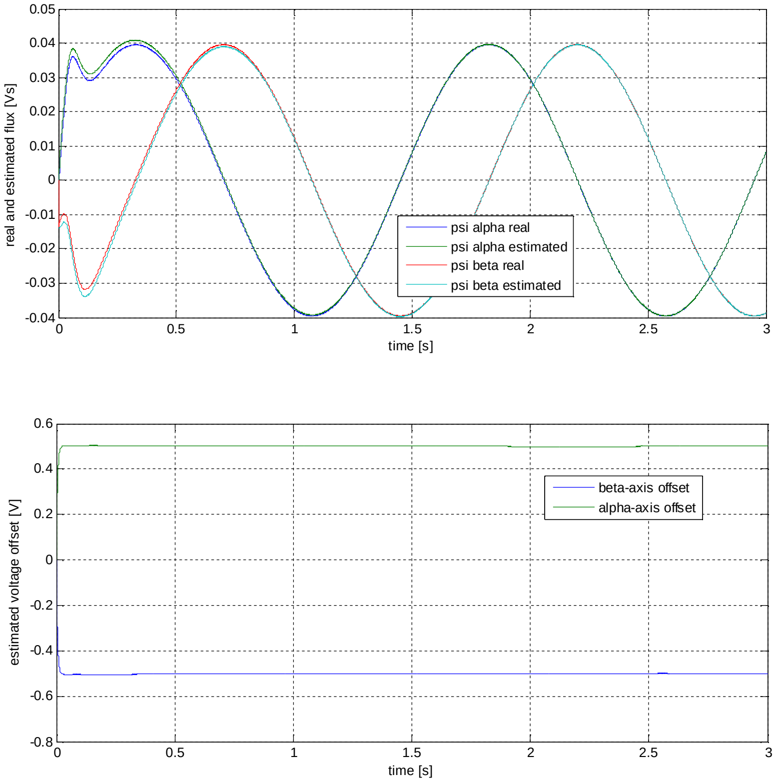

Fig. 5.22 Simulation results (from top to bottom): Actual and estimated stator flux ( ), estimation offset voltage ( )

Simulation results for the Case 5 and Case 6 proves that an increasing of the PI compensator values lead to a prevailing of the current model for low speed and consequently the voltage offset is rejected much faster.

5.6. State observers performance and experimental results

In order to calibrate the parameters of the active flux observer, position and speed estimator experiments were performed in a wide speed range: 2000rpm, 200rpm, 20rpm and 2rpm.

The target motor speed profile and speed response for a startup to 2000rpm followed by a few reversals are shown in Fig. 5.23. A zoom in on the estimated rotor position during startup, transients and steady-state is shown in Fig. 5.23c, Fig. 5.23d and Fig. 5.23a respectively. During startup 10ms is necessary for the position to converge from 90 electrical degrees to 55 electrical degrees. The additional 50ms are needed for the error to drop below 25 degrees. Then the error reaches a value of 2-4 degrees at steady state. During speed reversal a maximum error of 37 degrees is observed when the motor switches from positive to negative speed. When the machine switches from negative to positive speed the position error is below 40 degrees.

The estimated speed has a negative spike immediately after the command is set, but this seems to be favourable to the startup because the reference torque will be a bit higher. The estimated speed error is acceptable, with a maximum of 90rpm during transients.

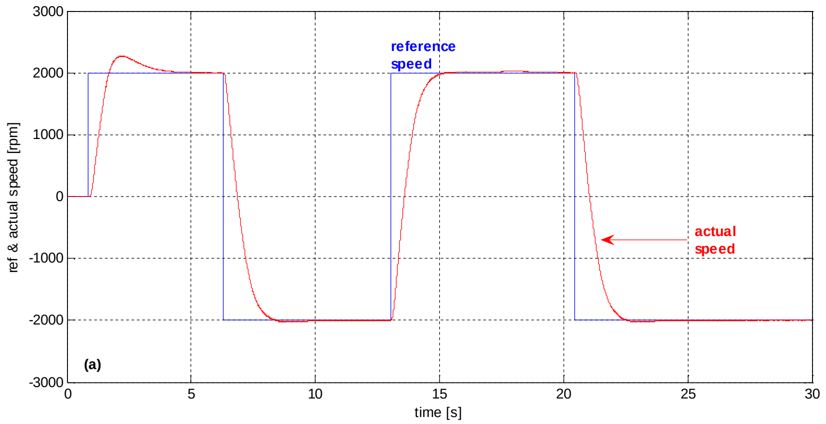

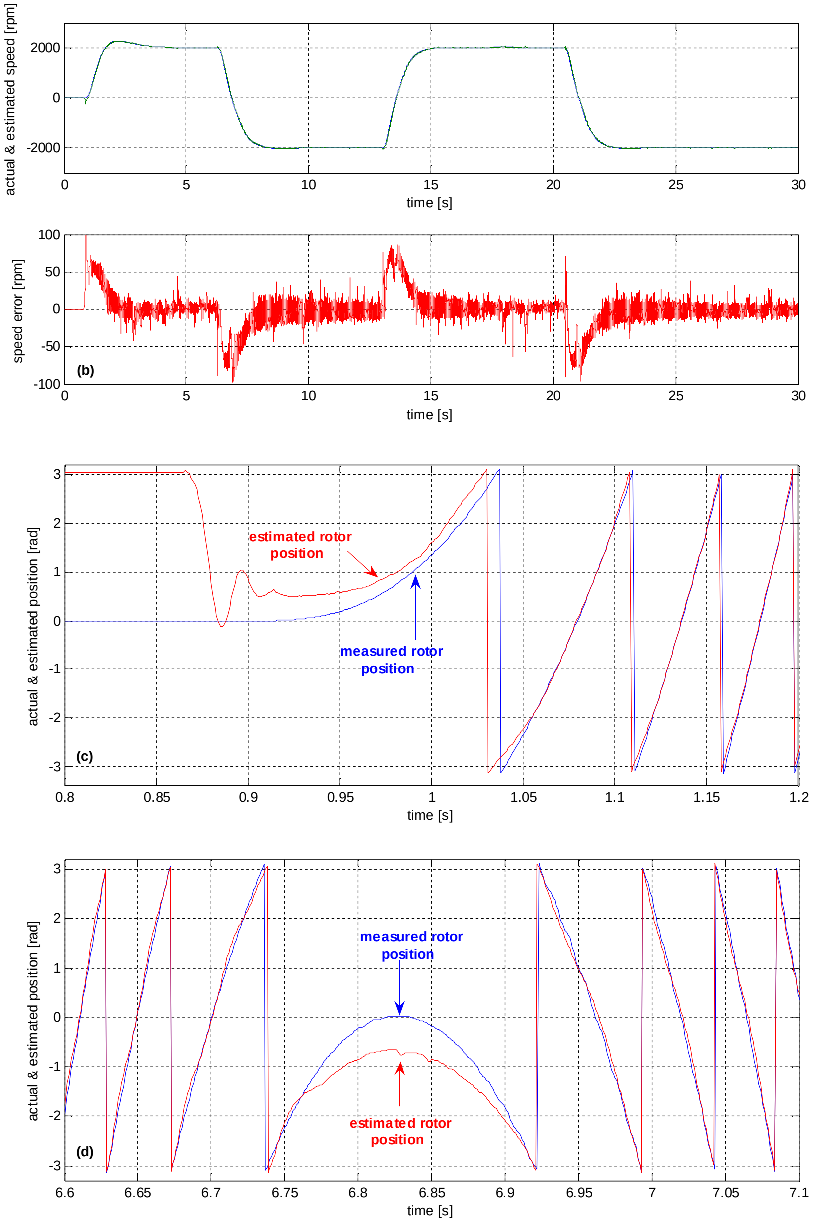
actual & estimated speed [rpm]
2000
0
-2000
0
5
10
15
20
25
30
time [s]
speed error [rpm]
100
50
0
-50
-100
(b)
0
5
10
15
20
25
30
time [s]
actual & estimated position [rad]
3
2
1
0
-1
-2
-3
estimated rotor position
measured rotor position
(c)
0.8
0.85
0.9
0.95
1
1.05
1.1
1.15
1.2
time [s]
actual & estimated position [rad]
3
2
1
0
-1
-2
-3
measured rotor position
estimated rotor position
(d)
6.6
6.65
6.7
6.75
6.8
6.85
6.9
6.95
7
7.05
7.1
time [s]

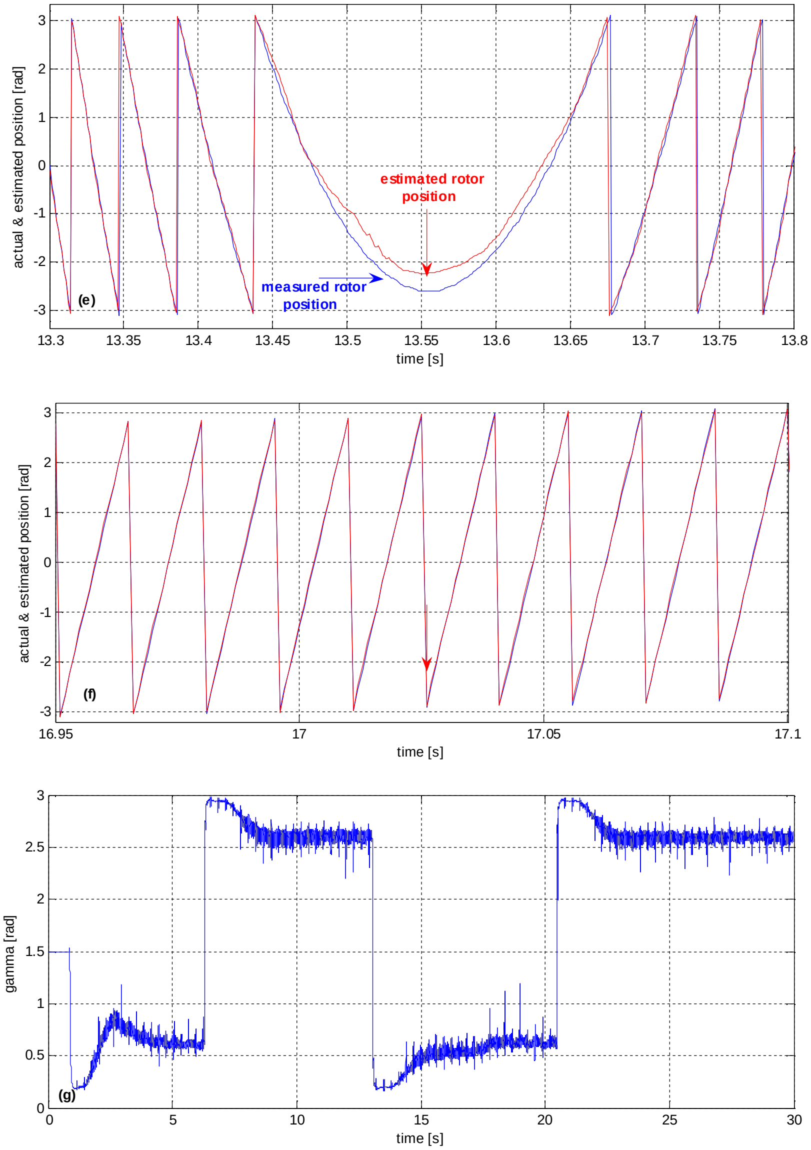

Fig. 5.23. Startup with load, ±2000 rpm speed reversal with load. From top to bottom: (a) reference and measured rotor speed, (b) measured and estimated speed, speed error, (c) zoom on actual and estimated rotor electrical position, rotor position error during startup (d), (e) zoom on actual and estimated rotor electrical position, rotor position error during speed reversal, (f) zoom on actual and estimated rotor electrical position, rotor position error during steady state, (g) torque angle(δ)

In a second experiment the performance of the observer and estimators are evaluated for a speed of ±200rpm, speed that can be considered somewhere between the high speed and low speed range. The experimental results are shown in Fig. 5.24. The estimated speed error is maximum (300rpm) at startup, and is decreasing then to ±10rpm at steady state and below 50rpm during speed reversal. Estimated position has some oscillations, around 30 degrees, during startup but in 150ms from the command, the position error drops below 5 degrees. During speed reversal the maximum error is 30 degrees.

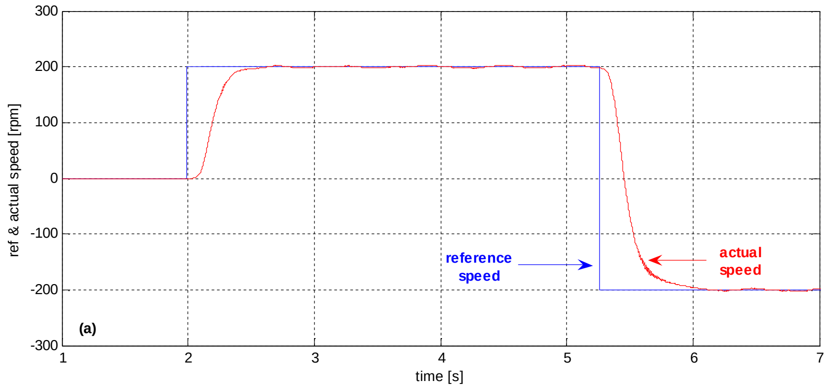

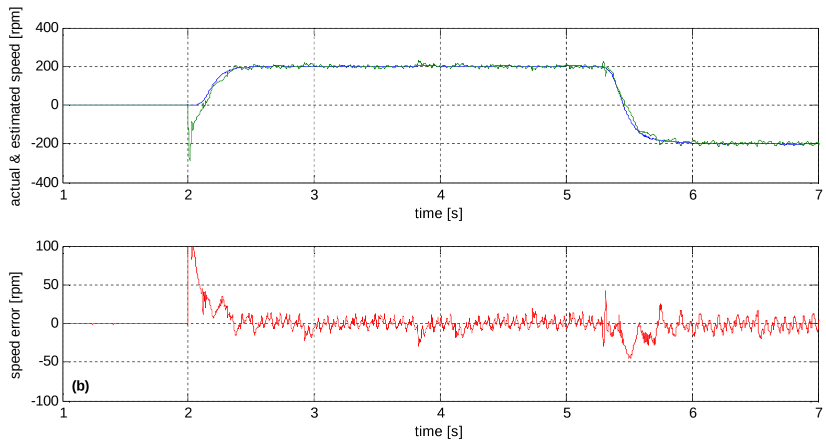

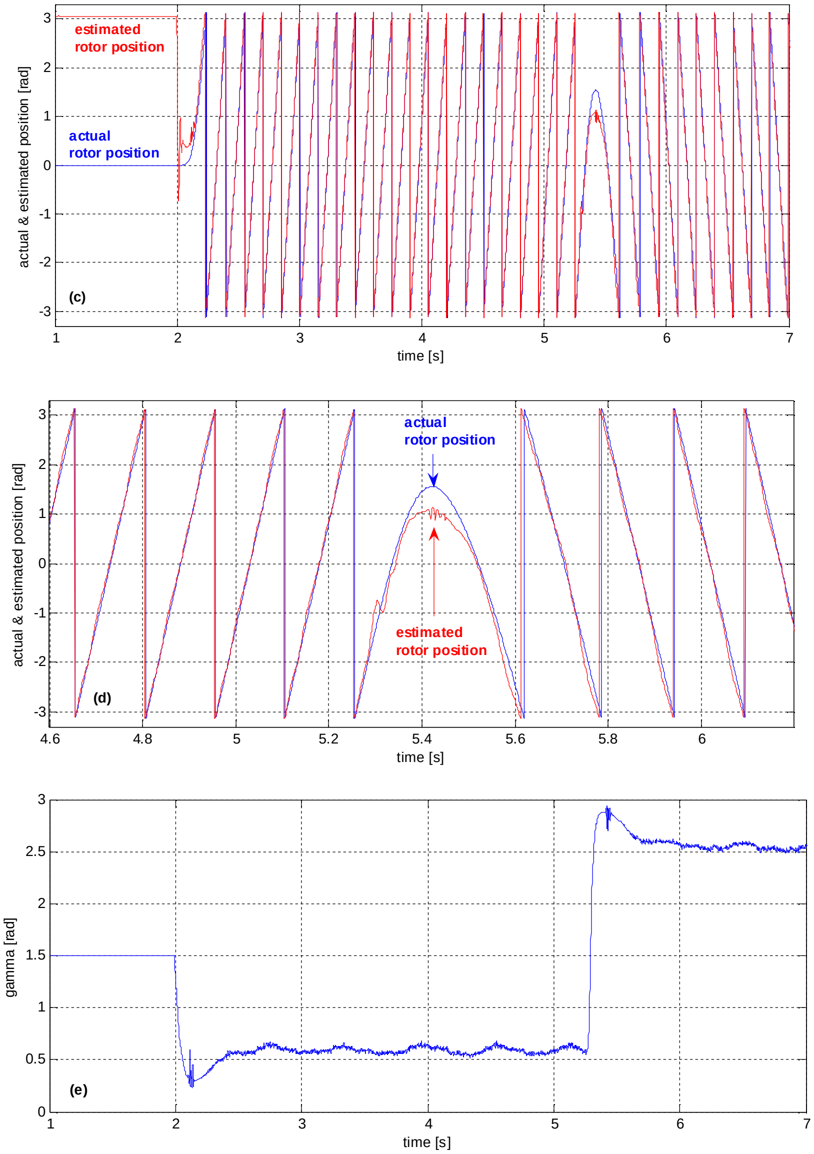

Fig. 5.24. Startup with load, ±200 rpm speed reversal with load. From top to bottom: (a) reference and measured rotor speed, (b) actual and estimated speed, speed error, (c) actual and estimated rotor electrical position, rotor position error, (d) zoom in on rotor position (e) torque angle (δ)

In the low speed region the first experiment is performed at 200rpm. The speed profile includes a motor step change in the load torque from negative to positive (time=6s) and a speed reversal from -20rpm to 20rpm (time=12.7s). The actual and estimated are shown in Fig. 5.25b. The estimated speed error is shown in Fig. 5.25c. In the estimated speed can be seen some spikes, but in general the error is between 5rpm. The fact that the actual speed is not smooth is due to the load. The load was an induction machine driven sensorless (in torque control mode) by an ACS600 inverter. At very low speed it is very difficult to control an induction machine sensorless with torque reference. This is the reason for load torque pulsations, which furthermore are reflected in BEGA speed oscillations. In Fig. 5.25a a negative spike in the actual motor speed can be seen. That is due to the load torque which changes its sign. For 20rpm the position error is below 3 electrical degrees during steady state and transients.

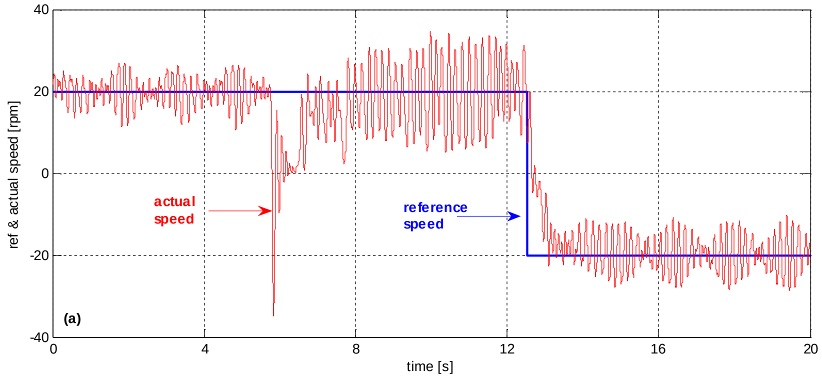

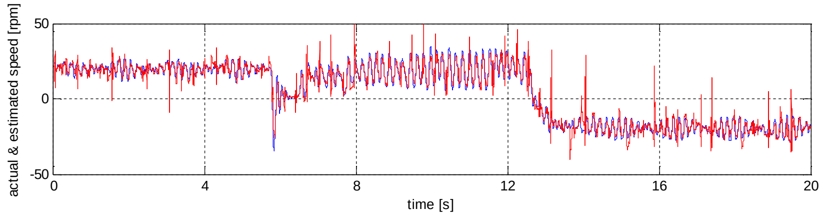

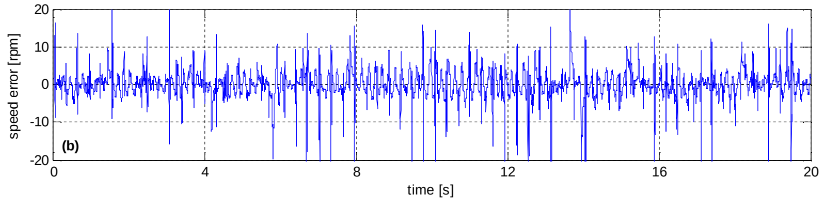

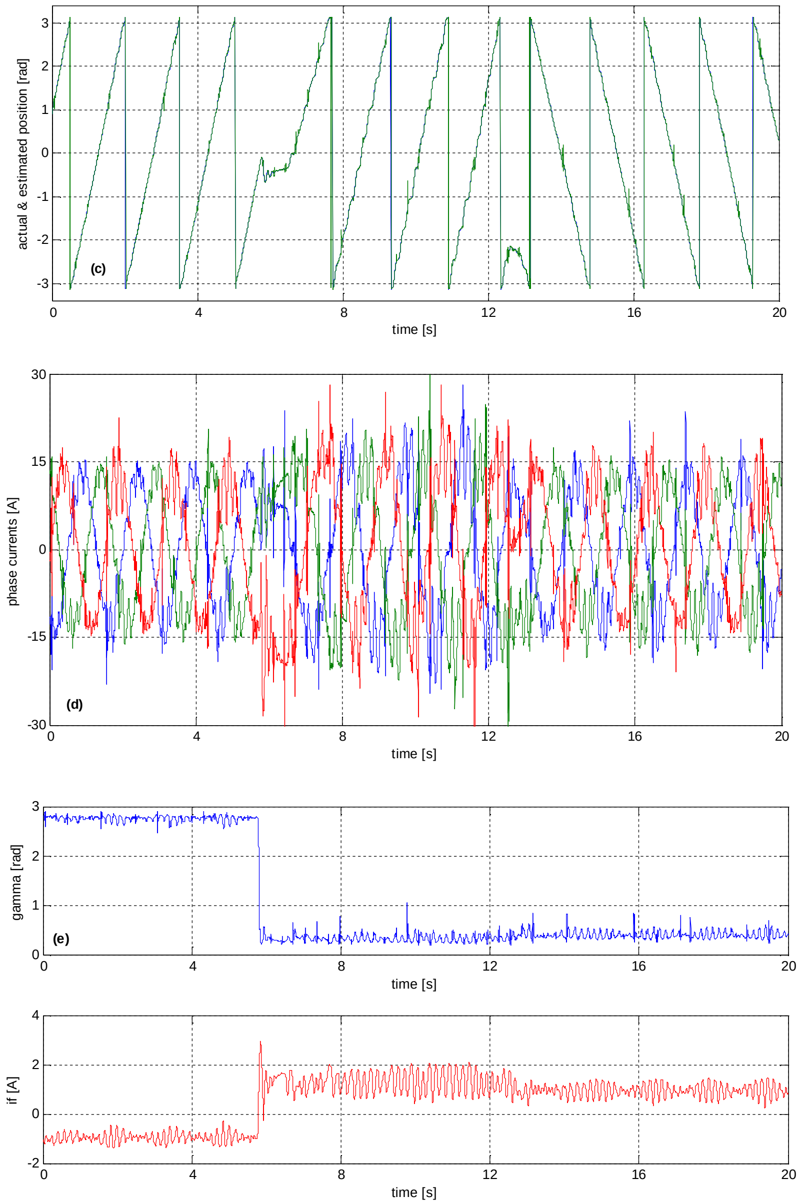

Fig. 5.25. Startup with load, ±20 rpm speed reversal with load. From top to bottom: (a) reference and measured rotor speed, (b) load and electromagnetic torque,(b) actual, estimated speed and speed error, (c) actual and estimated position, (d) phase currents (e), torque angle (δ) and dc field current

The last experiment performed presents the startup performance with a very low-speed step reference of 2rpm without load, followed by a speed reversal. The experimental results are shown in Fig. 5.26. The estimated speed is smoother than the actual one, but this is due to the large time constant of the estimated speed filter. Actual speed is not filtered. The position error is very small (below 3 electrical degrees). It has to be noted that the position accuracy is very good in spite of high current pulsations in phase currents and dc current.

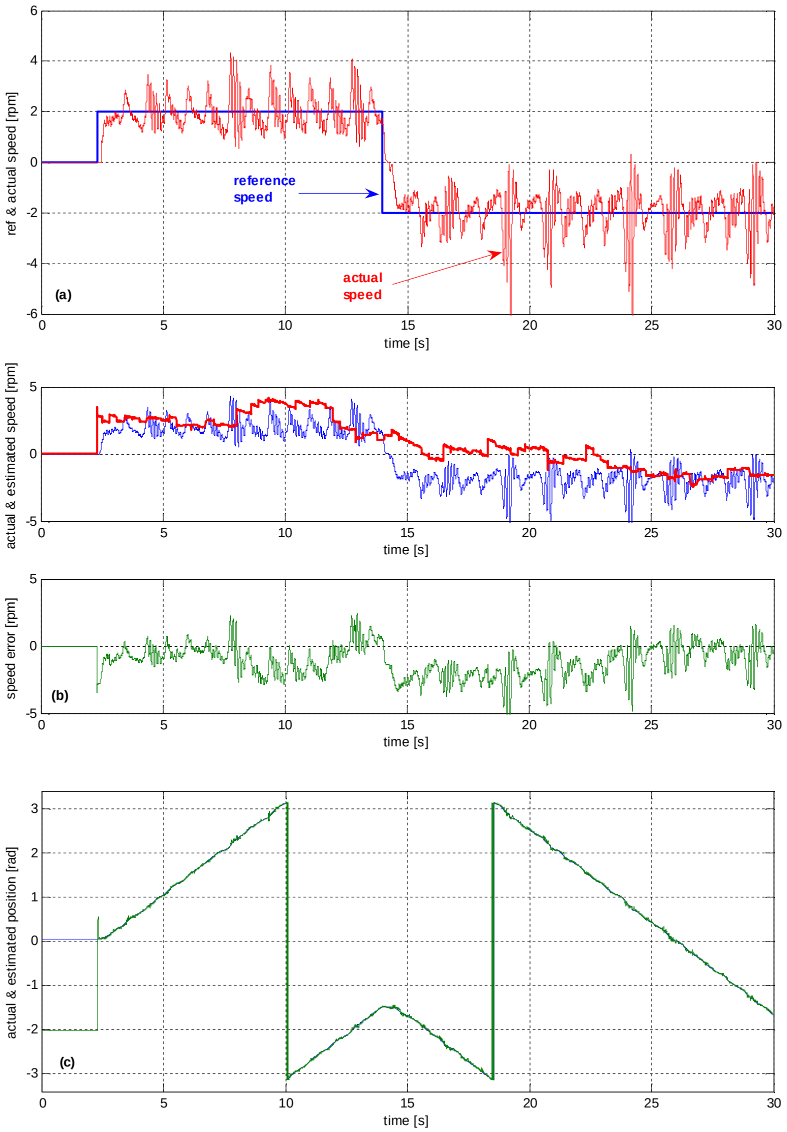

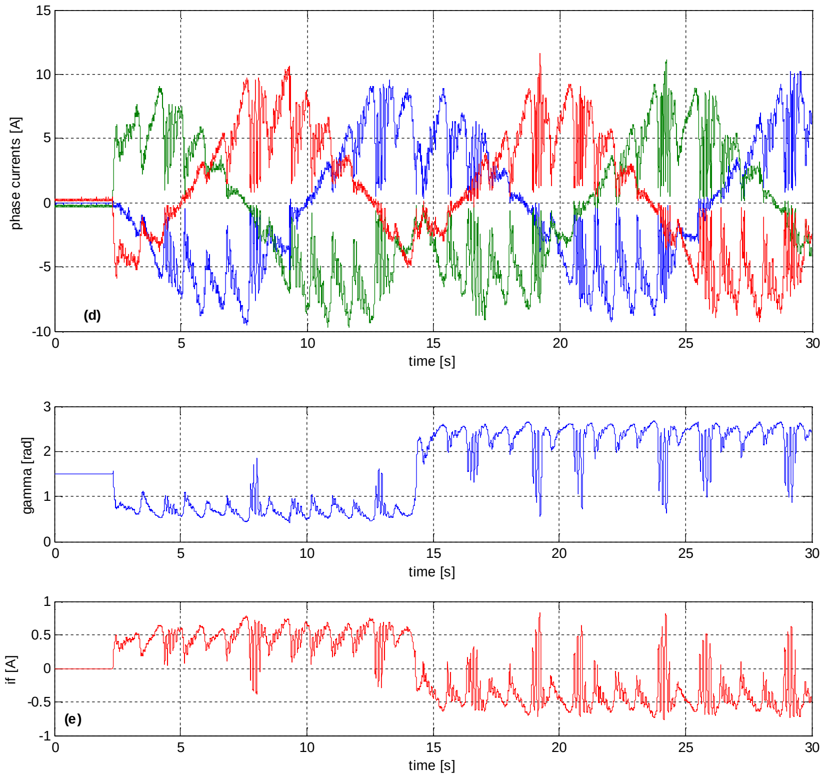

Fig. 5.26. Startup with load, ±2 rpm speed reversal with load. From top to bottom: (a) reference and measured rotor speed, (b) actual, estimated speed and speed error, (c) actual and estimated position, (d) phase currents (e), torque angle (δ) and dc field current

SUMMARY

In this chapter a review of existing sensorless control methods for permanent magnet synchronous motors is performed. Then the active flux concept and observer, for BEGA, is introduced. Based on simulation results the active flux concept is validated. Two solutions proposed for speed estimation based on estimated rotor position are compared. An analysis of the active flux compensator properties is done, based on simulations results. Finally, the performance of the active flux observer and estimators are performed based on experimental results.

REFERENCES

[5.1] A B Kulkarni, M Ehsani. “A Novel Position Sensor Elimination Technique For The Interior Permanent-Magnet Synchronous Motor Drive,” IEEE Transactions on Industry Applications, 1992, 28(1), pp.144-150

[5.2] Wu R, Slemon G R. “A Permanent Magnet Motor Drive Without A Shaft Sensor,” IEEE Industry Applications Society Annual Meeting, 1990, vol.1, pp. 553-558.

[5.3] M. Shin, D. Hyun, S. Cho, S. Choe, “An Improved Stator Flux Estimation For Speed Sensorless Stator Flux Orientation Control Of Induction Motors” IEEE Trans. Power Electron., Vol.15, No. 2, pp. 312–318.

[5.4] Zhiqian Chen, Tomita,M, Ichikawa S, Doki S, Okuma S. “Sensorless Control Of Interior Permanent Magnet Synchronous Motor By Estimation Of An Extended Electromotive Force,” Conference Record of the 2000 IEEE Industry Applications Conference, Oct. 2000, vol.3, pp. 1814-1819

[5.5] Morimoto S, Kawamoto K, Sanada M, Takeda Y. “Sensorless Control Strategy For Salient-Pole PMSM Based On Extended EMF In Rotating Reference Frame” IEEE Transactions on Industry Applications, Volume 38, Issue 4, July/Aug. 2002, pp. 1054-1061.

[5.6] Zhiqian Chen, Tomita M, Doki S, Okuma S. “An Extended Electromotive Force Model for Sensorless Control of Interior Permanent-Magnet Synchronous Motors,” IEEE Transactions on Industrial Electronics, Volume 50, Issue 2, April 2003, pp.288-29.

[5.7] M. Schrodl, M. Hofer, W. Staffler, "Extended EMF- And Parameter Observer For Sensorless Controlled PMSM-Machines At Low Speed", European Conference on Power Electronics and Applications, 2-5 Sept. 2007, pp.1 - 8

[5.8] Hasegawa M, Hatta H, Matsui K. “Adaptive Flux Observer on Stator Frame and Its Design Based on γ−Positive Real Problem for Sensorless IPM Drives,” 32nd Annual Conference of IEEE Industrial Electronics Society, 2005, 6-10 Nov, 2005, pp. 6.

[5.9] Bolognani S, Oboe R, Zigliotto M. “Sensorless Full-Digital PMSM Drive With EKF Estimation of Speed and Rotor Position,” IEEE Transactions on Industrial Electronics, Volume 46, Issue 1, Feb. 1999, pp.184-191.

[5.10] Bolognani S, Tubiana L, Zigliotto M. “EKF-Based Sensorless IPM Synchronous Motor Drive For Flux-Weakening Applications,” IEEE Transactions on Industry Applications, Volume 39, Issue 3, May/June 2003, pp.768-775.

[5.11] A. Bado, S. Bolognani, M. Zigliotto. “Effective Estimation Of Speed And Rotor Position Of A PM Synchronous Motor Drive By A Kalman Filtering Technique,” PESC'92, June/July 1992, vol. 2, pp. 951–957.

[5.12] Huang M C, Moses A J, Anayi F, Yao X G. “Linear Kalman Filter (LKF) Sensorless Control For Permanent Magnet Synchronous Motor Based On Orthogonal Output Linear Model,” International Symposium on Power Electronics, Electrical Drives, Automation and Motion, 2006. May, 23rd - 26th, 2006, pps.1381-1386.

[5.13] Y. Kim and Y. Kook, "High Performance IPMSM Drives Without Rotational Position Sensors Using Reduced-Order EKF", IEEE Transactions on Energy Conversion, vol. 14, pp. 868-873, Dec.1999.

[5.14] Z. Zheng, Y. Li, M. Fadel, "Sensorless Control of PMSM Based on Extended Kalman Filter ", Proc. of EPE 2007

[5.15] G D Andreescu. “Position And Speed Sensorless Control Of PMSM Drives Based On Adaptive Observer,” EPE’ Proc. 1999.

[5.16] Piippo A, Luomi J. “Adaptive Observer Combined With HF Signal Injection for Sensorless Control of PMSM Drives,” IEEE International Conference on Electric Machines and Drives, 15- 8 May 2005, pp. 674-681.

[5.17] A. Piippo, M. Hinkkanen, J. Luomi, “Analysis of an Adaptive Observer for Sensorless Control of PMSM Drives”, IECON 2005. 6-10 Nov. 2005

[5.18] Yan Liang, Yongdong Li. “Sensorless Control Of PM Synchronous Motors Based On MRAS Method And Initial Position Estimation,” Sixth International Conference on Electrical Machines and Systems, Vol.1, 9-11 Nov. 2003, pp.96-99

[5.19] Changsheng Li; Elbuluk M. “A Sliding Mode Observer For Sensorless Control Of Permanent Magnet Synchronous Motors,” Conference Record of the 36th IAS Annual Meeting. Sept./Oct. 2001, Vol.2, pp. 1273-1278.

[5.20] Salvatore L, Cupertino F, Cascella G L. “A New Approach To Sensorless Vector Control Of SMPM With Adaptive Sliding-Mode Observer,” Proceedings of the 2002 IEEE International Symposium on Industrial Electronics, SIE 2002,Vol.2, 8-11 July 2002, pp. 489-494.

[5.21] Song Chi, Longya Xu. “Position Sensorless Control of PMSM Based on a Novel Sliding Mode Observer over Wide Speed Range,” Power Electronics and Motion Control Conference, 2006. IPEMC '06, Vol.3, Aug. 2006, pp. 1-7.

[5.22] Yoon-Seok Han, Jung-Soo Choi, Young-Seok Kim. “Sensorless PMSM Drive with a Sliding Mode Control Based Adaptive Speed and Stator Resistance Estimator,” IEEE Transactions on Magnetics, Vol.36, Issue 5, Part 1, Sept. 2000, pp. 3588-3591.

[5.23] T. Furuhashi, S. Sangwongwanich, and S. Okuma, “A position - and – velocity sensorless control for brushless DC motors using an adaptive sliding mode observer," IEEE Trans. Industrial Electronics, Vol.39, 1992, pp. 89 - 95.

[5.24.] Z.M.A. Peixoto, Sa F.M Freitas, P.F. Seixas, and B.R. Menezes, “Application of sliding mode observer for induced e.m.f., position and speed estimation of permanent magnet motors," in Proc.Power Electronics and Drive Systems Int. Conf.,1995, pp.599 - 604.

[5.25] M. Ertugrul, O. Kaynak, A. Sabanovic, and K. Ohnishi, “A generalized approach for Lyapunov design of sliding mode controllers for motion control applications," in Proc. AMC'96-MIE Conf.,1996, pp.407 - 412.

[5.26] M. Elbuluk, and Li Changsheng, “Sliding Mode Observer for wide-speed sensorless control of PMSM drives," IAS Annual Meeting Conf, 2003, pp.480 - 485.

[5.27] K. Paponpen, M Konghirun, “Speed Sensorless Control of PMSM Using an Improved Sliding Mode Observer With Sigmoid Function”

[5.28] S. Chi, J. Sun, " A Novel Sliding Mode Observer with Multilevel Discontinuous Control for Position Sensorless PMSM Drives ", Proc. of APEC 2008

[5.29] P.L. Jansen and R.D. Lorenz, “Transducerless position and velocity estimation in induction and salient AC machines,” IEEE Trans. Ind. Appl.,Vol. 31, No. 2, pp. 240–247, Mar./Apr. 1995.

[5.30] Yu-seok Jeong, R.D. Lorenz, T.M. Jahns, and Seung-Ki Sul, “Initial rotor position estimation of an interior permanent-magnet synchronous machine using carrier-frequency injection methods” IEEE Trans. Ind. Appl., Vol. 41,No 1, pp. 38–45, Jan./Feb. 2005.

[5.31] J.M. Guerrero, M. Leetmaa, F. Briz, A. Zamarron, and R.D. Lorenz; “Inverter nonlinearity effects in high-frequency signal-injection-based sensorless control methods,” IEEE Trans. on Ind. Appl., Vol. 41, No. 2, pp. 618 – 626, Mar.-Apr. 2005

[5.32] C.-H. Choi and J.-K. Seouk, “Compensation of Zero-Current Clamping Effects for Sensorless Drives Based on High-Frequency Signal Injection,” IEEE Trans.on Ind. Appl., Vol. 43, No. 5, pp. 1258 – 1265, Sep.-Oct. 2007. [5.33] Dejan Raca, Pablo García, David Reigosa, Fernando Briz, and Robert Lorenz, “A Comparative Analysis of Pulsating vs. Rotating Vector Carrier Signal Injection-Based Sensorless Control,” Proc. of APEC2008, pp.879 – 885, Feb. 2008.

[5.34] D. Raca, P. García, D. Reigosa, F. Briz, R. D. Lorenz. “Carrier Signal Selection for Sensorless Control of PM Synchronous Machines at Zero and Very Low Speeds.” Proc. of IEEE IAS Conf. Oct. 5-9, 2008, Edmonton, Canada.

[5.35] J.-I. Ha, K. Ide, T. Sawa, and S.-K. Sul, “Sensorless rotor position estimation of an interior permanent-magnet motor from initial states,” IEEE Trans. on Ind. Appl., vol. 39, pp. 761-767, May-June 2003.

[5.36] I. Boldea, C. I. Pitic, C. Lascu, G.-D. Andreescu, L. Tutelea, F. Blaabjerg, P. Sandholdt, "DTFC-SVM motion-sensorless control of a PM-assisted reluctance synchronous machine as starter-alternator for hybrid electric vehicles", IEEE Transaction on Power Electronics, Volume 21, Issue 3, May 2006 Page(s):711 – 719

[5.37] G.-D. Andreescu, C. I. Pitic, F. Blaabjerg, I. Boldea, "Combined Flux Observer With Signal Injection Enhancement for Wide Speed Range Sensorless Direct Torque Control of IPMSM Drives", IEEE Transaction on Energy Conversion, Volume 23, Issue 2, June 2008 Page(s):393 - 402

[5.38] C. I. Pitic, G.-D. Andreescu, F. Blaabjerg, I. Boldea, "IPMSM motion-sensorless direct torque and flux control", Industrial Electronics Society, 2005. IECON 2005. 31st Annual Conference of IEEE 6-10 Nov. 2005

[5.39] S. Shinnaka, "A New Speed-Varying Ellipse Voltage Injection Method for Sensorless Drive of Permanent-Magnet Synchronous Motors With Pole Saliency—New PLL Method Using High-Frequency Current Component Multiplied Signal", IEEE Transactions on Industry Applications, Volume 44, Issue 3, May-june 2008 Page(s):777 – 788

[5.40] S. Shinnaka, "A Robust Single-Phase PLL System With Stable and Fast Tracking", IEEE Transactions on Industry Applications, Volume 44, Issue 2, March-April 2008 Page(s):624 – 633

[5.41] S. Shinnaka, "A new characteristics-variable two-input/output filter in D-module-designs, realizations, and equivalence", Transactions on Industry Applications, Volume 38, Issue 5, Sept.-Oct. 2002 Page(s):1290 – 1296

[5.42] S. Shinnaka, "New "mirror-phase vector control" for sensorless drive of permanent-magnet synchronous motor with pole saliency", IEEE Transactions on Industry Applications, Volume 41, Issue 3, May-June 2005 Page(s):825 – 833

[5.43] S. Shinnaka, "New "D-State-Observer"-based vector control for sensorless drive of permanent-magnet synchronous motors", IEEE Transactions on Industry Applications, Volume 41, Issue 3, May-June 2005 Page(s):825 - 833

[5.44] J.-H. Jang, J.-I. Ha, M. Ohto, K. Ide, and S.-K. Sul, "Analysis of permanent-magnet machine for sensorless control based on highfrequency signal injection," IEEE Transactions on Industry Applications, vol. 40, pp. 1595-1604, Nov./Dec. 2004.

[5.45] M. J. Corley and R. D. Lorenz, "Rotor Position and Velocity Estimation for a Salient-Pole Permanent Magnet Synchronous Machine at Standstill and High Speeds," IEEE Transactions on Industry Applications, vol. 34, pp. 784-789, 1998.

[5.46] T. Noguchi and S. Kohno, "Mechanical-sensorless permanent magnet motor drive using relative phase information of harmonic currents caused by frequency-modulated three-phase PWM carriers," IEEE Transactions on Industry Applications, vol. 39, pp. 1085-1092, 2003.

[5.47] M. Linke, R. Kennel, and J. Holtz, "Sensorless speed and position control of synchronous machines using alternating carrier injection," presented at IEEE International Electric Machines and Drives Conference, 2003. IEMDC'03, 2003.

[5.48] M. Linke, R. Kennel, and J. Holtz, "Sensorless position control of permanent magnet synchronous machines without limitation at zero speed," presented at IEEE 2002 28th Annual Conference of the Industrial Electronics Society, 2002.

[5.49] S. Östlund and M. Brokemper, "Sensorless Rotor-Position Detection from Zero to Rated Speed for an Integrated PM Synchronous Motor," IEEE Transactions on Industry Applications, vol. 32, pp. 1158-1165, Sep./Oct. 1996.

[5.50] Jeong Y, Lorenz R D, Jahns T M, Sul S. “Initial Rotor Position Estimation Of An Interior Permanent Magnet Synchronous Machine Using Carrier-Frequency Injection Methods,” IEEE International Electric Machines and Drives Conference, IEMDC'03. Vol.2, 1-4 June 2003, pp. 1218-1223.

[5.51] Ji-Hoon Jang, Seung-Ki Sul, Jung-Ik Ha, Ide K, Sawamura, M. “Sensorless Drive of Surface-Mounted Permanent-Magnet Motor by High-Frequency Signal Injection Based on Magnetic Saliency,” IEEE Transactions on Industry Applications, Vol.39, Issue 4, July/Aug. 2003, pp. 1031-1039.

[5.52] Corley M J, Lorenz R D. “Rotor Position And Velocity Estimation For A Permanent Magnet Synchronous Machine At Standstill And High Speeds,” Industry Conference Record of the 21st IAS Annual Meeting, IAS '96, Vol.1, 6-10 Oct. 1996, pp. 36-41.

[5.53] Saltiveri D, Asher G, Sumner M, Arias A, Romeral L. “Application Of The Matrix Converter For The Sensorless Position Control Of Permanent Magnet AC Machines Using High Frequency Injection,” European Conference on Power Electronics and Applications, 11-14 Sept. 2005, pp. 10.

[5.54] Eskola M, Tuusa H. “Sensorless Control Of Salient Pole PMSM Using A Low-Frequency Signal Injection,” European Conference on Power Electronics and Applications, 11-14 Sept. 2005, pp. 10.

[5.55] Schroedl M. “Operation Of The Permanent Magnet Synchronous Machine Without A Mechanical Sensor,” 4th IEE Conference On Power Electronics and Variable-Speed Drives, 1990, pp.51-56.

[5.56] M. Schroedl, “Sensorless control of AC machines at low speed and standstillbased on the “INFORM” method,” in Conf. Rec. IEEE-IAS Annu. Meeting, vol. 1, 1996, pp. 270–277.

[5.57] Schrodl M, Lambeck M. “Statistic Properties Of The INFORM Method For Highly Dynamic Sensorless Control Of PM Motors Down To Standstill,” The

29th Annual Conference of the IEEE Industrial Electronics Society, IECON '03. Vol.2, 2-6 Nov. 2003, pp. 1479-1486.

[5.58] E. Robeischl, M. Schroedl, “Optimized INFORM Measurement Sequence for Sensorless PM Synchronous Motor Drives With Respect to Minimum Current Distortion”, IEEE Transactions on Industry Applications, Vol. 40, No. 2, March/April 2004

[5.59] E. Robeischl, M. Schroedl, and K. Salutt, “Improved INFORM-measurementsequence and evaluation for sensorless permanent magnet synchronous motor drives,” presented at the 10th Int. Power Electronics and Motion Control Conf., Cavtat and Dubrovnik, Croatia, Sept. 9–11, 2002.

[5.60] A. Zentai1, T. Daboczi, “Improving INFORM calculation method onpermanent magnet synchronous machines”, IMTC 2007 – IEEE Instrumentation and MeasurementTechnology Conference Warsaw, Poland, May 1–3, 2007

[5.61] Rasmussen H, Vadstrup R, Borsting H. “Adaptive observer for speed sensorless PM motor control,” Conference Record of the 38th IAS Annual Meeting. Vol.1, 12-16 Oct. 2003, pp. 599-603.

[5.62] E. Urlep, K. Jezernik, "Low and Zero Speed Sensorless Control of nonsalient PMSM ", Proc. of ISIE 2007

[5.63] I. Boldea, M. C. Paicu, G.-D. Andreescu, "Active Flux Concept for Motion-Sensorless Unified AC Drives", IEEE Transactions on Power Electronics, 2008

[5.64] I. Boldea, M. C. Paicu, G.-D. Andreescu, "Active Flux Orientation Vector Sensorless Control of IPMSM", Proc. of OPTIM'08

[5.65] I. Boldea, M. C. Paicu, G.-D. Andreescu, "Direct torque and flux control of IPMSM"

[5.66] M. Fatu, L. Tutelea, I. Boldea, G.-D. Andreescu, "Motion sensorless control for ALA reluctance synchronous motor using “active-flux” concept", CNAE'08, Timisoara, Romania

[5.67] J. Holtz, J. Quan, "Drift and Parameter Compensated Flux Estimator for Persistent Zero Stator Frequency Operation of Sensorless Controlled Induction Motor", IEEE Transactions on Industry Applications, 2003

[5.68] V. Coroban, I. Boldea, G. D. Andreescu, “Active-flux based observer for motion sensorless control of biaxial excitation generator/motor for automobiles (BEGA)”, CNAE Sept. 2008

6. ACTIVE-FLUX MOTION SENSORLESS CONTROL OF BEGA: DIGITAL SIMULATIONS AND EXPERIMENTAL VALIDATION

The scope of this chapter is to present the performance of the active-flux based motion sensorless control of BEGA. The active-flux observer, position and speed estimator are tested for a wide speed range. In a first step the investigations were performed by simulations in a speed range of 20 to 2000rpm. In the second step the proposed solution was validated on the real setup in a speed range of 50 to 2000rpm. In the low speed range, the performance of the observer is acceptable, but for speeds below 50rpm, problems rise during startup and speed reversal.

In Chapter 5 the investigation of the active flux observer and position and speed estimator were performed with the machine driven with position and speed sensor. The aim of this chapter is to find out the performance of the observer and estimators with the machine driven without position and without speed sensor information. The position and speed information are provided by position and speed estimator instead of mechanical sensor. The proposed motion sensorless vector control structure for BEGA is shown in Fig. 6.1.

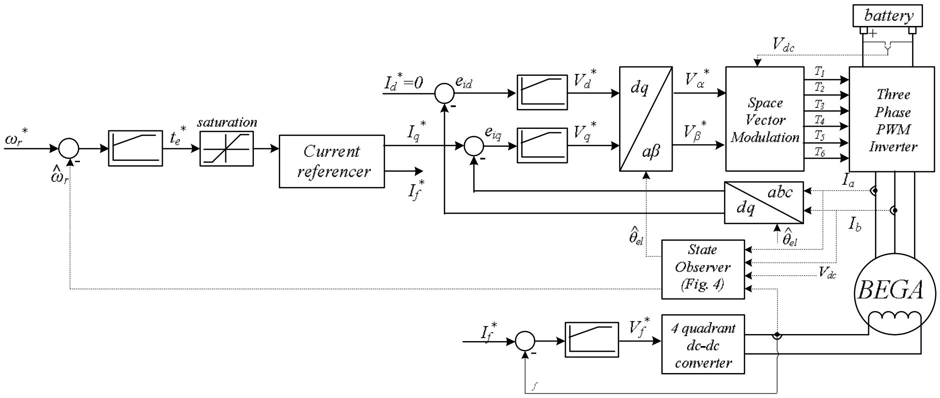

Fig. 6.1. Proposed BEGA Sensorless Vector Control Structure

Position information is needed only for coordinate's transformation, while speed information is used to close the speed loop. The control strategy remains the same as that one described in Chapter 4, where unity and high power factor operation was investigated.

6.1. Digital simulations

A set of simulations has been run to investigate the performance of the active flux observer, position and speed estimator for BEGA sensorless vector control using the “active flux “concept. Simulations have been run at 2000rpm, 200rpm and 20rpm. This way the performance of the observers and estimators are tested over a very large speed range.

6.1.1 High speed operation

For high speed operation a value of 2000rpm, for target speed, has been chosen. This speed is high enough so that to be considered representative for high speed range. It is well know, that for sensorless control of electric machines, in the high speed operation range, the observers and estimators are enough robust due to increased value of the back-emf. In fact not the back-emf itself is essential - important is the effect of the back-emf on the commanded stator voltage. In our system configuration only dc-link (battery) information is available.

In the active flux observer the stator supply voltage in stator coordinates is needed. Based on the dc-link voltage information and the calculated duty cycle values (in space vector modulation block) the stator voltage is estimated and furthermore used as an input in the active flux observer. The accuracy of the stator voltage estimation increases with the increase of its magnitude – the effect of inverter nonlinearities over the voltage distortion is less at high value of the voltage magnitude. The stator voltage magnitude increases with increasing the back-emf magnitude. This is the cause-effect relationship between back-emf and better performance of the observer in the high speed range.

As mention above in the first simulation scenario the motor target speed is set to 2000rpm. After 0.5s the target speed is set to -2500rpm. The motor speed, position, load and electromagnetic torque, torque angle, phase and dc field current are shown in Fig. 6.2.

The speed response is good without significant overshoot and oscillations. The actual and estimated speed, as well as the estimated speed error is shown in Fig. 6.2c. Speed errors below 10rpm are and up to 100rpm during transients are reported. Actual and estimated rotor position and estimated position error is shown in Fig. 6.2d.
During steady state the maximum position error is 5o (electrical), while during transients it reaches a value of 13 degrees. A position error of 90 electrical degrees exists when the dc current rise from zero. In other words if there is no current in the dc excitation and a speed command is set, the initialization value of rotor position will be 90 electrical degrees and will goes down to zero with the increase of the dc current in the excitation. The torque angle and dc field current is shown in Fig. 6.2e.

For positive dc currents (motoring) the torque angle is below 90 degrees (closer to 0^o- positive direction of d-axis) while for negative current (generating) the angle is above 90 degrees (closed to 180^o - negative direction of d-axis). The torque angle is as expected – below 90 degrees during motoring and above 90 degrees during generating.

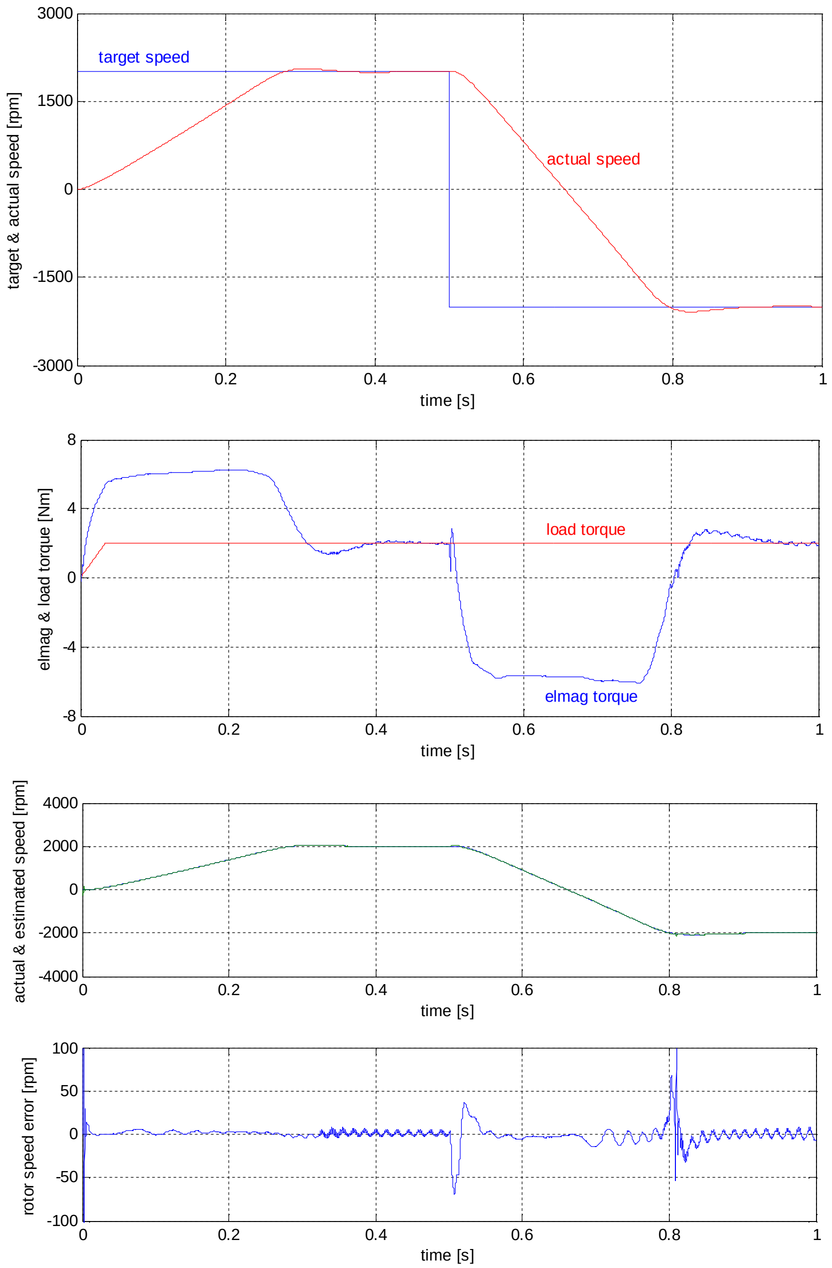
3000
1500
0
-1500
-3000
target & actual speed [rpm]
target speed
actual speed
0
0.2
0.4
0.6
0.8
1
time [s]
8
4
0
-4
-8
elmag & load torque [Nm]
load torque
elmag torque
time [s]
4000
2000
0
-2000
-4000
actual & estimated speed [rpm]
time [s]
100
50
0
-50
-100
rotor speed error [rpm]
time [s]

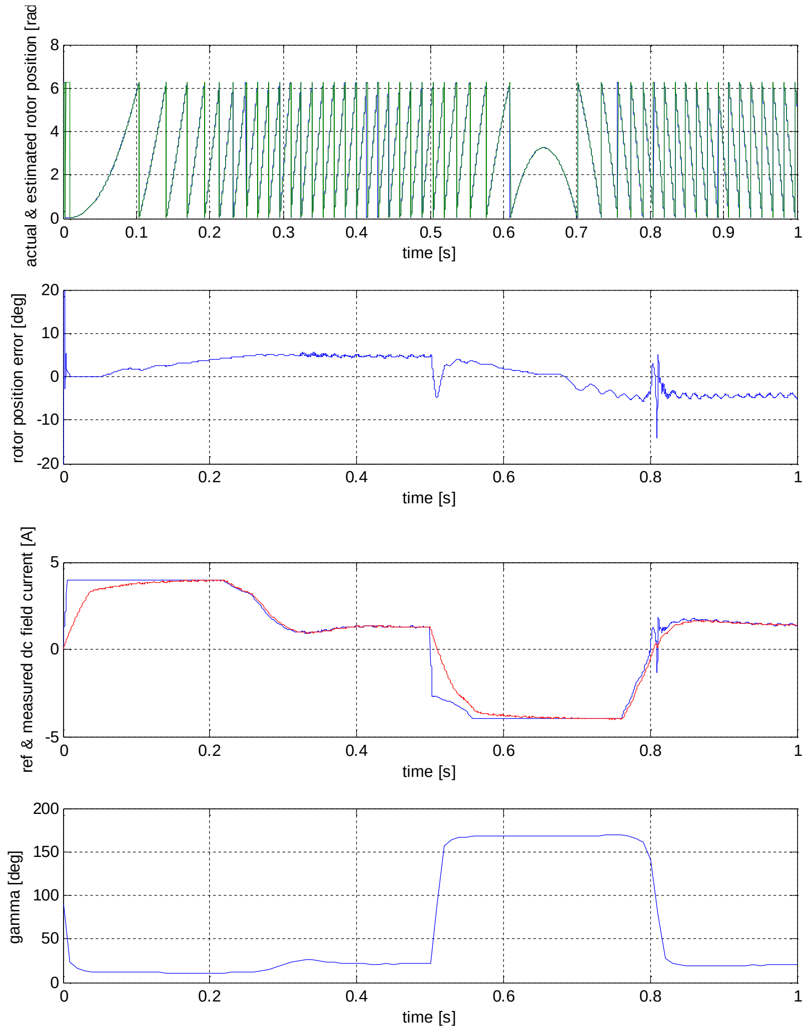

Fig. 6.2. Simulation results: startup with load, ±2000 rpm speed reversal with load. From top to bottom: (a) reference and measured rotor speed, (b) load and electromagnetic torque, (c) measured and estimated speed, speed error, (d) actual and estimated rotor electrical position, rotor position error (e) reference and measured dc field current, torque angle(δ)

6.1.2 Medium speed operation

For the medium speed operation a value of 200rpm is considered representative since for this speed value the back-emf is not so high, especially if the motor is running at no-load. In this second scenario the performance of the observer and estimator are evaluated for a startup at 200rpm, followed by a speed reverse after 400ms, with the motor loaded at half of the rated torque. The simulation results are presented in Fig. 6.3.

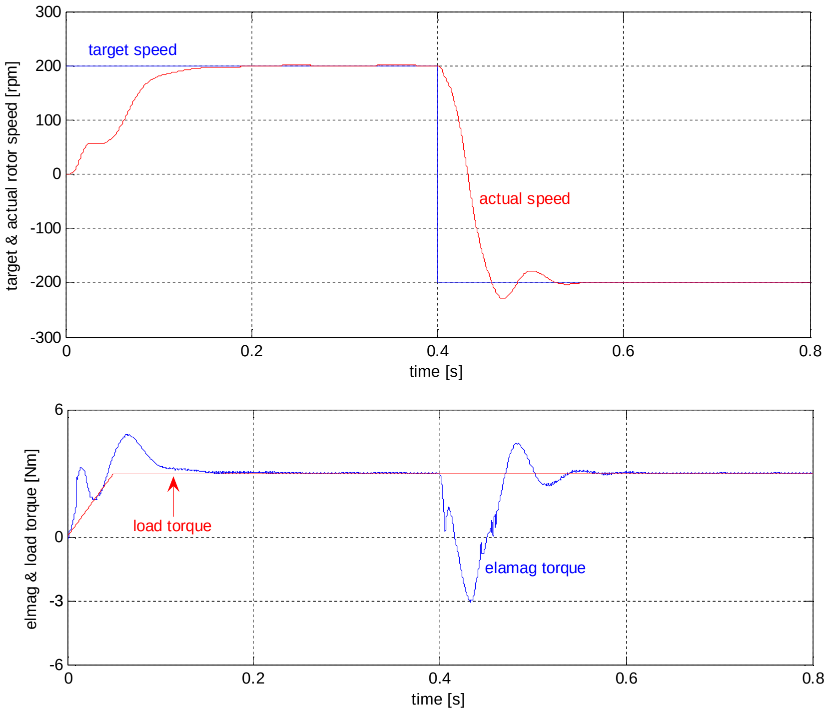

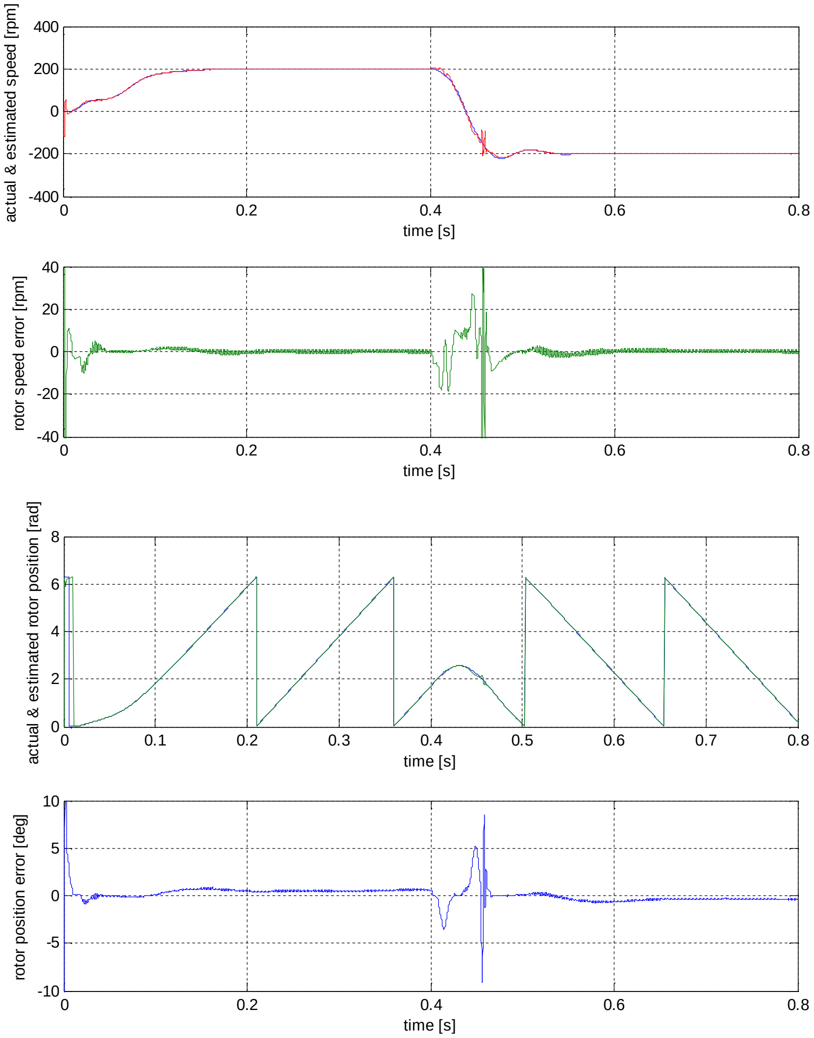
actual & estimated speed [rpm]
400
200
0
-200
-400
0
0.2
0.4
0.6
0.8
time [s]
rotor speed error [rpm]
40
20
0
-20
-40
0
0.2
0.4
0.6
0.8
time [s]
actual & estimated rotor position [rad]
8
6
4
2
0
0
0.1
0.2
0.3
0.4
0.5
0.6
0.7
0.8
time [s]
rotor position error [deg]
10
5
0
-5
-10
0
0.2
0.4
0.6
0.8
time [s]

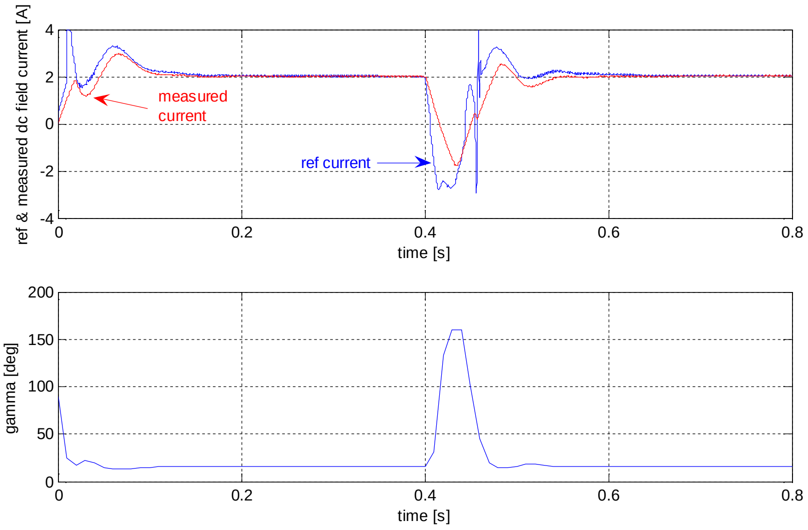

Fig. 6.3. Simulation results: startup with load, ±200 rpm speed reversal with load. From top to bottom: (a) reference and measured rotor speed, (b) load and electromagnetic torque, (d) measured and estimated speed, speed error, (d) actual and estimated rotor electrical position, rotor position error (e) reference and measured dc field current, torque angle(δ)

The estimated speed error during steady state is below 3rpm. For transients, errors up to 40rpm are recorded, when some small chattering in the dc current occurs. Notable oscillations in the estimated speed, for a short time, during startup can be seen. These oscillations are due to estimated position oscillations. Since the estimated speed is calculated based on the position derivation the link between position and speed oscillations is obvious. A maximum value of 9 degrees, in the estimated position error, is recorded during transients. At steady state the position error is very small – less than 1.5 degrees.

6.1.3 Low speed operation

Low speed operation is more than desirable and challenging for electric machines used as integrated starter-alternators in hybrid electric vehicles. This is request when the vehicle is driving forward at low speed or reverse gear. For low speed operation in the literature, PMSM sensorless control with speeds down to 1rpm, with full load, were reported. Such low speeds are, in general, with position estimators based on signal injection technique. The target is to use only one kind of observer/estimator for position and speed, over the whole operation range.

For low speed operation range a speed of 20rpm was chosen. The simulation results are shown in Fig. 6.4. Simulations with speed of a few rpm were performed, also, but without satisfactory results. The main problem of such low speed sensorless operation is the slow torque response that causes high speed transients during load disturbances, which can not be rejected in the end. A high overshoot in the motor speed is noted when a disturbance of 50% of the rated torque, with negative sign, is applied at the motor shaft. This way the motor is switching from motoring to generating. The load disturbance rejection is not very fast due to slow response of dc excitation current. The speed response is getting better when speed reversal is requested, from 20 to -20rpm.

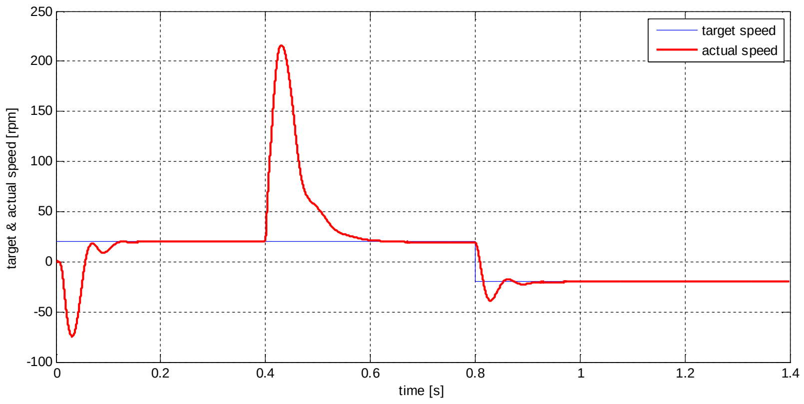

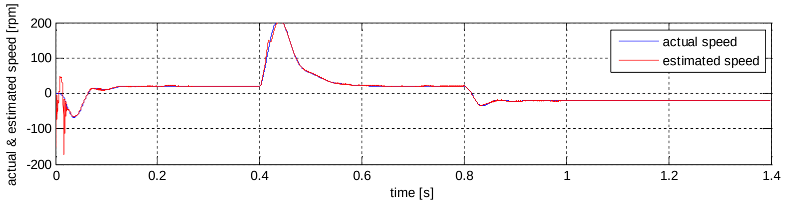

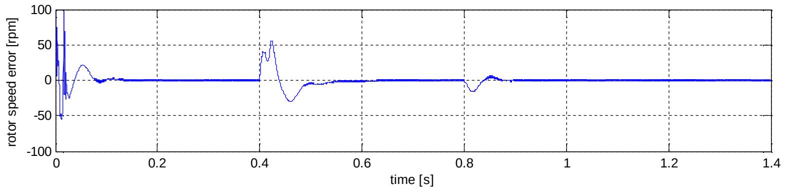

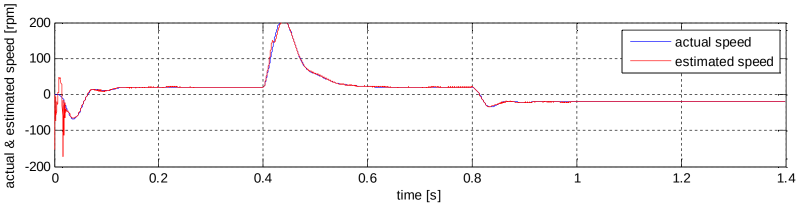
actual & estimated speed [rpm]
200
100
0
-100
-200
0
0.2
0.4
0.6
0.8
1
1.2
1.4
time [s]
actual speed
estimated speed

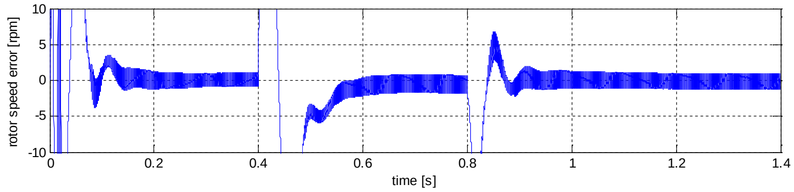
rotor speed error [rpm]
10
5
0
-5
-10
0
0.2
0.4
0.6
0.8
1
1.2
1.4
time [s]

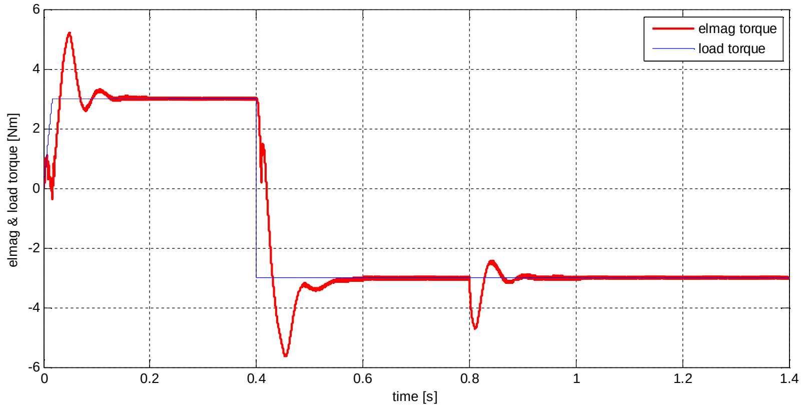
elmag & load torque [Nm]
6
4
2
0
-2
-4
-6
0
0.2
0.4
0.6
0.8
1
1.2
1.4
time [s]
elmag torque
load torque

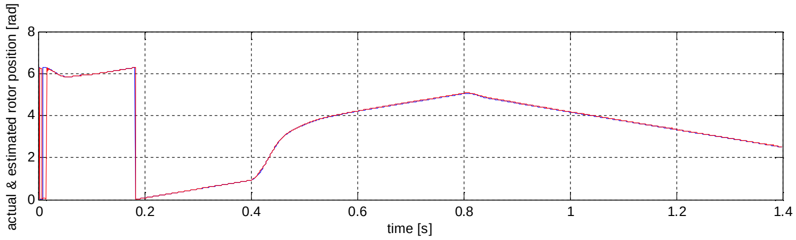
actual & estimated rotor position [rad]
8
6
4
2
0
0
0.2
0.4
0.6
0.8
1
1.2
1.4
time [s]

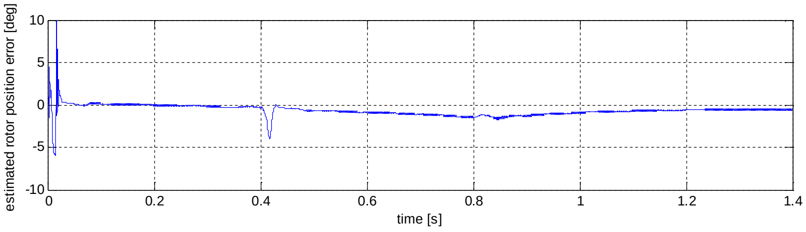
estimated rotor position error [deg]
10
5
0
-5
-10
0
0.2
0.4
0.6
0.8
1
1.2
1.4
time [s]

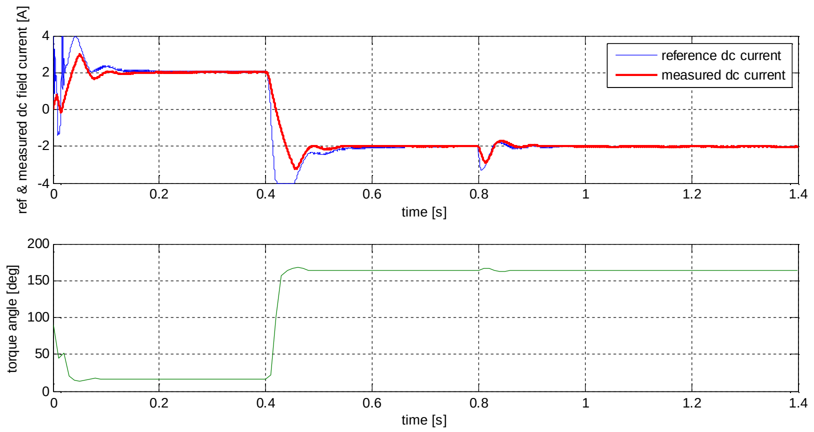

Fig. 6.4. Simulation results: startup with load, ±20 rpm speed reversal with 50% load. From top to bottom: (a) reference and measured rotor speed, (b) actual and estimated speed; estimated speed error, (c) actual and estimated speed; zoom on estimated speed error, (d) load and electromagnetic torque, (e) actual and estimated rotor electrical position; estimated rotor position error (f) reference and measured dc field current; torque angle(δ)

6.2. Experimetal results

With the sensorless vector control system proposed in Fig. 6.1 a set of experiments on the testbench described in Chapter 4 will be run in order to validate the theoretical background of the active flux concept and to find out the performance and the limits of the proposed observer.

As it is was mentioned above, for sensorless control of electric drives the performance of the position and speed observers/estimators degrades at low speeds, and therefore the first experiments will be performed at in the high speed range where the observer's performance is not too sensitive to the machine and observer parameters.

Therefore in the first experiment a target speed of 2000rpm will be set. The complete reference speed profile is as follows: a) time=0.75s the target speed is set to 2000rpm, b) time=4.75s the target speed is set to -2000rpm, time=8.75s the target speed is set to 2000rpm, time=12.75s the target speed is set again to -2000rpm. The experimental results for such a target speed profile are presented in Fig. 6.5. The scope of our investigation is to analyse the performance of the observer in all conditions: start-up, steady-state and reversal.

Startup:
Some oscillation can be observed in the estimated speed for a very short time of 150ms. The speed oscillations are more on the negative side of the speed axis and it is due to the fast transient of the estimated position from the initial value of π/2 towards zero, which is the initial position of the machine rotor. Looking on the

estimated position (Fig. 6.5d) and estimated speed (Fig.5a) we see the correspondence between estimated position and estimated speed which are linked by a derivative relationship. Of course a soft filtering is applied on the estimated speed to remove the high frequency noise. The negative oscillations in the estimated position "prevent" a possible starting of the machine in the opposite direction of the target. The estimated position error converges to zero after 30-40ms and after it stays below 10 (electrical degrees). After around 170ms from the control triggering, the error position drops below 2-3 electrical degrees. According to Fig. 6.5b a spike of 225rpm (for a very short time) is in the estimated speed. After that an error of maximum 60rpm is reported, which is decreasing to ±12rpm during steady state.

Steady-state:

The estimated position error is below 2-3 degrees, while the estimated speed error is below 12rpm according to Fig. 6.5f and 6.5b, respectively.

Speed reversal:

During speed reversal, immediately after the command switches its sign, some spikes in the estimated speed occur due to higher dynamic of the dc current. After 500ms the estimated speed drops below the acceptable limit of ±10rpm. The error of the estimated position reaches o maximum of 33 degrees.

A zoom on the estimated stator and active flux (in stator coordinates) is presented in Fig. 6.5i and Fig. 6.5j, at steady state and speed reversal respectively. It can be noted that the active flux angle is a few degrees before the stator flux angle and the magnitude of the active flux is lower than the magnitude of the stator flux. Both remarks are in an agreement with the theory behind active flux concept.

The reference, actual dc field current and torque angle are given in Fig. 6.5.k

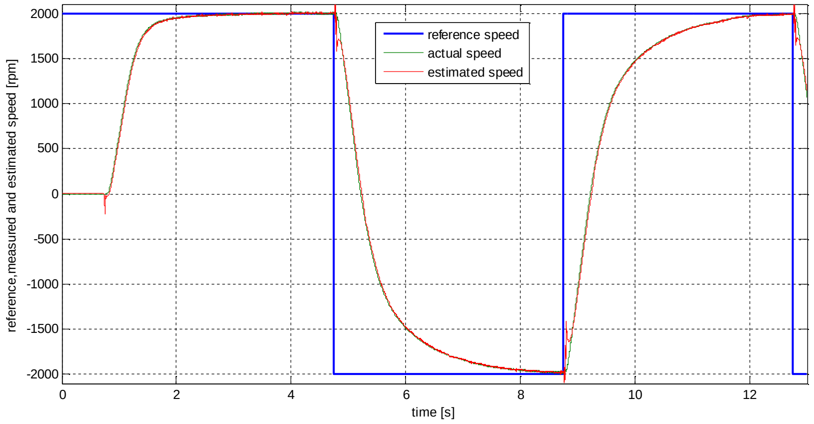

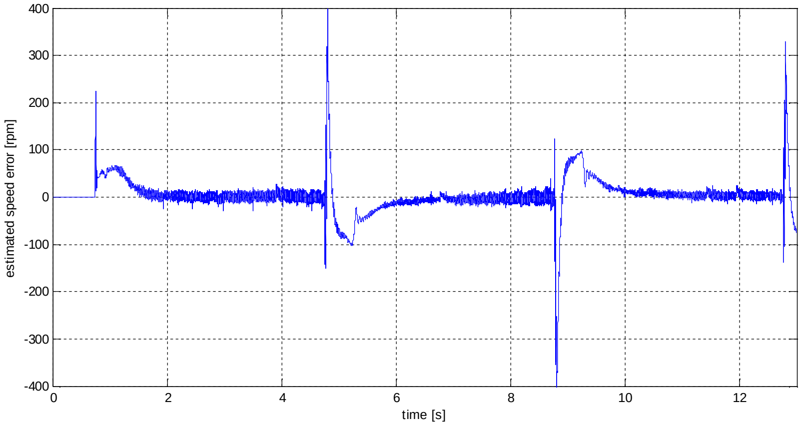
400
300
200
100
0
-100
-200
-300
-400
estimated speed error [rpm]
0
2
4
6
8
10
12
time [s]

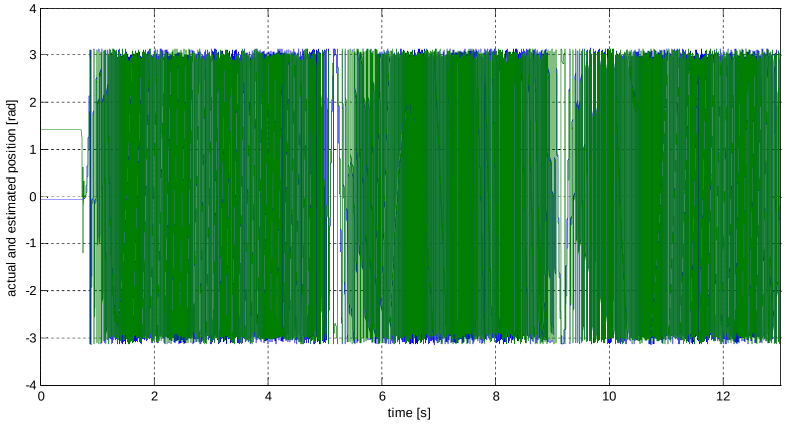
4
3
2
1
0
-1
-2
-3
-4
actual and estimated position [rad]
0
2
4
6
8
10
12
time [s]

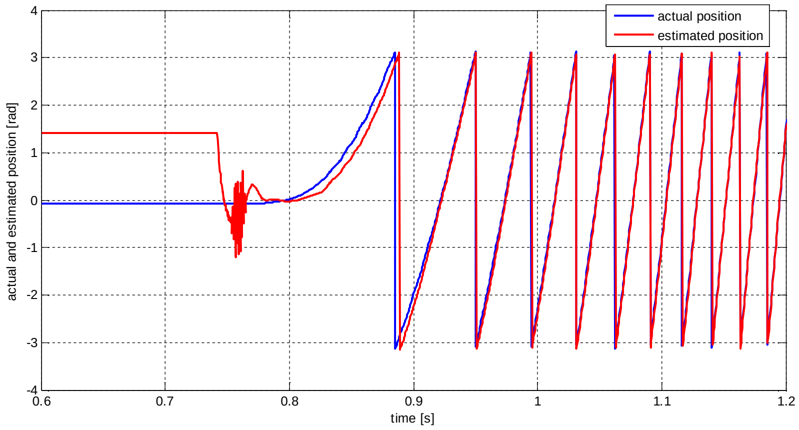
actual position
estimated position
4
3
2
1
0
-1
-2
-3
-4
actual and estimated position [rad]
0.6
0.7
0.8
0.9
1
1.1
1.2
time [s]

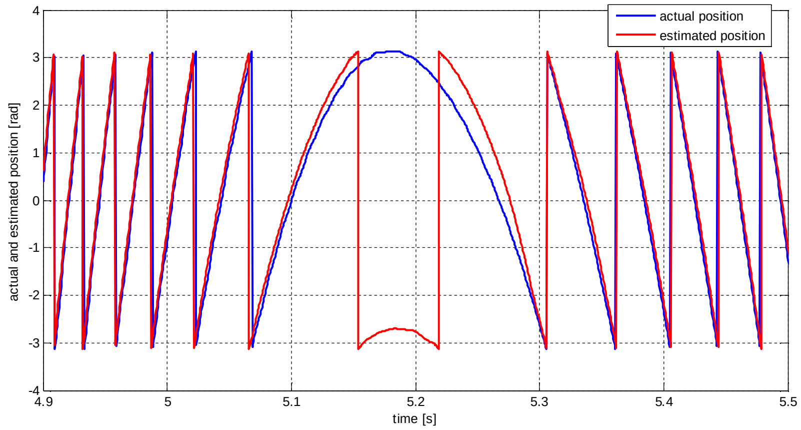
actual position
estimated position
actual and estimated position [rad]
time [s]
4
3
2
1
0
-1
-2
-3
-4
4.9
5
5.1
5.2
5.3
5.4
5.5

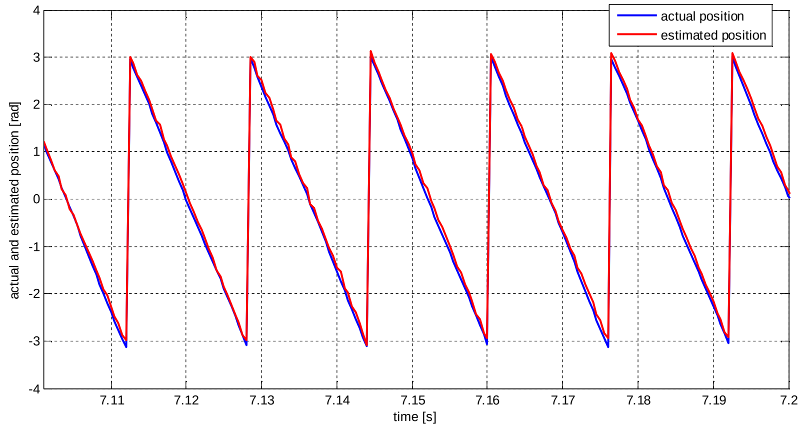
actual position
estimated position
actual and estimated position [rad]
time [s]
4
3
2
1
0
-1
-2
-3
-4
7.11
7.12
7.13
7.14
7.15
7.16
7.17
7.18
7.19
7.2

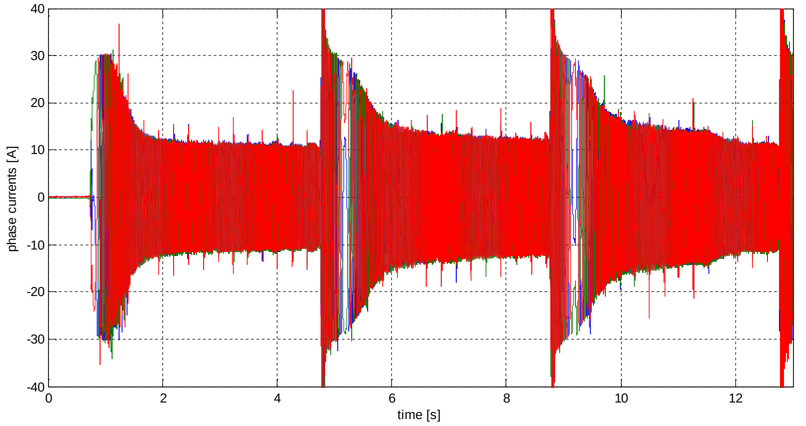
phase currents [A]
time [s]
40
30
20
10
0
-10
-20
-30
-40
0
2
4
6
8
10
12

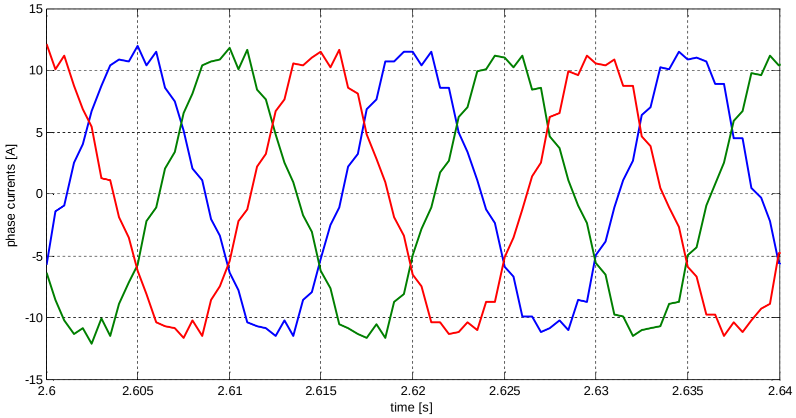
phase currents [A]
15
10
5
0
-5
-10
-15
2.6
2.605
2.61
2.615
2.62
2.625
2.63
2.635
2.64
time [s]

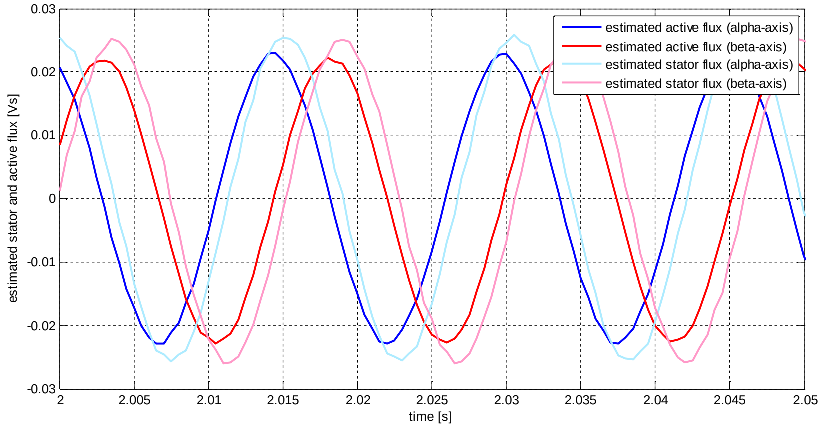
estimated stator and active flux [Vs]
0.03
0.02
0.01
0
-0.01
-0.02
-0.03
2
2.005
2.01
2.015
2.02
2.025
2.03
2.035
2.04
2.045
2.05
time [s]
estimated active flux (alpha-axis)
estimated active flux (beta-axis)
estimated stator flux (alpha-axis)
estimated stator flux (beta-axis)

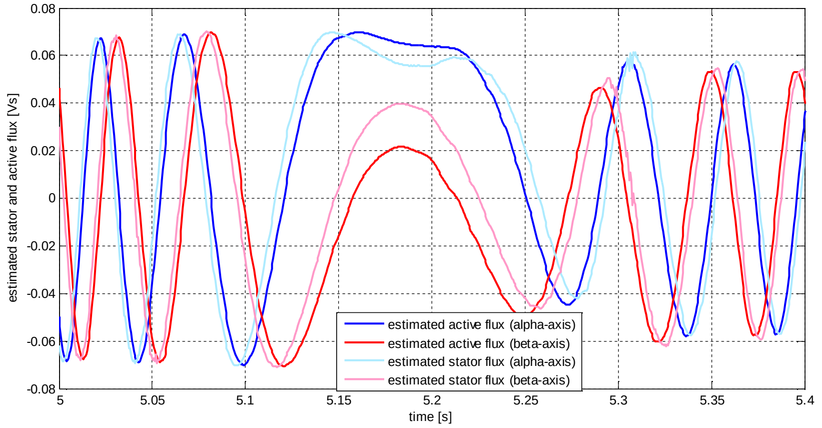
estimated stator and active flux [Vs]
0.08
0.06
0.04
0.02
0
-0.02
-0.04
-0.06
-0.08
5
5.05
5.1
5.15
5.2
5.25
5.3
5.35
5.4
time [s]
estimated active flux (alpha-axis)
estimated active flux (beta-axis)
estimated stator flux (alpha-axis)
estimated stator flux (beta-axis)

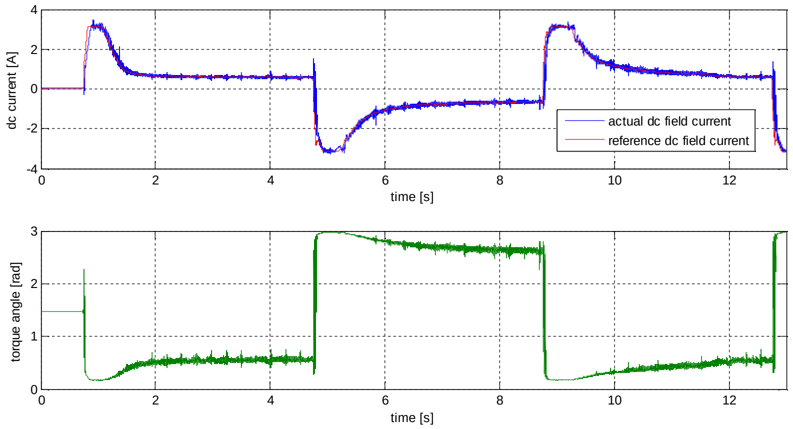

Fig. 6.5. Experimental results: startup to 2000rpm followed by ±2000 rpm speed reversal without load. From top to bottom: (a) reference, measured and actual rotor speed, (b) estimated speed error, (c) actual and estimated rotor electrical position, (d),(e),(f) zoom on c), (g) phase currents, (h) zoom on g), (i),(j) zoom on estimated stator and active flux in stator coordinates, (k) reference and actual dc field current (upper side) and torque angle δ (lower side)

Within the second experiment, the performances of the observer are evaluated for a speed of 500rpm, in the medium speed range. The experimental results are shown in Fig. 6.6. The estimated speed shape is very similar to the previous case: some oscillations immediately after the command is enable; some spikes when the commanded speed is change to the opposite way; during speed reversal the estimated speed errors become smaller in time to a value of ±5rpm at steady state.

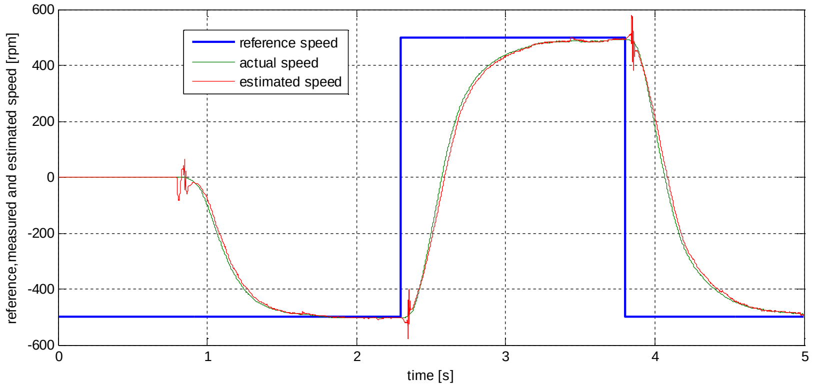

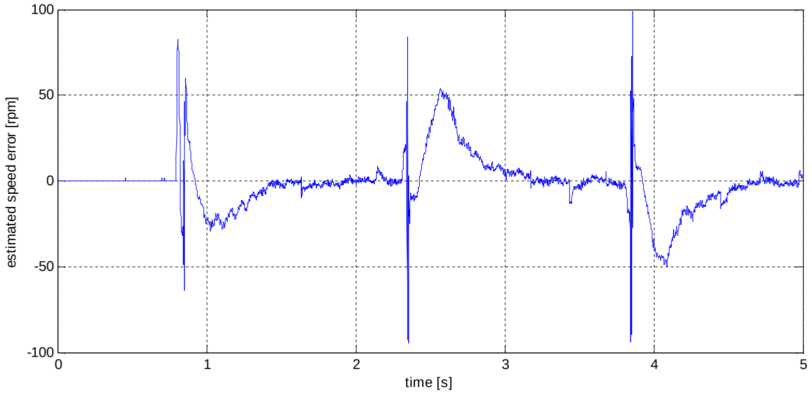
100
50
0
-50
-100
estimated speed error [rpm]
0
1
2
3
4
5
time [s]

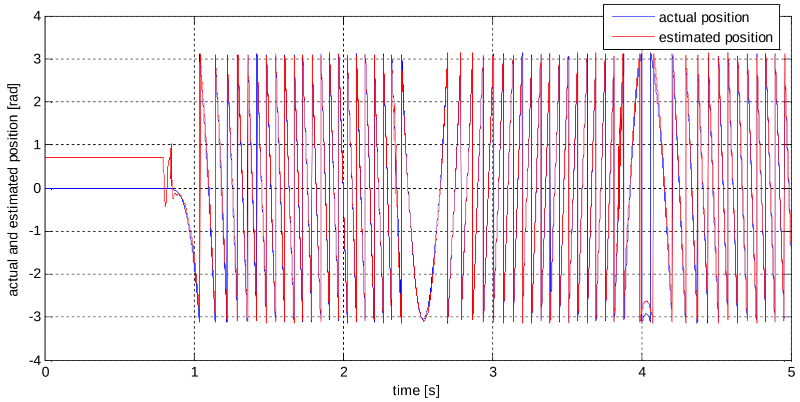
actual position
estimated position
4
3
2
1
0
-1
-2
-3
-4
actual and estimated position [rad]
0
1
2
3
4
5
time [s]

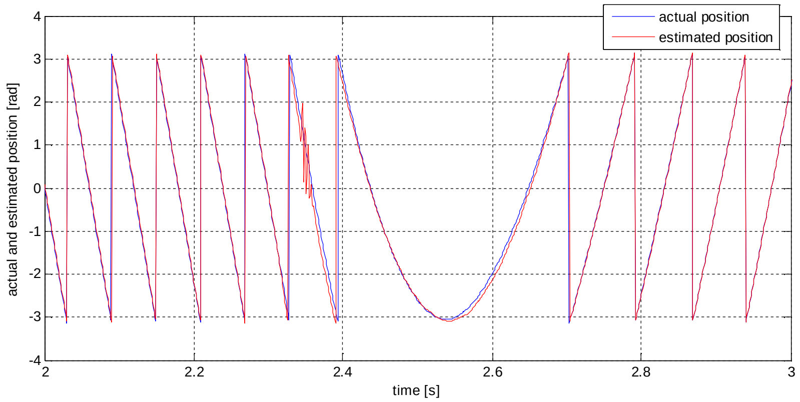
actual position
estimated position
4
3
2
1
0
-1
-2
-3
-4
actual and estimated position [rad]
2
2.2
2.4
2.6
2.8
3
time [s]

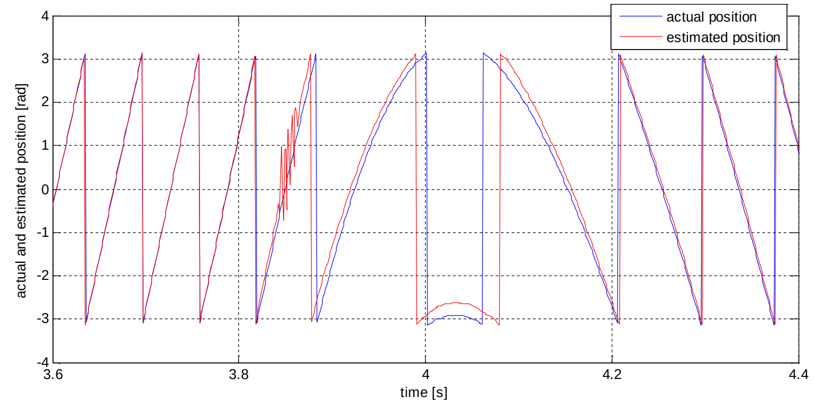
actual position
estimated position
actual and estimated position [rad]
time [s]
4
3
2
1
0
-1
-2
-3
-4
3.6
3.8
4
4.2
4.4

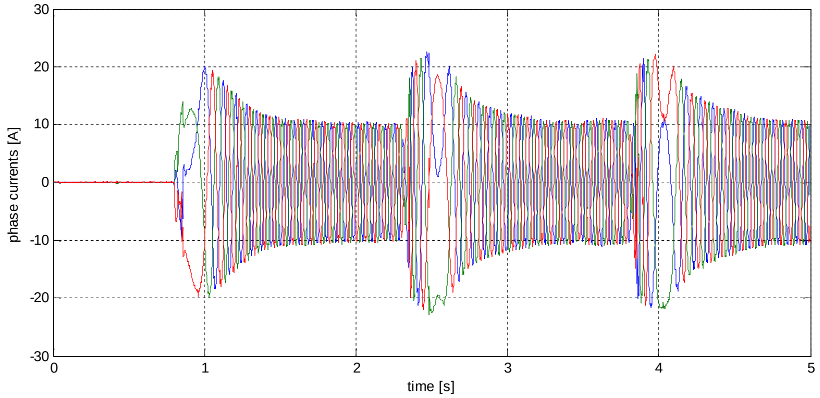
phase currents [A]
time [s]
30
20
10
0
-10
-20
-30
0
1
2
3
4
5

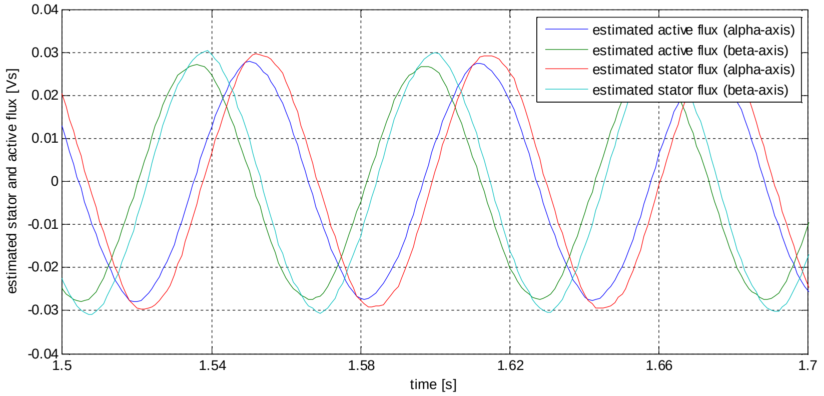
estimated active flux (alpha-axis)
estimated active flux (beta-axis)
estimated stator flux (alpha-axis)
estimated stator flux (beta-axis)
estimated stator and active flux [Vs]
time [s]
0.04
0.03
0.02
0.01
0
-0.01
-0.02
-0.03
-0.04
1.5
1.54
1.58
1.62
1.66
1.7

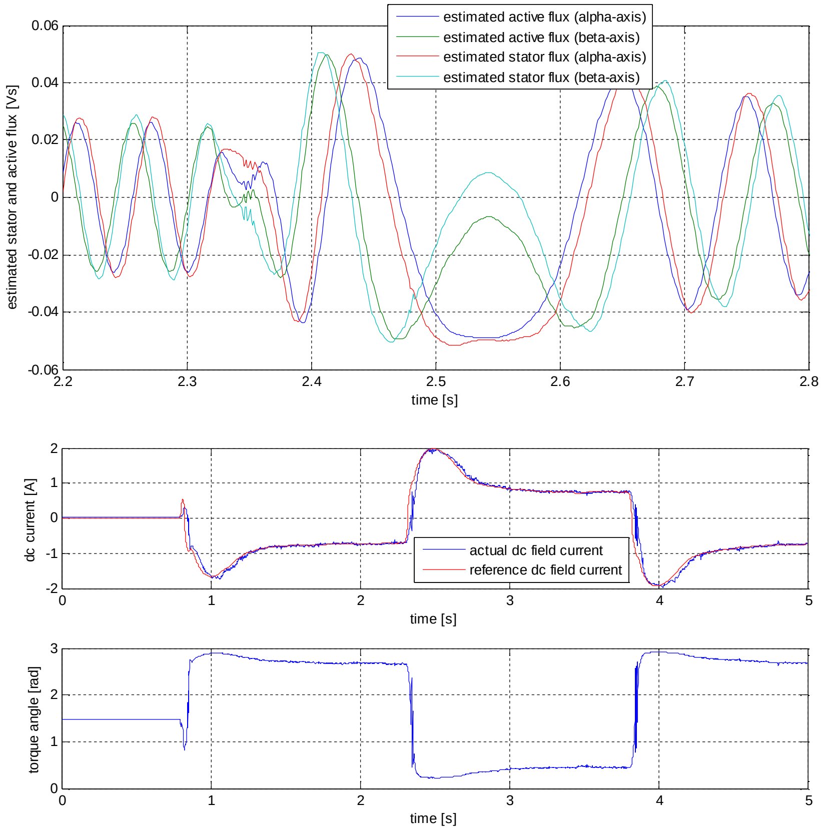

Fig. 6.6. Experimental results: startup to 500rpm followed by ±500 rpm speed reversal without load. From top to bottom: (a) reference, measured and actual rotor speed, (b) estimated speed error, (c) actual and estimated rotor electrical position, (d),(e) zoom on c), (f) phase currents, (g),(i) zoom on estimated stator and active flux in stator coordinates, (h) reference and actual dc field current (upper side) and torque angle δ (lower side)

The estimated position converges fast to real position during starting. During speed reversal the estimated position is overlapping with the actual position – when the reference speed changes from negative to positive – and an error of maximum 20 degree can be noted when the speed changes from positive to negative. The active flux is in front of the stator flux both during motoring and generating. This is accordance with the theory.

Figure 6.7 shows experimental results for speed sensorless operation at 200rpm. The motor is starting under no-load condition. At time=6s a load (approx. 50% of rated torque) is applied to BEGA shaft via the induction machine which is sensorless torque controlled via three-phase bidirectional inverter. The load does not increase suddenly due to low performance of the load drive in the low speed range. Before loading, BEGA is running as a motor (negative speed, negative toeque) and after loading BEGA switches in generating (negative speed, positive torque). After the startup, the estimated speed error stays within ±8rpm. The absolute deviation of estimated position is increasing after BEGA loading, reaching an average value of 30o electrical. The correspondence between torque angle (γ) and dc excitation current can be seen in Fig. 6.7.g) and h). Values of torque angle above π/2 are characteristics for generating while values below π/2 are characteristics for motoring.

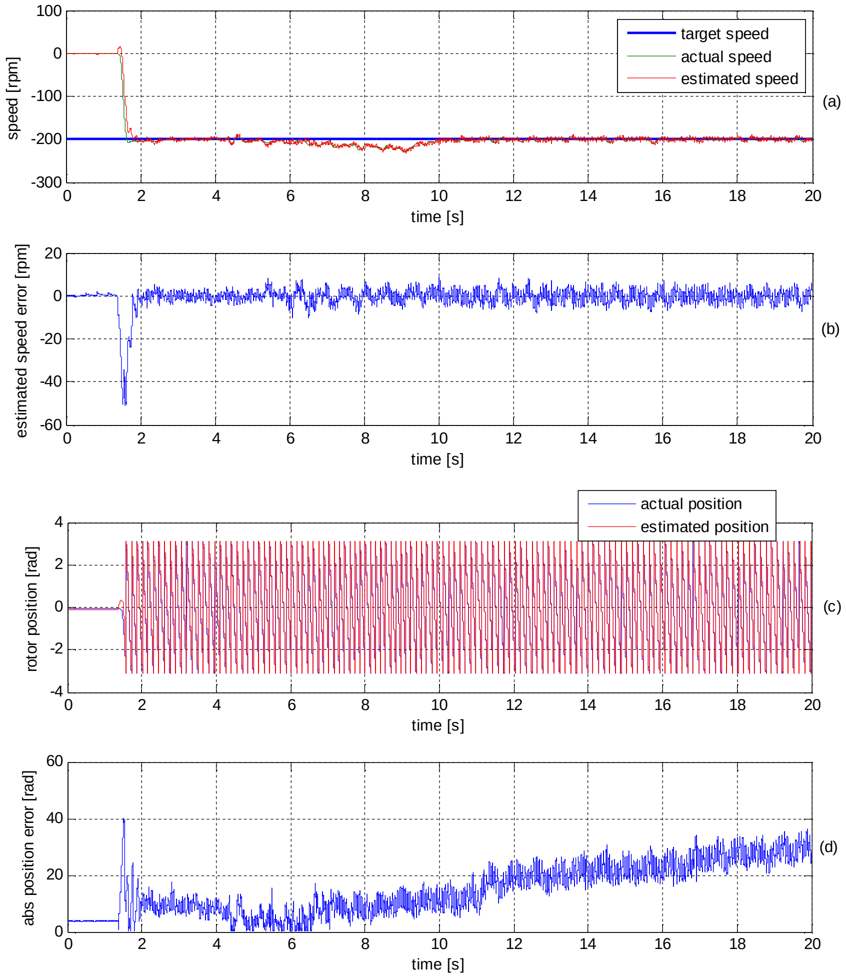

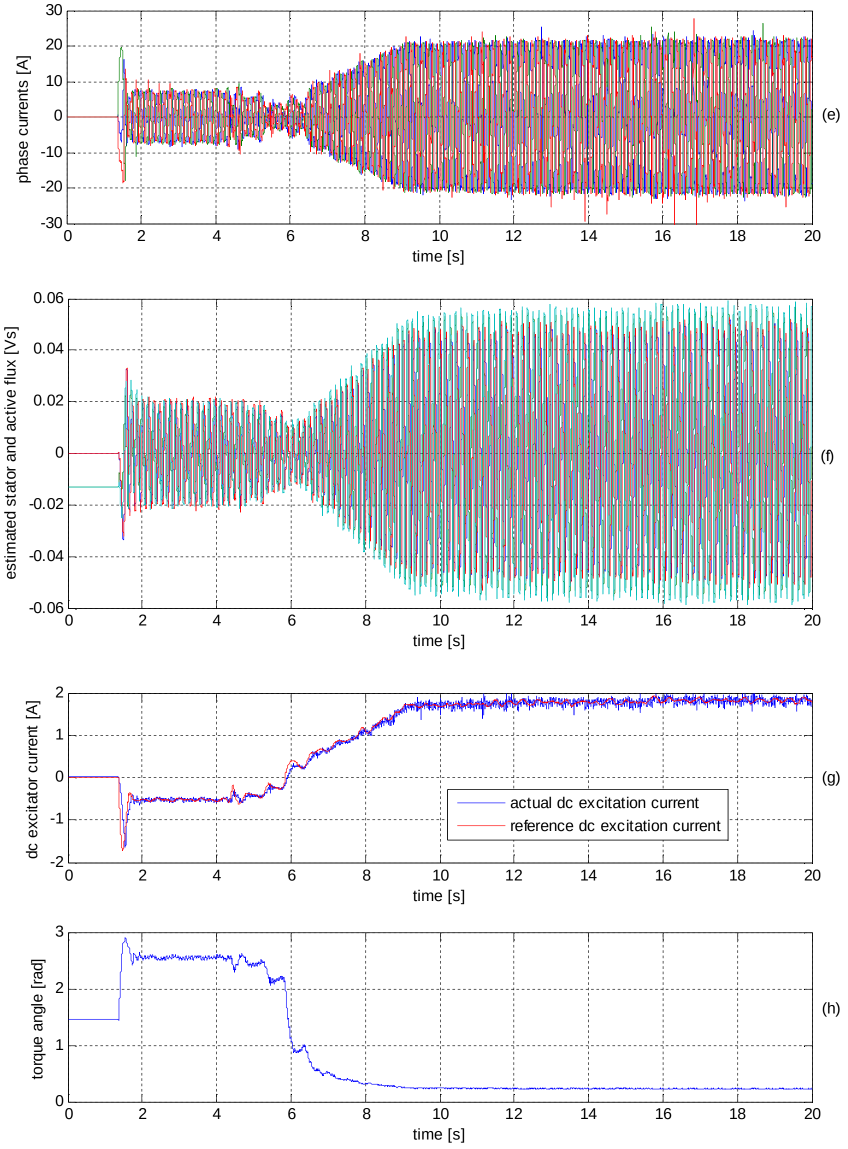

Fig. 6.7. Experimental results: startup to 200rpm followed by loading to 50%: (a) reference, measured and actual rotor speed, (b) estimated speed error, (c) actual and estimated rotor electrical position, (d) estimated rotor position error,(e) phase currents, (f) zoom on estimated stator and active flux in stator coordinates, (g) reference, actual dc field current, h) torque angle (δ)

Another experiment performed in the low speed range is a startup to 150rpm followed by four speed reversals at the same target speed, without loading – the performance of the load drive degrades seriously in the low speed range. This is the reason why the experiments, at low speed, are performed at no-load. Experimental results are shown in Fig. 6.8. Speed deviations below ±8rpm, in steady state are considered acceptable. During transients deviations of the estimated speed up to ±60rpm are noticed. According to Fig. 6.8.d, the average value of the estimated position is higher in motoring (10°) than in generating (4°). A zoom on stator and active flux during stratup is shown in Fig. 6.8.f.

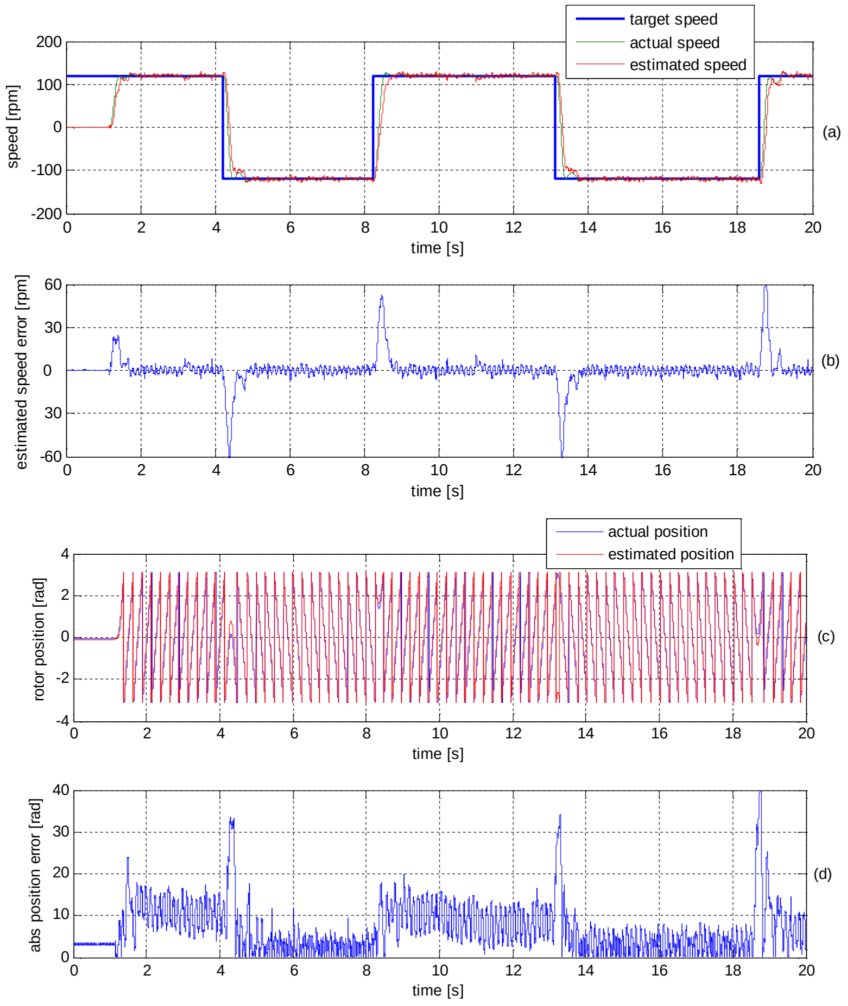

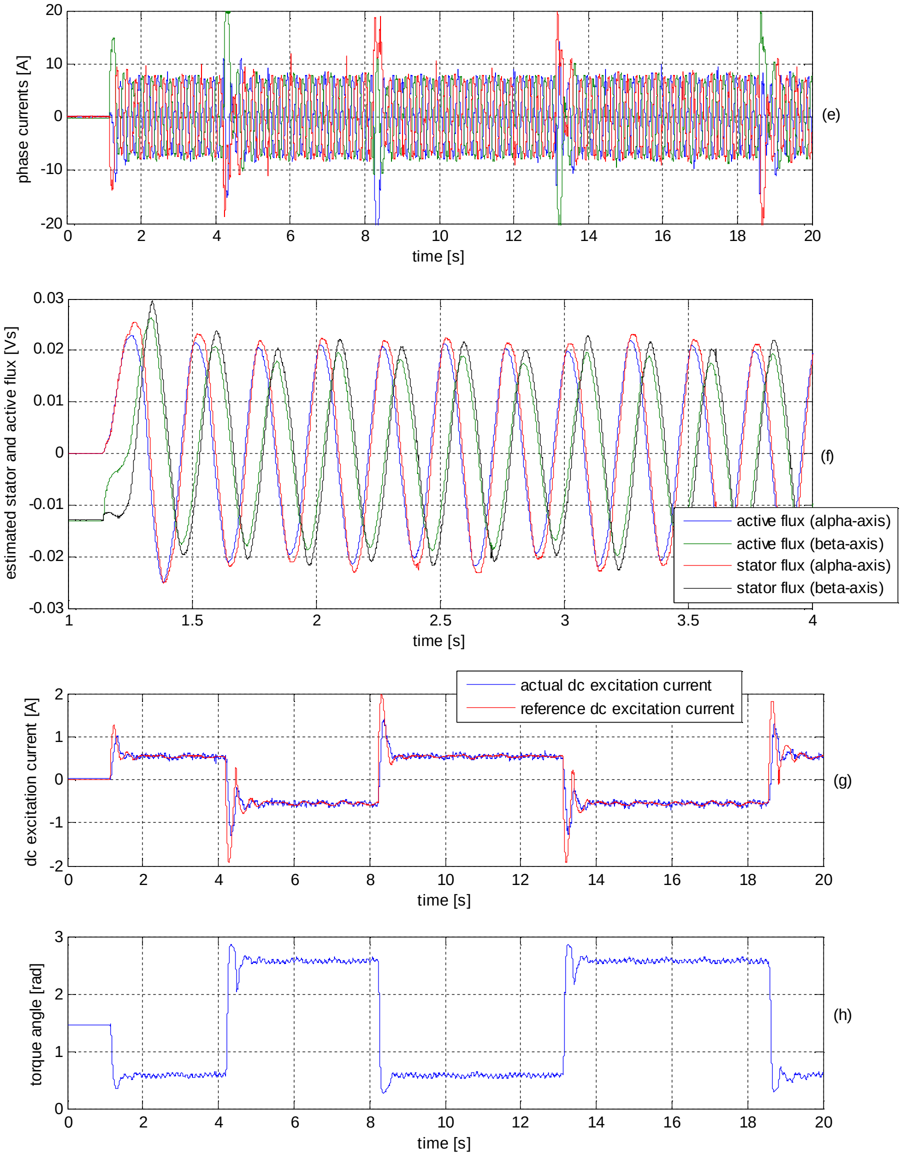

Fig. 6.8. Experimental results: startup to 150rpm followed by ±150 rpm speed reversal without load: (a) reference, measured and actual rotor speed, (b) estimated speed error, (c) actual and estimated rotor electrical position, (d) estimated rotor position error,(e) phase currents, (f) zoom on estimated stator and active flux in stator coordinates, (g) reference, actual dc field current, h) torque angle (δ)

Fig. 6.9 shows the no-load startup to 50rpm followed by two speed reversal at ±50rpm under no-load conditions, also. At steady-state the estimation speed deviation is about ±7rpm. The absolute average error of the estimated position is about 20^o during motoring and about 11^o during generating.

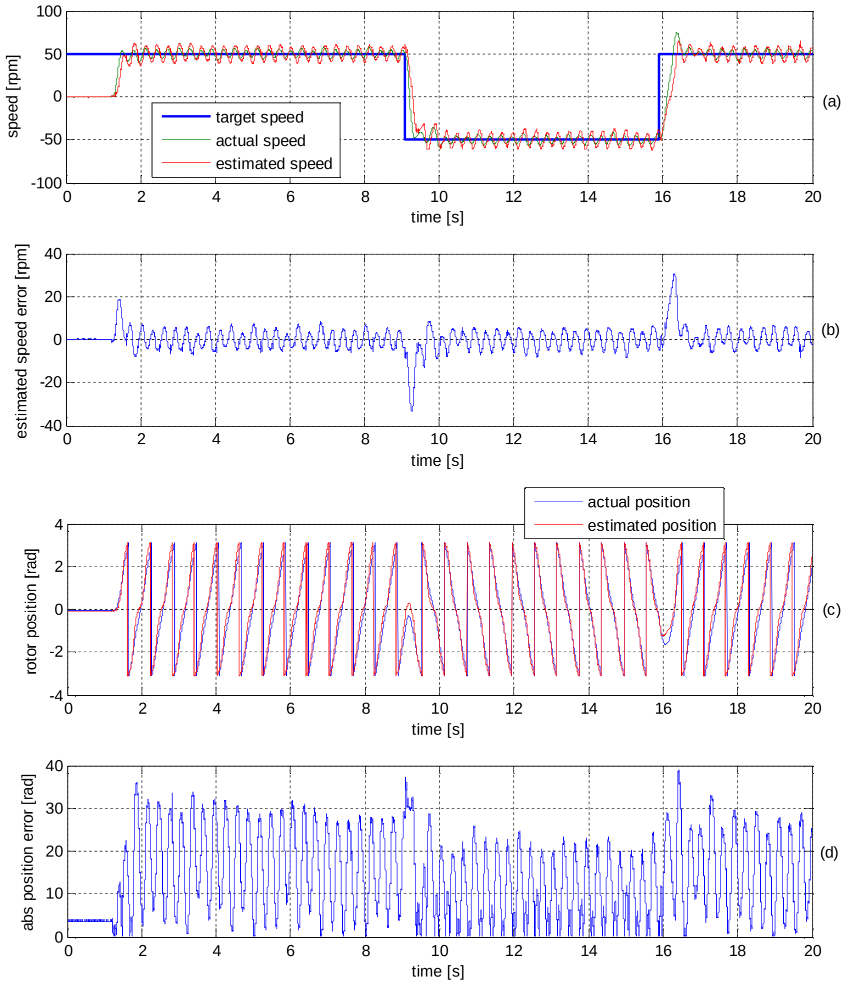

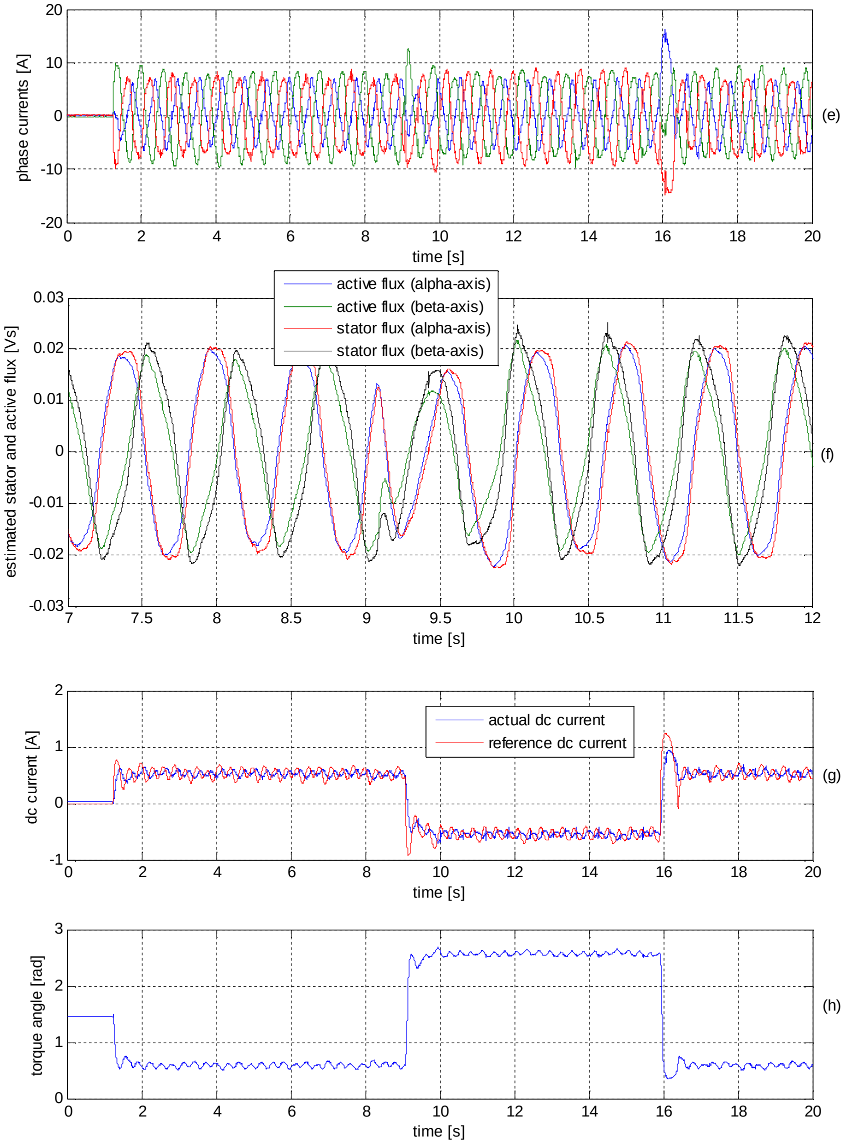

Fig. 6.9. Experimental results at startup to 50rpm followed by ±50 rpm speed reversal without load: (a) reference, measured and actual rotor speed, (b) estimated speed error, (c) actual and estimated rotor electrical position, (d) estimated rotor position error,(e) phase currents, (f) zoom on estimated stator and active flux in stator coordinates, (g) reference, actual dc field current, h) torque angle (δ)

6.3. Initial rotor position detection

The knowledge of initial rotor position of BEGA is essential for a safe starting when the machine is vector control driven. Therefore the initial rotor position detection with a good accuracy is required. There are in the literature many papers describing different solutions for initial rotor position detection of permanent magnet synchronous machines. These solutions can be classified into the following categories, based on their principles [6.1]:

- Voltage and reactive power harmonics [6.2], [6.3]
- Variation of inductance [6.4], [6.5], [6.6], [6.7]
- Patterns of voltage and current vectors [6.8]
- Observer and Kalman filter techniques
- Pulse voltage vectors [6.9]
- High frequency signal injection [6.10], [6.11], [6.12], [6.13]

In [6.14] an algorithm is proposed for initial position estimation of a dc-excited synchronous machine. The same principle is used, in what follows, for BEGA initial rotor position estimation. The algorithm principle is represented in Fig. 6.10 and 6.11.

A voltage pulse is applied to the dc field excitation. The dc excitation current starts to increase until a steady-state value is reached. During transients, an induced voltage is generated in the stator windings. The magnitude of the induced voltage is proportionally with the current variation (the highest magnitude of the induced voltage occurs at the beginning of the applied voltage pulse - when the current slope is maximum; zero voltage is induced in the stator when dc excitation current reaches the steady state value). The stator windings are shortcircuited by applying a zero voltage vector (upper transistors on the inverter legs are turned off while the lower transistors on the inverter legs are turned on. This way a shortcircuit current flows through the machine stator windings. All this time the phase currents are sampled with 100us reccurence. Only two current sensors are needed since the third one is calculated based on two measured currents. It is important to distinguish between the north and south magnetic pole, to avoid failures or oscillation at the startup. Therefore the sign of the phase currents is used to distinguish between north and south pole.

Briefly, the steps are:

- ❖ The stator is shortcircuited by a zero voltage vector applied to the inverter (Da=Db=Dc=100%)
- ❖ A short pulse step voltage is applied in the dc excitation circuit
- ❖ The induced stator currents are sampled
- ❖ Position is calculated after 50ms from the voltage pulse start, with the relationship (6.1)

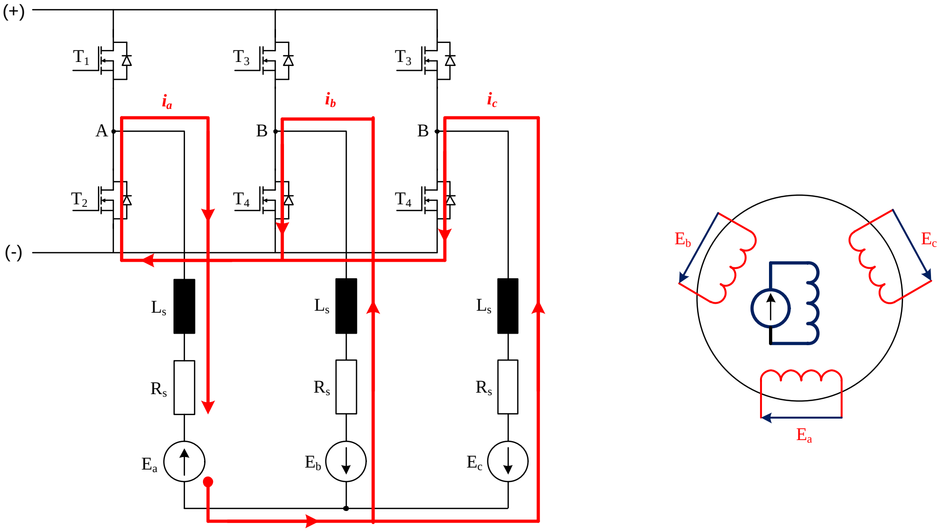

Fig. 6.10. Phase currents flowing path with the stator windings shortcircuited (zero voltage vector)

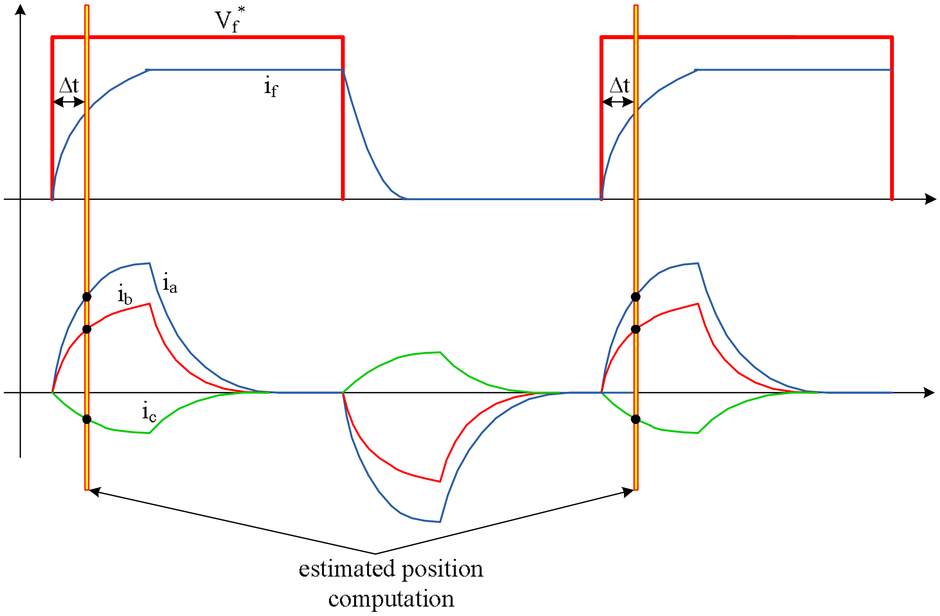

estimated position computation

Fig. 6.11. Initial rotor position estimation: phase currents, dc excitation pulse voltage and dc excitation current

$$i_\alpha = i_a \quad , \quad i_\beta = \left(i_a + 2i_b\right)/\sqrt{2} \quad , \quad i_s = \sqrt{i_\alpha^2 + i_\beta^2} \tag{6.1}$$
$$\hat{\theta}_{er} = \cos^{-1}\left(i_\alpha / i_s\right)$$

To validate the principles and the performance of this solution, experimental results were carried out on the testbench. In Fig. 6.12 and 6.13 two experimental results are shown. During the experiments the BEGA rotor has been moved by hand. This is the reason why the actual rotor position, measured with an incremental encoder, is not very linear. Errors in the range of [-12….12] electrical degrees were recorded. The pulse width of the applied dc excitation voltage was 0.3s. The initial rotor position was calculated after *Δt=1ms* from the beginning of the voltage pulse.

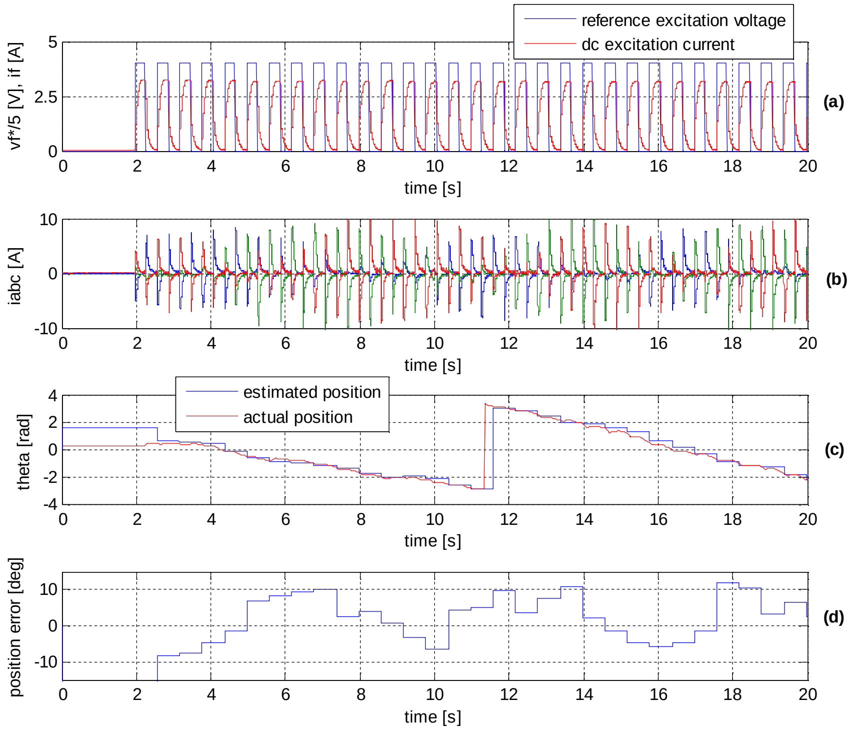

Fig. 6.12. Initial rotor position detection (position calculated at 1ms after voltage step): a) reference dc excitation voltage and actual dc excitation current, b) phase currents, c estimated and actual rotor position (electrical degrees) and estimated position error

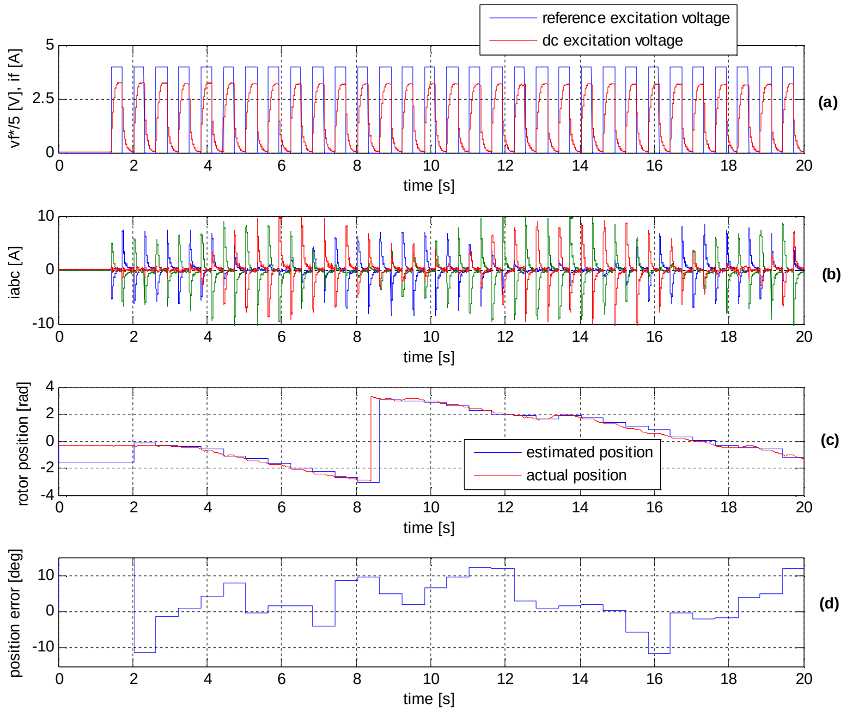

Fig. 6.13. Initial rotor position detection (position calculated at 1ms after voltage step): a) reference dc excitation voltage and actual dc excitation current, b) phase currents, c estimated and actual rotor position (electrical degrees) and estimated position error

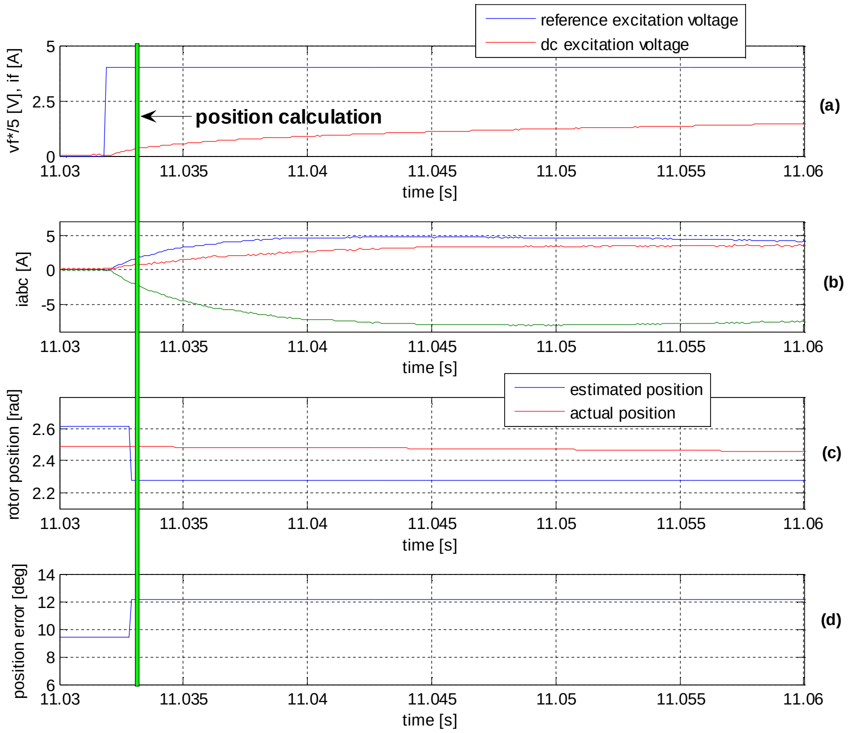

Fig. 6.14. Initial rotor position detection - zoom on Fig. 6.13: a) reference dc excitation voltage and actual dc excitation current, b) phase currents, c estimated and actual rotor position (electrical degrees) and estimated position error

In Fig. 6.15 are presented the experimental results for a rotor target position of 215 electrical degrees. The estimation position error is in a range of [-8…4] electrical degrees.

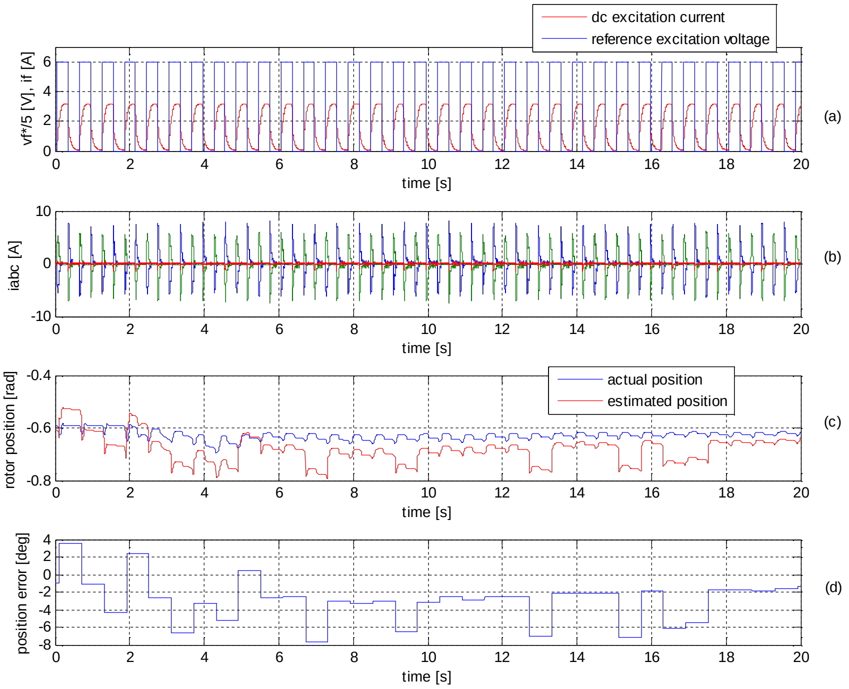

Fig. 6.15. Initial rotor position detection (position calculated at 50ms after voltage step): a) reference dc excitation voltage and actual dc excitation current, b) phase currents, c estimated and actual rotor position (electrical degrees) and estimated position error

The great advantage of the solution is that it has a good accuracy and the identification of north (or south) pole is very simple. The sensitivity to the inverter and machine parameters are minimum. The implementation is very simple, also. Rotor position identification takes less than 50ms.

SUMMARY

In this chapter an active-flux based motion sensorless control of BEGA is investigated based on simulation and experimental results. The active-flux observer, position and speed estimators are tested for a wide speed range. In a first step the investigations were performed by simulations in a speed range of 20 to 2000rpm. In the second step the proposed solution was validated on the real setup in a speed range of 50 to 2000rpm. In the low speed range, the performance of the observer is acceptable, but for speeds below 50rpm, problems rise during startup and speed reversal.

REFERENCES

[6.1] Y. Yan, J. G. Zhu, "A Survey of Sensorless Initial Rotor Position Estimation Schemes for Permanent Magnet Synchronous Motors"

[6.2] J. C. Moreira, "Indirect sensing for rotor flux position of permanent magnet AC motors operating in a wide speed range", Conference Record of the Industry Applications Society Annual Meeting,Volume , Issue , 2-6 Oct 1994 Page(s):401 – 407, vol.1

[6.3] Noguchi T., Yamada K., Kondo S., Takahashi I., Initial Rotor Position Estimation Method of Sensorless PM Motor with No Sensivity to Armature Resistance, Ieee Transactions on Ind. Electronics, Vol. 45, pp-118-125, 1998,

[6.4] M. Schroedl, "Detection of the Rotor Position of a Permanent. Magnet Synchronous Machine at Standstill", in Proc. of ICEM/1988, pp. 195–197, Pisa, Italy.

[6.5] M. Schroedl, "Sensorless control of AC machines at low speed and standstill based on the "INFORM" method", in Conf. Rec. IEEE-IAS Annual Meeting, vol. 1, pp. 270–277, San Diego, CA

[6.6] E. Robeischl, M. Schroedl, K. Salutt, "Improved INFORM-measurement Sequence and Evaluation for Sensorless Permanent Magnet Synchronous Motor Drives", Record of EPE-PEMC, Dubrovnik, 2002, Croatia

[6.7] A. B. Kulkarni, M. Ehsani, "A Novel Position sensor Elimination Technique for the Interior Permanent Magnet Synchronous Motor Drive," IEEE Trans. Ind. App., Vol. 28, No. 1, Jan/Feb. 1992, pp. 144-150.

[6.8] S. Kondo, A. Takahashi, T. Nishida, "Armature current locus based estimation method of rotor position of permanent magnet synchronous motor without mechanical sensor", Record of the 30th IEEE IAS Annual Meeting, 8-12 Oct. 1995

[6.9] N. Matsui, T. Takeshita, "A novel stating Method of Sensorless Salient Pole Brushless Motor", Conf. Record of IEEE. IAS Annual Meeting, 1994

[6.10] H. Kim, K.-K. Huh, R. D. Lorenz, and M. T. Jahns, "A Novel Method for Initial Rotor Position Estimation for IPM Synchronous Machine Drives", IEEE Trans. Ind. Appl., vol. 40, no. 5, pp. 1369–1378, Sep.-Oct. 2004.

[6.11] J. Holtz and H. Pan, "Acquisition of rotor anisotropy signals in sensorless position control systems," IEEE Trans. Ind. Appl., vol. 40, no. 5, pp. 1379–1387, Sep.-Oct. 2004.

[6.12] S. Shinnika, "New "Mirror-phase vector control" for sensorless drive of permanent magnet-magnet synchronous motor with pole saliency," IEEE Trans. Ind. Appl., vol. 40, no. 2, pp. 599–606, Mar./Apr. 2004.

[6.13] A. Consoli, G. Scarcella, G. Tutino, A. Testa, "Zero Frequency Rotor Position Detection for Synchronous PM Motors", Record of Power Electronics Specialists Conference, 2000

[6.14] I. Boldea, C. Rossi, G. D. Andreescu, A. Pillati, D. Casadei, "Active Flux Based Motion-Sensorless Vector Control of DC-Excited Synchronous Machines", submitted to ECCE2009, San Jose, USA

[6.15] I. Boldea, V. Coroban, G. D. Andreescu, F. Blaabjerg, "Active-flux based motion sensorless control of biaxial excitation generator/motor for automobiles (BEGA)", submitted to ECCE 2009, San Jose

7. EXPERIMENTAL PLATFORM AND SOFTWARE IMPLEMENTATION

This chapter discusses the experimental setup and software implementation used for testing of BEGA as starter-alternator with vector control. Although, the experimental setup has been described in the previous chapters, briefly, a more in detail description, in this chapter, is required.

7.1. Experimental platform

The block diagram and a picture of the real setup is shown in Fig. 7.1.

The main components of the experimental setup are:

- BEGA – electrical machine used for investigation
- Induction machine and ACS600 bidirectional inverter used as a load drive
- Three-phase inverter used to supply BEGA stator windings
- Dc-dc converter used to supply the dc excitation winding
- dSpace 1103 rapid prototyping system
- 4 x 12V, 55A valve regulated lea-acid batteries

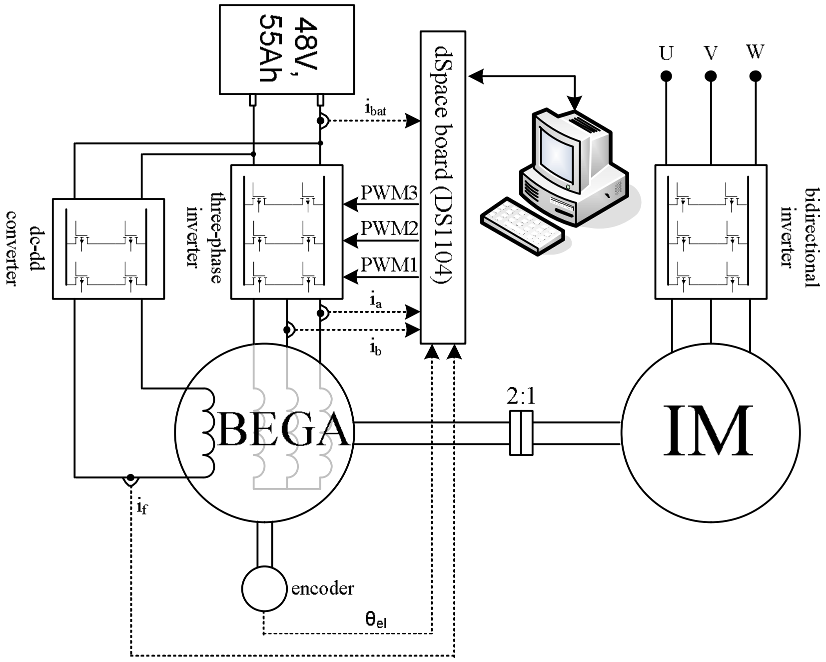

a)

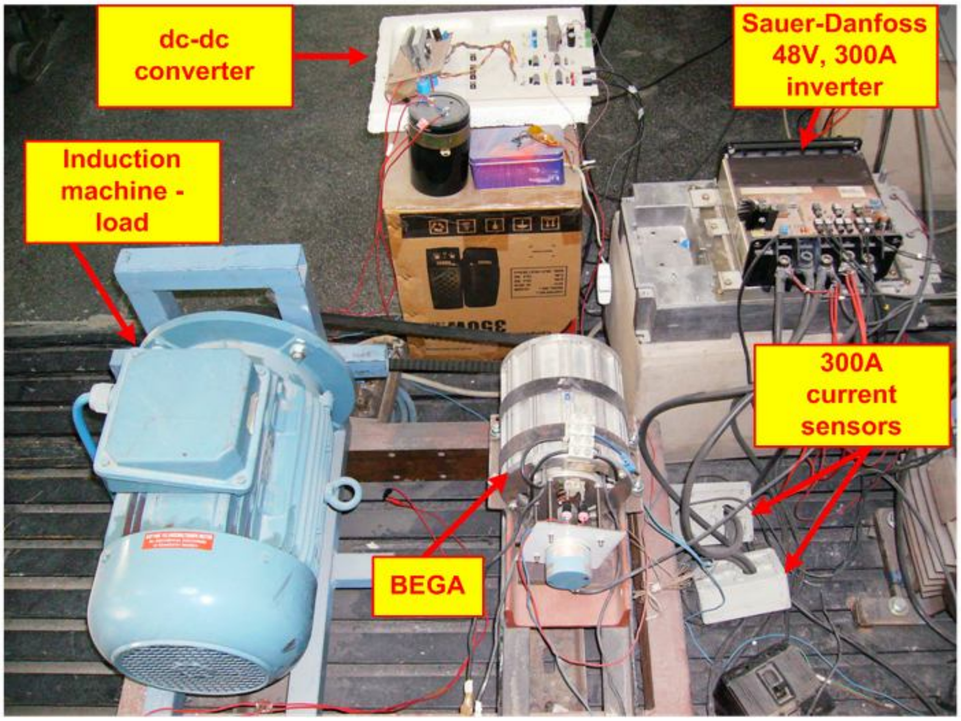

b)

Figure 7.1. Experimental setup for BEGA vector control driven: a) the scheme; b) the real setup containing the PM-RSM, the load machine, the belt-transmission, the batteries and the Sauer-Danfoss inverter

7.2. Induction machine and bidirectional power inverter

An induction machine driven by a bidirectional PWM converter has been used as a load for BEGA. The induction machine was sensorless driven. The inductiona machine specifications are given in Table 7.1. The bidirectional inverter is shown in Fig. 7.2. Three operation modes can be set via a remote control: sensorless speed control, sensorless torque control and V/f scalar.

Table 7.1. Induction machine specifications

Rated power [kW]	5.5
Rated voltage [V]	380
Rated current [A]	15
Rated speed [rpm]	2945
Rate torque [Nm]	17.2
Power factor	0.74

Fig. 7.2. Bidirectional three phase inverter ACS600

7.3. Three phase inverter

The three phase inverter is a Sauer-Danfoss inverter built for research activities – it is not a mass production inverter. The inverter is connected to the dSpace 1103 acquisition board via six fiber optics transmitter/receiver channels. Three channels are used for PWM, the fourth channel for enable, the fifth one for stop and the sixth one is used as a feedback for protection. The specifications of the inverter are given in Table 7.2. The switching frequency during experiments was set to 10kHz.

Table 7.2. Power inverter specification

Rated power	14 kW
Rated voltage	48V
Rated current [A]	300A
Switching frequency	10 kHz

7.4 Dc-Link Power Supply

The dc-link power supply voltage consists on four BOSCH valve regulated lead-acid batteries connected in series. The main specifications of the batteries are given in Table 7.3. A picture of the battery bank is shown in Fig. 7.3.

Table 7.3. Batteries specification

Manufacturer	BOSCH
Voltage [V] (100% SOC)	12.75
Maximum current [A]	450A

Fig. 7.3. 4x12V valve regulated lead acid batteries

7.5. Current measurement

The current measurement is performed using four sensors: three sensors on BEGA phases, one sensor in dc-link for battery current measurement as it is shown in Fig. 6.4. The current range is:
[-300...300]A. The link between current sensors and dSpace acquisition board, including voltage range is shown in Fig. 7.4. Between the current sensors and dSpace acquisition board an adaptation box (amplifier) is used to amplify the voltage from the output of current sensors.

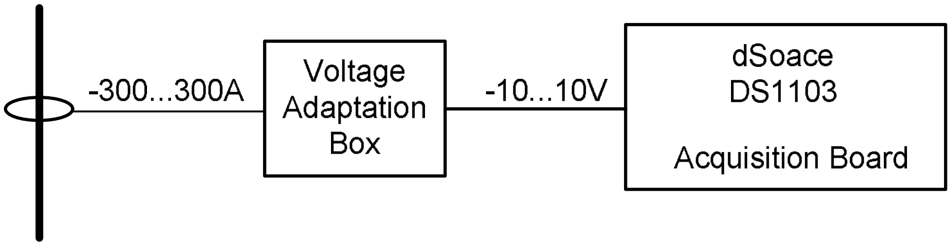

Fig. 7.4 Battery and phase currents measurement layout

The gain of the sensors is:

$$K = \frac{I_{sensor}}{V_{sensor}} = 38.6 \tag{7.1}$$

7.6. Position and speed measurement

To prove the sensorless position estimation techniques, a position estimator had to be included in the system. The chosen device was a Telemecanique encoder type XCC which provides a resolution of 5000 lines per revolution. The output is a usual A QUAD B (A+, A-, B+, B-, N+, N-) which can be directly connected to the control system as it provides encoder interfaces.

7.7. DC-DC converter for dc excitation

The dc-dc converter is used to supply the dc field excitation circuit. It is a four quadrant dc-dc converter. It is linked to dSpace 1103 control board via fiber optics transmitters/receivers SFH566. The operating principle was described in Chapter 3. the specifications of the converter are given in table 7.4. The built dc-dc converter is shown in Fig. 7.5.

Table 7.4. DC-DC converter specification

Rated power	500 W
Rated voltage	100 V
Rated current [A]	5A
Switching frequency	5 kHz

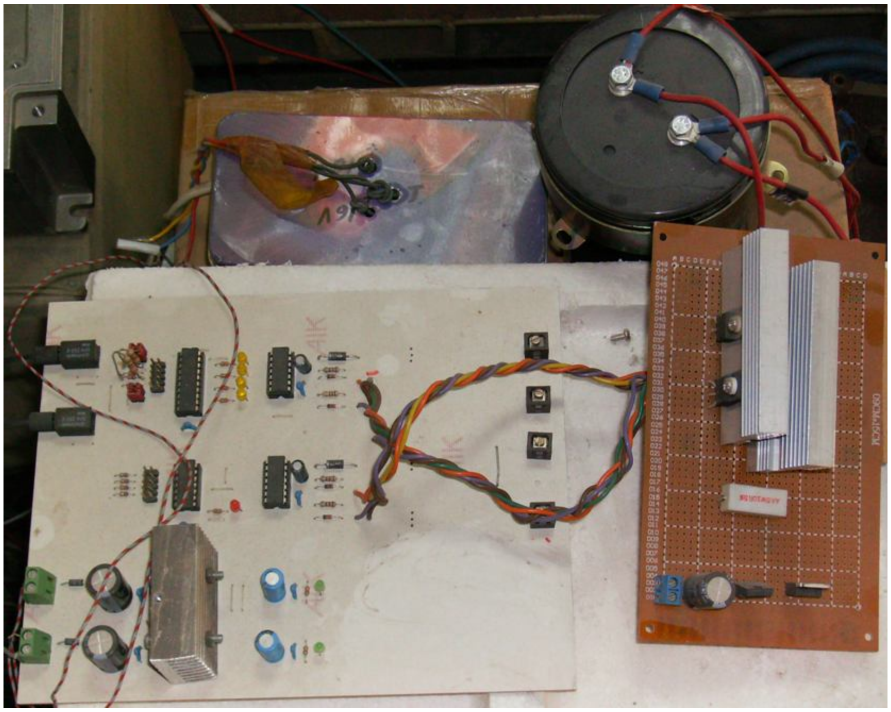

Fig. 7.5. 4-Quadrant DC-DC converter

7.8 Control hardware dSpace DS1103

The DS1103 PPC is a very flexible and powerful system featuring both high computational capability and comprenhensive I/O periphery. Additionally, it features a software SIMULINK interface that allows all applications to be developed in the MATLAB®/Simulink friendly environment. All compiling and downloading processes are carried out automatically in the background. A real-time interface called Control Desk, allows real-time management of the running process by providing a virtual control panel with instruments and scopes (Figure 7.8).

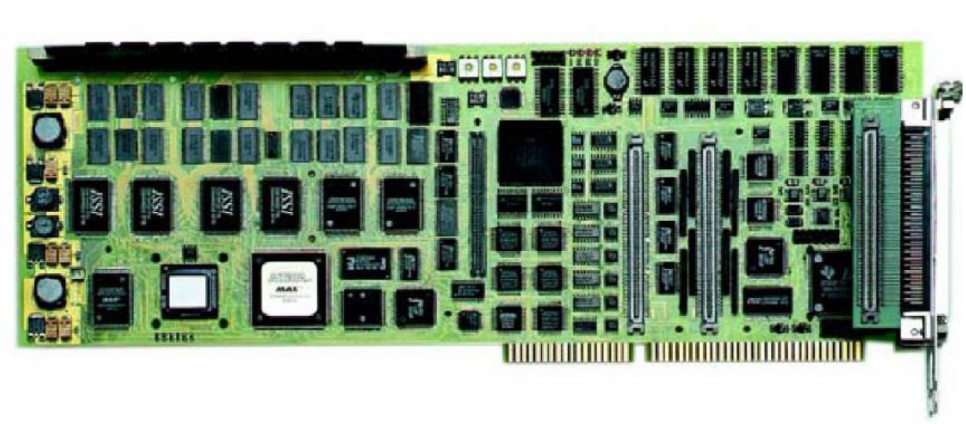

Fig. 7.6. The single board control system dSpace DS 1103

The DS1103 is a single board system based on the Motorola PowerPC 604e/333MHz processor (PPC), which forms the main processing unit.
The DSP subsystem, based on the Texas Instruments TMS320F240 DSP fixed-point processor, is especially designed for the control of electric drives. Among other I/O capabilities, the DSP provides 3-phase PWM generation making the subsystem useful for drive applications.

I/O Units

A set of on-board peripherals frequently used in digital control systems has been added to the PPC. They include: analog-digital and digital-analog converters, digital I/O ports (Bit I/O), and a serial interface. The PPC can also control up to six incremental encoders, which allow the development of advanced controllers for robots.

DSP Subsystem

The DSP subsystem, based on the Texas Instruments TMS320F240 DSP fixed-point processor, is especially designed for the control of electric drives. Among other I/O capabilities, the DSP provides 3-phase PWM generation making the subsystem useful for drive applications.

CAN Subsystem

A further subsystem, based on Siemens 80C164 micro-controller (MC), is used for connection to a CAN bus.

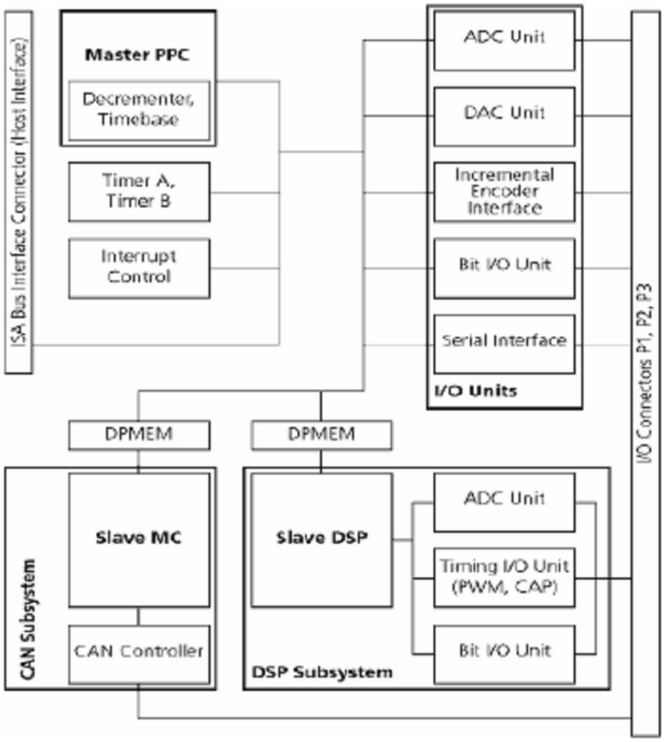

Legend:

ADC	Analog/Digital Converters
MC	CAN Microcontroller 80C164
CAP	Capture
DAC	Digital/Analog Converters
DPMEM	Dual-Port Memory
DSP	Digital Signal Processor TMS320F240
PPC	Power PC 604e Processor
PWM	Pulse Width Modulation

Fig. 7.7. DS1103 internal functional block diagram

Master PPC Slave DSP Slave MC

The PPC has access to both the DSP and the CAN subsystems. Spoken in terms of inter-processor communica-tion, the PPC is the master, whereas the DSP and the CAN MC are slaves.

The DS1103 PPC Controller Board provides the following features summarized in alphabetical order:

- A/D Conversion

ADC Unit providing:
- 4 parallel A/D-converters, multiplexed to 4 channels each, 16-bit resolution, 4 µs sampling time, ± 10V input voltage range
- 4 parallel A/D-converters with 1 channel each, 12-bit resolution, 800 ns sampling time ± 10V input voltage range

Slave DSP ADC Unit providing:
- 2 parallel A/D converters, multiplexed to 8 channels each, 10-bit resolution, 6 µs sampling time ± 10V input voltage range

- Digital I/O

Bit I/O Unit providing:
- 32-bit input/output, configuration byte-wise

Slave DSP Bit I/O-Unit providing:
- 19-bit input/output, configuration bit-wise

- CAN Support

Slave MC fulfilling CAN Specifications 2.0 A and 2.0 B, and ISO/DIS 11898.

- D/A Conversion

DAC Unit providing:
- 2 D/A converters with 4 channels each, 14-bit resolution ±10 V voltage range

- Incremental Encoder Interface

Incremental Encoder Interface comprising:
- 1 analog channel with 22/38-bit counter range,
- 1 digital channel with 16/24/32-bit counter range, and
- 5 digital channels with 24-bit counter range.

- Interrupt Control - Interrupt Handling.
- Serial I/O

Serial Interface providing:
- standard UART interface, alternatively RS-232 or RS-422 mode.

- Timer Services

Timer Services comprising:
- 32-bit downcounter with interrupt function (Timer A),
- 32-bit upcounter with pre-scaler and interrupt function
- 32-bit downcounter with interrupt function (PPC built-in Decrementer), and
- 32/64-bit timebase register (PPC built-in Timebase Counter).

- Timing I/O

Slave DSP Timing I/O Unit comprising:
- 4 PWM outputs accessible for standard Slave DSP PWM Generation,
- 3 x 2 PWM outputs accessible for Slave DSP PWM3 Generation and Slave DSP PWM-SV Generation
- 4 parallel channels accessible for Slave DSP Frequency Generation, and

- 4 parallel channels accessible for Slave DSP Frequency Measurement (F2D) and Slave DSP PWM Analysis (PWM2D).

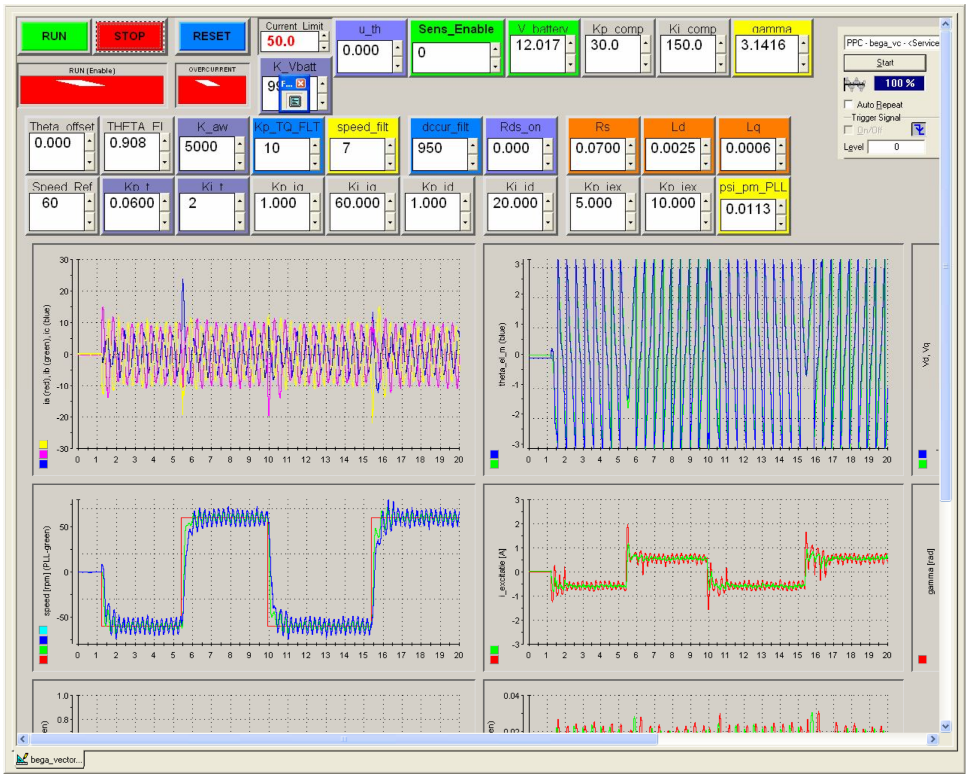

Current Limit 50.0
u_th 0.000
Sens_Enable 0
V_battery 12.017
Kp_comp 30.0
Ki_comp 150.0
gamma 3.1416
K_Vbatt 99
Level 0
Theta_offset 0.000
THETA_EL 0.908
K_aw 5000
Kp_TQ_FLT 10
speed_filt 7
dccur_filt 950
Rds_on 0.000
Rs 0.0700
Ld 0.0025
Lq 0.0006
Speed_Ref 60
Kp_t 0.0600
Ki_t 2
Kp_iq 1.000
Ki_iq 60.000
Kp_id 1.000
Ki_id 20.000
Kp_iex 5.000
Kp_iex 10.000
psi_pm_PLL 0.0113

Figure 7.8. dSpace Control Desk real-time interface

7.9 BEGA Control Software

The measure and protection is the first main part of the developed software and has three main parts (Fig. 7.9):
- signal acquisition and digital filtering of the acquired signals
- encoder interface
- protection

The speed control and position and speed estimator is the second main part of the software.

In the acquisition software (Fig. 7.10) the ADC channels are settled for acquiring the above discussed 4 currents and 1 voltage. The dc and phase currents are acquired on the 3 non-multiplexed A/D channels with 12-bit resolution, 800 ns sampling time. The dc excitation current and battery voltage are acquired on the multiplexed channels with 16-bit resolution, 4 μs sampling time. The acquisition process is triggered with the help of the slave-DSP timer interrupt with the same frequency as the switching (10 kHz).

Afterwards the measured quantities are scaled taking into account the scaling factors of the sensors. The third phase current is calculated from the two measured. The current protection implementation is shown in Fig. 7.11.

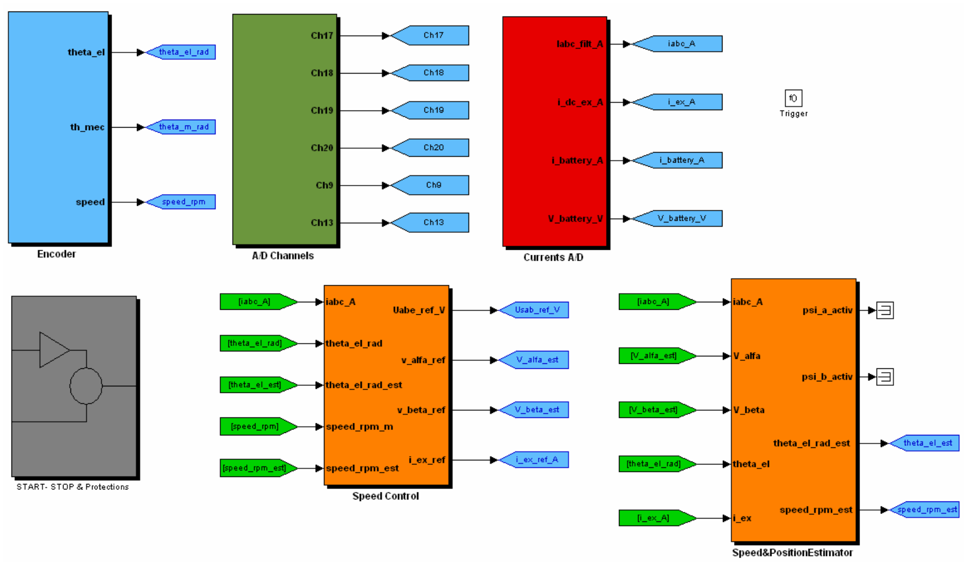

Fig. 7.9. Control software in Matlab-Simulink: encoder, current acquisitions, current protection, speed control algorithm, position and speed estimator

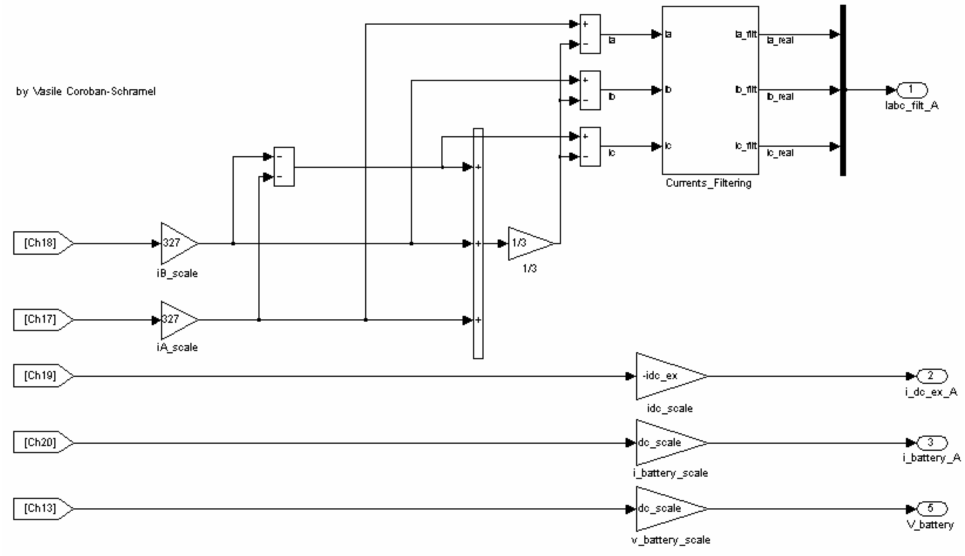

Fig. 7.10. Currents and voltage measurement

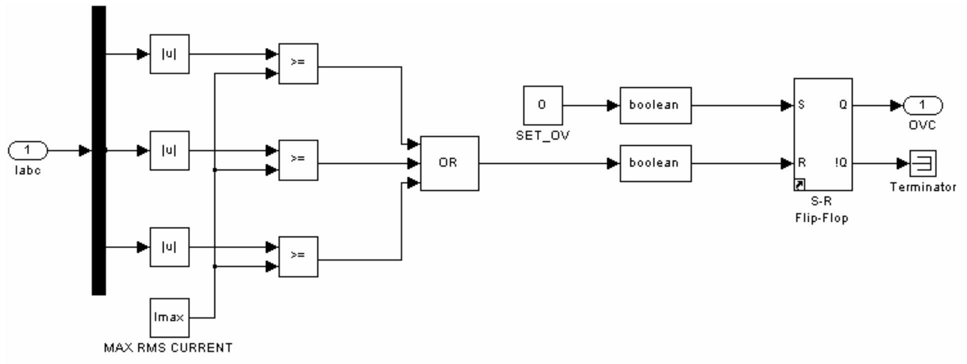

Fig. 7.11. Current protection implementation

In the encoder interface the electrical rotor position of the rotor and its speed are calculated. This could be done counting the pulses coming on the dedicated hardware interface and knowing the resolution of the encoder (number the pulses for one revolution) and the sampling time the encoder is “readed” with.

The space vector implementation, dc excitation controller and the link between the speed controller and PWM channels connected to the dc-dc excitation converter, via two optic fibers, is shown in Fig. 7.12.

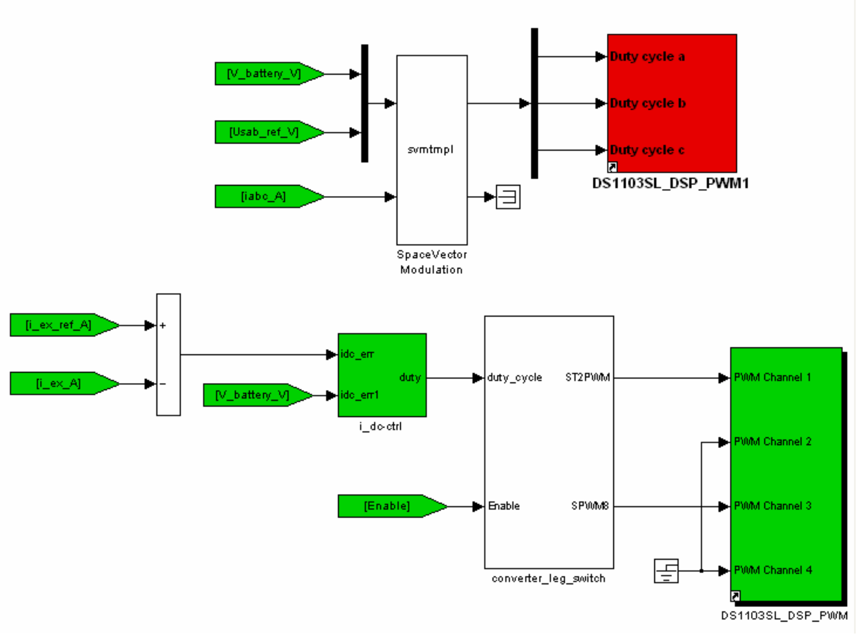

Fig. 7.12. Control software in Matlab-Simulink: space vector modulation connected to the three phase inverter PWM channels (DS1102SL_DSP_PWM1) and dc excitation controller connected to the dc-dc converter PWM channels (DS1102SL_DSP_PWM1)

SUMMARY

The experimental test platform used during the testing of BEGA with vector control was presented in this chapter. All hardware components of the testbench were presented. The software was implemented in Matalb-Simulink and with Real-Time-Workshop and automatic code was generated which was later flashed on the microprocessor. Control-Desk, a real-time interface was used to control the machine and to acquire all signal considered relevant.

-

8. CONCLUSION AND CONTRIBUTIONS

8.1. Conclusion

The present work is dedicated to the advanced control of biaxial excitation generator for automobiles proposed as integrated starter/alternator system for hybrid electric vehicle. The valve regulated lead acid batteries, a modern topic in automobiles industry, was approached, also.

Based on the results presented in the thesis, the main conclusions are summarized as follows:

- The number of automotive applications that use electric actuators, instead of conventional hydraulic and pneumatic actuators, has increased in the last decade. The “X-by-wire” technology has a great potential in the future and is expected to witness considerable growth in the next years. At the moment due to safety and reliability concerns the automotive manufacturers are cautious regarding the adoption of this technology.
- Battery management systems are request in modern and hybrid electric vehicles in order to prolong the battery life and to manage properly the electric power distribution in the vehicles. Battery state-of-charge, battery state-of-health, battery charge/discharge capability, battery overcharging and overdischarging are key function of a battery management systems. All these functions demand the knowledge with a high accuracy of the battery internal resistance.
- Battery internal resistance is state-of-charge, state-of-health and temperature dependent. With so many dependencies relationship, it is obvious that the internal resistance must be estimated on-line.
- Battery state-of-charge estimation is a challenge in automotive industry since electrochemical batteries are highly complex non-linear systems and an accuracy of minimum 5% is requested for battery state-of-charge estimation.
- Investigations on the battery internal resistance measurement (estimation) were performed. It was shown that the accuracy of internal resistance estimation is increasing with increasing of battery current discharge slope.
- A novel on-line and self-reconfigurable battery state-of-charge algorithm, for battery state-of-charge, has been introduced.
- BEGA is capable of unity power factor operation with zero id and zero Ψq both in motoring and generating.
- BEGA has a very large constant power speed range, theoretically to infinite. A constant power speed range up to 8 has been proved with the machine supplied at ¼ from the rated voltage
- A current referencer has been proposed to minimize the total copper losses in the machine. This way the efficiency of the machine is improved with the penalty of a lower power factor

- With zero id, the torque response of the machine is not fast due to the larger time constant of the dc excitation
- With non zero id during an error in the dc field current the torque response quickness is improved
- A sensorless control strategy based on the “active flux concept” has been introduced. Very good results were obtained for medium and high speeds. In the low speed range the position estimator worked satisfactorily down to 0rpm.

8.2. Original contributions

The present thesis includes, from the author, point of view, the following original contributions:

- An overview of the automotive electrification trends;
- Development of an high accuracy method for battery internal resistance measurement necessary in the battery management system used in modern automobiles and hybrid electric vehicles
- Development and implementation of a novel on-line battery state-of-charge algorithm for valve regulated lead acid batteries
- Development of a Matlab-Simulink® model for investigation of BEGA performance during transients and steady state. The model includes: BEGA modeled based on the dq equations, three-phase inverter with the dead time and voltage drop on the transistors, dc-dc converter for the dc excitation, vector control strategy;
- Implementation of a vector control strategy for BEGA
- Development of a control strategy that allows BEGA to operate at unity power factor for motoring and generating
- A current referencer used to minimize the total copper losses in BEGA
- Torque improvement strategy based on no-zero id during transients
- Introducing of the “active flux” concept for BEGA
- Development and implementation of a sensorles vector control strategy for BEGA operation in a wide speed range, from 50rpm to 3000rpm

Author's papers related to the Ph. D. thesis

[1] V. Coroban, I. Boldea, G.D. Andreescu, F. Blaabjerg, "BEGA - Motor/generator Vector Control for Wide Constant Power Speed Range", in Proc. 10th Int. Conf. on Optimization of Electrical and Electronic Equipment OPTIM 2006, Brasov, 18-19 May, 2006.

[2] V. Coroban, I Boldea, "Valve-Regulated Lead-Acid. Batteries Characterization for Hybrid Electric Vehicles", in Proc. 10th Int. Conf. on Optimization of Electrical and Electronic Equipment OPTIM 2006, 18- 19 May, Brasov 2006, Romania

[3] V. Coroban, I. Boldea, F. Blaabjerg, "A Novel on-line State-of-Charge Estimator Algorithm for Valve Regulated Lead-Acid Batteries used in Hybrid Electric Vehicles", Proc. ACEMP'07 & Electromotion'07, Bodrum, Turkey, pp.39-47, Sept. 2007.

[4] I. Boldea, V. Coroban-Schramel, G.-D. Andreescu, S. Scridon, F. Blaabjerg, "BEGA starter/alternator – Vector Control Implementation and Performance for Wide Speed Range at Unity Power Factor", Proc. IEEE-IAS 2008, 43nd IAS Annual Meeting, Industry Applications Conference

[5] I. Boldea, V. Coroban-Schramel, G.-D. Andreescu, S. Scridon, F. Blaabjerg, "BEGA starter/alternator – Vector Control Implementation and Performance for Wide Speed Range at Unity Power Factor", accepted for publication in IEEE Trans. On Industry Applications

[6] V. Coroban, I. Boldea, G. D. Andreescu, "Active-flux Based Observer for Motion Sensorless Control of Biaxial Excitation Generator/Motor for Automobiles (BEGA)", CNAE Sept. 2008

[7] I. Boldea, V. Coroban, G. D. Andreescu, F. Blaabjerg, "Active-flux Based Motion Sensorless Control of Biaxial Excitation Generator/Motor for Automobiles (BEGA)", submitted to ECCE 2009, San Jose